NTNU – Trondheim
Norwegian University of
Science and Technology

Impact Against Offshore Pipelines

Tom Inge Asheim
Ivar Mogstad

Civil and Environmental Engineering
Submission date: June 2013
Supervisor: Tore Børvik, KT
Co-supervisor: Martin Kristoffersen, KT
Magnus Langseth, KT

Norwegian University of Science and Technology
Department of Structural Engineering

Department of Structural Engineering
Faculty of Engineering Science and Technology
NTNU- Norwegian University of Science and Technology

ACCESSIBILITY

OPEN

MASTER'S THESIS 2013

SUBJECT AREA:	DATE:	NO. OF PAGES:
Computational Mechanics	09 June 2013	16 + 148 + 33

TITLE:

Impact Against Offshore Pipelines

BY:

Tom Inge Asheim
Ivar Mogstad

SUMMARY:
Impact against offshore pipelines is investigated in this thesis. Introductory low velocity experiments on pipeline specimens using the stretch bending rig at the Department of Structural Engineering, NTNU, were carried out. A wedge shaped indenter, previously used for impact tests on similar pipelines, were used to subject pipes to bending. The experimental set-up allowed for application of axial loads and inner pressure to pipes during bending. This thesis is a continuation of three previous master's theses and is part of a ongoing research program between CRI-SIMLab, NTNU, and Statoil ASA.

Three pipes were tested in the stretch bending rig while being subjected to different axial loads during bending. The pipes were first bent at a low velocity of 25 mm/min before being stretched. A slight relative rotation of the connection between the pipe and the rig was discovered for experiments with applied axial loads. This affected the measurements. Surface cracks were discovered in the indentation zone for all pipes after stretching. Experiments involving pressurized pipes were planned, but were not conducted due to issues with pipe delivery.

Numerical analyses were performed using Abaqus/Explicit. Material models calibrated in previous theses were used, and implemented in numerical models using SIMLab Metal Model. Simulations corresponded well with the bending step of the pipes, but the stiffness was overestimated by numerical analyses of the stretch step. Numerical analyses revealed that pipes subjected to axial loads during bending experienced less strain in the critical area of the indentation zone, where cracks occurred in the experiments.

The indentation zones of the pipeline specimens were studied metallurgically. It was discovered that surface cracks initiated in lathing grooves that originated from the lathing process of the pipes. No significant internal fracturing was discovered. The results were compared to findings from a similar study on pipes subjected to impact loading. It was found that the bending experiments with subsequent stretching failed to recreate the same fracture mechanisms as discovered in impacted pipeline specimens.

RESPONSIBLE TEACHER: Tore Børvik
SUPERVISOR(S): Tore Børvik, Martin Kristoffersen and Magnus Langseth
CARRIED OUT AT: Norwegian University of Science and Technology (NTNU)

Institutt for konstruksjonsteknikk
Fakultet for ingeniørvitenskap og teknologi
NTNU- Norges teknisk- naturvitenskapelige universitet

TILGJENGELIGHET

ÅPEN

MASTEROPPGAVE 2013

FAGOMRÅDE:	DATO:	ANTALL SIDER:
Beregningsmekanikk	09 Juni 2013	16 + 148 + 33

TITTEL:

Støt på offshore rørledninger

BY:

Tom Inge Asheim
Ivar Mogstad

SAMMENDRAG:
I denne oppgaven blir støt mot offshore rørledninger med stålkvalitet X65 undersøkt. Innledende lavhastighetsforsøk på rør ved bruk av en strekkbøyerigg ble gjennomført ved Institutt for konstruksjonsteknikk, NTNU. Et kilformet stållegme, tidligere benyttet i støtforsøk på lignende rør, ble benyttet til bøying av rør. Det eksperimentelle oppsettet gjorde det mulig å påføre rør aksiale laster og indre overtrykk under bøying. Denne oppgaven er en videreføring av tre tidligere masteroppgaver, og er en del av et pågående forskningsprosjekt mellom CRI-SIMLab, NTNU, og Statoil ASA.

Tre rør ble testet i strekkbøyeriggen, der de ble påført forskjellige aksiale laster under bøying. Rørene ble først bøyd med en lav hastighet på 25mm/min, før de ble strukket ut. Det ble oppdaget en liten rotasjon i forbindelsen mellom rørendene og riggen for forsøkene hvor det ble påført aksiallast, noe som påvirket målingene. Overflatesprekker ble funnet i bøyesonen for alle rør etter strekking. Det ble planlagt å gjøre forsøk på trykksatte rør, men disse ble ikke gjennomført grunnet problemer med rørleveransen.

Numeriske analyser ble utført med Abaqus/Explicit. Det ble benyttet materialmodeller som hadde blitt kalibrert i tidligere masteroppgaver. Disse materialmodellene ble implementert i de numeriske analysene ved bruk av SIMLab Metal Model. De numeriske simuleringene av bøyingen samsvarte bra, men stivheten ble overestimert for simuleringer av strekkingen. Numeriske analyser viste at rør som ble utsatt for aksiale laster gjennomgikk mindre tøyning i de mest utsatte sonene, hvor sprekker oppstod i eksperimentene.

Metallurgiske undersøkelser av de mest deformerte sonene viste at overflatesprekkene oppsto i riller på røroverflaten. Rørene var dreide, og rillene var spor fra dreiingen av rørene. Det ble ikke funnet noe betydelig indre brudd i noen av rørene. Disse resultatene ble sammenlignet med en tilsvarende metallurgisk undersøkelse fra rør som hadde blitt utsatt for støtlast. Det ble funnet at rørene som ble testet i strekkbøyeriggen ikke gjenskapte de samme bruddmekanismene som oppstod i rør utsatt for støtlast.

FAGLÆRER: Tore Børvik
VEILEDER(E): Tore Børvik, Martin Kristoffersen og Magnus Langseth
UTFØRT VED: Norges Teknisk Naturvitenskapelige Universitet (NTNU)

Department of Structural Engineering

FACULTY OF ENGINEERING SCIENCE AND TECHNOLOGY
NTNU – Norwegian University of Science and Technology

MASTER THESIS 2013

for

Tom Inge Asheim og Ivar Mogstad

Impact against offshore pipelines

Støt på offshore rørledninger

Following the discussions with the Norwegian offshore industry, there is a need for new insight and more competence regarding the behaviour, modelling and design of subsea structures exposed to impact loading caused by e.g. trawler gear and falling objects. Experimental tests and metallurgical studies have shown that such impacts can lead to cracking in the pipe wall, which may be very difficult to detect through inspections. If such fractures are allowed to develop, it can lead to serious economic and environmental consequences. In this master thesis low velocity impact loads on pipelines should be studied by doing idealized experiments in a new test rig. Experiments are to be conducted in combination with advanced numerical simulations. The long term goal of this research is to be able to predict the likelihood of fracture after low velocity impact against offshore pipelines. The present study is part of an on going research programme between CRI-SIMLab, NTNU, and Statoil ASA.

The master thesis should contain the following main activities:

1. Literature study: Previous works regarding impact against offshore pipelines, various numerical methods and models, material- and fracture models.
2. Experimental tests: A new test rig should be utilized for idealized tests on pipeline specimens. The experimental tests should be sufficiently instrumented, and the experimental data should be validated against earlier test results. Metallurgical investigations of the tested specimens should be conducted, and compared with previously tested specimens.
3. Numerical simulations: Non-linear finite element analyses of the experiments should be conducted. Previously calibrated material models should be used in accordance with the SIMLab Metal Model.
4. Validation and reporting: Simulations are to be verified versus experimental data.

Supervisors: Tore Børvik, Martin Kristoffersen and Magnus Langseth

The thesis must be written according to current requirements and submitted to the Department of Structural Engineering, no later than June 10th, 2013.

NTNU, January 16th, 2013

Tore Børvik
Professor

Preface

This thesis was written in the spring of 2013 and submitted as a requirement for the degree of Master of Science in Civil and Environmental Engineering, with a specialization in Computational Mechanics at the Norwegian University of Science and Technology. The problem statement was formulated by the Structural Impact Laboratory (SIMLab) at the Department of Structural Engineering.

Trondheim, June 9, 2013

Tom Inge Asheim

Ivar Mogstad

Acknowledgements

We would like to thank our supervisors Professor Tore Børvik and PhD Candidate Martin Kristoffersen. Through weekly meeting they provided encouragement and guidance which were highly appreciated. Kristoffersen also provided us with necessary input concerning numerical analysis by use of SALOME. In addition, we would like to thank Professor Magnus Langseth for valuable input regarding the experiments. We thank Håvard Ilstad at Statoil ASA for providing pipeline specimens for experimental tests.

Part of this thesis was to use and test SIMLab Metal Model for Abaqus/Explicit. This would not have been possible without David Morin, who always were available to answer questions and provided great insight to mechanics of materials. We would also like to thank Professor Torodd Berstad for input considering numerical models and for quickly updating computer resources for the purpose of this thesis. PhD Candidate Vegard Aune, who wrote a thesis on the same matter during the spring of 2012 is also appreciated for providing insight for previous work.

Professor Arild Clausen had previously used the stretch bending rig for his Dr.ing thesis and provided valuable knowledge concerning the rig. A great thanks also goes to Trond Auestad for performing the experiments and Tore Wisth for preparing the pipeline specimens for testing.

Egil Fagerholt set up DIC for the experiments and processed the data, making it available for us to easily implement results into our thesis. He spent many hours working for the purpose of this thesis and is greatly appreciated. We would also like to thank Dr. Ida Westermann for conducting the metallurgical study and providing great insight regarding the topic.

Last but not least, we would like to thank Kristian Lauknes, whom we shared office with. Through discussions he provided valuable insight to practical issues concerning the experiments.

Abstract

Impact against offshore pipelines is investigated in this thesis. Introductory low velocity experiments on pipeline specimens using the stretch bending rig at the Department of Structural Engineering, NTNU, were carried out. A wedge shaped indenter, previously used for impact tests on similar pipelines, were used to subject pipes to bending. The experimental set-up allowed for application of axial loads and inner pressure to pipes during bending. This thesis is a continuation of three previous master's theses and is part of a ongoing research program between CRI-SIMLab, NTNU, and Statoil ASA.

Three pipes were tested in the stretch bending rig while being subjected to different axial loads during bending. The pipes were first bent at a low velocity of $25mm/min$ before being stretched. A slight relative rotation of the connection between the pipe and the rig was discovered for experiments with applied axial loads. This affected the measurements. Surface cracks were discovered in the indentation zone for all pipes after stretching. Experiments involving pressurized pipes were planned, but were not conducted due to issues with pipe delivery.

Numerical analyses were performed using Abaqus/Explicit. Material models calibrated in previous theses were used, and implemented in numerical models using SIMLab Metal Model. Simulations corresponded well with the bending step of the pipes, but the stiffness was overestimated by numerical analyses of the stretch step. Numerical analyses revealed that pipes subjected to axial loads during bending experienced less strain in the critical area of the indentation zone, where cracks occurred in the experiments.

The indentation zones of the pipeline specimens were studied metallurgically. It was discovered that surface cracks initiated in lathing grooves that originated from the lathing process of the pipes. No significant internal fracturing was discovered. The results were compared to findings from a similar study on pipes subjected to impact loading. It was found that the bending experiments with subsequent stretching failed to recreate the same fracture mechanisms as discovered in impacted pipeline specimens.

Contents

1 Background and Motivation

There is great risk related to transport of oil and gas using offshore pipelines. If such pipes should be damaged, a leak can be hard to detect and repairs difficult to conduct. Offshore pipelines may be subjected to impact by objects such as trawling gear, falling object and anchors from ships. Interference between trawl gear and pipelines is to an extent covered by guidelines developed by Det Norske Veritas (DNV) [1]. However, a special case is when a hooking first causes a pipeline to be dragged along the seabed, resulting in development of large axial forces in the pipe. When the hooking object is released these axial forces cause the pipe to spring back towards its initial positions. This leads to a complex stress/strain history in the material and the case is inadequately covered by DNV's guidelines.[1]

Such an incident happened at the Kvitebjørn gas field, which is operated by Statoil, in the autumn of 2007. Impact and hooking was caused by an anchor dropped by a ship and the pipeline was dragged along the seabed. The anchor chain eventually snapped, causing the pipeline to rebound due to the present axial forces. Damage to the pipe was detected during an inspection and production was shut down. The anchor and the damaged pipe can be seen in Figure 1.1. Production resumed in January 2008 as investigations concluded that the pipeline retained sufficient residual strength. During a routine inspection in August 2008 a gas leak was discovered. This led to a production shut down until repairs were finished in January 2009.[2, 3]

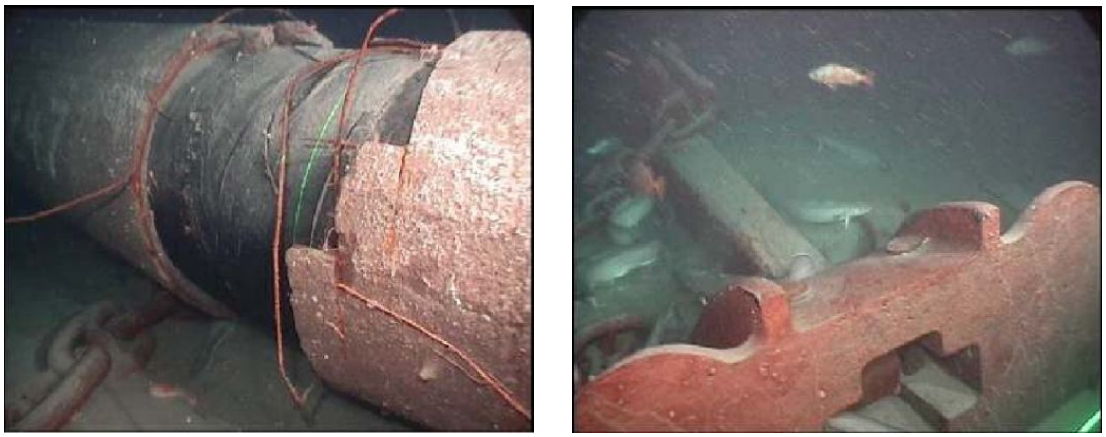

(a) Damaged pipeline (b) Anchor

Figure 1.1: Damaged pipeline at the Kvitebjørn Field. [2]

Such incidents have created a need for new insight and more competence regarding the behaviour, modelling and design of subsea structures exposed to impact loading caused by e.g. trawler gear and falling objects. Experimental tests and metallurgical studies have shown that such impact loads on pipelines can lead to cracking in the pipe wall, which may be very difficult to detect through inspections [4]. If such fracturing is allowed to develop, it can lead to serious economic and environmental consequences.

This thesis is part of an ongoing research program at CRI SIMLab, in cooperation with Statoil ASA. The research program is motivated by a need of further knowledge related to calculating residual strength in damaged offshore pipelines. Three master's theses have previously been delivered on this subject. Slåttedalen and Ørmen [5] delivered the first master's thesis in the spring of 2010. Their work was continued by Fornes and Gabrielsen [6] in 2011 and Aune and Hovdelien [7] in 2012.

Slåttedalen and Ørmen [5] established an experimental set-up for scaled pipelines in an attempt to recreate the scenario that occurred at the Kvitebjørn field. As the Kvitebjørn incident was complex it was difficult to recreate directly in a laboratory. Therefore, the issue was simplified and experiments were carried out in two steps. First, the pipes were exposed to impact loads by a wedge-shaped indenter using the pendulum accelerator [8], also known as the kicking machine, at the Department of Structural Engineering, NTNU. This was to represent the impact and hooking phase. Thereafter, the pipes were stretched at Statoil's laboratory in Trondheim. This was to represent the rebound due to axial forces in the pipes. Figure 1.2 shows the experimental set-up for the two different experiments.

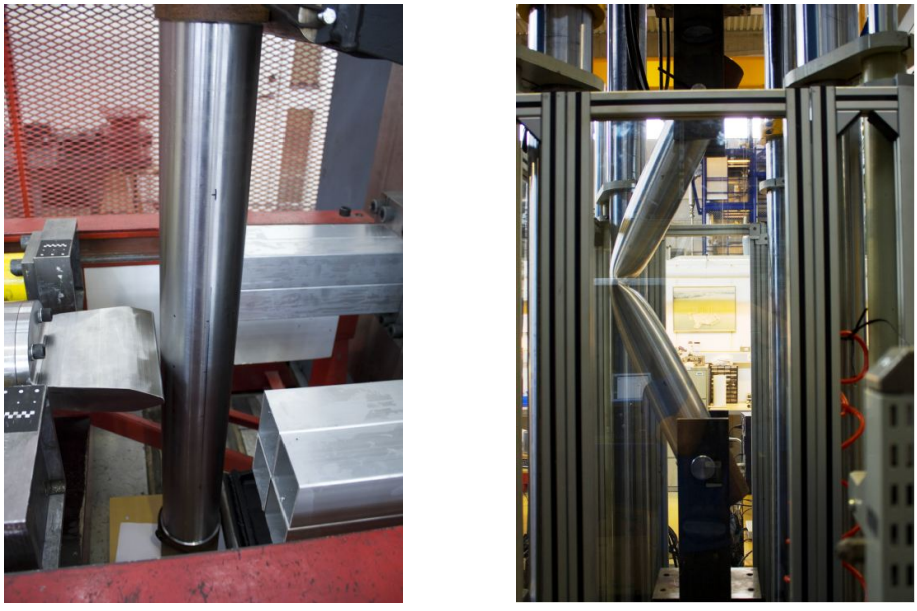

(a) Set-up for impact step

(b) Set-up for stretch step

Figure 1.2: Experimental setup used in previous theses. [5]

The three previous master's theses [5, 6, 7] used this experimental set-up to conduct impact tests on pipelines with steel grade X65. Material tests were carried out and material models used in numerical simulations were calibrated in attempts to recreate the material behaviour of X65 steel pipelines. In additions, a metallurgical investigation of impacted pipes was conducted to examine the microstructure of the deformed pipes in order to better understand and investigate incipient fracture.

In the scenario were an offshore pipeline is hooked and dragged out of it initial position, axial forces build up during the deformation of the pipeline. In order to further investigate this, a stretch bending rig that allows for application of axial loads during low velocity bending of specimens is used to conduct experiments on pipes in this thesis. The rig set-up also allows for application of inner water pressure in the pipeline specimens, but experiments with inner pressure were not conducted due to issues with delivery of pipes. Numerical models are established in order to further investigate the experiments. In addition, metallurgical investigations, where the main interest was incipient fracture in the pipes, were carried out and compared to findings in impacted pipes. In agreement with the supervisor, it was also decided to make a thorough recap of the previous master's theses regarding impact on offshore pipelines. The thesis is organized as follows:

Chapter 2, Theory: Gives an introduction to the theoretical basis needed to understand the material behaviour during bending of pipeline specimens. Previous findings from experiments of tubes are presented, followed by theory regarding mechanics of materials and fracture mechanics. In addition theory concerning the finite element method is presented, which is needed in the establishment of numerical models.

Chapter 3, Previous Work: Presents a recap of the three previous master's theses delivered on the same subject as this thesis. In addition, a brief presentation on work concerning low-velocity impact of pressurized pipes is presented.

Chapter 4, Material Model: Gives a brief introduction to the SIMLab Metal Model and MatPrePost, and how these tools may be used to implement material models in numerical finite element simulations. In this chapter the material input for numerical simulations in this thesis is established.

Chapter 5, Preliminary Studies: Presents the experimental set-up for the stretch bending rig and what modifications that needed to be made in order to conduct experiments on pipeline specimens. In addition, preliminary numerical simulations and their respective findings are presented.

Chapter 6, Experimental Tests: Performed experiments are presented with their respective results. This chapter also contains descriptions of the pipe measurements, load cell calibrations and Digital Image Correlation which was utilized in the experiments. In addition, findings from the metallurgical investigation are presented.

Chapter 7, Numerical Simulation: Presents finite element analyses of the experiments

carried out using Abaqus/Explicit. The effects of applying axial force and inner pressure during bending is also investigated.

Chapter 8, Discussion: Gives a comparison of results obtained from the experimental tests and the numerical simulations. This chapter also presents a discussion concerning findings from the metallurgical investigations carried out in this thesis compared with previous metallurgical studies on similar pipelines subjected to impact.

Chapter 9, Conclusion: Presents a short summary and assessments of the results from the experimental and numerical work.

Chapter 10, Further Work: Suggestions for further work concerning the experiments and numerical analyses.

2 Theory

Impact against offshore pipelines is a complex problem. In this thesis the matter is investigated by conducting low velocity experiments where simply supported pipes are bent by a wedge shaped indenter. This leads to large plastic deformations in the specimen. The objective of this chapter is to give an introduction to the theoretical basis needed to understand the material behaviour for large deformations. Previous findings regarding different modes of deformation that occur in such circumstances are presented in the following section. Theory regarding mechanics of materials and fracture mechanisms, which is necessary to investigate the experiments and to perform numerical simulations, are then presented. Finally, this chapter presents theory regarding the finite element method, which is needed in the establishment of numerical models.

2.1 Deformation of Simply Supported Circular Tubes

Thomas and co-workers [9, 10, 11] conducted a series of quasi-static experiments on simply supported circular tubes under transverse loading from a wedge-shaped indenter, where the behaviour up to the point of maximum load was examined. An Avery test machine was used, and the test set-up is seen in Figure 2.1

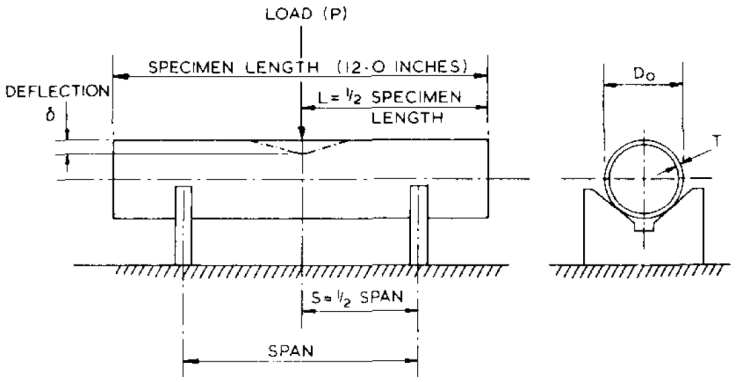

Figure 2.1: Experimental set-up for bending of thin-walled tubes. [9]

The experiments consisted of three groups:

1. Tests with various initial diameters D_0 and thickness's T at a fixed span.
2. Tests with various D_0/T-ratios at a fixed span, and almost constant diameter.
3. Tests with various D_0 and T values, at various spans.

Aluminum tubes were used in groups 1 and 2, while both aluminum and steel tubes were used in group 3 [9]. The force-displacement curves from group 1 are shown in Figure 2.2(b). During these tests three modes of deformation were identified, and they are illustrated in Figure 2.2(a).

- Pure crumpling mode:
  Initially, localised crumpling at the top surface of the tubes was observed. During this period the force increased quite rapidly until deformation occurred at the bottom of the tubes, as seen in Figure 2.2(b). The force at which this occurred was denoted P_B. This force is the maximum pure crumpling load or, alternatively, the force at which the pure crumpling mode changes to one of both crumpling and bending.
- Bending and crumpling mode:
  The secondary mode of deformation involves further crumpling in combination with bending of the tubes. During this period the slope of the force-displacement curve decreased slightly. This is seen in Figure 2.2(b). The force increased further until maximum force P_{max} was reached.

- Structural collapse:
  After reaching maximum force P_{max} the tubes collapsed, resulting in decreasing force. This collapse mode was characterized by large rotations of the tube ends. Four different sizes of tubes was considered in this test group, and all exhibited the same modes.

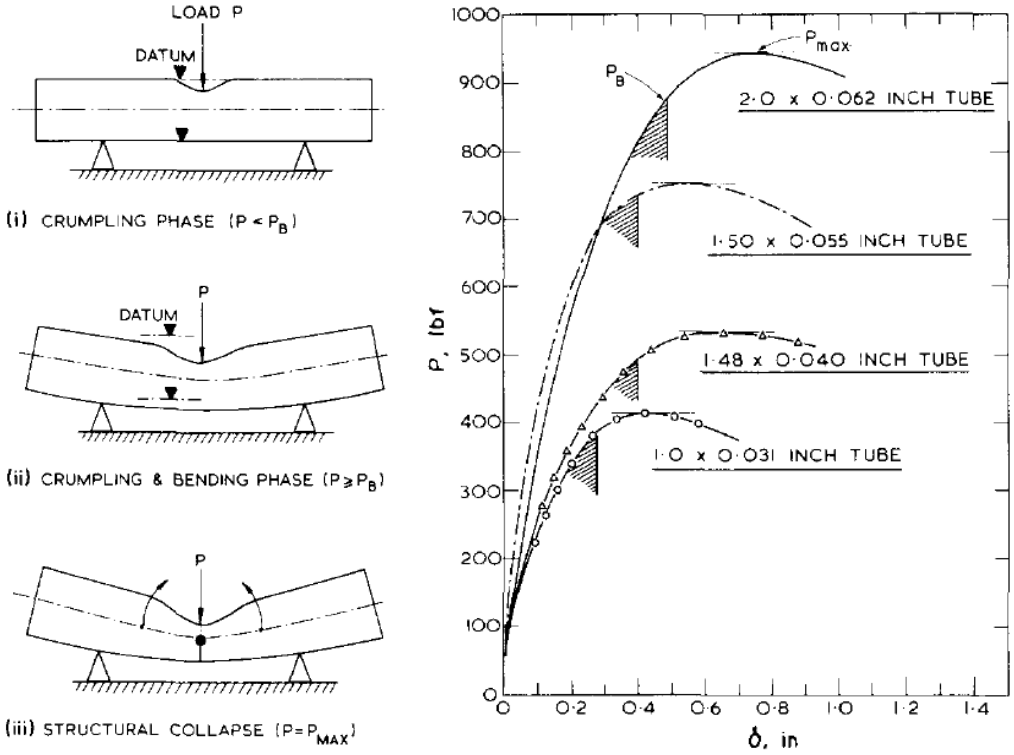

(a) Deformation modes

(b) Force-displacement curves

Figure 2.2: Three deformation modes identified by Thomas et al. [9]

To try to obtain a greater understanding of how the modes of deformation varied with the proportions of the tubes, tests of group 2 were conducted. As mentioned the span was still fixed and only the D_0/T-ratio was varied. It was significant that as the D_0/T-ratio increased, the onset of the second deformation mode occurred later. Test group 3, tests with various D_0 and T values at various spans, showed that the amount of deformation experienced by the tubes in the first deformation mode was greatly reduced by increasing the span.

2.2 Mechanics of Materials

As this thesis deals with large deformation of circular tubes or pipelines, an understanding of the mechanics of materials is necessary. The steel pipes were subjected to large plastic deformations and thus the basis of plasticity theory is presented here. Fracture criteria used in material models from the previous theses are also presented.

2.2.1 Large Strains

When a pipe is subjected to bending, large local deformations may occur. To be able to understand how the material behaves during this deformation, material tests are often conducted. The uniaxial tension test is a widely used material test, from which information regarding the mechanical properties of a material can be extracted. The test involves a suitable test specimen that is subjected to an increasing axial tensile elongation until it fails. From this test a force-displacement curve can be constructed, based on measurements of e.g. applied force F, change of length ΔL and change in diameter Δd.

For many engineering applications, typically assuming small strains, the use of engineering stress and strain will be sufficient for obtaining good approximations in a plasticity analysis [12]. Engineering stresses and strains are related to the initial geometry of the specimen. In a conventional tensile test of a metal, the engineering stress is

$$\sigma_e = \frac{F}{A_0} \tag{2.1}$$

where F is the applied force and A_0 is the initial cross-sectional area of the tests specimen [13]. The engineering strain can be expressed as

$$\varepsilon_e = \frac{\Delta L}{L_0} = \frac{L - L_0}{L_0} \tag{2.2}$$

where L is the current specimen gauge length, L_0 is the initial gauge length and ΔL is the change of the gauge length. The engineering strain is the average strain over the specimen gauge length, and the engineering stress is the average longitudinal stress in the specimen. A typical engineering stress-strain curve for a mild steel is illustrated in Figure 2.3. From point A to point B the stress is in the elastic region. This region is described by Hooke's law and the slope is given by the modulus of elasticity E, named the Young's modulus. The stress increases linearly with increasing strain. At point A, the upper yield limit is reached. If the material is further strained, it will experience permanent plastic deformation. A drop in the stress is seen after point B and the lower yield limit is reached. This limit is often set as the initial yield limit σ_0 [14]. From point C the material work-hardens making the material stronger, see Section 2.2.4.

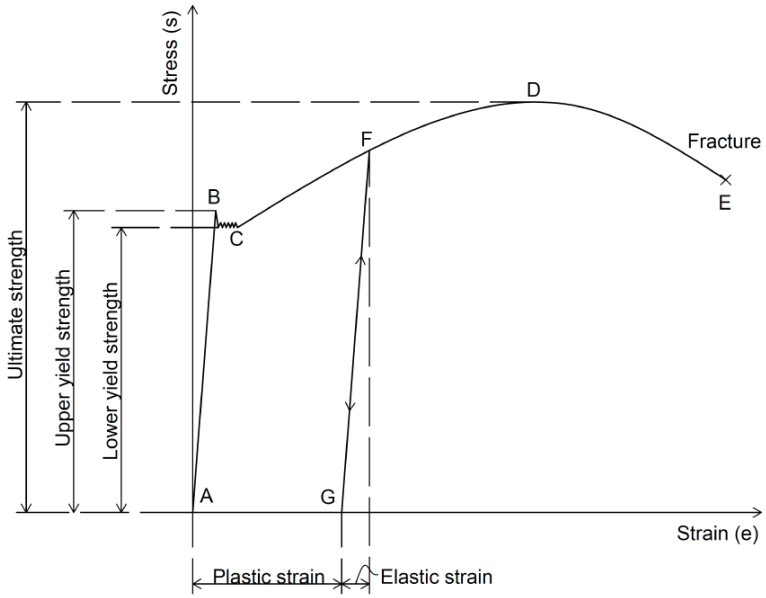

Figure 2.3: Graphical representation of a typical engineering stress-strain curve for a mild steel. [5]

If the material is unloaded in this region, say from point F to point G, the slope will be determined by the Young's modulus and some strain will be recovered. This is called the elastic strain, while the unrecoverable strain is called the plastic strain. When the material is strained to point D the load reaches its maximum value and the ultimate tensile strength is obtained. Beyond this point, the stress will decrease due to instability caused by diffuse necking, where the cross section of the specimen reduces rapidly [12], i.e. the strain hardening cannot keep pace with the loss in the cross-sectional area [15]. This continues to point E, where the material fails.

The engineering stress and strain is as mentioned based on the assumption of small strains, and associated with the initial geometry of the test specimen. As the strains become larger, the geometrical changes of the specimen must be taken into account. The true strain accounts for the geometrical changes in the specimen [12]. A small change in length dL leads to a strain increment $d\varepsilon$, so that

$$d\varepsilon = \frac{dL}{L} \tag{2.3}$$

The true or logarithmic strain is defined as the accumulation of these strain increments over the total length, so that

$$\varepsilon_l = \int_{l_0}^{l} \frac{dL}{L} = \ln\left(\frac{L}{L_0}\right) \tag{2.4}$$

By combining Equation (2.2) and Equation (2.4) the relation between the engineering and

the true strain can be obtained, and is expressed as

$$\varepsilon_l = \ln(1 + \varepsilon_e) \tag{2.5}$$

The true stress is referred to the current or deformed configuration, so that

$$\sigma_t = \frac{F}{A} \tag{2.6}$$

Based on experiments ductile materials like mild steel are usually assumed incompressible [14]. This implies that plastic deformation is volume preserving, meaning that $AL = A_0 L_0$ The reason for this is that plastic strains occur by plastic slip [12]. This gives a relation between the true stress and the engineering stress and strain for a tensile test, expressed as

$$\sigma_t = \frac{F}{A} = \frac{F}{A_0}\frac{A_0}{A} = \sigma_e(1 + \varepsilon_e) \tag{2.7}$$

As mentioned, when the force reaches its maximum value the specimen becomes unstable a neck develops. This implies that the strain or deformation becomes highly localized in the neck region [16]. After yielding, the material experiences geometrical softening and strain-hardening. When this two effects are in equilibrium, the ultimate tensile strength is reached. From this the necking criterion is defined as $d\sigma_e = 0$, and used together with Equation (2.7), the necking criterion is rewritten as

$$d\sigma_e = 0 \Longrightarrow \sigma_t = \frac{d\sigma_t}{d\varepsilon_l} \tag{2.8}$$

where $d\sigma_t$ and ε_l are the incremental change in true stress and logarithmic strain respectively. The necking criterion is illustrated graphically in Figure 2.4 [12].

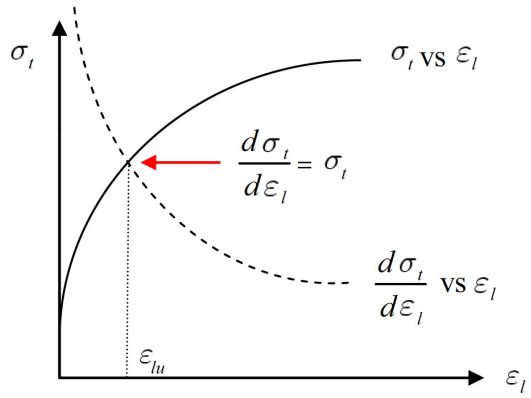

Figure 2.4: Graphical representation of necking criterion, where ε_{lu} is the true strain at necking. [12]

2.2.2 Yield Criterion

The yield criterion states that there exists a limit to the stress level at which the response stops being elastic, and plastic yielding initiates. Some mild steels exhibit a sharp yield point, while other materials like most aluminum alloys show a gradual transition into the plastic domain [12]. The yield limit is described by the yield criterion, and is mathematically given as $f(\sigma) = 0$, where $f(\sigma)$ is called the yield function. The yield criterion $f(\sigma) = 0$ can geometrically be described as a surface in stress space, which is denoted the yield surface. A representation of a two-dimensional yield surface is illustrated in Figure 2.5

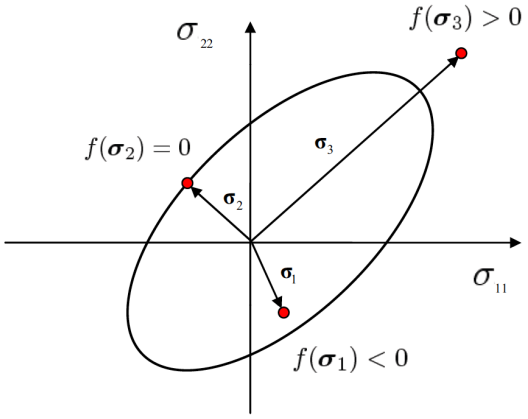

Figure 2.5: Elastic domain $f(\boldsymbol{\sigma}_1) < 0$, yield surface $f(\boldsymbol{\sigma}_2) = 0$ and inadmissible region $f(\boldsymbol{\sigma}_3) > 0$. [12]

The elastic domain is enclosed by the yield surface, while the plastic domain is the surface itself. In Figure 2.5, $\boldsymbol{\sigma}_1$, $\boldsymbol{\sigma}_2$ and $\boldsymbol{\sigma}_3$ represents three different stress states, namely the elastic domain, plastic domain and inadmissible region respectively. For convenience the yield function is expressed as

$$f(\boldsymbol{\sigma}) = \varphi(\boldsymbol{\sigma}) - \sigma_Y \tag{2.9}$$

where $\sigma_{eq} = \varphi(\boldsymbol{\sigma})$ measures the magnitude of the stress state to which the material is subjected, and is called the equivalent stress. σ_Y is the yield stress of the material. The yield stress is a material property and is determined by mechanical material tests. Worth noting is that the equivalent stress is assumed to be a homogeneous function of order one of the stress. [12]

The yield criterion can for some materials, like most metals and alloys, be assumed to depend only on the deviatoric stress state. These materials are regarded as pressure insensitive, because the plastic deformation predominantly takes place by plastic slip which is a shear-driven deformation mode. In many cases the plastic yielding of metals is assumed to be isotropic, meaning that the yield function is independent of the loading direction within

the material. This can be assumed due to the random texture in metals, i.e. arbitrary grain orientation in space. Two of the most common yield criteria for ductile metals undergoing plastic deformation is the Tresca criterion and the von Mises criterion [12]. In terms of the principal stresses the criteria can be expressed as

$$f(\boldsymbol{\sigma}) = f(\sigma_1, \sigma_2, \sigma_3) = \sigma_{eq}(\boldsymbol{\sigma}) - \sigma_Y \tag{2.10}$$

where

$$\sigma_{eq}(\boldsymbol{\sigma}) = \sqrt[n]{\frac{1}{2}\left[|\sigma_1 - \sigma_2|^n + |\sigma_2 - \sigma_3|^n + |\sigma_3 - \sigma_1|^n\right]} \tag{2.11}$$

where $n = 1$ for the Tresca criterion and $n = 2$ for the von Mises criterion. The Tresca criterion is isotropic, pressure insensitive and is based on the assumption that the yielding initiates when the maximum shear stress τ_{max} reaches a critical value τ_Y. The von Mises criterion is also isotropic and pressure insensitive, but is based on the assumption that yielding initiates when the second principal invariant of the stress deviator J_2 reaches a critical value k^2. This assumption is based on experimental evidence [12]. The von Mises criterion is also commonly expressed with the deviatoric stress components so that

$$f(\boldsymbol{\sigma}) = \sqrt{\frac{3}{2}\sigma'_{ij}\sigma'_{ij}} - \sigma_Y = 0 \tag{2.12}$$

Figure 2.6 displays a graphical representation of the Tresca and the von Mises yield criterion in a two-dimensional stress space.

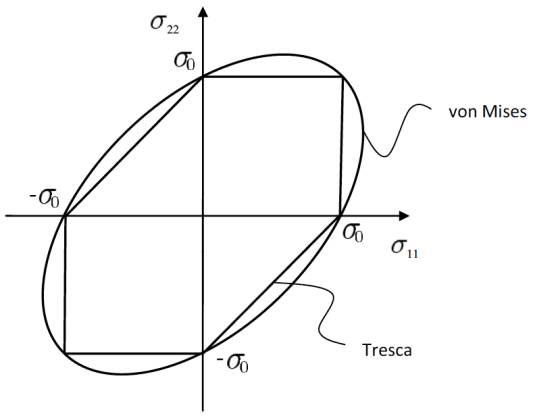

Figure 2.6: Graphical representation of the Tresca and the von Mises yield criterion in plane stress conditions i.e. $\sigma_{12} = \sigma_{33} = \sigma_{23} = \sigma_{31} = 0$. *[12]*

2.2.3 Plastic Flow Rule

Plastic deformation is a energy-dissipative deformation process, and the plastic flow rule defines the plastic strain rate tensor $\dot{\varepsilon}_{ij}^{p}$ so that non-negative dissipation is ensured [12]. Generally, the plastic flow rule is defined by

$$\dot{\varepsilon}_{ij}^{p} = \dot{\lambda} h_{ij} \tag{2.13}$$

where h_{ij} is the flow function, depending on the state of the material. $\dot{\lambda}$ is denoted the plastic parameter and is a non-negative scalar, and is determined based on the consistency condition, i.e. the stress must be located on the yield surface during continuous plastic flow [12]. It can be assumed that h_{ij} is derived from a plastic potential function $g = g(\boldsymbol{\sigma}) \geq 0$, so that

$$h_{ij} = \frac{\partial g}{\partial \sigma_{ij}} \tag{2.14}$$

If the plastic potential function g is assumed to be defined by the yield function f, the plastic flow rule is called the associated flow rule, and can be expressed as

$$\dot{\varepsilon}^{p} = \dot{\lambda} g = \dot{\lambda} \frac{\partial f}{\partial \sigma} \tag{2.15}$$

The associated flow rule implies that the plastic strain increment vector $d\boldsymbol{\varepsilon}^{p} = \dot{\boldsymbol{\varepsilon}} dt$ is parallel to the gradient of the yield surface, and thus directed along the outward normal of the surface. The associated flow rule is therefore also called the normality rule. The normality rule implies that the shape of the yield surface not only determines the stress state at which the yielding initiates, but also the direction of the plastic flow. Figure 2.7 displays a graphical representation of the associated flow rule for the Tresca and the von Mises yield surface in plane stress condition. [12]

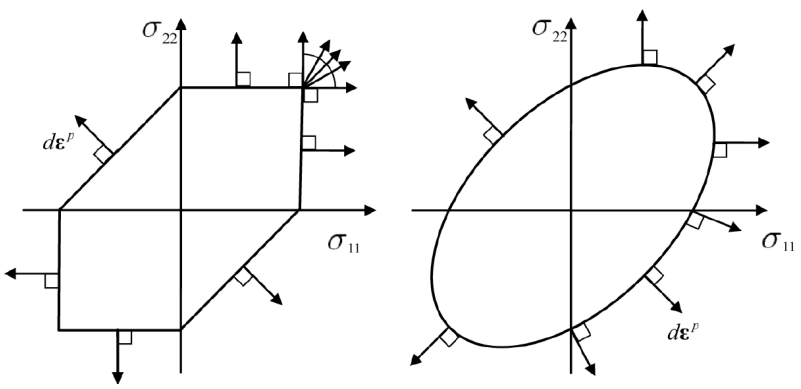

Figure 2.7: Graphical representation of the associated flow rule for the Tresca and the von Mises yield surface. [12]

The equivalent plastic strain p is an important function regarding the loading history. The equivalent plastic strain may also be referred to as the accumulated plastic strain as it is monotonically increasing. By assuming $\dot{p} = \dot{\lambda}$ the equivalent plastic strain may be expressed as

$$p = \int_0^t \dot{p} dt = \int_0^t \dot{\lambda} dt \tag{2.16}$$

The plastic strain rate may be found by assuming $\dot{p} = \dot{\lambda}$ as

$$\dot{p} = \sqrt{\frac{2}{3}\dot{\varepsilon}_{ij}^p \dot{\varepsilon}_{ij}^p} \tag{2.17}$$

which is often considered the most convenient expression for the equivalent plastic strain rate.[12]

2.2.4 Work-Hardening

In general, the strength of a material increases when it is plastically deformed, which is a result of material work-hardening. Therefore, it is necessary to include an additional parameter in the yield function. There are different approaches on how to account for work-hardening, and two of the most common are known as isotropic hardening and kinematic hardening. Isotropic hardening means that the elastic domain expands while keeping its position fixed in stress space when the material experiences plastic deformation. Kinematic hardening implies that the elastic domain is rigidly translated in the stress space during plastic deformation. Kinematic behaviour is also required to take the Bauschinger effect into account, which introduces a strain-induced anisotropy into the material model. This thesis also includes the a combined hardening model, which is a combination of isotropic and kinematic hardening. This makes it possible to combine both expansion and translation of the elastic domain during plastic deformation. [12]

Isotropic work-hardening is introduced with the isotropic hardening variable R, which depends on the accumulated plastic strain p. The yield function can then be expressed as

$$f(\boldsymbol{\sigma}, R) = \varphi(\boldsymbol{\sigma}) - \sigma_Y(R) \leq 0 \tag{2.18}$$

where $\sigma_{eq} = \varphi(\boldsymbol{\sigma})$ is the equivalent stress, $\sigma_Y(R) = \sigma_0 + R(p)$ is the flow stress of the material and σ_0 is the initial yield stress. Figure 2.8 illustrates how the elastic domain is expanded in stress space, due to an increase of the hardening variable R and thus the flow stress σ_Y, as the material is plastically deformed. [12]

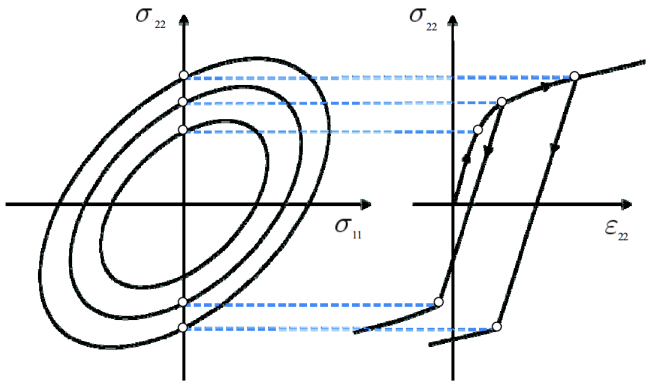

Figure 2.8: Expansion of the elastic domain in stress space due to isotropic work-hardening. [12]

As mentioned, the work-hardening is usually assumed to depend on the accumulated equivalent plastic strain $p = \int \dot{p} dt$, which is defined as the energy conjugate variable to the equivalent stress, such that

$$\sigma_{ij}\dot{\varepsilon}^p_{ij} = \sigma_{eq}\dot{p} \tag{2.19}$$

Generally, the isotropic hardening rule is defined as

$$\dot{R} = H_R\dot{\lambda} \tag{2.20}$$

where H_R is the hardening modulus, depending on the state of the material [12]. By introducing the associated flow rule the plastic strain rate is equal to the plastic parameter, i.e. $\dot{p} = \dot{\lambda}$. Two frequently used isotropic hardening rules are the Power law and the Voce rule, expressed in Equation (2.21) and Equation (2.22) respectively. For these rules the work-hardening is uniquely defined by the equivalent plastic strain [12].

$$R(p) = Kp^n \tag{2.21}$$

$$R(p) = \sum_{i=1}^{N} Q_{Ri} \cdot \left[1 - e^{-b_{Ri}p}\right] \tag{2.22}$$

where K, n, Q_{Ri} and b_{Ri} are hardening parameters determined from material tests.

Kinematic work-hardening can be looked upon as a translation of the elastic domain in the direction of the plastic loading. Let the initial yield stress of a material be σ_0, and assume that initial yielding occurs at this level of stress independent of the loading direction. Say that the material is loaded in tension into the plastic domain, until a stress σ_A is reached. The material work-hardens in the plastic domain, so that $|\sigma_A| > \sigma_0$. Let

the material be unloaded elastically to zero stress, and then reloaded in compression in the reversed direction. Assume that yielding in the reversed direction occurs at the stress σ_B. For most materials experience show that $|\sigma_B| < |\sigma_A|$, and often it is seen that $|\sigma_B| < \sigma_0$. This reduction of the yield stress is denoted the Bauschinger effect, and is illustrated in Figure 2.9. Here a directional hardening is seen, leading to a higher strength in the direction of plastic loading. This is called kinematic hardening. [12]

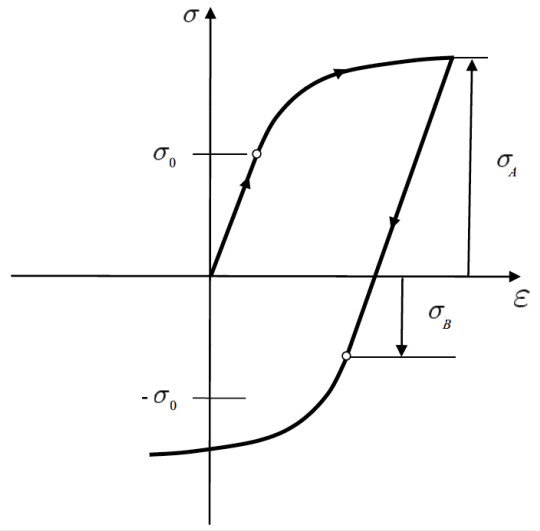

Figure 2.9: Graphical representation of the Bauschinger effect. [12]

To account for kinematic hardening, the yield function can be expressed as

$$f(\boldsymbol{\sigma} - \boldsymbol{\chi}, R) = \sigma_{eq}(\boldsymbol{\sigma} - \boldsymbol{\chi}) - (\sigma_0 + R) \leq 0 \tag{2.23}$$

where the kinematic hardening variable $\boldsymbol{\chi}$ is denoted the backstress tensor, and acts as a residual stress that lowers the yield strength during reversed loading i.e. accounting for the Bauschinger effect. It is seen that $|\boldsymbol{\sigma} - \boldsymbol{\chi}|$ acts as an effective stress, and it is the magnitude of this stress that determines whether or not a material yields plastically for given values of the stress σ_0 and isotropic hardening R. Figure 2.10 illustrates how the elastic domain is translated in stress space. To describe the Bauschinger effect, $\boldsymbol{\chi}$ should develop positive values in tension and negative values in compression. [12]

Generally, the evolution of the backstress tensor is defined by

$$\dot{\chi}_{ij} = H^{\chi}_{ij}\dot{\lambda} \tag{2.24}$$

where the second-order tensor $\mathbf{H}^{\chi}$ depends on the state of the material through $\boldsymbol{\sigma}$, $\boldsymbol{\chi}$ and R [12]. Equation (2.25) shows a linear kinematic hardening rule proposed by Ziegler [17],

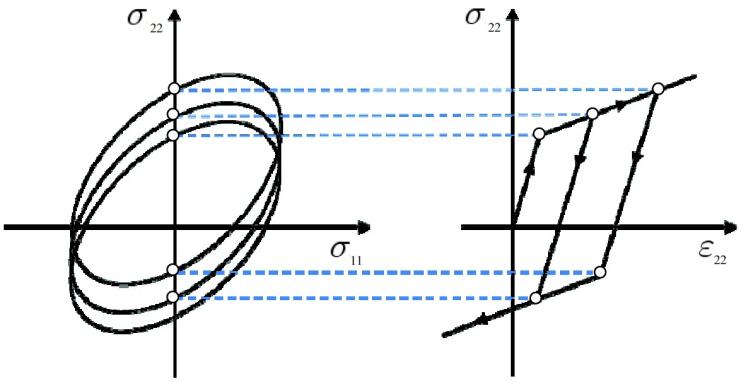

Figure 2.10: Translation of the elastic domain due to kinematic work-hardening. [12]

obtained by assuming that the rate of the backstress tensor is proportional to the tensor $(\boldsymbol{\sigma} - \boldsymbol{\chi})$.

$$\dot{\chi}_{ij} = C_\chi \frac{\sigma_{ij} - \chi_{ij}}{\sigma_{eq}} \dot{p} \tag{2.25}$$

where C_χ is a constant. Equation (2.26) shows a frequently used non-linear kinematic hardening rule, proposed by Armstrong and Fredrick [17].

$$\dot{\chi}_{ij} = \left(C_\chi \frac{\sigma_{ij} - \chi_{ij}}{\sigma_{eq}} - \gamma_\chi \chi_{ij} \right) \dot{p} \tag{2.26}$$

where C_χ and γ_χ are constants, or depending in the equivalent plastic strain p.

Combined work-hardening was presented by the yield function expressed in Equation 2.23. As seen the combined hardening is a combination of the isotropic and kinematic hardening, letting the yield surface both expand and translate in the stress space. Chaboche and Lemaitre [18] proposed a combined hardening rule, which expresses the equivalent stress σ_{eq} as the sum of the initial yield stress σ_0, $R = \sum_{i=1}^{N} R_i$ and $\chi = \sum_{j=1}^{N} \chi_j$. [19]

2.2.5 Fracture Criteria

Dey [16] stated that a material model is not complete without some form of material degradation or failure. The degradation or the damage in a material is usually given in the form of a damage parameter, and failure occurs through damage evolution. Dey [16] discussed in detail that ductile fracture arises from the nucleation, growth and coalescence of microscopic voids that initiates at inclusions and second phase particles. This is also discussed by Aune and Hovdelien [7]. The voids around particles grow when subjected to plastic strain and hydrostatic tension. Moreover, many experimental investigations clearly show that the nucleation of voids and the ductility depends markedly on the triaxiality of

the stress state [16]. Thus, it follows that a model for ductile failure should depend on the stress triaxiality. Most failure criteria that are based on void growth are of the type:

$$D_{cr} = \int_{\varepsilon_n}^{\varepsilon_f} f(\sigma^*)\, d\varepsilon_{eq} \tag{2.27}$$

, where σ^* is the stress triaxiality. The damage evolution begins when the voids start to nucleate, i.e. when the equivalent strain equals ε_n. Fracture occurs at the value of damage D_{cr}, where the equivalent strain equals the fracture strain ε_f. [16]

As for the three previous master theses [5, 6, 7], this thesis will be limited to consider two ductile fracture criteria, namely the Johnson-Cook criteria and the Cockcroft-Latham critera. Johnson and Cook [20] introduced a fracture criterion depending on temperature, strain rate and strain path. They defined the failure strain ε_f as

$$\varepsilon_f = (D_1 + D_2 e^{D_3 \sigma^*})(1 + D_4 ln\dot{\varepsilon}^*_{eq})(1 + D_5 T^*) \tag{2.28}$$

where D_1 through D_5 are material constants. The fracture criterion is based on damage evolution. The damage D of a material element is expressed as

$$D = \sum \frac{dp}{\varepsilon_f} \tag{2.29}$$

where dp is the increment of accumulated equivalent plastic strain that occurs during an integration cycle. Failure is assumed to occur when the damage D equals unity.

Cockcroft and Latham [21] introduced a very simple fracture criterion which was first based on total plastic work per unit volume. The concept of their criterion was that damage accumulates during straining until a critical value $W = W_c$ was reached at $\varepsilon_{eq} = \varepsilon_f$. They reasoned that the fracture criterion needed to be based on some combination of stress and strain, and not on either of these quantities separately [16]. Initially, the fracture criterion was dependent on the deviatoric stress. To account for the hydrostatic tension they modified their criterion so that it was based on the magnitude of the major principle stress, i.e.

$$\int_0^{\varepsilon_{eq}} \langle \sigma_1 \rangle\, d\varepsilon_{eq} = W_c \tag{2.30}$$

where W_c is the Cockcroft-Latham parameter based on material tests. $\langle \sigma_1 \rangle = \sigma_1$ when $\sigma_1 \geq 0$, and $\langle \sigma_1 \rangle = 0$ when $\sigma_1 < 0$. This way the criterion take the hydrostatic tension into account. Fracture will be dependent on the stress imposed as well as on the strains developed. [16]

2.3 Fracture Mechanisms in Metals

The following section briefly describes some of the most common fracture mechanisms in metals and alloys, and it is mainly based on the theory presented by Anderson [15]. Table 2.1 presents the three most common fracture mechanisms in metals and alloys.

Table 2.1: Fracture mechanisms for metals and alloys [15].

Fracture mechanism	Description
Ductile fracture	Ductile materials usually fail as the result of nucleation, growth and the coalescence of microscopic voids that initiate at inclusions and second-phase particles.
Cleavage fracture	Cleavage fracture involves separation along specific crystallographic planes. The fracture path is transgranular, meaning that the propagating crack seeks the most favourably orientated cleavage plane in each grain.
Intergranular fracture	As the name implies, the intergranular fracture occurs when the grain boundaries are the preferred fracture path in the material.

Figure 2.11 shows the three micromechanisms of fracture in metals described in Table 2.1.

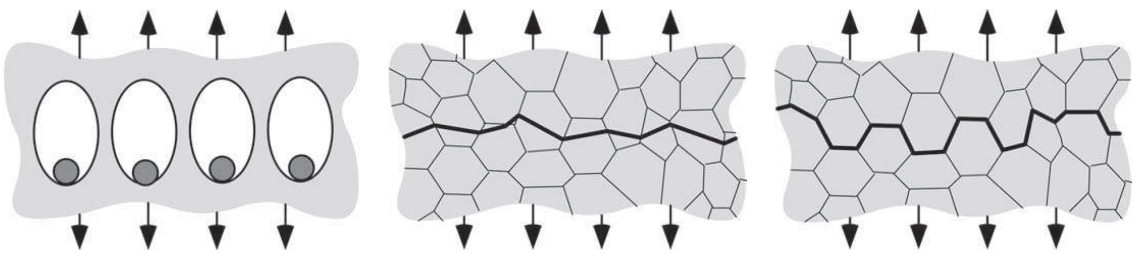

(a) Ductile fracture. (b) Cleavage. (c) Intergranular fracture.

Figure 2.11: Three micromechanisms of fracture in metals [15].

Only ductile fracture and cleavage will be discussed in this thesis, as in most cases metals do not fail along grain boundaries. As mentioned, ductile metals fail by nucleation, growth and the coalescence of microscopic voids that initiate at inclusions and second-phase particles, while brittle metals often fail by transgranular cleavage. [15]

2.3.1 Ductile Fracture

The majority of metals used for industrial purposes usually contains impurities, due to the high cost of pure metals. Metals that contain impurities fail at a much lower strains than pure metals. Microvoids nucleate at inclusions and second-phase particles, and the voids grow together from a macroscopic flaw, which leads to fracture. Three stages are commonly observed in ductile fracture. [15]

1. Formation of a free surface at an inclusion or second-phase particle by either interface decohesion or particle cracking.
2. Growth of the void around the particle, by means of plastic strain and hydrostatic stress.
3. Coalescence of the growing void with adjacent voids.

Figure 2.12 illustrates void nucleation, growth and coalescence in ductile metals.

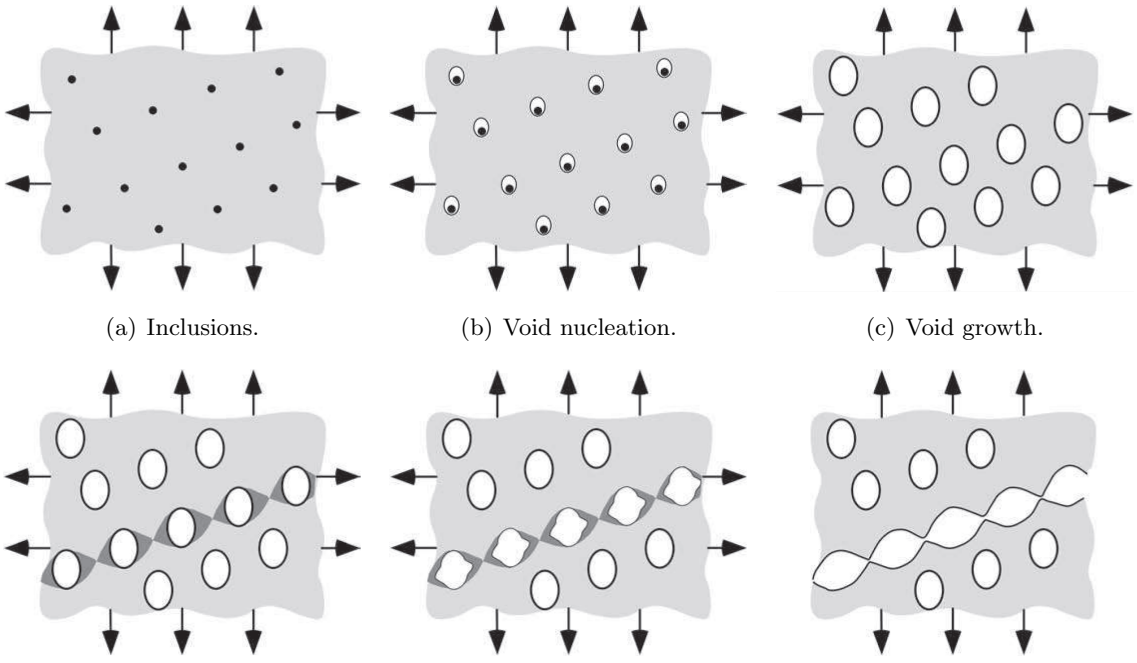

(a) Inclusions. (b) Void nucleation. (c) Void growth.

(d) Strain localization. (e) Necking between voids. (f) Void coalescence and fracture.

Figure 2.12: Illustration of void nucleation, growth and coalescence in ductile metals [15].

In materials where the second-phase particles and inclusions are well bonded to the matrix void nucleation is often the critical step, where fracture occurs soon after the voids form. A void forms around a second-phase particle or inclusion when sufficient stress is applied to break the interfacial bonds between the particle and matrix. Once the voids form, further plastic strain and hydrostatic stress cause the voids to grow and eventually coalesce. If void nucleation occurs with little difficulty, the fracture properties are controlled by the

growth and coalescence of the voids. The growing voids reach a critical size, relative to their spacing, and a local plastic instability develops between the voids resulting in failure. If the initial void fraction is low ($< 10\%$), each void can be assumed to grow independently before interacting with neighbouring voids. Plastic strain is concentrated along a sheet of voids, and local necking instabilities develop. The orientation of the fracture path depends on the stress state. [15]

2.3.2 Cleavage

Cleavage fracture was by Anderson [15] defined as the rapid propagation of a crack along a particular crystallographic plane. Cleavage may be brittle, but can be preceded by large-scale plastic flow and ductile crack growth. The preferred cleavage planes are those with the lowest packing density, since fewer bonds must be broken and the spacing between planes is greater.

Figure 3.14(a) shows a scanning electron microscopy (SEM) image indication ductile fracture, with a fracture surface showing large dimples along with spherical particles, typically located at the bottom of the dimples. Figure 3.14(b) shows a SEM image of a classic brittle cleavage fracture with no sign of ductility observed in samples from pipes subjected to impact by Kristoffersen et al [4]. [15]

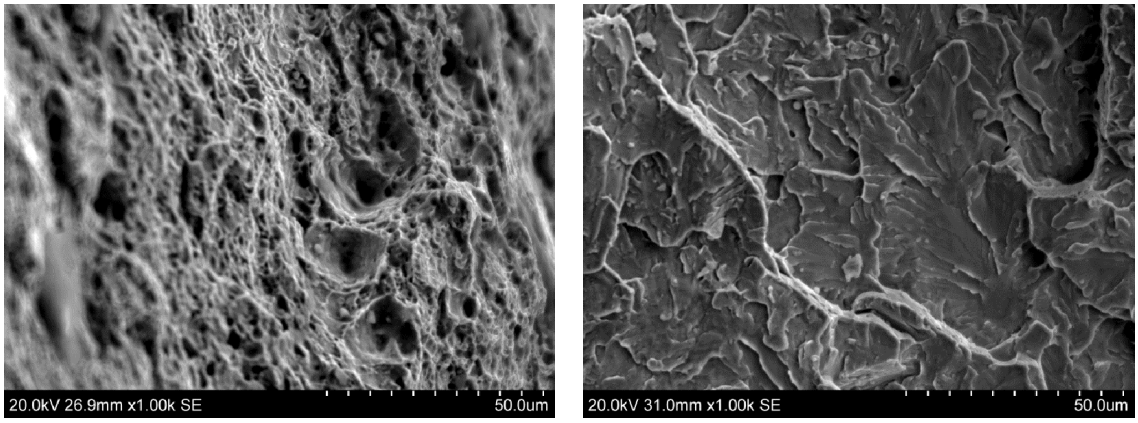

(a) Ductile fracture (b) Cleavage

Figure 2.13: SEM image of typical ductile fracture and cleavage. [4]

2.4 Finite Element Method Theory

In this thesis, Abaqus/Explicit was used for numerical analyses. Abaqus CAE is the corresponding graphic user interface (GUI) used for both pre- and post-processing. The Abaqus software is a product of Dassault Systemés Simulia Corporation. The following sections gives a brief introduction and an overview and formulations of explicit solutions. The finite element method theory described in this section is mainly an excerpt from lecture notes given by Kjell Magne Mathisen in Nonlinear Finite Element Analysis [22].

2.4.1 Dynamic Equilibrium

The dynamic equilibrium equation for a multi degree of freedom systems render

$$\left\{\mathbf{R}^{ine}(t)\right\} + \left\{\mathbf{R}^{dmp}(t)\right\} + \left\{\mathbf{R}^{int}(t)\right\} = \left\{\mathbf{R}^{ext}(t)\right\} \tag{2.31}$$

$\left\{\mathbf{R}^{ine}(t)\right\}$ is the inertia force vector, which may be expressed in terms of the systems mass matrix and nodal point accelerations and $\left\{\mathbf{R}^{dmp}(t)\right\}$ is the damping force vector, which may be expressed in terms of the systems damping matrix and nodal point velocities. $\left\{\mathbf{R}^{int}(t)\right\}$ is the internal force vector and refers to the the stiffness properties of the system. Thus, it may be expressed by the systems stiffness matrix and nodal point displacements and rotations. $\left\{\mathbf{R}^{ext}(t)\right\}$ is the external force vector.

Introducing relations between the force vectors and the system's properties matrices gives

$$\left\{\mathbf{R}^{ine}(t)\right\} = [\mathbf{M}]\left\{\ddot{\mathbf{D}}(t)\right\} \tag{2.32}$$

$$\left\{\mathbf{R}^{dmp}(t)\right\} = [\mathbf{C}]\left\{\dot{\mathbf{D}}(t)\right\} \tag{2.33}$$

$$\left\{\mathbf{R}^{int}(t)\right\} = [\mathbf{K}]\left\{\mathbf{D}(t)\right\} \tag{2.34}$$

The governing equation for dynamic equilibrium may then be written as

$$[\mathbf{M}]\left\{\ddot{\mathbf{D}}(t)\right\} + [\mathbf{C}]\left\{\dot{\mathbf{D}}(t)\right\} + [\mathbf{K}]\left\{\mathbf{D}(t)\right\} = \left\{\mathbf{R}^{ext}(t)\right\} \tag{2.35}$$

This equation may be solved using either explicit or implicit methods.

2.4.2 Explicit Direct Integration

Explicit solution methods utilizes known values of accelerations, velocities and displacements for a time t to calculate new values at a time $t + \Delta t$ directly, without equation solving. This means that the cost per time increment is low as equilibrium iterations are not necessary. However, explicit methods are conditionally stable, meaning that there exists a critical time step Δt_{cr}, which may not be exceeded if a stable solution is to be obtained. Generally, the explicit solution algorithm can be expressed on the form

$$\mathbf{D}_{n+1} = f\left(\mathbf{D}_n, \dot{\mathbf{D}}_n, \ddot{\mathbf{D}}_n, \mathbf{D}_{n-1}\right) \tag{2.36}$$

The Central Difference Method

The explicit integration scheme may be solved incrementally by performing a Taylor series expansion of the displacements $\{\mathbf{D}\}_{n+1}$ and $\{\mathbf{D}\}_{n-1}$ and neglecting higher order terms. By doing this, approximations for velocities and accelerations may be expressed as the conventional central difference approximations

$$\left\{\dot{\mathbf{D}}\right\}_n = \frac{\{\mathbf{D}\}_{n+1} - \{\mathbf{D}\}_{n-1}}{2\Delta t} \tag{2.37}$$

$$\left\{\ddot{\mathbf{D}}\right\}_n = \frac{\{\mathbf{D}\}_{n+1} - 2\{\mathbf{D}\}_n + \{\mathbf{D}\}_{n-1}}{\Delta t^2} \tag{2.38}$$

Inserting the approximated terms into the dynamic equilibrium equation (2.35) and solving for $\{\mathbf{D}\}_{n+1}$ gives the incremental solution

$$\{\mathbf{D}\}_{n+1} = \left[\mathbf{K}^{eff}\right]^{-1} \left\{\mathbf{R}^{eff}\right\}_n \tag{2.39}$$

where

$$\left[\mathbf{K}^{eff}\right] = \frac{1}{\Delta t^2}[\mathbf{M}] + \frac{1}{2\Delta t}[\mathbf{C}] \tag{2.40}$$

and

$$\left\{\mathbf{R}^{eff}\right\}_n = \left\{\mathbf{R}^{ext}\right\}_n - \left(\frac{1}{\Delta t^2}[\mathbf{M}] - \frac{1}{2\Delta t}[\mathbf{C}]\right)\{\mathbf{D}\}_{n-1} - \left([\mathbf{K}] - \frac{2}{\Delta t^2}[\mathbf{M}]\right)\{\mathbf{D}\}_n \tag{2.41}$$

However, unless the mass and damping matrices $[\mathbf{M}]$ and $[\mathbf{C}]$ are diagonal, the effective stiffness matrix $\left[\mathbf{K}^{eff}\right]$ will have to be factorized in order to obtain the displacements $\{\mathbf{D}\}_{n+1}$. This would greatly increase the computational cost. In general dynamic response

analysis it can be desirable to include stiffness proportional damping $[\mathbf{C}] = \beta[\mathbf{K}]$ in order to damp high frequency numerical noise. This will indeed make $\left[\mathbf{K}^{eff}\right]$ non-diagonal. In order to circumvent this issue, it may be shown that if the equilibrium equations are established with velocity lagging by half a step, the problem may be overcome. This leads to the establishment of the half-step central difference method.

The Half-Step Central Difference Method

The half-step central differences may be expressed as

$$\left\{\dot{\mathbf{D}}\right\}_{n-1/2} = \frac{1}{\Delta t}\left(\{\mathbf{D}\}_n - \{\mathbf{D}\}_{n-1}\right) \tag{2.42}$$

$$\left\{\dot{\mathbf{D}}\right\}_{n+1/2} = \frac{1}{\Delta t}\left(\{\mathbf{D}\}_{n+1} - \{\mathbf{D}\}_n\right) \tag{2.43}$$

This gives the incremental acceleration

$$\left\{\ddot{\mathbf{D}}\right\}_n = \frac{1}{\Delta t}\left(\left\{\dot{\mathbf{D}}\right\}_{n+1/2} - \left\{\dot{\mathbf{D}}\right\}_{n-1/2}\right) = \frac{1}{\Delta t^2}\left(\{\mathbf{D}\}_{n+1} - 2\{\mathbf{D}\}_n + \{\mathbf{D}\}_{n-1}\right) \tag{2.44}$$

By approximating the velocity as

$$\left\{\dot{\mathbf{D}}\right\}_{n+1/2} = \left\{\dot{\mathbf{D}}\right\}_{n-1/2} + \Delta t\left\{\ddot{\mathbf{D}}\right\}_n \tag{2.45}$$

the incremental displacement $\{\mathbf{D}\}_{n+1}$ may be expressed as

$$\{\mathbf{D}\}_{n+1} = \{\mathbf{D}\}_n + \Delta t\left\{\dot{\mathbf{D}}\right\}_{n+1/2} = \{\mathbf{D}\}_n + \Delta t\left\{\dot{\mathbf{D}}\right\}_{n-1/2} + \Delta t^2\left\{\ddot{\mathbf{D}}\right\}_n \tag{2.46}$$

With velocity lagging behind half a step the dynamic equilibrium equation becomes

$$[\mathbf{M}]\left\{\ddot{\mathbf{D}}\right\}_n + [\mathbf{C}]\left\{\dot{\mathbf{D}}\right\}_{n-1/2} + [\mathbf{K}]\{\mathbf{D}\}_n = \left\{\mathbf{R}^{ext}\right\}_n \tag{2.47}$$

Substituting the half-step central differences into the equilibrium equation yields

$$\frac{1}{\Delta t^2}[\mathbf{M}]\{\mathbf{D}\}_{n+1} = \left\{\mathbf{R}^{ext}\right\}_n - [\mathbf{K}]\{\mathbf{D}\}_n + \frac{1}{\Delta t^2}[\mathbf{M}]\left(\{\mathbf{D}\}_n + \Delta t\left\{\dot{\mathbf{D}}\right\}_{n-1/2}\right) - [\mathbf{C}]\left\{\dot{\mathbf{D}}\right\}_{n-1/2} \tag{2.48}$$

where

$$\{\mathbf{D}\}_{n+1} = \Delta t^2[\mathbf{M}]^{-1}\left\{\mathbf{R}^{eff}\right\}_n \tag{2.49}$$

and

$$\left\{\mathbf{R}^{eff}\right\}_n = \left\{\mathbf{R}^{ext}\right\}_n - [\mathbf{K}]\{\mathbf{D}\}_n + \frac{1}{\Delta t^2}[\mathbf{M}]\left(\{\mathbf{D}\}_n + \Delta t\left\{\dot{\mathbf{D}}\right\}_{n-1/2}\right) - [\mathbf{C}]\left\{\dot{\mathbf{D}}\right\}_{n-1/2} \tag{2.50}$$

For the half-step central difference method it is necessary determine $\left\{\dot{\mathbf{D}}\right\}_{-1/2}$ by initial calculations. A backward difference approximation yields

$$\left\{\dot{\mathbf{D}}\right\}_{-1/2} = \{\mathbf{D}\}_0 - \frac{\Delta t}{2}\left\{\ddot{\mathbf{D}}\right\}_0 \tag{2.51}$$

where $\left\{\ddot{\mathbf{D}}\right\}_0$ may be obtained by evaluating the equilibrium equation at $t = 0$ as

$$\left\{\ddot{\mathbf{D}}\right\}_0 = [\mathbf{M}]^{-1}\left(\left\{\mathbf{R}^{ext}\right\}_0 - [\mathbf{K}]\{\mathbf{D}\}_0 - [\mathbf{C}]\left\{\dot{\mathbf{D}}\right\}_0\right) \tag{2.52}$$

The central difference method and the half step central difference method only guarantee first order accuracy. In order for the central difference method to be explicit, lumped mass representation must be employed. As mentioned, there exists a critical time step Δt_{cr}, which may not be exceeded as this will cause the analyses to become unstable and oscillations will occur in the response history. The stability limit can be defined in terms of the eigenfrequency ω_j and the fraction of critical damping ξ_j of eigenmode ϕ_j as

$$\Delta t_{cr} \leq min\left[\frac{2}{\omega_j}\left(\sqrt{1-\xi_j^2} - \xi_j\right)\right] \tag{2.53}$$

For practical purposes damping is likely to be small for all modes meaning that the critical time step Δt_{cr} will be decided by ω_{max} and the corresponding damping ratio ξ.

$$\Delta t_{cr} \leq min\left[\frac{2}{\omega_{max}}\left(\sqrt{1-\xi^2} - \xi\right)\right] \tag{2.54}$$

For an undamped material the critical time step may be found as

$$\Delta t_{cr} = \frac{2}{\omega_{max}} = \frac{L}{c_d} \tag{2.55}$$

where L is the length of the smallest element and $c_d = \sqrt{\frac{E}{\rho}}$ is the speed of sound in the material. The physical interpretation is that Δt must be small enough that information does not propagate more than the distance between adjacent nodes during a single time step. Applying lumped mass will increase the critical time step compared to consistent mass.

2.4.3 Contact

Abaqus/Explicit uses two different methods to enforce contact constraints, namely the kinematic contact algorithm and the penalty contact algorithm. The penalty contact algorithm was utilized in this thesis as it is more flexible in combination with rigid bodies. [17]

The penalty method impose constraints by augmenting the potential energy of the system, Π_p, by a penalty term so that

$$\Pi_p^* = \Pi_p + \frac{1}{2}\alpha[C(u)]^2 = \frac{1}{2}ku^2 - mgu + \frac{1}{2}\alpha(u-h)^2 \tag{2.56}$$

where the penalty parameter α can be interpreted as a spring stiffness in the contact interface, as illustrated by the one-degree of freedom in Figure 2.14. This is due to the fact that the penalty term in Equation (2.56) has the same structure as the potential energy of a simple spring.

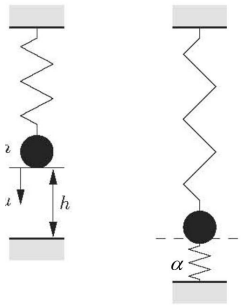

Figure 2.14: Penalty. [22]

In order to make the new function for the potential energy Π_p^* stationary the following equation has to be satisfied:

$$\left\{\frac{\partial \Pi_p^*}{\partial u}\right\} = 0 \qquad \Rightarrow \qquad (k+\alpha)u = mg + \alpha h \tag{2.57}$$

The expression in Equation (2.57) may then be solved for the displacement u as

$$u = \frac{mg + \alpha h}{k + \alpha} \tag{2.58}$$

The value for the contact condition $C(u)$ then becomes

$$C(u) = u - h = \frac{mg - kh}{k + \alpha} \tag{2.59}$$

The contact force for the penalty method may be obtained as the interface spring force and thus becomes

$$\lambda = \alpha C(u) = \frac{\alpha}{k + \alpha}(mg - kh) \tag{2.60}$$

Penetration in to rigid surfaces will be decided by the penalty parameter α. Large values for α will make the penalty spring stiffness very large and thus making the penetration in to the rigid surface very small. A too large value for α may produce an ill-conditioned set of equations. Applying a small value the penalty parameter will result in large penetrations of the rigid surface. An advantage by using the penalty method is that the number of unknowns remain constant and it does not destroy the positive definiteness of the system.[22]

3 Previous Work

In this chapter findings from previous work regarding impact against offshore pipelines is presented. As this thesis is a continuation of three previous master's theses it was decided, in agreement with the supervisor, to provide a thorough presentation of work done by Slåttedalen and Ørmen [5], Fornes and Gabrielsen [6] and Aune and Hovdelien [7]. Related work by Kristoffersen et al. [4] are also presented. One of the main parts in the previous theses consisted of establishing material models by use of results from material tests carried out on steel grade X65. Impact experiments on pipe components consisting of this material were conducted and analysed through metallurgical investigations. In addition, numerical simulations of the component tests were carried out. A brief presentation on work done by Jones and Birch [23] regarding impact against pressurized pipes is also given. Firstly, an introduction the X65 steel pipelines is given along with an overview of the production process of X65 steel pipelines tested in this thesis and in the previous theses.

3.1 X65 Steel Pipes

Manes et al. [24] did an extensive study on plate strips consisting of API (American Petroleum Institute) steel grade X65, including a series of material test. The uniaxial tension tests on specimens cut out from different orientations in the material indicated anisotropic plastic flow and fracture properties. The pipe material used in this study is similar to the X65 steel grade used by Manes et al. [24]. However, the pipes have been made by two different manufacturing processes. The pipes used by Manes et al. [24] were produced from rolled plates, where they were formed and welded longitudinally. The pipes used in this study are made seamless through a process utilizing the Mannesmann effect, described in Section 3.1.2. As the pipes were made in seamless a more isotropic material behaviour would apply compared to the pipes tested by Manes et al [24]. Three previous master's theses [5, 6, 7] and Kristoffersen et al. [4] have carried out an extensive investigation of the pipe material used in this study. The material tests indicated that anisotropy was not present, and the material was assumed isotropic and homogeneous.

3.1.1 Steel Grade X65

One of the primary steel grades used in pipes for the oil and gas industries is X65. The combination of its strength and low cost makes it attractive compared with higher-performing steel grades, since these industries use huge amounts of pipes [25]. The X65 steel has sufficient strength for most pressurized pipelines and its weldability is excellent, ensuring strong seals. In addition, Oh et al. [26] found through material tests that the X65 steel displays good ductile behaviour. X65 is a low-carbon steel with a carbon content of 0.10%, which is very low compared with other steel grades. After iron, manganese is the most abundant mineral at 1.50%. The composition also contains silicon (0.35%), phosphorus (0.15%), nitrogen (0.015%) and sulfur (0.005%). Vanadium and titanium are sometimes found in small quantities and they add toughness to the steel. The material certificate provided by Tenaris [27] can be found in Appendix A and gives more details concerning the material composition.

3.1.2 The Mannesmann Process

In contrast to the longitudinally welded pipes tested by Manes et al. [24], the pipes used in this thesis are made seamless utilizing the Mannesmann effect. This effect refers to the formation of a cavity along the longitudinal axis in a solid metal cylinder, due to radial compression during a metalworking operation [28]. The cavity appears in the middle of the cross section for the cylinder. As illustrated in Figure 3.1, two skewed rotating rolls force the solid metal cylinder towards a stationary plug resulting in an expansion of the cavity. Thus, a shell can be formed to the desired thickness and diameter [27].

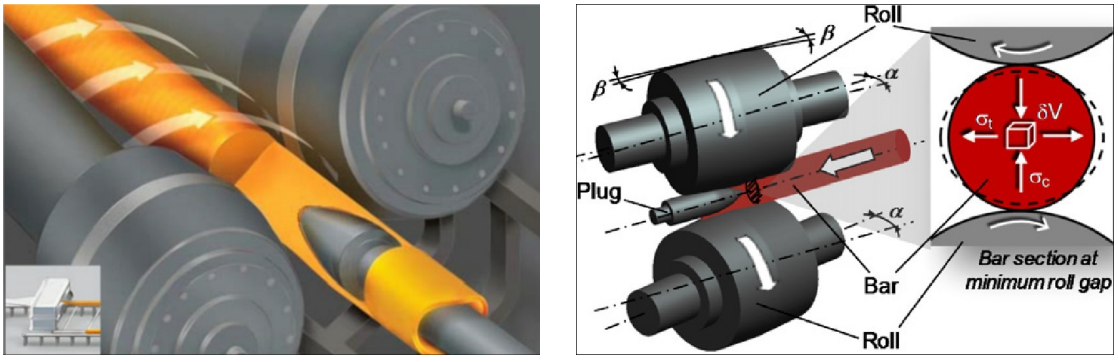

(a) Illustration 1. [27]

(b) Illustration 2. [28]

Figure 3.1: Illustration the Mannesmann process. [27, 28]

The pipelines have been produced by the Argentinian supplier Tenaris in accordance with the guidelines given by Det Norske Veritas [29]. Further details concerning the Mannesmann process are provided by Tenaris [27].

3.2 Material Tests

The material models used in this thesis are based on the findings from material tests carried out in the three previous master's theses [5, 6, 7]. This section presents these material tests and their respective results. Slåttedalen and Ørmen [5] performed quasi static tensile tests to study possible anisotropy and homogeneity, in addition to work-hardening effects. It was suggested by Slåttedalen and Ørmen that a combined isotropic/kinematic material model could improve numerical results of component tests [5]. Fornes and Gabrielsen [6] investigated possible kinematic hardening by reversing the loading for uniaxial compression or tension tests. Aune and Hovdelien [7] performed compression tests with reversed loading on notched specimens, to further investigate the kinematic behaviour by exposing the material to larger compressive strains. Metallurgical investigations of the notched tests were also carried out by Aune and Hovdelien [7] and Kristoffersen et al. [4] to study the microstructural behaviour of the material for large strains. Krisoffersen et al. [4] also performed material tests where notched specimens were exposed to true strains in compression of up to 100% before reversed loading was applied.

3.2.1 Quasi Static Tensile Tests

Test specimens were cut out from a pipe at different locations and orientations as seen in Figure 3.2.

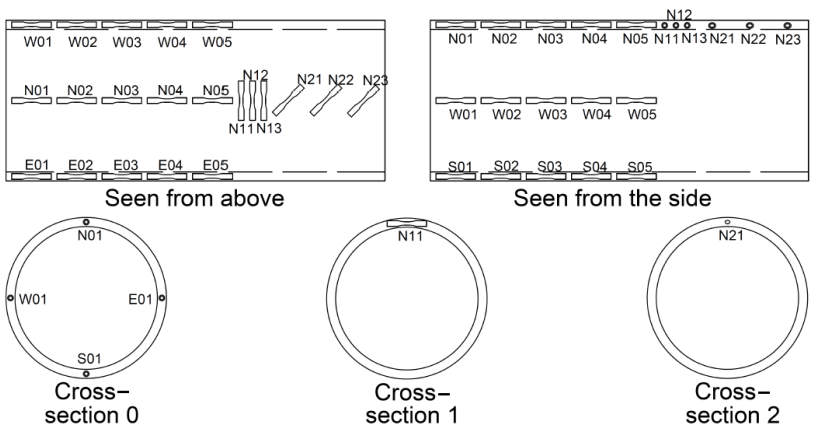

Figure 3.2: Location and orientation of test-specimens cut out from the pipe.[5]

Most of the specimens were stretched quasi-statically in a Zwik test machine at room temperature. Laser equipment was mounted and used to measure the diameter reduction in two perpendicular directions. The rate of deformation was kept constant at 0.3 mm/min, which is equivalent to an initial strain rate of 10^{-3} s^{-1}. When maximum load was reached, the strain-rate increased due to strain localization. Beyond the point of necking, the true stress was corrected for the triaxial stress state that occurs in the constriction. This was

done according to a simplified mathematical model proposed by Bridgman [30]. For more details concerning machine set-up and geometry, see Slåttedalen and Ørmen [5].

To identify any differences between the specimens, two parallel tests were conducted at each location. The true stress-true strain curves from the different tests of specimens at zero degrees showed almost identical behaviour, as seen in Figure 3.3(a).

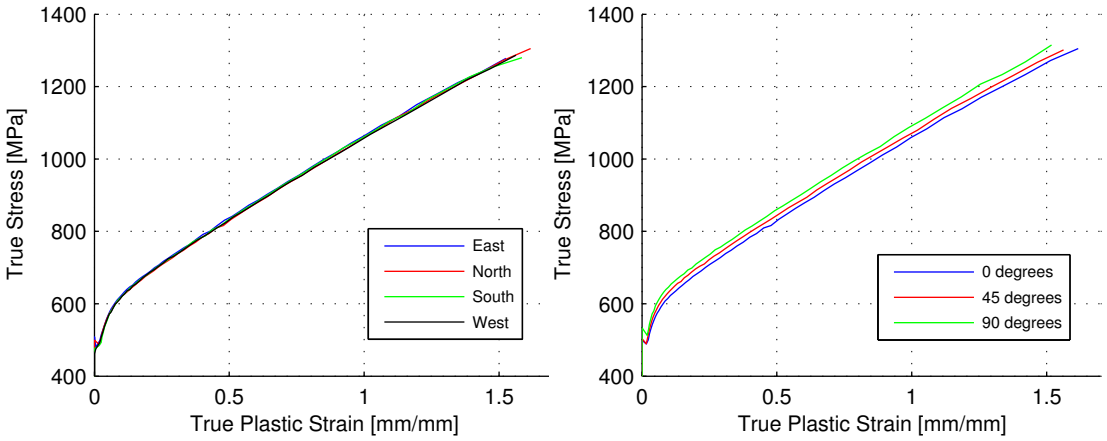

(a) Different locations in cross section.

(b) Different specimen orientations.

Figure 3.3: True stress - true plastic strain from uniaxial tension tests from different locations and orientations. [5]

Figure 3.3(a) indicates that the material was homogeneous over the cross section. By comparing the curves from tests taken at 0, 45 and 90 degrees a small deviation was found, as seen in Figure 3.3(b). Nevertheless, this deviation was deemed insignificant compared to the deviation between the parallel tests. Therefore, the material was assumed isotropic, and this assumption was further supported by an almost perfect circular fracture as seen in Figure 3.4. By calculation the Young's modulus E, the initial yield limit σ_0 and the ultimate yield stress σ_u was set to 208000 MPa, 472 MPa and 565 MPa respectively. [5]

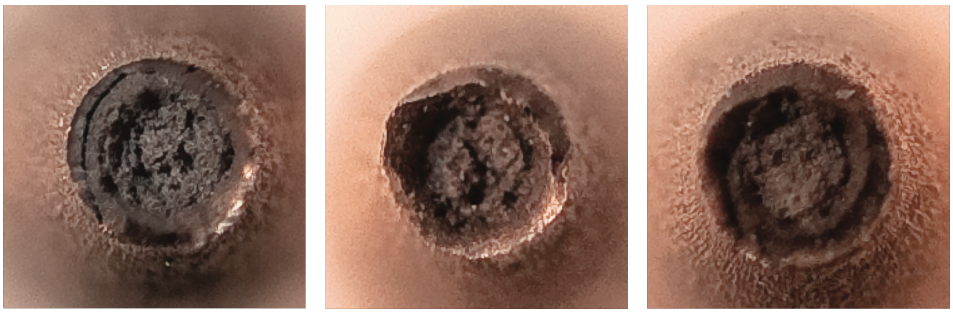

(a) 0^o

(b) 45^o

(c) 90^o

Figure 3.4: Fracture surface of tensile tests conducted by Slåttedalen and Ørmen. [5]

3.2.2 Dynamic Tensile Tests

The rest of the specimens cut out from the pipe were used to investigate material behaviour for higher strain-rates. This was done by conducting dynamic tensile tests using a Split-Hopkinson Tension Bar. Two parallel tests were performed at three different strain-rates, namely $\dot{\varepsilon} = 240\ s^{-1}$, $\dot{\varepsilon} = 535\ s^{-1}$ and $\dot{\varepsilon} = 830\ s^{-1}$. Based on two stress-wave measurements the stress-strain curves were calculated by adopting uniaxial wave theory. The dynamic tensile tests showed that the flow stress and to some extent the fracture strain was affected by the strain-rate, as seen in Figure 3.5. The flow stress increased with increasing strain-rate. The fracture strain was slightly reduced with increasing strain-rate, but this was deemed negligible [5].

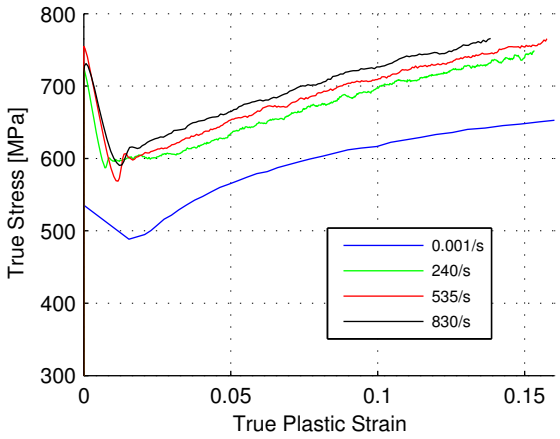

Figure 3.5: Stress - strain curve at different strain-rates. [5]

3.2.3 Uniaxial Tests With Reveresed Loading

Uniaxial tests with reversed loading were performed on a Dartek 20 kN Universal testing machine. The critical areas on the pipes studied experienced compression before they were stretched out [6]. It was decided to perform compression tests with reversed loading, in addition to tension tests with reversed loading. This would show if the material behaviour was independent of the order of loading. The strains were measured by double-sided extensometers, where the buckling tendency would be registered by comparing the measurements from the extensometers. See Fornes and Gabrielsen [6] for more details concerning machine set-up and geometry.

Figure 3.6 shows the true stress - true strain curves for both initial tension and initial compression. The curves showing initial compression was multiplied with -1 for better comparison.

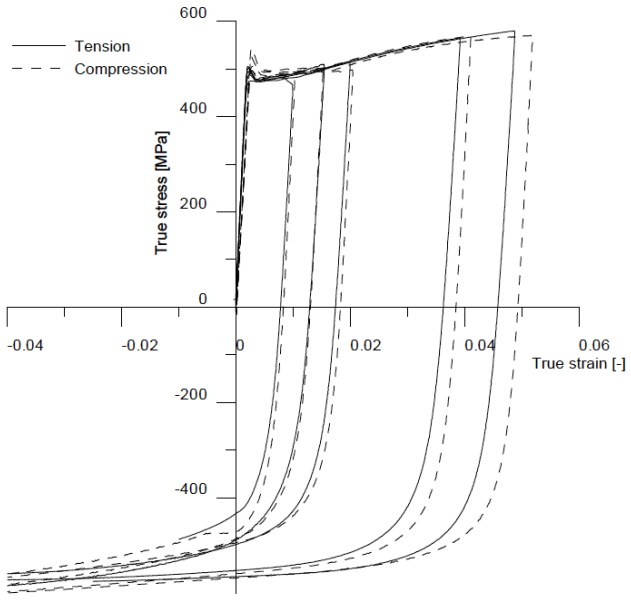

Figure 3.6: Stress-strain curves for uniaxially loaded specimens in compression-tension and tension compression. [6]

The true stress - true strain curves revealed no significant difference in the loading step between initial tension and initial compression. However, the reversed loading curves differed some for the largest strains. This was believed to be due to manually unloading done by a machine operator, who based the reversed loading on the measurements from the extensometers. These measurements varied at large compressive strains making it difficult to unload at the desired strains. It was evident that a Bauschinger effect occurred as the reversed yielding initiated at a lower stress than the initial yielding. Hence, a combined material model was believed to be more accurate in describing the material behaviour for the X65 steel, than a pure isotropic model. It should be emphasized that these tests were conducted for small strains, causing the material description to be valid up to 10% only. Fornes and Gabrielsen [6] calculated the initial yield stress σ_0 to be 480 MPa.

3.2.4 Notched Tests With Reversed Loading

In order investigate if larger compressive strains with reversed loading affected behaviour of the material, the fracture strain, ductility and kinematic hardening, Aune and Hovdelien [7] conducted material tests exposing notched specimens to up to 40% true strain in compression before reversing the load. In addition to compression tests with reversed loading a selection of test specimens were exposed to compressive strains only, up to 80%. The

results for compression tests with up to 40% true strain before reversed loading can be seen in Figure 3.7(a). See Aune and Hovdelien [7] for more details concerning machine set-up and geometry.

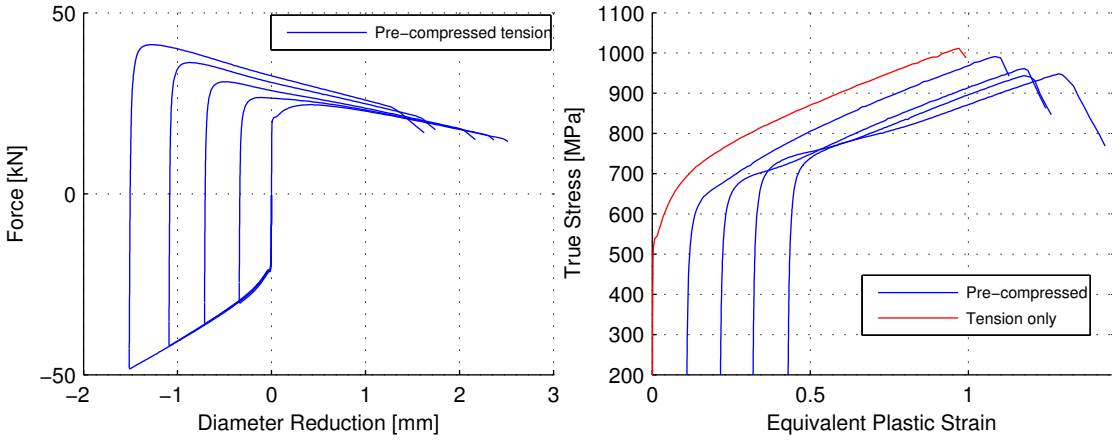

(a) Force vs diameter reduction.

(b) True stress-true strain.

Figure 3.7: Experimental results for notched compression tests with reversed loading. [7]

Figure 3.7(a) clearly show a distinct Bauchinger effect, which is characterized by early re-yielding during the reversed loading. As seen in Figure 3.7(b), the force-displacement curves for inital compression behaved differently than the one from tension only. After re-yielding, Aune and Hovdelien [7] stated that the work-hardening for the compression tests with reversed loading displayed a stagnation, as the work-hardening rate during compression was larger than the work-hardening rate during the reversed loading.

Kristoffersen et al. [4] continued the work started by Aune and Hovdelien [7] by performing compression tests with reversed loading, where the specimens were compressed to true strains of 40%, 60%, 80%, 90% and 100% before being stretched to fracture. Figure 3.8 displays the true stress - true strain curves for the compression tests with reversed loading. The test were 100% strains in compression was applied displayed a visible barrelling effect and is not included in the Figure 3.8.

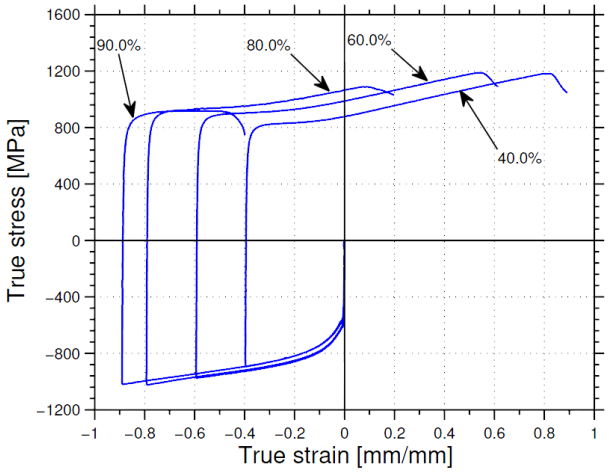

Figure 3.8: True stress - true strain curves for notched compression tests with reversed loading. [4]

Figure 3.8 displays a clear tendency reduction in ductility for large compression. Compressing the specimen to 90% appears to decrease the ductility to a significant extent. However, it was believed that a slight barrelling effect could have been present also for this specimen. [4]

3.2.5 Metallurgical Investigations

The basis for the metallurgical investigation of the material tests conducted by Aune and Hovdelien [7], was the compression tests with reversed loading and the tests with compression only, with strains reaching 80%. Investigations of the compression tests with reversed loading revealed at high magnification that particles appeared to be crushed, with rather large voids surrounding them. This finding was deemed important because such crushed particles lowers the fracture strength of the material. [7]

Kristoffersen et al. [4] investigated material tests further, and found that compressing the specimens appeared to reduce ductility. Tendencies to cleavage fracture was observed on the fracture surfaces when tension was preceded by large compressive strains [4]. Figure 3.9 shows scanning electron microscope (SEM) images of the specimen subjected to tension only and the specimen compressed to a true strain of 40% before being stretched to fracture.

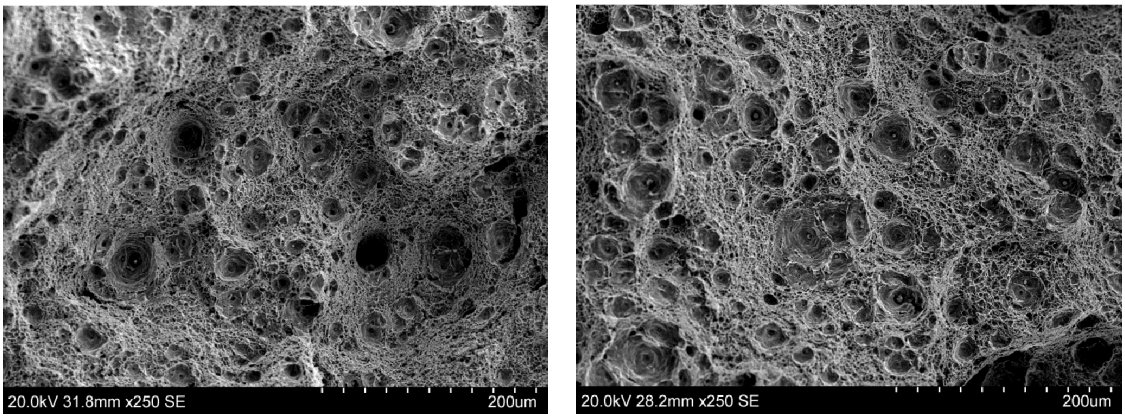

(a) Deep voids for tension only.

(b) Shallow voids for 40% compression.

Figure 3.9: SEM images of fracture surface of notched specimens subjected to compression and reversed loading at 250 times magnification. [4]

The SEM images displayed in Figure 3.9 reveals large and small dimples in the centre of the test specimens. Further, the larger dimples appear to be deeper in the uncompressed specimen than those in the specimen loaded in compression first. This suggests that voids can grow to a larger extent with less compression, which indicates a reduction in ductility when compressing the specimens. Figure 3.10 reveals calcium aluminate particles in all dimples and by further magnification cracked particles are clearly visible [4].

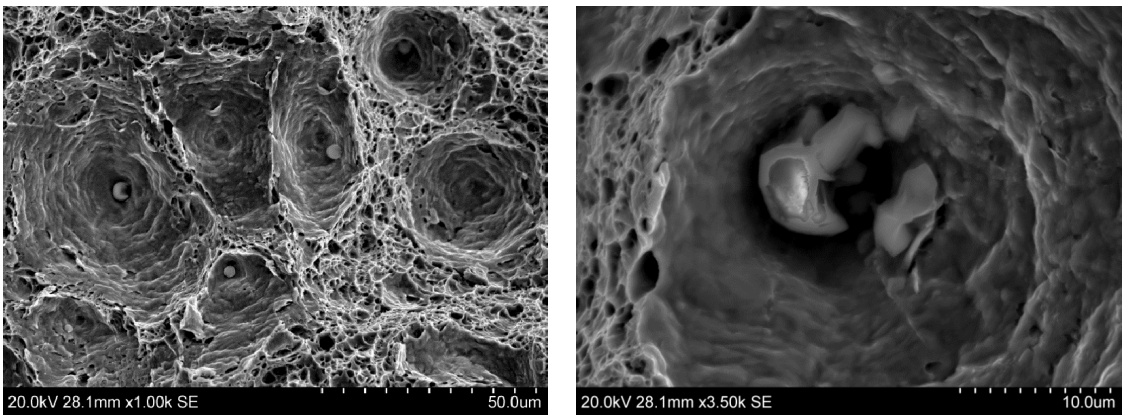

(a) SEM image 1000 times magnified.

(b) SEM image 3500 times magnified.

Figure 3.10: SEM images of cracked particles in the specimen compressed to 40% at different levels of magnification. [4]

As Figure 3.10 shows, cracked particles were found as a consequence of compression. Kristoffersen et al. [4] discussed that voids may initiate during compression, leading to a more brittle fracture if allowed to grow extensively. Brittle fracture is caused by large local stresses that arises from cracked particles, void nucleation on the sides of particles during compression or a combination of both [4].

3.3 Material Models

This thesis does not contain any material model calibrations. Instead the material model developed in previous master's theses [5, 6, 7] were used to represent the material behaviour in the low velocity bending tests performed in this thesis. To be able to utilize the data extracted from the material tests described in Section 3.2, the material models needed to be calibrated and the material parameters identified. This section provides a brief recap of the calibrations done and the material parameters found by Slåttedalen and Ørmen [5], Fornes and Gabrielsen [6] and Aune and Hovdelien [7].

Slåttedalen and Ørmen [5] calibrated the Johnson-Cook constitutive relations described in Section 2.2.5. The temperature dependence was excluded, so only the work-hardening and the strain-rate effects were included. The work-hardening term was calibrated from the quasi static tension tests, and the material parameters were found by the method of least squares. The same method was used to calibrate the strain-rate term from the dynamic tensile tests. Based on the quasi static tension tests the Cockcroft-Latham fracture criterion described in Section 2.2.5 was calibrated. Because Abaqus/Explicit can not use the Cockcroft-Latham criterion directly, the criterion was manipulated following the procedure proposed by Dey [16] making it equivalent to the Johnson-Cook fracture criterion. This was done by assuming an axisymmetric stress state in the specimen. Further the stress triaxility, strain-rate, and temperature were assumed constant during the tensile test. This is only an approximation, due to increasing stress triaxility and strain-rate in a developing neck. The values obtained from this manipulation was implemented into Abaqus/Explicit for numerical simulations.

Fornes and Gabrielsen [6] implemented non-linear combined hardening into the material model. As described in Section 2.2.4, combined hardening consist of both isotropic and kinematic hardening. A procedure to decide the evolution of the combined hardening has been proposed by Opheim [31]. From this a method to distinguish between the contributions from the isotropic and the combined hardening, proposed by Manes et. al. [24], was used to separate the experimental data. Based on these separated data the combined hardening was calibrated by the method of least squares. Due to small strains in the reversed loading experiment, the calibration of the combined hardening was only valid for strains up to 10%. Since the material model needed to consider high strains, test data from Slåttedalen and Ørmen [5] was used to extrapolate the combined hardening up to the fracture strain.

Aune og Hovdelien [7] investigated the previous material models and revealed a deviation between the experiments and the constitutive relation in terms of the reversed loading gradient. An overly stiff behaviour was observed for large deformations in the reversed loading. This was probably due to the extrapolation of the constitutive relation for large strains based on the tension test performed by Slåttedalen and Ørmen [5]. Aune and Hovdelien [7] pointed out the importance of calibrating the material parameters in terms of the expected strain range. Therefore, the material parameters were calibrated based on the

compression test with reversed loading exposed to the largest compressive strains. Due to the triaxial stress state in the notched test specimens it was preferred to adopt an inverse modelling approach, by optimizing the material parameters in LS-OPT and implementing them into the SIMLab Metal Model [7]. Table 3.1 shows the key features of the material models and how they have evolved through three master's theses [5, 6, 7] by different calibrations.

Table 3.1: The development of the material model done by Slåttedalen and Ørmen [5], Fornes and Gabrielsen [6] and Aune and Hovdelien [7].

	Isotropic hardening								
	A [MPa]	B	n	C	$\dot{\varepsilon}_0$ $[s^{-1}]$				
Direct calibration [5]	465.5	410.83	0.4793	0.0104	0.000806				
	Combined hardening								
	Isotropic hardening					Kinematic Hardening			
	σ_0 [MPa]	Q_1 [MPa]	b_1	Q_2 [MPa]	b_2	C_1 [MPa]	γ_1	C_2 [MPa]	γ_2
Direct calibration [6]	330.3	703.6	0.47	50.5	34.7	115640.0	916.0	2225.0	22.0
Direct calibration [7]	310.3	35.3	223.2	846.8	0.42	67440.3	425.1	716.3	9.3
Inverse modelling [7]	299.0	160.0	25.0	400.0	0.25	50401.0	390.7	1279.0	12.8
Fracture criterion [5]	Cockcroft-Latham		Cockcroft-Latham based Johnson-Cook						
	W_c [MPa]		D_1	D_2	D_3	D_4	D_5	$\dot{\varepsilon}_0$	
	1595		0.7	1.79	1.21	-0.00239	0	0.000806	
Properties	E [MPa]		ν		ρ $tonn/mm^3$				
	208000		0.3		$7.85 \cdot 10^{-9}$				

3.4 Component Tests

The purpose of the component tests carried out in the three previous master's theses [5, 6, 7] was to recreate the scenario were a pipeline is first impacted, hooked and dragged along the seabed by an object, followed by the pipeline being released and straitened due to axial forces. As this problem is highly complex it was necessary to make simplifications in order to carry out experimental tests. The problem was divided into two steps, namely the impact step and the stretch step. The impact step will, in the real case, cause local indentation and hooking that will result in large global deformations. Experiments of the impact step would be executed using a pendulum accelerator. Afterwards the pipes would be mounted in a stretch rig, which was to represent the rebound due to axial forces. During the course of previous research, experiments have been conducted on twelve pipeline specimens, labelled A through L.

Slåttedalen and Ørmen [5] conducted experiments on the first four pipeline specimens, labelled A-D. Pipe E and F were later tested by Kristoffersen et al. [4]. These pipes, which were open and empty, were impacted at different velocities to obtain sets of data for different levels of kinetic energy. Fornes and Gabrielsen [6] tested pipes G-J. Pipe G and H were filled with water during impact in order to investigate the effect of pipe fillings. Pipe I and J were both filled with water and closed by welding membranes to the ends [6]. Experiments on pipe K and L were conducted by Aune and Hovdelien [7]. These pipes were not stretched after impact as they were to provide samples for a metallurgical study from the impact step only.

3.4.1 Impact and Stretching of Empty Pipes

The impact tests were carried out using the pendulum accelerator at SIMLab's laboratory [8]. The pipes were mounted in a simply supported manner with a free span of $1m$ and impacted by a trolley with a given mass of $1472kg$ at different velocities. The diameter of the indenter was $10mm$, which is recommended by Det Norske Veritas [1] for dynamic impact testing procedures. The set-up may be seen in Figure 1.2(a). For details concerning test rigs and set-up, please revisit the previous master's thesis by Slåttedalen and Ørmen [5].

Results from experimental tests on pipes A-F are displayed in Figure 3.11. Figure 3.11(a) shows the response for the impact tests as force versus transverse displacement. These impact tests were carried out at different impact velocities. An overview of the initial velocities, measured pipe thickness and measurements taken after the pipes were subjected to impact is given in Table 3.2. Figure 3.11(b) displays force-displacement for the subsequent stretching of the pipes.

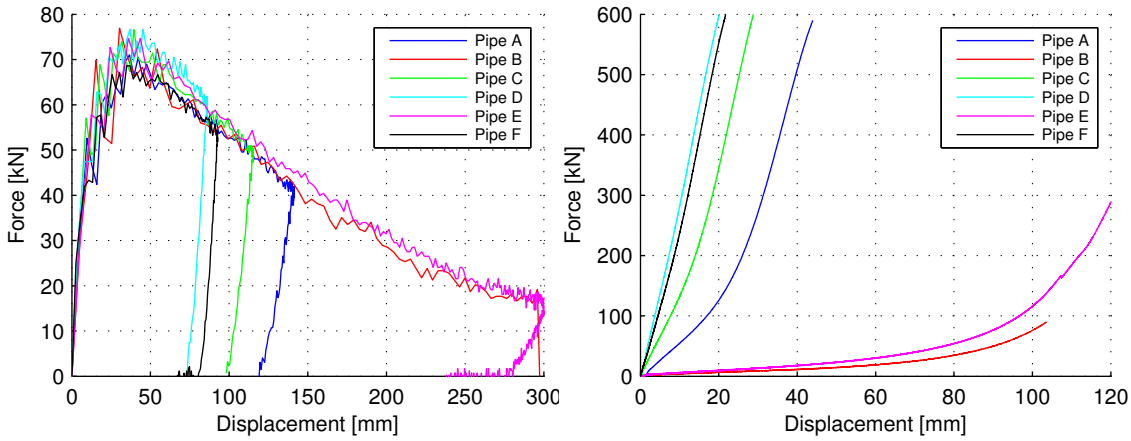

(a) Impact step.

(b) Stretch step.

Figure 3.11: Experimental results from impact and stretch tests for pipes A-F. [5, 4]

As seen in Figure 3.11(a), the results from the impact experiments coincide very well, even for different impact velocities. This implies that the difference in dynamic effects are relatively small, which was most likely a result of the large mass of the trolley compared to the pipes. As seen in Table 3.2 the thickness of the pipes varied significantly, and the difference in peak forces in Figure 3.11(a) was ascribed to this thickness variation. Pipe B and E were impacted using higher initial velocities than the other pipes. The result was that the pipes were not able to absorb all the kinetic energy and the trolley was stopped by the buffers in the rig. This explains the large displacement for these pipes. [5, 4]

Table 3.2 displays some results from the impact tests. The measurements are explained in Figure 3.12.

Table 3.2: Impact results for pipes A-F. [5]

Pipe		A	B	C	D	E	F
Average Thickness	$[mm]$	3.89	3.86	4.04	4.26	4.19	4.09
Standard Deviation	$[mm]$	0.36	0.34	0.18	0.38	0.32	0.30
Initial Velocity	$[m/s]$	3.24	5.13	3.06	2.72	4.14	2.69
Inner Deformation	$[mm]$	170	333	142	105	330	101
Distance North-North	$[mm]$	1250	1104	1267	1286	1123	1288
Angle at Supports	$[degrees]$	12	30	9	3	30	3

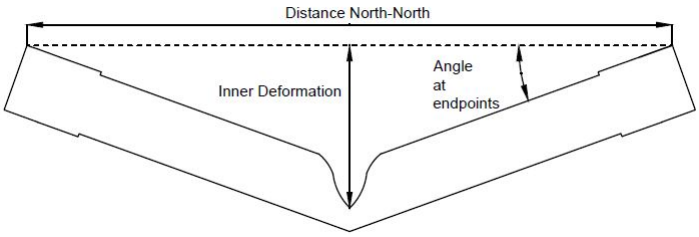

Figure 3.12: Explanation of measurements after pipe impact.

Stretching of the pipes was performed quasi-statically using a $1200kN$ Instron testing machine. As seen in Figure 3.11(b) the force level is lower for pipes with less inner deformation. The stretching force is largely dependent on the transverse displacement of the pipes that had occurred during impact, as larger transverse displacement increases the inner moment arm of the stretching force. This explains the relatively low force levels for pipe B and E in Figure 3.11(b). Surface cracks were visible for all pipes after stretching. Pipe B displayed large through thickness cracks. [5]

3.4.2 Impact against Pipes Filled with Water

Impact experiments conducted by Fornes and Gabrielsen [6] on open and closed pipes filled with water showed little difference in peak force. Force-displacement curves during impact of an empty pipe, an open pipe filled with water and a closed pipe filled with water is compared in Figure 3.13. The sample data in Figure 3.13 is taken from pipe A, G and I, which all were subjected to approximately the same impact velocity. The difference in peak force were, by Fornes and Gabrielsen [6], ascribed to the difference in pipe thickness.

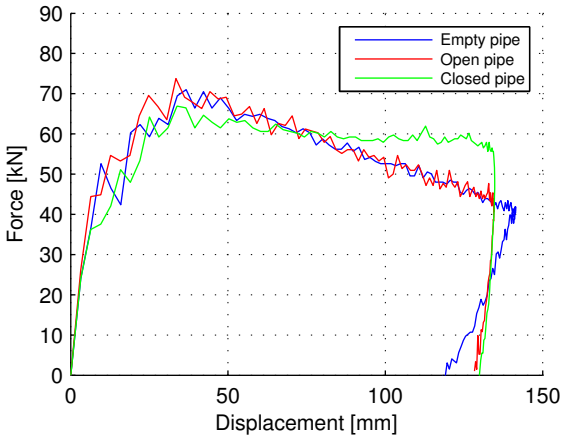

Figure 3.13: Comparison between empty pipe, open pipe filled with water and closed pipe filled with water. [6]

As seen in Figure 3.13, the closed pipeline specimen behaves in a different way than the open ones during impact. A high force level was retained throughout the deformation for the closed pipe. The reason for this is believed to be a result of the pressure build-up, which occurs in the closed pipes. Also, the similarities between the force-displacement path for empty pipes and open pipes filled with water suggests that the mass of pipe fillings may be neglected in this case, as the mass of the trolley is much larger than the mass of a pipe. By use of a trolley with less mass results could prove otherwise. [6]

3.4.3 Metallurgical Investigations

Fracture was discovered for all pipes exposed to impact and subsequent stretching [4]. Thus, it was of great interest to investigate how, and by which mechanisms fracture initiated. Aune and Hovdelien [7] found that fracture initiated earlier than previously thought when they conducted a metallurgical study for pipes subjected to both impact and stretching, and pipes subjected to impact only. The results for pipes subjected to impact only, depicted that fracture and internal damage became more evident when the velocity of the indenter was increased. However, fracture and internal damage were also apparent in pipes subjected to lower impact velocities when investigated at high magnification. Aune and Hovdelien [7] discussed that the notched tests described in Section 3.2.4 failed due to ductile fracture in tension. On the other hand, the metallurgical investigations of the component tests indicated that the pipes exposed to both impact and stretching failed due to both ductile shear and cleavage, as seen in the SEM images presented by Kristoffersen et al. [4] for pipe B in Figure 3.14.

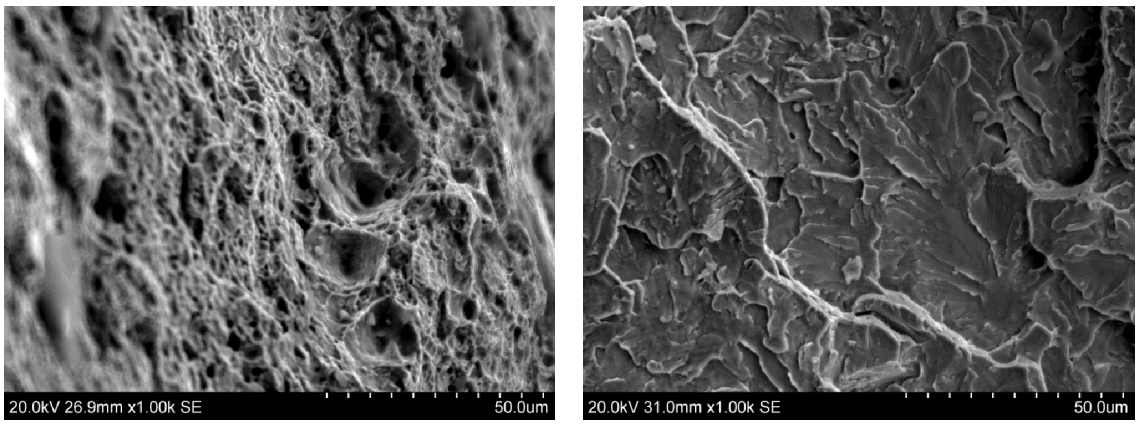

(a) Ductile fracture.

(b) Cleavage.

Figure 3.14: SEM image of fracture zones for pipe B, which displays ductile fracture and cleavage. [4]

Pipe K and L were not subjected to stretching after impact. Pipe K ($v = 5.18m/s$) was impacted using high velocity similar to pipe B, while pipe L ($v = 3.26m/s$) was struck at

a lower velocity similar to pipe A. Kristoffersen et al. [4] did a macroscopic investigation of pipe K and pipe L. The investigation of pipe K revealed a fracture already after impact and elastic rebound, causing fracture through 75% of the wall thickness of the pipe. The crack extended to the inner pipe surface, but internal cracks of the same magnitude were also discovered [4]. Figure 3.15(a) shows an image of the crack extending to the surface, while 3.15(b) shows an image of the internal crack discovered.

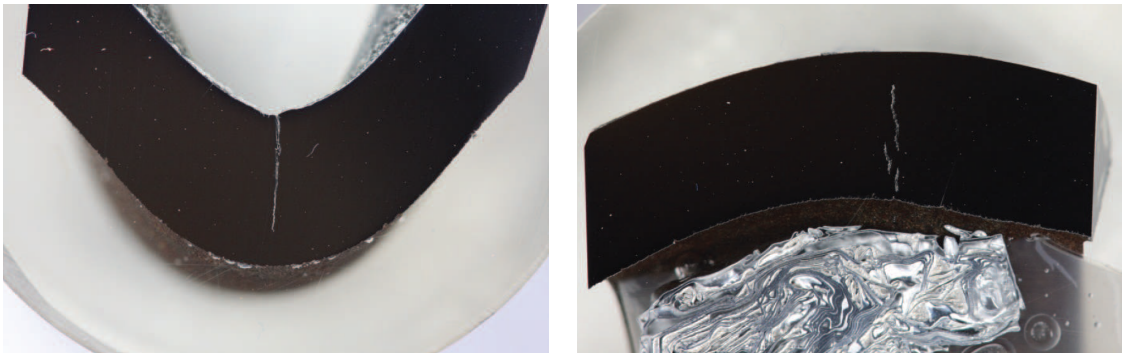

(a) Surface crack through 75% of the thickness. (b) Internal crack through 75% of the thickness.

Figure 3.15: Magnified images of cracks in pipe K subjected to impact only. [4]

At first, the visual inspection of pipe L did not seem to produce the same fracture mechanisms as for pipe K. However, after more thorough investigation in the microscope, cracks were indeed found without any visible signs of the surface. Figure 3.16(a) displays surface cracks, while Figure 3.16(b) displays a internal crack for pipe L. The surface cracks were likely to be a result of traces of grooves from the lathing process, even though the pipe was polished before being subjected to impact. [4]

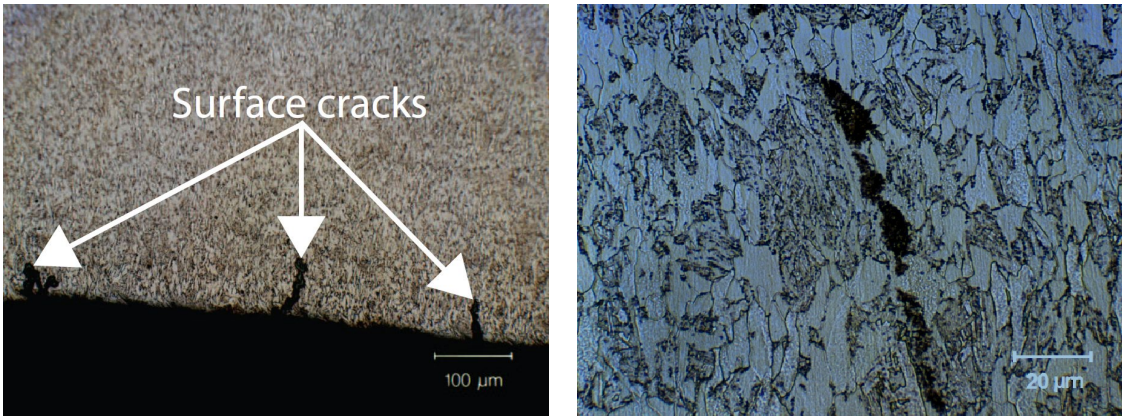

(a) Surface cracks. (b) Internal crack.

Figure 3.16: Cracks discovered on the outer surface and inside the thickness for pipe L. [4]

3.4.4 Low Velocity Impact of Pressurised Pipelines

Jones and Birch [23] conducted experimental tests on steel pipes, which were struck by a wedge-shaped mass travelling up to $10.4m/s$. The pipes were fully clamped at both ends, and most of the pipes were pressurized with a nitrogen gas. Jones and Birch [23] claimed that any content of a pipe would provide an inertial resistance to the deformation of a pipe wall, through an "added mass" effect. This effect was stated to increase with increasing density of the content. Further, Jones and Birch [23] stated that the addition of any content, whether pressurized or not, caused smaller deformations to develop in the vicinity of the impact site when compared with the behaviour of similar empty pipes. In addition, the experiments studied by Jones and Birch [23] indicated that, perhaps, the density of the content was the most significant parameter.

Jones and Birch [23] stated that previous discussions on pipe deformation had been confined almost exclusively to the maximum permanent transverse displacements, referred to as W_f. However, they saw from experiments that the total displacement consisted of local squashing of the pipe cross section in addition to global beam-like displacement. Jones and Birch [23] introduced a method which idealises the deformed pipe cross section in order to estimate the local and global components of the total displacement from experimental measurements. This would make it possible to achieve better insight into pipe behaviour, than with values of the maximum permanent transverse displacement only. Table 3.3 gives some definitions introduced by this method.

Table 3.3: Definitions presented by Jones and Birch [23].

r_0	radius of deformed pipe	D_m	max. width of deformed pipe
ϕ_0	angle, see Figure 3.17(a)	W_l	local indentation
β	angle, see Figure 3.17(a)	W_g	global displacement
T_r	local permanent thickness of deformed pipe	W_f	total displacement

Figure 3.17 illustrates an idealised cross section with the definitions given in Table 3.3, making it possible to develop estimates for experimental values of local and global deformations.

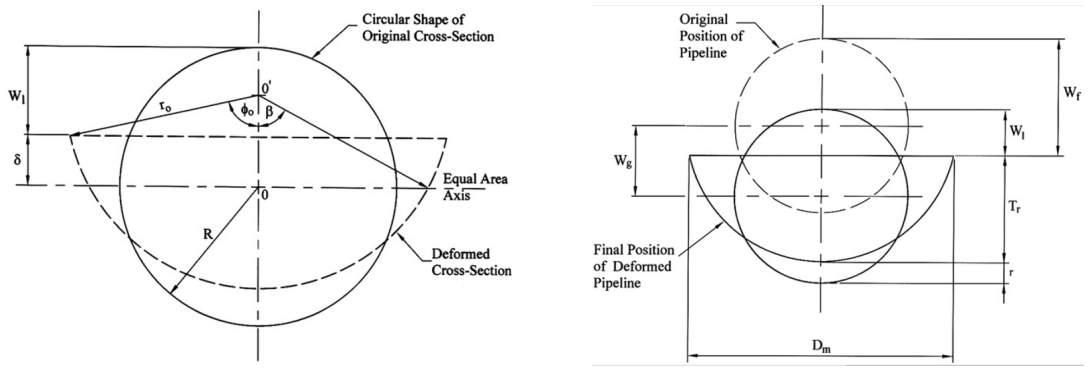

(a) Original and idealised deformed cross section. (b) Definitions for idealised deformed cross section.

Figure 3.17: Original and deformed cross section of a pipe with visualization of r_0, ϕ_0, β, T_r, D_m, W_l, W_g and W_f. [23]

The estimates are based on the assumption that the cross section underneath the wedge is deformed inextensionally in the circumferential direction, into a circular profile with a radius r_0 and closed with a line as illustrated with the dashed line in Figure 3.17(a). Furthermore, the center of the undeformed pipe, which is used to define the global displacement, is assumed to coincide with the equal area axis of the deformed section. With these assumptions it was possible to obtain the local indentation and the global displacement from the three measurements W_f, T_r and D_m, defined in Table 3.3.

First the radius of the deformed pipe is found by

$$r_0 = T_r \left\{ 1 + \left(\frac{D_m}{2T_r} \right)^2 \right\} \frac{1}{2} \tag{3.1}$$

where both D_m and T_r can be measured after an experimental test. The angles ϕ_0 and β are given by

$$cos\phi_0 = 1 - \frac{T_r}{R_0} \tag{3.2}$$

and

$$\beta = \frac{\pi R}{2r_0} \tag{3.3}$$

The quantity δ, as defined in Figure 3.17(a), is calculated by

$$\delta = r_0 \left(cos\beta - cos\phi_0 \right) \tag{3.4}$$

From this the local indentation can be calculated by

$$W_l = R - \delta \tag{3.5}$$

and the permanent global displacement can be found by

$$W_g = W_f - W_l \tag{3.6}$$

Jones and Birch [23] found that the $\frac{W_l}{W_g}$-ratio of the pipe calculated by Equations (3.5) and (3.6) generally decreased as the internal pressure increased for a given value of the impact energy. Generally speaking, this decrease was largely driven by a reduction in the local indentation. The magnitude of the local indentation increased as the impact energy increased, although as a proportion of the total displacement it tended to decrease. They also found that as the internal pressure increased, more impact energy was likely to be absorbed in an global deformation mode at the expense of the local energy absorption underneath the wedge. This could be seen from e.g. a decrease in the local deformation of 30.6% when comparing an non-pressurized pipe to a pipe with internal pressure of 10MPa [23]. For the same two experiments the global displacement increased by 3.5% [23].

3.5 Numerical Simulations

This section gives a brief summary of some numerical pipe simulations carried out in the previous master's theses [5, 6, 7]. This includes a parametric study and simulations using different material models. Although different experiments and thereby different simulations would be carried out in this thesis, findings in previous theses were thought highly relevant. Slåttedalen and Ørmen [5] established both shell and solid models for pipes A through D. These models were established by use of the graphical pre/post-processor Abaqus/CAE. Figure 3.18 displays an overview of the shell model.

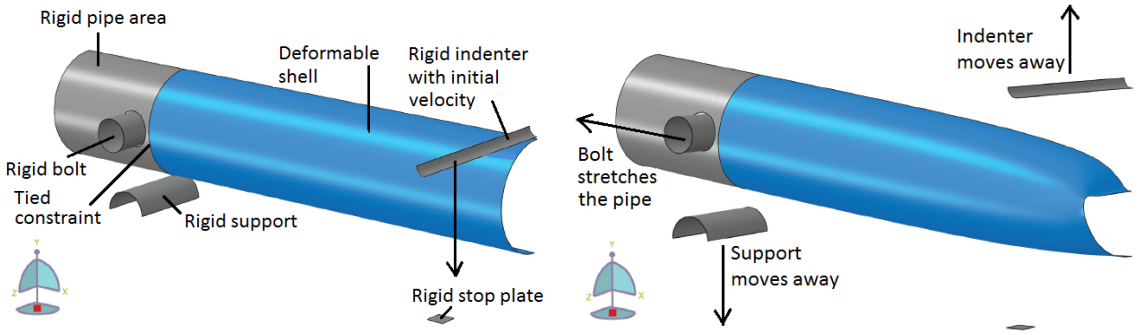

(a) Shell model during impact step [5].

(b) Shell model during stretching step [5].

Figure 3.18: Shell model provided by Slåttedalen and Ørmen [5].

Figure 3.18(a) represents the impact step conducted in the pendulum accelerator and Figure 3.18(b) represents the stretch step. The models established by Slåttedalen and Ørmen [5] were the basis for simulations done by Fornes and Gabrielsen [6], as well as simulations done by Aune and Hovdelien [7]. The simulations presented in this chapter were performed with the finite element solver Abaqus/Explicit.

Figure 3.19 displays the global response from numerical simulations done by Slåttedalen and Ørmen [5] with a base shell model for pipe A. The simulation of the impact step displays a slightly too stiff global response and the final deformation was found slightly too small compared with the experimental response. The stretch step showed an overly stiff global response. [5]

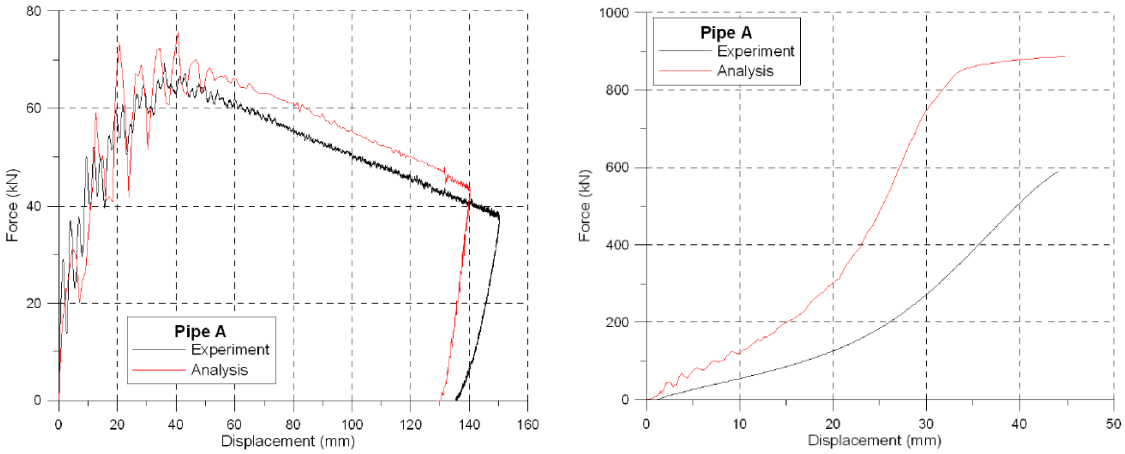

(a) Numerical simulation of impact step [5].

(b) Numerical simulation of stretch step [5].

Figure 3.19: Comparison between the global response from simulations with base shell model for pipe A and the response from the experiments. [5]

The thickness of the pipes was an important parameter and generally varied a lot in measurements. Small variations in thickness was seen to give large differences in response both for the impact step and for the stretch step. By trial and error, different pipe thicknesses were applied in the models in order to obtain better correspondence between the numerical simulations and the experimental data. Slåttedalen and Ørmen [5] pointed out that the applied thicknesses giving response closest to the experimental data, was close to the average measured pipe thicknesses. The stretch step did not improve significantly when thickness giving an excellent fit to the impact step was applied. Shell models were used to fit the simulations to the impact step as they had a much lower computational cost than models using solid elements. Solid models were made after the pipe specific thickness had been decided upon through trial and error by use of shell models.[5]

A parametric study regarding mesh sensitivity was conducted by Slåttedal and Ørmen [5]. For shell models, the response from simulations using element sizes $10mm$, $5mm$ and $2mm$ were compared. It was concluded that the global response was not to any large extent sensitive to the studied shell element size range. On the other hand, the strains were found

much more mesh sensitive. The magnitude and location of the maximum equivalent plastic strain for the simulations with different shell element size can bee seen in Figure 3.20. As the mesh was refined, the local plastic strains increased significantly. Slåttedalen og Ørmen [5] pointed out that if the elements were made so small that the thickness of the shell became larger than the other dimensions of the element, the response could be inaccurate. Since the smallest element size already had shorter lengths compared to the thickness, the mesh was not further refined. [5]

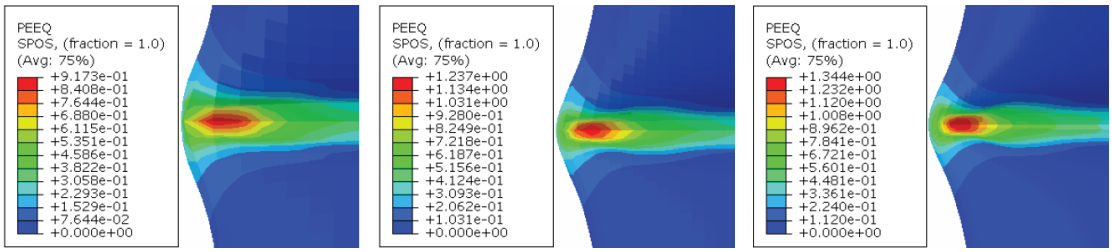

(a) 10mm shell elements. (b) 5mm shell elements. (c) 2mm shell elements.

Figure 3.20: Location and magnitude of equivalent plastic strain after impact step, for different shell element size. [5]

A mesh sensitivity study was also carried out for models using solid elements were different numbers of elements were applied over the pipe thickness. The responses from simulations with one, two, three and four elements over the thickness were compared, and the comparison showed convergence. One element over the thickness deviated significantly from the other simulations, while simulations with two elements only deviated slightly from the simulation with four elements over the thickness. Response with three elements over the thickness was almost identical to response with four elements. Slåttedalen and Ørmen [5] pointed out that increasing the number of elements over the thickness increased the computational expense of the simulations severely. The Cockcroft-Latham based Johnson-Cook fracture criterion also failed to capture fracture in the numerical models. Figure 3.21 displays a visual comparison between numerical simulations conducted by Slåttedalen and Ørmen [5] and photos of the pipes post stretching.

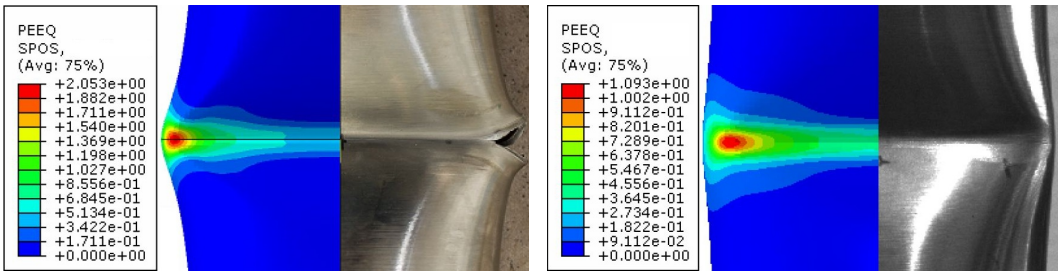

(a) Pipe B. (b) Pipe D.

Figure 3.21: Location and magnitude of plastic strain, together with photo of tested pipes. [5]

Excellent agreement between numerical simulations performed by Slåttedalen and Ørmen [5] and experimental data were found for all impact steps, but the stretch steps were not captured in a satisfactory manner. In an attempt to improve simulations of the stretch step, combined isotropic/kinematic material models were calibrated first by Fornes and Gabrielsen [6] and subsequently by Aune and Hovdelien [7]. Table 3.1 displays an overview of the material models used in previous theses. Aune and Hovdelien [7] made a comparison of the response provided by the different material models both for the impact step and the stretch step of pipe A. The comparison is displayed in Figure 3.22, where Figure 3.22(a) dispays results from the impact step and Figure 3.22(b) displays results from the stretch step.

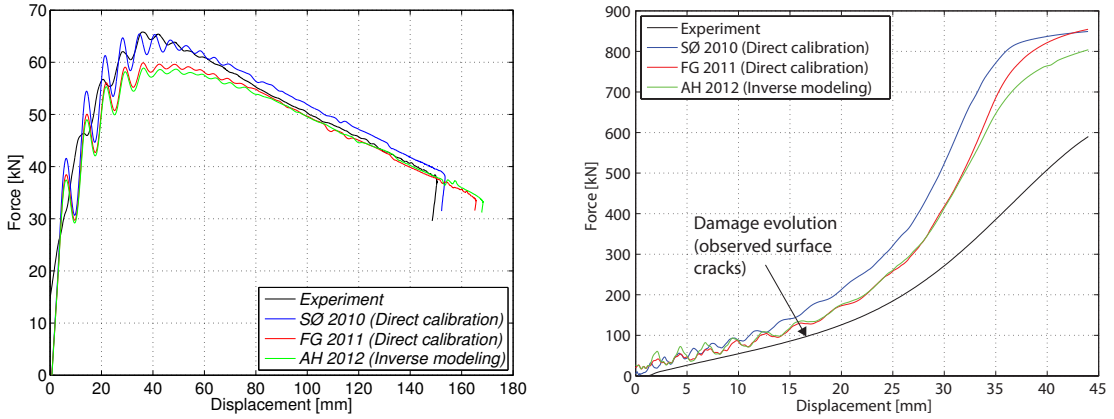

(a) Numerical simulations of the impact step [7].

(b) Numerical simulations of the stretch step [7].

Figure 3.22: Global response of numerical simulations with different material models. Simulations are related to pipe A in the experiments done by Slåttedalen and Ørmen [5].

While use of the the isotropic material model calibrated by Slåttedalen and Ørmen [5] coincided better with the impact step, the combined isotropic/kinematic material model calibrated by inverse modelling by Aune and Hovdelien [7] gave results best fitting with the stretch step. However, the numerical results were still overly stiff for the stretch step. The reason for this was believed to be that the numerical models failed to produce fracture, which was evidently found in the pipes. [7]

4 Material Model

In this chapter the material input for use in numerical simulations is established. The following sections provide a brief introduction to the SIMLab Metal Model and MatPrePost, and how these tools may be used to implement metal material models in numerical finite element simulations. The numerical material input for X65 steel used in this thesis is then established and evaluated.

It was decided to work off two material models, namely one with isotropic hardening only and one with combined isotropic and kinematic hardening. As seen in Figure 3.22, these models gave a slightly different response for the pipe simulations. It was desirable to see how these two different material models affected the results for simulations regarding the experiments conducted in this thesis. Implementation of strain-rate sensitivity was deemed unnecessary as the experiments would be conducted in a quasi static manner. A damage criterion would also be implemented.

4.1 SIMLab Metal Model

SIMLab Metal Model (SMM) is a tool developed by Structural Impact Laboratory. This tool allows for material models used in finite elements simulations to be defined by a number of constants. These constants consist of parameters for density, elastic properties, hardening, strain rate sensitivity etc. The number of constants used when defining the material depends on the amount of properties one would like to add. SIMLab Metal Model was only recently made available for use of Abaqus/Explicit. It was desirable to use SIMLab Metal Model for simulations using Abaqus/Explicit in this thesis because of its simplicity and the fact that this product soon will be made available for SIMLab partners, and thus require testing.

MatPrePost is an additional tool that works in combination with SMM. MatPrePost allows for processing of experimental data, typically from tension and compression tests, using a graphical user interface. The desired material parameters may be found directly by using built-in applications of MatPrePost and used to generate a material card, that may be used as input for Abaqus/Explicit.

By use of SIMLab Metal Model a material library has to be added to the FEM software. The material properties is then applied by input of a material card containing the desired number

of material parameters. This allows the Voce hardening parameters to be implemented directly and not input as tabulated values as one would have to do using Abaqus normally. Also, one may use the Cockcroft-Latham damage criterion directly, which was previously not possible in Abaqus. It should be noted that the notation used when implementing the material constants by use of SMM is different from the ones displayed in Table 3.1. Also, by use of shell elements one would have to calculate and implement the initial transverse shear stiffness of the elements manually. The relations between material parameters stated in Table 3.1 will be explained in the following sections.

4.1.1 Isotropic Hardening

The SIMLab Metal Model Theory Manual [32] states for isotropic hardening

$$R = \sum_{i=1}^{N_R} R_i \tag{4.1}$$

where N_R us the number of isotropic hardening terms. The variables R_i is defined as

$$R_i = \theta_{Ri}(T) r_i \tag{4.2}$$

The evolution equation for r_i is defined as

$$dr_i = \theta_{Ri} \left(1 - \frac{R_i}{Q_{Ri}(T, \dot{p})} \right) dp \tag{4.3}$$

Assuming constant temperature T and constant plastic strain rate $\dot{p}$ Equations (4.2) and (4.3) may be combined and integrated analytically to become

$$R_i = Q_{Ri} \left(1 - exp \left(-\frac{\theta_{Ri}}{Q_{Ri}} p \right) \right) \tag{4.4}$$

This is a Voce hardening term with a saturation value Q_{Ri} as $p \to \infty$.

Comparing Equation (4.4) with the Voce term as stated in Equation (2.22) gives the following relations for the isotropic hardening parameters as written in Table 3.1

$$Q_{Ri} = Q_{Ri}, \quad \theta_{Ri} = b_i Q_{Ri} \tag{4.5}$$

4.1.2 Kinematic Hardening

For kinematic hardening the SIMLab Metal Model Theory Manual [32] states

$$\hat{\boldsymbol{\chi}} = \sum_{i=1}^{N_\chi} \hat{\boldsymbol{\chi}}_i \tag{4.6}$$

where N_χ is the number of kinematic hardening terms and $\hat{\boldsymbol{\chi}}_i$ is defined as

$$\hat{\boldsymbol{\chi}}_i = \theta_{\chi i}(T)\hat{\boldsymbol{\alpha}}_i \tag{4.7}$$

The evolution equations for the tensor $\hat{\boldsymbol{\alpha}}_i$ is defined as

$$d\hat{\boldsymbol{\alpha}}_i = \left(\frac{\hat{\boldsymbol{\eta}}}{\phi(\hat{\boldsymbol{\eta}})} - \frac{\hat{\boldsymbol{\chi}}_{\boldsymbol{i}}}{Q_{\chi i}(T,\dot{p})}\right) dp \tag{4.8}$$

Here, $\hat{\boldsymbol{\eta}}$ is the corotational overstress tensor and $\phi(\hat{\boldsymbol{\eta}}) = \sigma_{eq}$.

Combining Equations (4.7) and (4.8) and inserting $\phi(\hat{\boldsymbol{\eta}}) = \sigma_{eq}$ gives

$$d\hat{\boldsymbol{\chi}}_i = \theta_{\chi i}\left(\frac{\hat{\boldsymbol{\eta}}}{\sigma_{eq}} - \frac{\hat{\boldsymbol{\chi}}_{\boldsymbol{i}}}{Q_{\chi i}}\right) dp \tag{4.9}$$

This is analogous to Equation (2.26), the Armstrong-Fredericks nonlinear kinematic hardening rule. Comparing these equations gives the relations needed for use of the kinematic hardening parameters as stated in Table 3.1

$$Q_{\chi i} = \frac{C_i}{\gamma_i}, \quad \theta_{\chi_i} = C_i \tag{4.10}$$

4.1.3 Damage

In order to model damage in the material SMM starts with the Extended Cockcroft-Latham criterion

$$\dot{D}\left\langle \frac{\phi\hat{\sigma}_I + (1-\phi)(\hat{\sigma}_I - \hat{\sigma}_{III}}{S_0}\right\rangle^{\gamma} \dot{p} \tag{4.11}$$

Setting $\phi = 1$ and $\gamma = 1$, the Cockcroft-Latham criterion is obtained on the form

$$\dot{D} = \frac{\langle\hat{\sigma}_I\rangle}{S_0}\dot{p} \tag{4.12}$$

By integration, the Cockcroft-Latham parameter W_c is identified as

$$W_c = \int_0^{p_f} \langle\hat{\sigma}_I\rangle dp = D_c S_0 \tag{4.13}$$

In addition to the stated parameters there is a parameter β which is used for damage coupling. In this case it will be set to zero as damage coupling is not to be implemented. Thus, in order to model damage using the Cockcroft-Latham criterion, a total of 5 parameters are needed, namely S_0, D_c, ϕ, γ and β.

4.1.4 Transverse Shear Stiffness

When using shell element sections in Abaqus/Explicit in combination with SMM the initial transverse shear stiffness has to be input manually. The transverse shear stiffness for quadratic shell elements may be calculated as

$$K_{11}^{ts} = K_{22}^{ts} = \frac{5}{6}Gt, \qquad K_{12}^{ts} = 0 \tag{4.14}$$

where G is the shear modulus of the material and t is the shell thickness [17].

4.1.5 Limitations of SIMLab Metal Model

SIMLab Metal Model was at the time of writing in development for Abaqus/Explicit. This meant that there were several limitations which had to be dealt with. Energy output would not be generated correctly, meaning that models would have to be checked thoroughly for dynamic effects and hourglassing by use of a material model compatible with Abaqus/-Explicit before implementing the SMM input. Use of axisymmetric elements was not yet implemented for use with SMM. This meant that simulations involving the axisymmetric tensile specimens would have to be done with solid elements.

4.2 Material Input

As mentioned, it was desirable to establish material cards for both isotropic hardening only, and for combined isotropic/kinematic hardening, in order to investigate how this would affect the simulations of the experiments. Strain-rate sensitivity was omitted for both material cards as it was deemed not necessary considering that the experiments were performed in a quasi-static manner.

Input for the isotropic hardening material was generated by use of the Johnson-Cook parameters found by Slåttedalen and Ørmen [5]. SMM is not compatible with input on the form of the Johnson-Cook constitutive relation, meaning that they had to be transformed to the Voce form. The Voce hardening parameters were obtained on the form as stated in Equation (4.4) by fitting a Voce function containing two terms to the Johnson-Cook parameters as stated in Table 3.1. A comparison between the obtained Voce parameters and the Johnson-Cook parameters may be seen in Figure 4.1. As seen, the match was very good. The obtained isotropic hardening parameters for SMM input are stated in Table 4.1

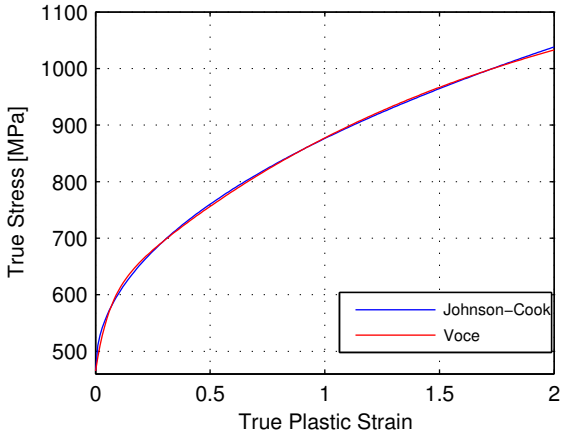

Figure 4.1: Voce hardening function fitted to rate independent Johnson-Cook.

The material parameters found by inverse modelling done by Aune and Hovdelien [7] were used for generation of the material containing combined isotropic/kinematic hardening, as they proved to give the best results for previous material tests considering kinematic hardening. The material card was made by transforming the parameters in Table 3.1 by use of Equations (4.5) and (4.10). The obtained parameters, which is listed in Table 4.1, were then used to generate the material card by use of MatPrePost.

For shell elements the initial transverse shear stiffness was calculated using Equation (4.14). Quadratic shells with sidelengths $4mm$ were used in this thesis as it was fitting with the pipe thickness. The transverse shear stiffness was not input via MatPrePost but in to the model itself.

A damage criterion would also be implemented in the same manner as in the previous theses. Although the damage criterion was believed to be incorrect for the fracture mechanisms that occurs with bending of pipes, it will give an indication to where fracture might occur by reviewing the value of the damage parameter in the numerical results. As mentioned, SMM allows for the Cockcroft-Latham damage criterion to be used directly, meaning that $W_{cr} = 1595$ MPa, found by Slåttedalen and Ørmen [5], may be used as direct input.

Table 4.1: Material parameters used for SIMLab Metal Model input.

Isotropic Hardening [MPa]	Yield Stress	Isotropic				Kinematic			
	σ_0	Q_{R1}	θ_{R1}	Q_{R2}	θ_{R2}	$Q_{\chi 1}$	$\theta_{\chi 1}$	$Q_{\chi 2}$	$\theta_{\chi 2}$
	465.5	627.1	379.5	127.1	2207	-	-	-	-
Combined Hardening [MPa]	Yield Stress	Isotropic				Kinematic			
	σ_0	Q_{R1}	θ_{R1}	Q_{R2}	θ_{R2}	$Q_{\chi 1}$	$\theta_{\chi 1}$	$Q_{\chi 2}$	$\theta_{\chi 2}$
	299	160	4000	400	100	129	50401	100	1279
Damage	Cockcroft-Latham								
	s_0	D_c	γ	ϕ	β				
	1595 MPa	1	1	1	0				
Transverse shear stiffness[1] $[N/mm]$	K_{11}^{ts}	K_{22}^{ts}	K_{12}^{ts}						
	$2.67 \cdot 10^5$	$2.67 \cdot 10^5$	0						
Properties	E	v	ρ						
	208000 MPa	0.3	$7.85 \cdot 10^{-9}$ $tons/mm^3$						

The material cards used in Abaqus/Explicit is appended in Appendix C.

4.3 Material Model Verification

It was desirable to verify that the SMM material models gave satisfactory results when compared to previous material tests. In order to do this, it was decided to do comparisons with material tests done by Slåttedalen and Ørmen [5] and tests dome by Aune and Hovdelien [7]. This way, the numerical results would be compared with both the test they were calibrated for and also an external test. It was also desirable to see how use of SMM compared against using Abaqus/Explicit normally, to make sure that SMM was working correctly.

The notched tension tests with $R = 0.8mm$ done by Slåttedalen and Ørmen [5], along with the notched precompressed tension tests with $R = 3.6mm$ done by Aune and Hovdelien [7] were used in the verification process. The notched tensile specimens were modelled using solid C3D8R elements as axisymmetric elements not yet were compatible for use of SMM. The Abaqus models of the notched tensile specimens may be seen in Figure 4.2. Only a quarter of the specimens were modelled in order to reduce the computational time. As seen, 10 elements were used across the radius. The elements were compressed in the center of the specimens in order to give better results for large strains.

[1] Shell models only

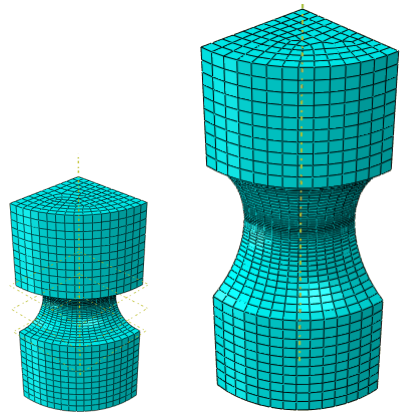

(a) $R = 0.8mm$ (b) $R = 3.2mm$

Figure 4.2: Abaqus models of notched tensile specimens.

Figure 4.3 shows comparisons between the simulations using SMM and the experimental results for tension tests. In Figure 4.3(a) the established isotropic and combined material models are compared with the experimental results using notches with $R = 0.8mm$. Both material models seem to differ slightly considering the peak force. It is also seen that the isotropic model hardens more for larger strains than the combined one. The same is seen in Figure 4.3(b). At the time of the simulations shown in Figure 4.3(a), the SMM damage criterion was not working properly. For the results in Figure 4.3(b) it is seen that fracture occurs slightly later for both simulations compared to the experimental results.

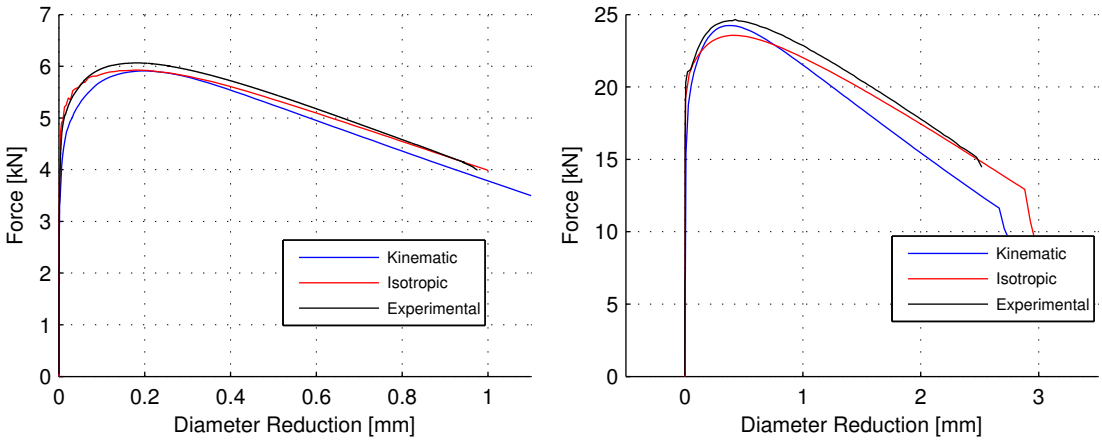

(a) Simulations of notched tests with $R = 0.8mm$ (b) Simulations of notched tests with $R = 3.2mm$

Figure 4.3: Comparison between experimental and numerical results for notched tensile specimen.

For a comparison of how SMM performed versus normal material input in Abaqus/Explicit,

there were carried out a series of simulations corresponding to the experiments done by Aune and Hovdelien [7] using notches with $R = 3.2mm$. SMM simulations were compared with normal Abaqus/Explicit simulations using the same material parameters. Only the combined isotropic/kinematic material were compared. The results from these simulations of the compression tests with reversed loading may be seen in Figure 4.4. The material models seem to behave in a very similar manner. However, a small difference in the response is noted in the peak force and just before fracture occurs. This is likely due to that normal Abaqus/Explicit and SMM may handle kinematic hardening in a slightly different manner. It is also worth noting that SMM gives slightly less hardening as the simulations using normal Abaqus retains a slightly higher force level for larger strains.

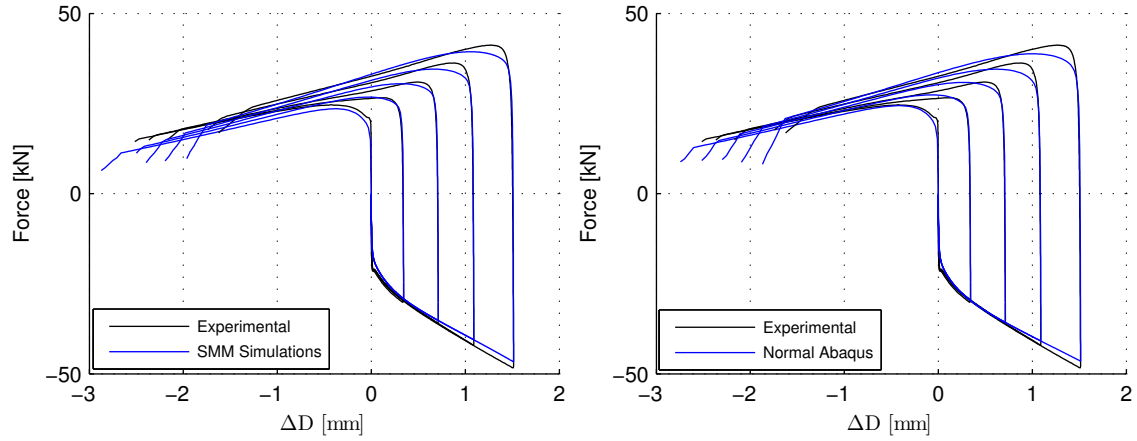

(a) SIMLab Metal Model

(b) Tabulated values

Figure 4.4: Comparison between experimental and numerical results for notched tensile specimen.

Overall the simulations using SMM seems to capture the response of the experiments reasonably well for both the isotropic and the combined material models. The combined hardening model was calibrated for strains up to 40%. This is likely to be the cause of the underestimation of the load levels for larger strains [5].

5 Preliminary Studies

A preliminary study was conducted prior to the experiments in order to get an idea of what could be expected from the experimental tests in the stretch bending rig for different loading scenarios. Base numerical models were established using the experimental set-up as basis. A parametric study regarding the effect of different pipe thicknesses and usage of different material models was carried out. It was also investigated how pressurizing pipes would affect the response during bending.

In contrast to the impact experiments conducted in previous theses [5, 6, 7], the experiments in this thesis were conducted at very low velocities of $25mm/min$. This would allow for controlled experiments regarding application of axial forces and inner pressure. The experiments in the stretch bending rig was assumed quasi-static for the purpose of numerical simulations. Experiments involving pressurized pipes were not conducted due to issues with delivery of pipes.

In the following sections the experimental set-up for testing of pipeline specimens in the stretch bending rig is explained. Base numerical models are then established and followed by the presentation of the respective numerical results.

5.1 Experimental Set-Up

The stretch bending rig used in this thesis can be seen in Figure 5.1. Its main features are that specimens may be mounted between two grips and bent at low welocities while applying axial forces. The rig has previously been utilized by Professor Arild Clausen [33], to perform stretch bending experiments on aluminium extrusions. For use in this thesis, adaptations were made in order to make pipeline specimens fit in the rig. This included new parts that made it possible to attach the pipeline specimens to the grips on the rig. A water accumulator system has also been constructed, which makes it possible to pressurize the pipeline specimens. The rig was thought suiting to represent the scenario where a pipeline is hooked by an object and dragged along the seabed, before being released. The two following sections contain descriptions of the stretch bending rig and what modifications that were done in order to make the pipeline specimens fit. The description of the rig given in Section 5.1.1 is a recap of the description given in *Stretch Bending Rig. Experimental Set-up* by Professor Arild Clausen et al. [34]

Figure 5.1: The stretch bending rig.

5.1.1 The Stretch Bending Rig

An illustration of the rig set-up is seen in Figure 5.2. The rig consists of a steel frame and three servo-hydraulic actuators. The locations of the actuators are displayed in Figure 5.2. The vertical actuator is mounted on the floor, while the horizontal actuators are connected to the steel frame through a cantilevered structure. The rather large dimensions of the steel frame is motivated by the need to avoid deflections that may influence the experiments. Bolted connections are used in the steel frame. This allows for flexibility concerning specimen lengths as the columns may be moved along the floor and the upper beam may be adjusted accordingly. The bending die that is connected to the vertical actuator is also easily replaceable. Note that the vertical bending die used in this thesis is different from the one displayed in Figure 5.2 and that the laser was not utilized.

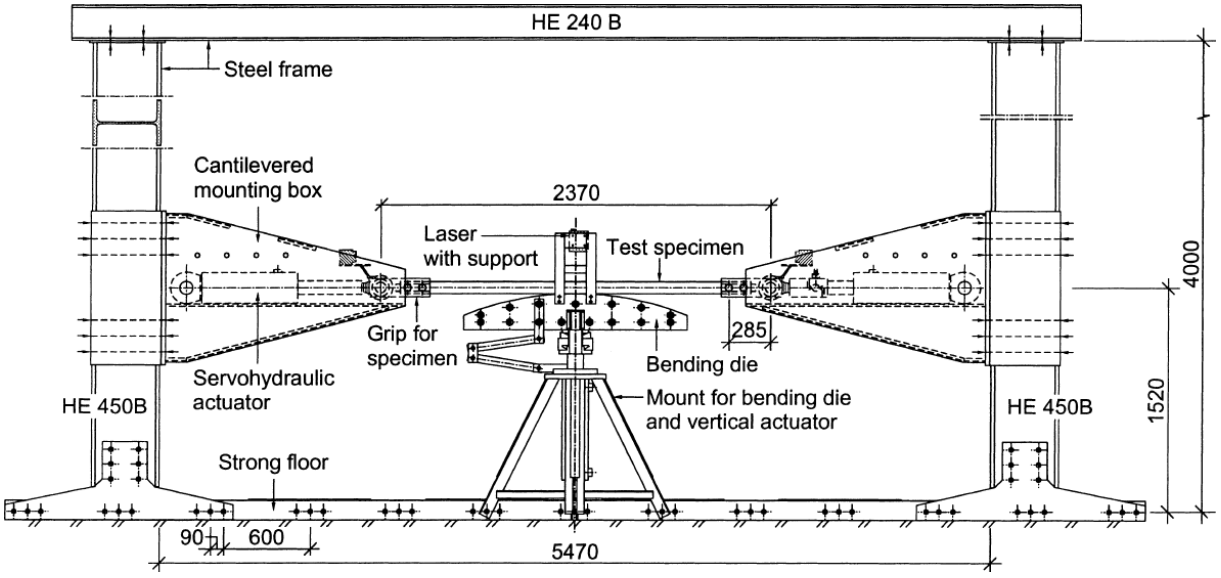

Figure 5.2: Illustration of the rig set-up for the experiments. [34]

All actuators have a load capacity of $330kN$. The main difference between the actuators is the stroke lengths. The two horizontal actuators have a stroke length of $300mm$, while the vertical actuator has a total stroke of $500mm$. The horizontal actuators may be used to apply both tensile and compressive forces. Only tensile forces were relevant for the experiments conducted in this thesis. The horizontal grips are connected to the horizontal actuators through a jointed connection leaving the test specimens free to rotate in the plane, i.e. simply supported.

Experiments in the stretch bending rig may be conducted using displacement control or load control. Displacement control can be used for example to bend the test specimen by prescribing a velocity for displacement of the vertical actuator. Load control may for example be used to apply linearly increasing axial loads with the horizontal actuators.

The vertical and one of the horizontal actuators are provided with load cells. The second horizontal actuator acts as a slave with regard to the other horizontal actuator, meaning that the applied horizontal forces always are equal on both sides. The horizontal load cell may measure both compressive and tensile forces while the vertical load cell may only measure compressive forces. In the experiments performed by Clausen [33] the load cell amplifiers were calibrated for a range of $200kN$, while the maximum available forces from the actuators are $330kN$. The reason for this was that small forces ($<50kN$) are measured more accurately when the range is reduced.

Displacements are independently measured for all three actuators. This is done by resistive displacement transducers supplied with the actuators. The displacement measurements have a resolution of $0.1mm$. In addition to displacements, the rotational angles are measured by two clinometers mounted close to the supports. The range of the clinometers are -60° to +60°. Any further details regarding the rig may be found in *Stretch Bending Rig. Experimental Set-up* by Clausen et al. [34].

5.1.2 Bending of Pipes in the Stretch Bending Rig

Figure 5.3 shows a sketch of the original pipeline specimens. $150mm$ from the ends the pipes were lathed in order to reduce the bending strength so that the stretch bending rig could be utilized. The pipe thickness was lathed from $9.50mm$ to $4mm$. However, when the first experiment was to be conducted it was found that the specimens were much too long. All the specimens needed to be shortened by approximately $250mm$ on both ends in order to fit into the rig.

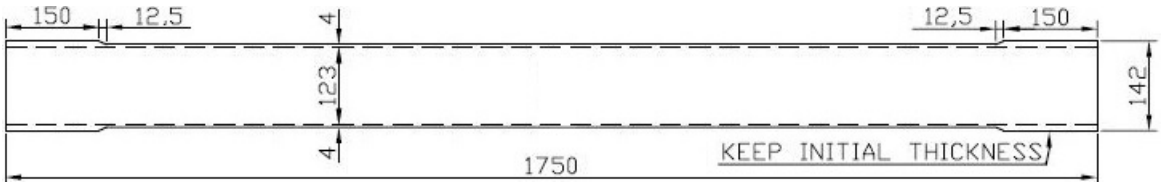

Figure 5.3: Original pipe dimensions in millimetre. Pipes needed to be cut additionally 250mm at each side to fit.

In order to connect the pipeline specimens to the rig, several new parts had been made. This included two flanges, two forks and two block bearings. These parts made it possible to attach pipeline specimens to the grips in the stretch bending rig. Figure 5.4 shows a flange welded on at the end of a pipeline specimen and how it can be connected to the fork. The flanges were fastened to the forks with twelve bolts. Figure 5.5(b) displays a fork and a block bearing. The block bearing was connected to the fork with a shaft. Figure 5.5(a) shows a grip on the stretch bending rig. The grips were connected to the block bearing with two bolts. Drawings of the new parts with measurements may be found in Appendix D.

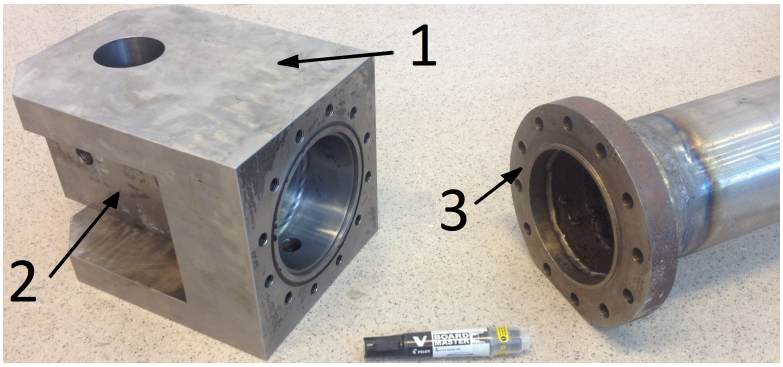

Figure 5.4: Photo of fork (1), block bearing (2) and flange (3)

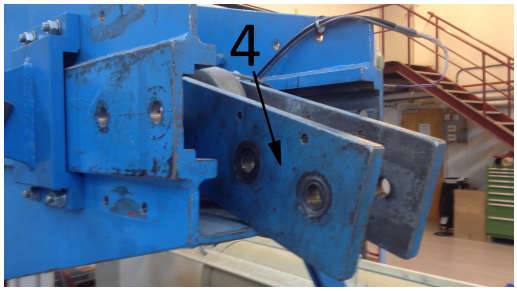

(a) Photo of grips (4) in the stretch bending rig.

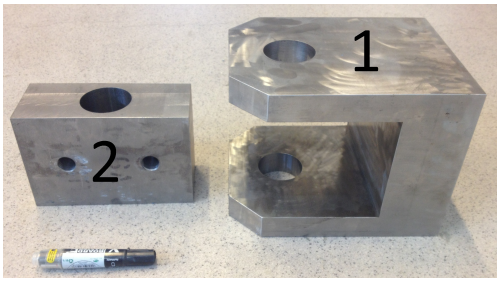

(b) Photo of fork (1) and block bearing (2).

Figure 5.5: Photo of fork (1), block bearing (2), flange (3) and grip (4), which connects the pipe to the stretch bending rig.

The flanges were originally designed to fit on the unlathed area of the pipeline specimen, where $30mm$ of the specimen should have been inserted into the flange before being welded. However, when the pipeline specimens had to be cut, gaps between the flanges and the lathed pipe ends were apparent. In order to solve this issue, $30mm$ was cut from the unlathed pipe area and kept inside the flange. The lathed pipeline specimen was then welded to the flange.

A sketch of the original pipe with flanges welded on can be seen in Figure 5.6(a), where $30mm$ of the unlathed pipe area is inserted into the flange. Figure 5.6(b) shows a sketch of the pipe after $250mm$ has been cut away at each end. As can be seen, $30mm$ of the unlathed pipe area is still inside the flanges.

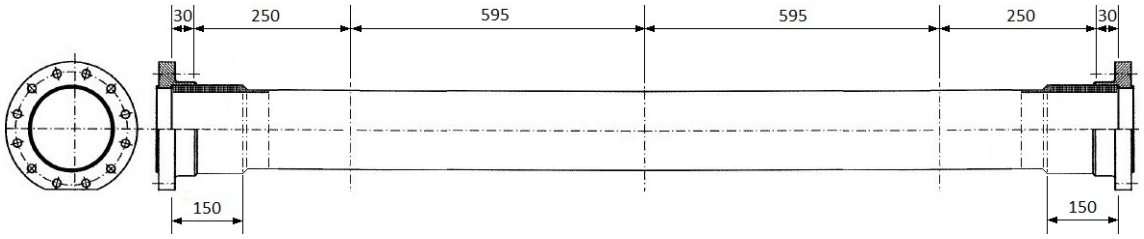

(a) Original pipeline specimen with flanges welded on.

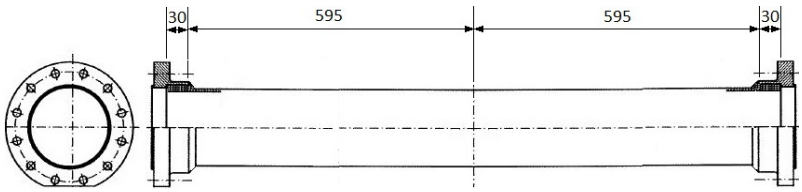

(b) Cut pipeline specimen with flanges welded on.

Figure 5.6: Sketches of original and cut pipeline specimens with flanges welded on.

Using the drawings in Appendix D and drawings of the rig found in Clausen et al. [34], the distance between the rotation point of the stretch bending rig and the weld at the pipe-flange connections were calculated to be $478mm$. This is sketched in Figure 5.7, which illustrates a vertical cut in the pipe-rig connection. The total length between the rotation points was found to be $2146mm$.

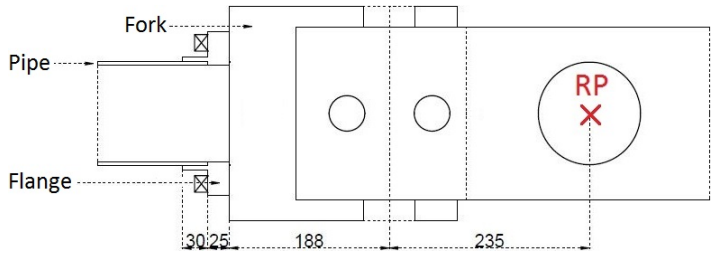

Figure 5.7: Sketch for distance between pipe weld and rotation point of the stretch bending rig. The sketch illustrates a vertical cut in the pipe-rig connection

For bending of the pipe, the original die seen in Figure 5.2 was replaced by the wedge shaped indenter used in the kicking machine in the three previous master's theses [5, 6, 7]. Although the experiments were conducted at low velocities the tip of the indenter had a radius of $10mm$, which is according to dynamic impact testing procedures recommended by Det Norsk Veritas [1]. The indenter is seen mounted on the vertical actuator in Figure

5.8. As the indenter was higher than the original die, the cantilevered structures with the horizontal actuators were moved up two notches in order to make room for the indenter beneath the pipe.

Figure 5.8: Indenter mounted on vertical actuator.

As mentioned, it was of interest to investigate how pressurizing the pipes would affect the global and local response during bending and stretching. Figure 5.9 shows the principal sketch of the accumulator system. It was planned to subject the pipes to 100*bar* water pressure. This is similar to pressure conditions in offshore pipelines. Experiments concerning pressurized pipes were not conducted in this thesis due to issues with pipe delivery.

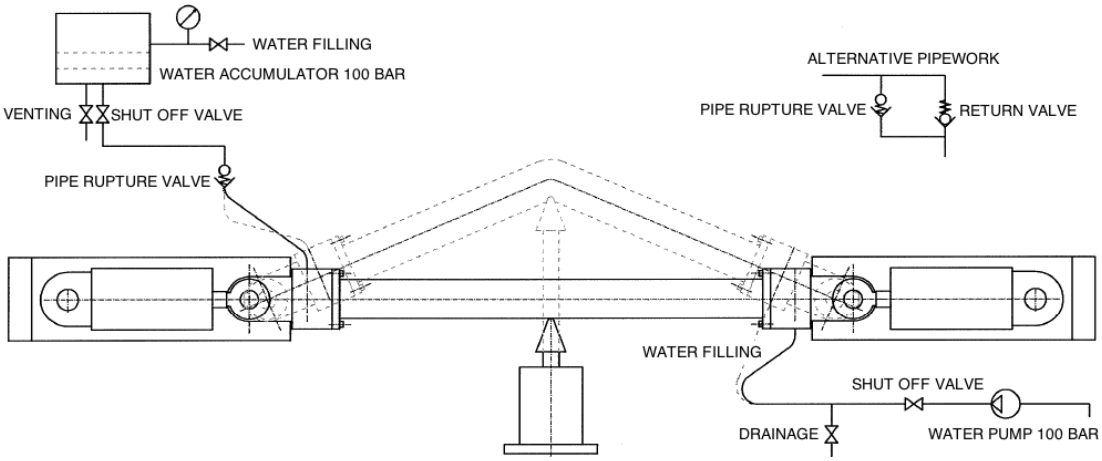

Figure 5.9: Principal sketch of water accumulator system.

5.2 Initial Strength Calculations

This section presents some initial strength calculations. This includes the axial and bending capacity of the pipe specimens and stress calculations for a pressurized pipe specimen.

Elastic Axial Capacity

The elastic axial limit load of the pipe specimens may be calculated considering the cross section in Figure 5.10.

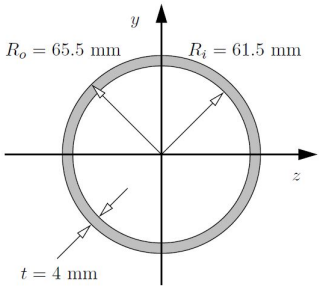

Figure 5.10: Cross section of the pipes with inner and outer diameter.

The elastic axial limit load may be calculated as

$$N_p = A_{pipe}\sigma_y \tag{5.1}$$

where $A_{pipe} = 2\pi R_m t$. Inserting $R_m = 63.5mm$, $t = 4mm$ and $\sigma_y = 472$MPa, as found by Slåttedalen and Ørmen [5], gives an elastic axial capacity for the pipes of $N_p = 753kN$.

An elastic axial capacity of $753kN$ is significantly larger than the load of $330kN$, which is the maximum load capacity of the actuators. The load is applied fixedly in the horizontal direction, resulting in an angle between the pipe and the loading direction during bending. This will increase the inflicted axial load on the pipe. The maximum stroke length of the vertical actuator is $500mm$ and half the length from rotation point to rotation point is approximately $1000mm$, which yields a maximum angle of $27°$. With the maximum angle the inflicted axial load is $370kN$, which is still far below the elastic axial capacity.

Plastic Limit Load

The plastic moment capacity of the pipe during testing in the stretch bending rig may be calculated by considering a simply supported beam as shown in Figure 5.11.

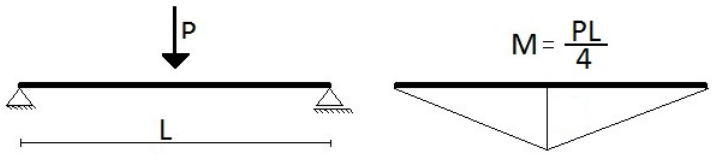

Figure 5.11: Simply supported beam subjected to a vertical load P at the center.

The plastic moment capacity is given as

$$M_p = W_p \sigma_y \tag{5.2}$$

where σ_y is the yield stress and W_p is the plastic section modulus defined as

$$W_p = \int_A |y| dA \tag{5.3}$$

when considering the coordinate system in Figure 5.10. Transforming to polar coordinates and inserting the correct integration limits gives

$$W_p = \int_0^{2\pi} \int_{Ri}^{Ro} |r \cdot sin(\theta)| r dr d\theta \tag{5.4a}$$

$$= 2 \int_0^{\pi} \int_{Ri}^{Ro} r^2 sin(\theta) dr d\theta \tag{5.4b}$$

$$= \frac{4}{3} \left(R_o^3 - R_i^3 \right) \tag{5.4c}$$

With $M = PL/4$ and inserting M_p for M the plastic limit load P_p may be calculated as

$$P_p = \frac{4M_p}{L} = \frac{16 \left(R_o^3 - R_i^3 \right)}{3L} \sigma_y \tag{5.5}$$

Inserting $\sigma_y = 472$MPa $R_o = 65.5mm$, $R_i = 61.5mm$ and $L = 2146mm$ gives the plastic limit load $P = 57kN$. This is well below the capacity of the vertical actuator.

Pressure Calculation

The pipe stresses due to the applied inner pressure may be calculated. Figure 5.12 illustrates a closed pressurized pipe.

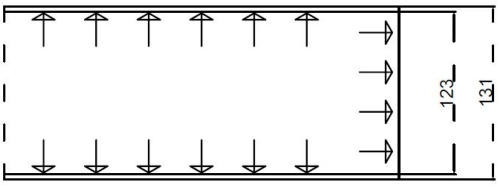

Figure 5.12: Illustration of pipe with inner pressure.

By assuming that the pipe is thin-walled, estimates of the longitudinal and the circumferential stress can be calculated. The longitudinal stress, or axial stress, σ_l can be calculated by

$$\sigma_l = p\frac{R_i}{2t} \tag{5.6}$$

where p is the applied inner pressure, R_i is the inner diameter of the cross section and t is the pipe thickness. By inserting $p = 100bar = 10\text{MPa}$, $R_i = 61.5mm$ and $t = 4mm$ the longitudinal stress is estimated to be $\sigma_l = 76.9\text{MPa}$. This results in a contribution to the axial force of $119kN$.

The circumferential stress, or hoop stress, σ_c can be calculated by

$$\sigma_c = p\frac{R_i}{t} \tag{5.7}$$

By inserting $p = 100bar = 10\text{MPa}$, $R_i = 61.5mm$ and $t = 4mm$ the circumferential stress is estimated to be $\sigma_c = 153.8\text{MPa}$

5.3 Establishment of Base Numerical Models

Numerical models were established with the experimental set-up as basis. The use of shell models was thought adequate for the preliminary studies. Essentially, two numerical models were established, namely one for non-pressurized simulations and one for pressurized simulations.

5.3.1 Non-Pressurized Pipes

A base numerical shell model for non-pressurized pipes was established as seen in Figure 5.13. The model consisted of three parts, namely a deformable part representing the pipe, a discrete rigid part representing the pipe-rig connection and a discrete rigid indenter. It was assumed that a rigid connection may be used, as the connection is very massive compared to the pipe. The length of the rigid connection was arbitrary. An offset reference point (RP) was assigned to the rigid connection. This reference point represented the point of rotation in the stretch bending rig and it provided the ability to inflict horizontal forces on the pipe. As Figure 5.13 shows, only one quarter of the pipe was modelled. This exploited the symmetry of the system, and it was motivated by a reduction of the computational effort needed to run the simulations.

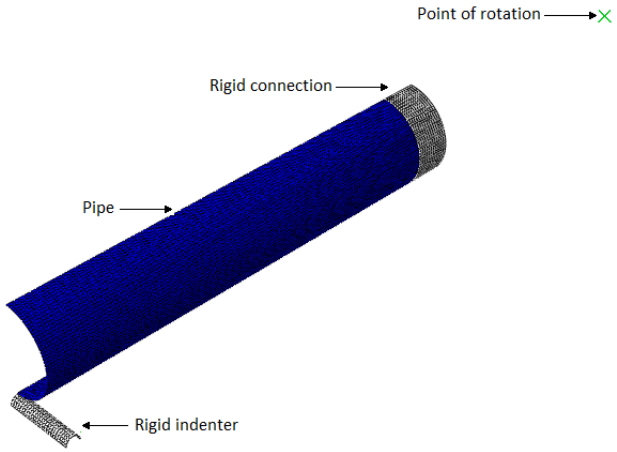

Figure 5.13: Base shell model for non-pressurized pipes.

Figure 5.14 shows the dimensions of the model. As sketched in Figure 5.6(b), the pipes were cut $250mm$ on both sides, leaving a pipe length of $1250mm$. Taking half the length and subtracting $30mm$ at each end, which would be inserted into the flanges, as seen in Figure 5.7, gives a deformable length of $595mm$. A shell thickness of $4mm$ and a mid-shell surface diameter of $127mm$ were applied. The rigid part was modelled separately with a length of $50mm$ and the same mid-shell surface diameter, and tied to the deformable part.

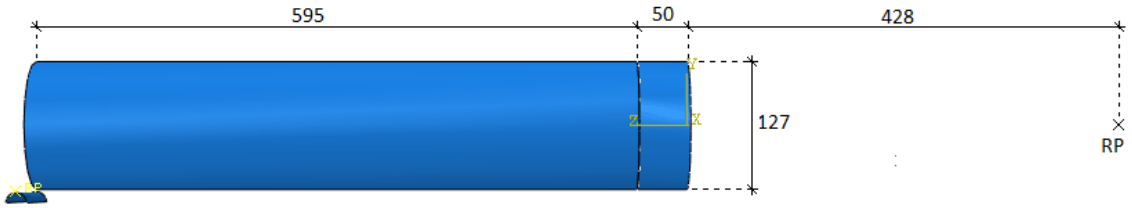

Figure 5.14: Dimensions for base shell model.

The deformable part was discretized with quadratic $4mm$ $S4R$ shell elements, resulting in a total of 7500 elements. The $S4R$ element is a four-node doubly curved thin or thick shell with reduced integration, hourglass control and finite membrane strains [17].

Symmetry boundary conditions were assigned to the deformable pipe to ensure that the symmetry of the system were sustained. Figure 5.15 illustrates the boundary conditions that were applied to the system.

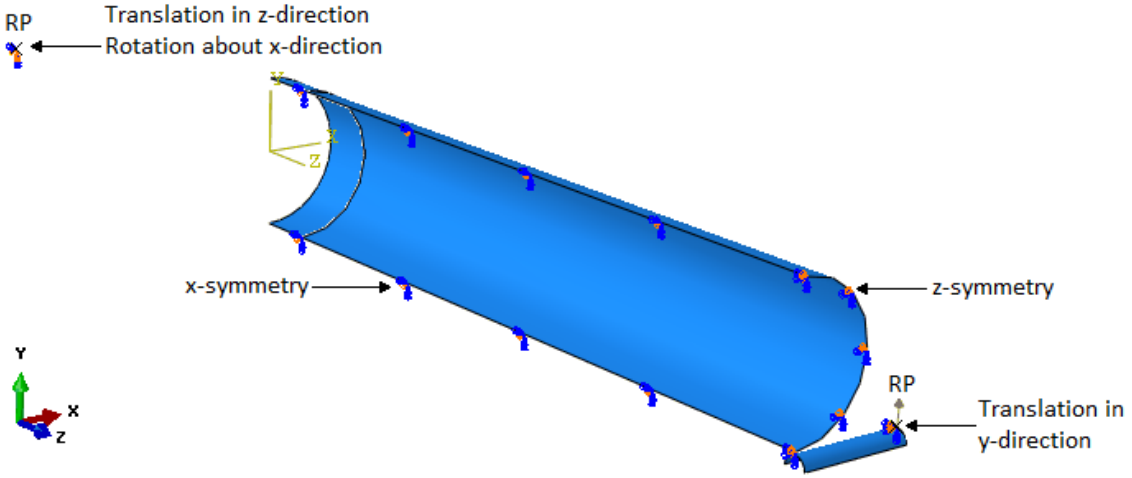

Figure 5.15: Visualization of the boundary conditions for the preliminary study.

The indenter was restricted to translation in y-direction only, as seen in Figure 5.15. Boundary conditions were assigned to the rigid connection by restricting the reference point to free rotation about the x-direction and free translation in z-direction only. This would make the model simply supported. As the stretch bending rig subjects the specimens to axial forces through horizontal actuators, the applied forces in the numerical model were assigned to act fixedly in the horizontal direction and not to rotate with the pipe. Suitable horizontal forces were therefore applied accordingly through this reference point during different analyses.

The material model assigned to the deformable pipe was the model with combined isotropic/kinematic hardening, described in Section 4.2. SIMLab Metal Model is currently only

available for the explicit solver in Abaqus, thus the simulations were carried out explicitly.

Since the experimental tests would take several minutes, the simulations needed to be time- and/or mass-scaled in order to obtain a workable computational time. Time-scaling was utilized in this thesis. As mentioned in Chapter 4, strain rate dependency was neglected in the used material models as the experiments were assumed to behave in a quasi static manner.

In order to deform the pipe an interaction between the indenter and the pipe was applied. A surface-to-surface contact definition was chosen, where the penalty contact method was used as the mechanical constraint formulation, as it is more flexible in combination with rigid bodies [17]. The contact was made frictionless as it was found through trial simulations that assigning friction had a negligible effect on the results.

A total vertical deformation of approximately $200mm$ was thought fitting, and it was found that an analysis time of $0.2s$ was able to provide satisfactory results for this displacement range. For this step time the indenter was given a velocity of $1000mm/s$ in y-direction as seen in Figure 5.15. Some numerical noise was observed for this velocity, but the results showed good compliance compared with trial simulations run with longer analysis time and lower velocity. Results for the contact force of the indenter were smoothed for better visibility. By comparing the kinetic energy to the total internal energy in a trial simulation, no significant dynamic effects were discovered.

5.3.2 Pressurized Pipes

A base numerical shell model for the pressurized pipes was established as seen in Figure 5.16. In the experiments, the pipes subjected to inner pressure would behave as closed pipes due to the fastening to the forks. Thus, in order to do simulations including inner pressure on the pipes, a rigid end cap was tied to the end of the modelled pipe as seen in Figure 5.16.

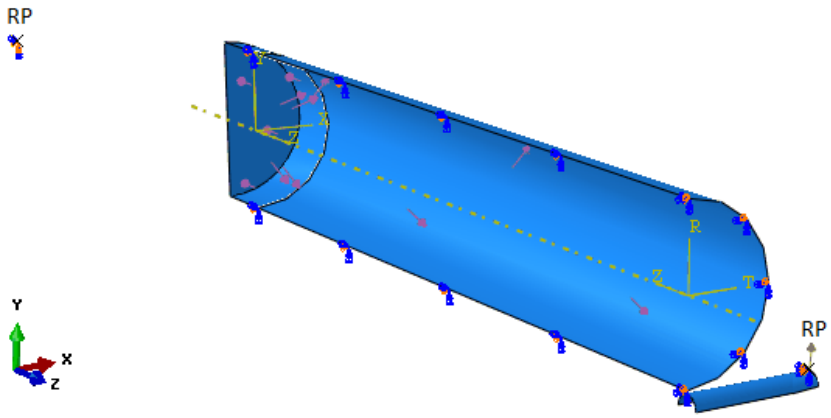

Figure 5.16: Illustration of model with end cap, with applied inner pressure.

Inner pressure was defined as a pressure load with the magnitude of 10MPa. Pressure works as a follower load, meaning that it always will be applied normally to the element surfaces [17]. It was preferred that the response from the applied inner pressure would stabilize before the indenter made contact with the pipe. This was done by assigning two different smooth amplitudes to the inner pressure and the indenter velocity. Otherwise, no alterations was made compared with the non-pressurized pipe

During the development of the pressurized shell model an interesting finding occurred. Simulations with inner pressure, but without the end cap, revealed that the pipe model became unstable during the course of deformation and the reaction force of the indenter dropped to zero. It was seen that when this force dropped to zero the pipe accelerated upwards and away from the indenter. This behaviour was not expected and the issue could be explained by considering that the pressure was defined as force per area. As the pipe was deformed, the area at the top of the pipe became larger than the area on the bottom. This gave a upwards resultant force as illustrated in Figure 5.17.

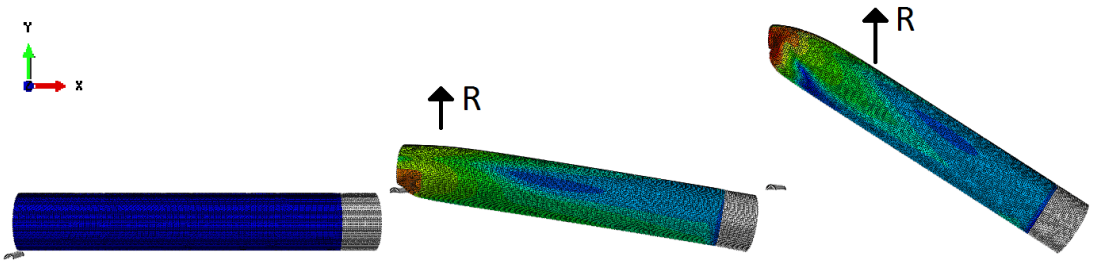

Figure 5.17: Illustration of instability in pressurized pipes.

In order to maintain inner equilibrium, the pipe would have to be closed, meaning that the end cap was needed. To check that inner equilibrium was indeed fulfilled, the indenter force was compared to the vertical reaction force at the rotation point. As these forces were found equal and in opposite direction, the inner equilibrium was fulfilled. As mentioned, experiments on pressurized pipes were not conducted in this thesis.

5.4 Simulation Results

Numerical simulations were carried out with the two base shell models described in Section 5.3.1 and 5.3.2. This was done to obtain an idea of what could be expected from the experimental tests in the stretch bending rig with different load scenarios. The graphical preprocessing was done using Abaqus/CAE, and the analysis were carried out using the explicit solver Abaqus/Explicit. The combined isotropic/kinematic material model was used in all the simulations, except for a comparison simulation for the isotropic material model. In total, 8 different simulations were carried out where different levels of horizontal loads were applied along with inner pressure. A vertical displacement of about $200mm$ was applied for all the simulations. A summary of the simulations can be seen in Table 5.1, with LI meaning linearly increasing horizontal force, C meaning constant horizontal force, *comb* meaning combined hardening and *iso* meaning isotropic hardening.

Table 5.1: Overview of simulations. C - Constant load, LI - Linearly increasing load, comb - combined hardening, iso - isotropic hardening.

Simulation	1	2	3	4	5	6	7	8
Horizontal BC	free	fixed	free	free	free	free	free	free
Applied Horizontal Load	-	-	$C50kN$	$LI50kN$	$C100kN$	$LI100kN$	-	-
Inner Pressure [MPa]	-	-	-	-	-	-	10	-
Material Model	comb	comb	comb	comb	comb	comb	comb	iso

5.4.1 Effects of Applying Axial Forces

It was of interest to investigate how applying horizontal forces affected the results for numerical pipe simulations. In the simulations the horizontal forces were multiplied with a factor of 0.5, as only half of the pipe cross section was modelled. Six different simulations were run using different boundary conditions and horizontal forces:

- One simulation where the pipe was free to translate horizontally with no horizontal load applied.
- One simulation where the pipe was fixed regarding horizontal translation.
- Two simulations where the pipe was free to translate horizontally while constant horizontal loads of $50kN$ and $100kN$ were applied.
- Two simulations where the pipe was free to translate horizontally while applying linearly increasing horizontal loads peaking at $50kN$ and $100kN$.

Table 5.2 summarizes the simulations, labelled 1 through 6. Due to modelling of only half of the cross section, only $25kN$ was applied in the simulations for $50kN$, and only $50kN$ in the simulation for $100kN$.

Table 5.2: Overview of preliminary non-pressurized simulations. C - Constant force, LI - Linearly increasing force.

Simulation	1	2	3	4	5	6
Horizontal BC	free	fixed	free	free	free	free
Applied Horizontal Load	0	-	$C50kN$	$LI50kN$	$C100kN$	$LI100kN$

Figure 5.18 displays a visualization of the deformed pipe from the simulation with free translation and no horizontal forces, i.e. simulation 1. It is seen that only a small part at the middle of the pipe undergoes large local deformations.

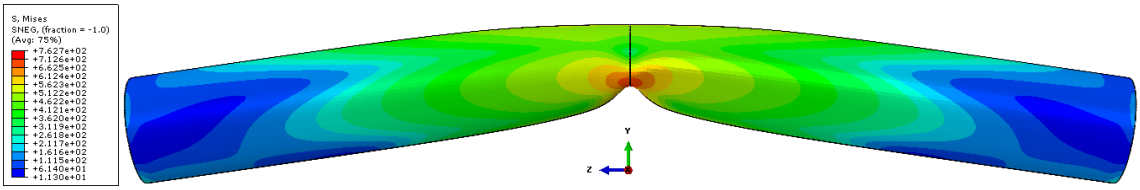

Figure 5.18: Visualization of deformed pipe for simulation 1.

Figure 5.19(a) shows the six different force-displacement curves for the indenter while Figure 5.19(b) displays the respective horizontal loading history. The indenter reaction force taken out from the output database for the simulations was multiplied by a factor of four in order to account for a whole pipe specimen. As seen in Figure 5.19(a), the force-displacement path for the free pipe peaks at approximately $35kN$. After passing the peak, the path declines steadily throughout the pipe deformation. From a displacement of $20mm$, the fixed pipe has a much steeper force-displacement path than the other simulations. It follows the same path as the pipe with constant horizontal force of $100kN$, but when the horizontal reaction force for the fixed pipe increases beyond this level it differs significantly.

The pipes subjected to constant horizontal forces proves to have a stiffer force-displacement response than the free pipe throughout the whole vertical deformation. The slope of the force-displacement curves for the pipes subjected to constant horizontal force seem to stabilize and become constant. It seems like the slope of the force-displacement curve depends on the applied horizontal force, where applying a higher force results in a steeper slope. For the pipes with linearly increasing horizontal load, the force-displacement paths follow the path for the free pipe longer. As the horizontal load increases throughout the simulations, the indenter force level seem to approach the same level as for the pipes with corresponding constant horizontal load. Generally all the simulations, except for the fixed pipe, showed

reasonable force levels with regard of conducting experiments, when compared with the analytically calculated capacities of the pipe and the capacities of the actuators.

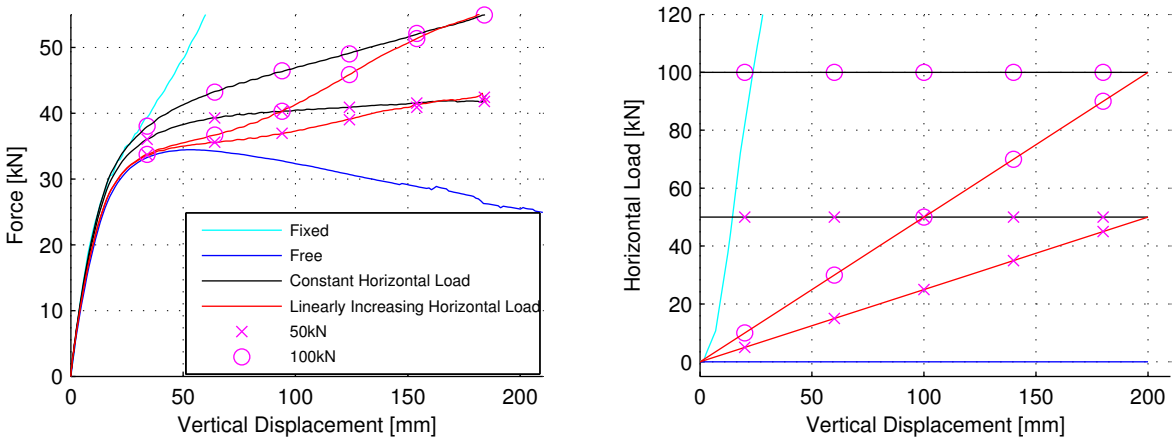

(a) Indenter force-displacement.

(b) Horizontal force versus vertical displacement.

Figure 5.19: Indenter force-displacement curves with different boundary conditions and horizontal forces, see Table 5.2.

Figure 5.20 displays horizontal displacement of the reference point versus vertical displacement of the indenter. The curves show that as the horizontal force increases, the horizontal displacement decreases. It can be seen that curves for constant and linearly increasing horizontal force deviates from each other at the start of the displacement. However, from vertical displacement of approximately 120-130mm the curves for constant and linearly increasing horizontal force seem to coincide.

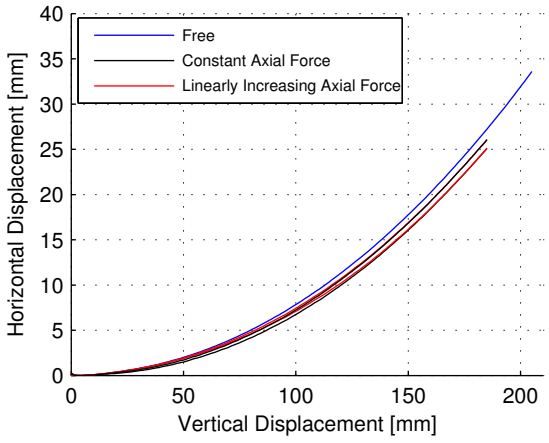

Figure 5.20: Indenter force-displacement curves for a non-pressurized and a pressurized simulation.

Figure 5.21 display a comparison between cross-sectional deformation for the free, $100kN$ constant horizontal force and fixed pipes, for the same vertical deformation range.

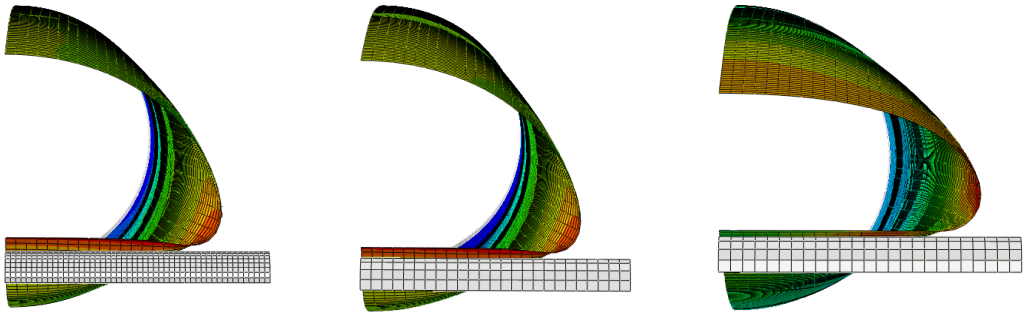

(a) Free (b) C $100kN$ (c) Fixed

Figure 5.21: Comparison between deformed cross sections for free, 100kN constant axial force and fixed pipe.

As seen in Figure 5.21, there is almost no difference between the free pipe and the pipe subjected to constant horizontal force. However, for the fixed pipe the cross section is a lot more flattened than for the other pipes. It should be mentioned that the case for the fixed pipe is somewhat unrealistic as the horizontal load will approach approximately the axial capacity of the pipe.

Regarding the three modes of deformation identified by Tomas and co-workers. [9, 10, 11], namely crumpling, crumpling and bending, and structural collapse, presented in Section 2.1, it seemed that the onset of the 2^{nd} mode of deformation happened immediately for the free pipe, followed by structural collapse. Thomas et al. [9] found that the onset of the 2^{nd} mode occurred earlier for small diameter-to-thickness ratios. It might be that the D/t ratio for these simulation was so small that it was not feasible to identify the 1^{st} mode of deformation.

5.4.2 Effects of Applying Inner Pressure

To investigate the effects of pressurizing the pipes, a simulation was run with 10MPa pressure applied to the inside of the pipe and the whole end cap. The other conditions were the same as the free pipe, as seen in Table 5.3, this simulation was labelled 7.

Table 5.3: Overview of comparable non-pressurized and pressurized simulations.

Simulation	1	7
Horizontal BC	free	free
Applied Pressure	-	10MPa

It was of interest to compare the analytically calculated stresses due to pressure to the numerical results. Thus, an analysis with pressure and without any indentation was run. Figure 5.22 shows the von Mises stress for the pipe subjected to pressure only.

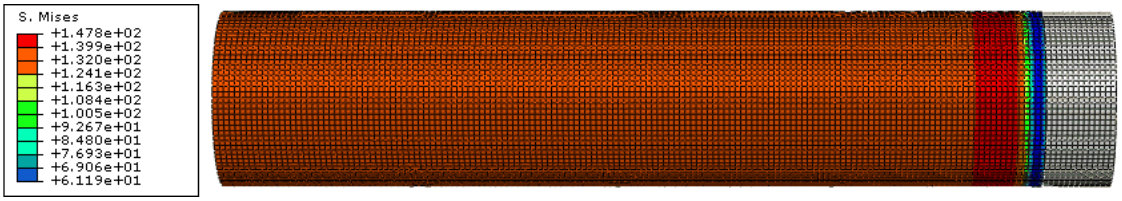

Figure 5.22: Visualization of pipe subjected to pressure only.

The simulation with pressure showed that $\sigma_{11} = 158.8$MPa and $\sigma_{22} = 79.4$MPa, where σ_{11} corresponds to the longitudinal stress σ_l and σ_{22} corresponds to the circumferential σ_c. By comparing the numerical results with the analytical results calculated in Section 5.2, it can be seen that the corresponding stresses are quite similar. The results are presented in Table 5.4.

Table 5.4: Analytical and numerical calculated pipe stresses and axial force.

Method of Calculation	Analytical	Numerical
Longitudinal Stress [MPa]	76.9	79.4
Circumferential Stress [MPa]	153.8	158.8
Axial Force [kN]	119	127

The deviation seen when comparing the analytical and the numerical circumferential strains is because the shell model bases its calculation on the mid-surface pipe diameter and the analytically calculation is based on the inner pipe diameter. Similarly, the longitudinal

stress in the numerical simulation is larger than the analytical stress, as the area of the end cap in the shell model is larger than the inner cross-sectional area of the pipe. The pressure acts on a larger area in the shell model, hence the larger strains and axial force. Thus, the numerical representation of the pressurization seem to slightly overestimate the pipe stresses and the axial force. However, using the mid-surface diameter in the analytical stress calculation in Section 5.2 gives the exact same stresses as the shell model. If shell models were to be used for simulations of experiments involving pressurized pipes an appropriate shell surface definition should be used.

Figure 5.23 shows the force-displacement paths for simulations with and without pressure, and for the pipe subjected to $100kN$ constant horizontal force.

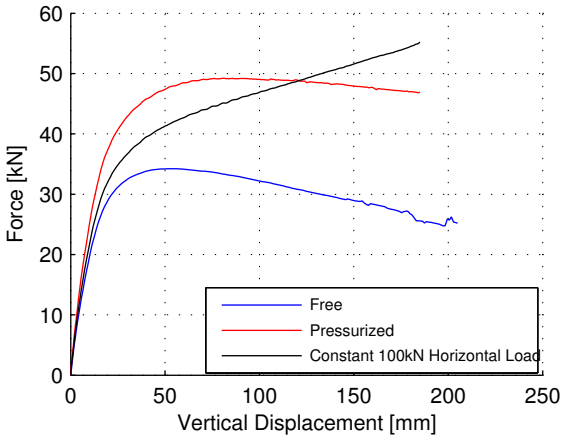

Figure 5.23: Indenter force-displacement curves for a non-pressurized and a pressurized simulation.

The pressurized pipe proves to have a much stiffer force-displacement response than the free pipe, but displays similar shape. As mentioned, the pipe pressurization of 10MPa results in axial force contribution of approximately $119kN$ by analytical calculation and slightly more in the simulation. This makes it interesting to compare the pressurized pipe to the pipe subjected to $100kN$ constant horizontal force. In the beginning of vertical displacement, the pressurized pipe clearly exhibits a stiffer behaviour than both the free pipe and the pipe subjected to $100kN$ horizontal load. This occurs as the cross section is stiffened by the inner pressure. It was verified that inner equilibrium was maintained by comparing the contact force from the indenter to the vertical reaction force at the rotation point. From a vertical displacement larger than $50mm$ the force-displacement curve for the pressurized pipe flattens out and initiates a decrease. As inner equilibrium is maintained the pipe acts similarly to the free pipe, only stiffer.

Figure 5.24 visualizes the deformed cross section for the simulations of the free and the pressurized pipe.

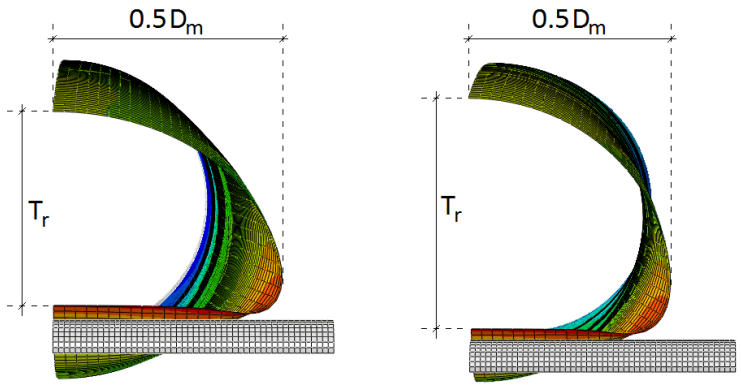

(a) Non-pressurized simulation 1 (b) Pressurized simulation 7

Figure 5.24: Visualization of the deformation for simulation 1 *and* 7.

From this visualization, it is seen that the cross section for the free pipe undergoes significantly larger cross-sectional deformation than the pressurized pipe, meaning that it is more flattened out. This is in good correspondence with the findings of Jones and Birch [23] regarding a decrease in the local to global deformation ratio when pressurizing the pipes, as presented in Section 3.4.4.

Considering the theory given by Jones and Birch [23] explained in Section 3.4.4, global and local deformations may be estimated as a function of T_r, D_m and W_f. T_r is the local permanent thickness of the deformed cross section, D_m is the maximum width of the deformed cross section and W_f is the maximum permanent transverse displacement of the pipeline. T_r, D_m and W_f was measured directly from the field output for the simulations. By use of Equations (3.1) through (3.6) it was possible to estimate the local indentation W_l and the global displacement W_g for simulation 1 and simulation 7. These estimates are given in Table 5.5.

Table 5.5: Estimates of local indentations and global deformations for simulations 1 *and* 7.

Deformations	T_r	D_m	Total W_f	Local W_l	Global W_g	$\frac{W_l}{W_g}$-ratio
Simulation 1	$69.9mm$	$163.6mm$	$188.3mm$	$46.4mm$	$141.9mm$	0.33
Simulation 7	$87.8mm$	$151.0mm$	$187.5mm$	$32.4mm$	$155.1mm$	0.21

As mentioned in Section 3.4.4, Jones and Birch [23] found that as the applied inner pressure increases, the local indentation to global displacement-ratio $\frac{W_l}{W_g}$ decreases. They found that this decrease was mainly driven by the reduction of the local indentation. Looking at the estimates given in Table 5.5, it is seen that the $\frac{W_l}{W_g}$-ratio decreases when pressure is applied to the pipe. However, the decrease is driven by both reduction of the local indentation and

an increase of the global deformation.

It was found that applying a pressure of 10MPa gives a decrease in the local indentation of approximate 30.2% compared with the non-pressurized simulation. In addition, an increase in the global deformation of approximately 9.3% is observed between the non-pressurized and the pressurized simulation. These results corresponds quite well with the results obtained by Jones and Birch [23], which are presented in Section 3.4.4. These results showed that pressurizing a pipe by 10MPa and keeping the impact energy constant decreased the local indentation by 30.6% and increase the global deformation by 3.5%.

5.4.3 Comparison Between Material Models

It was of interest to compare results from pipe simulations with combined isotropic/kinematic hardening and isotropic hardening only. This was mainly of interest due to the difference in force-displacement response these two models exhibited when considering numerical analyses performed in the previous master's theses [5, 6, 7]. Force-displacement curves for these numerical analyses are given in Figure 3.22, which describe the comparison done by Aune and Hovdelien [7]. The isotropic material model was able to describe the impact step very well, while the combined material model underestimated the response slightly. The combined material model was calibrated in an attempt to improve the results for the stretch step. Although the results regarding the stretch step improved slightly using the combined material model, they were not as good as for the impact step. The simulation with the free pipe was repeated with the isotropic material model described in Chapter 4. This simulation was labelled 8. Table 5.6 shows an overview of the two simulations.

Table 5.6: Overview of simulations with combined isotropic/kinematic hardening and isotropic hardening only.

Simulation	1	8
Horizontal BC	free	free
Hardening	combined	isotropic

Figure 5.25 shows the force-displacement paths for the simulations presented in Table 5.6. The results from these simulations revealed the same tendency as shown in Figure 3.22, which shows a comparison for different material models done by Aune and Hovdelien [7]. As Figure 5.25 shows, there is a difference in the force-displacement paths. The simulation with the isotropic material has a higher peak force than the simulation with the combined material model. The difference was found to be 7.1% in peak force compared to 8.6% in Figure 3.22. In addition, the isotropic material simulation displays a sharper peak compared with the more rounded peak for the combined material model. From a vertical displacement of $100mm$ the curves seems to have the same slope. As mentioned in Section 4.3 it was

seen from material tests that the isotropic model hardened more for large strains than the combined model, which can be an explanation of the higher force level in the pipe simulation.

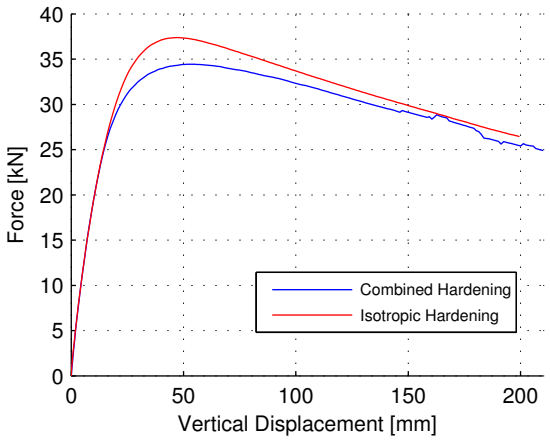

Figure 5.25: Comparison between simulation 1 *run with combined isotropic/kinematic hardening and simulation* 8 *with isotropic hardening only.*

Figure 5.26 displays the von Mises stress fields for the free pipe with combined hardening and the pipe with isotropic hardening only, at maximum vertical displacement. The von Mises stress fields were extracted from the integration points closest to the outer surface, where the stresses were largest.

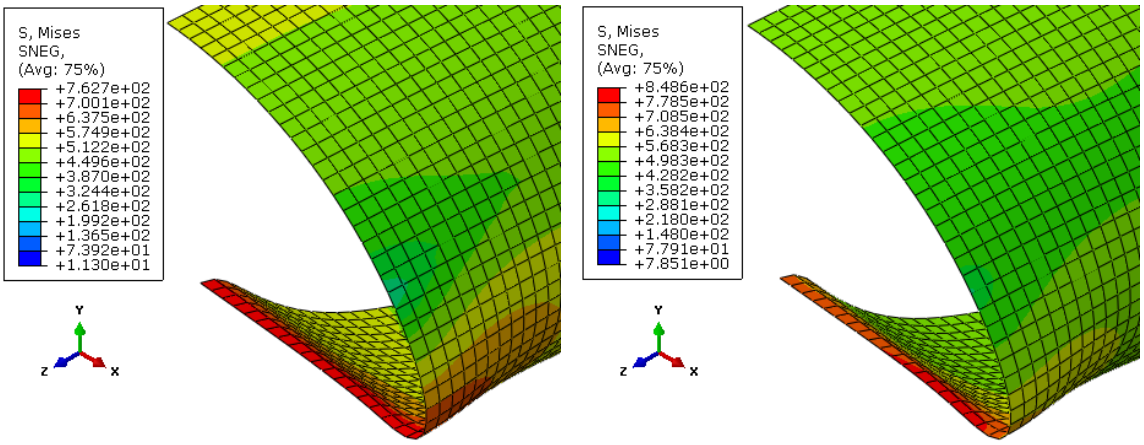

(a) von Mises stress field for simulation 1 (b) von Mises stress field for simulation 8

Figure 5.26: Location and magnitude of von Mises stresses extracted from the integration point closest to the outer pipe surface at maximum vertical displacement for simulation 1 and simulation 8.

By comparing the stress fields in Figure 5.26, a difference in the location of the maximum von Mises stress can be seen. For simulation 1, the von Mises stress is approximately 760MPa for all the elements along the length of the indentation zone. However, for simulation 8 some few elements experiences equivalent stresses up to 850MPa and their location can be seen in Figure 5.26(b). While the maximum von Mises stress is seen to be higher for the simulation with isotropic hardening only, the maximum principal stress was found to be lower than for the simulation with combined hardening. This indicates that the isotropic material model exhibits more work-hardening for other material directions.

5.4.4 Effects of Pipe Thickness

The three previous master's theses [5, 6, 7] have all expressed how the pipe thickness greatly influences the force-displacement response. They have shown that a slight difference in thickness may have a rather large effect on the force-displacement path. From an analytical approach the stiffness for plate bending is a function of the thickness to the power of three, implying that for rather large thickness variations the bending force would be greatly affected.

It was of interest to investigate how changing the pipe thickness would effect the force-displacement response for the experiments conducted in this thesis. In the previous master's theses [5, 6, 7] the thickness could deviate up to $\pm 0.50mm$ around the cross section of a pipe. Thus, the simulation with the free pipe was repeated with shell thicknesses of $3.50mm$ and $4.50mm$ and compared with the results using a thickness of $4.00mm$. The different force-displacement response curves are displayed in Figure 5.27(a), and it is seen that the force-displacement paths is highly sensitive regarding the pipe thickness. The paths displays similar shape, but increasing the thickness from $4.00mm$ to $4.50mm$ increases the force from $35kN$ to $41kN$. This corresponds to a 17.1% increase in force compared to an increase in thickness of 12.5%. It is evident that the thickness in the numerical simulations must be sought to be described as accurate as possible, in order to simulate the experiments in a satisfactory manner. Figure 5.27(b) displays horizontal displacement of the reference point versus vertical displacement of the indenter. It can be seen that the curves displays no significant difference from each other. This is reasonable as thickness will mainly affect the deformation of the cross section and not affect the length of the pipe.

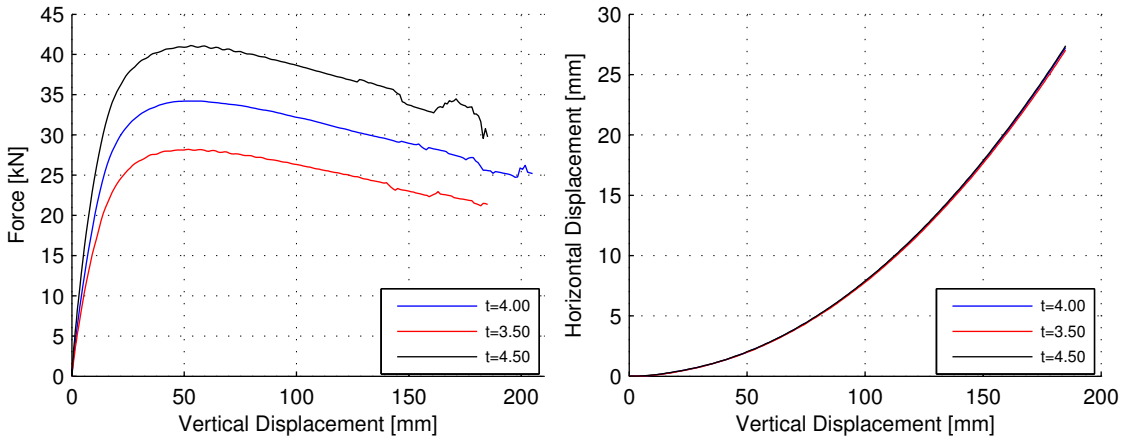

(a) Force-displacement curves for indenter with different thickness for the shell elements.

(b) Horizontal versus vertical displacement.

Figure 5.27: Results comparing effect of pipe thickness.

5.4.5 Equivalent Plastic Strain

As possible cracks are likely to be initiated where the equivalent strains are largest, it was of interest to compare the maximum equivalent plastic strains from the preliminary simulations. Results from simulation 2 were excluded in the comparison due to unrealistic force levels. Table 5.7 shows a comparison between different simulations. Simulation 1 and simulations 3 through 6 is the free pipe and pipes subjected to horizontal forces respectively. Simulation 7 is the simulation with applied inner pressure and simulation 8 includes the isotropic material model only. The equivalent plastic strains were extracted from the integration points closest to the outer surface at maximum vertical displacement, where the equivalent plastic strains was largest.

Table 5.7: Overview of pipe simulations and maximum equivalent plastic strain extracted from integration points closest to the outer pipe surface at maximum vertical displacement. C - Constant load, LI - Linearly increasing load, comb - combined hardening, iso - isotropic hardening.

Simulation	1	3	4	5	6	7	8
Applied Horizontal Force	-	C50kN	LI50kN	C100kN	LI100kN	-	-
Inner Pressure [MPa]	-	-	-	-	-	10	-
Material Model	comb	comb	comb	comb	comb	comb	iso
Equivalent Plastic Strain [%]	83.7	78.1	79.2	74.4	76.6	71.5	83.5

Looking at the maximum equivalent plastic strain in simulation 1 through 6, a slight decrease in strain is noticed as more horizontal force is applied to the system. As cracks are likely to be initiated where the equivalent strains are largest, it might be assumed that

there is a lesser possibility of crack-initiation for the simulations with applied horizontal force. When comparing the non-pressurized pipe from simulation 1 to the pressurized pipe from simulation 7, it is also seen a decrease in maximum equivalent plastic strain. This is most likely due to less local deformation for the pressurized pipe. Looking at Figure 5.28 the critical elements for simulation 1 are displayed.

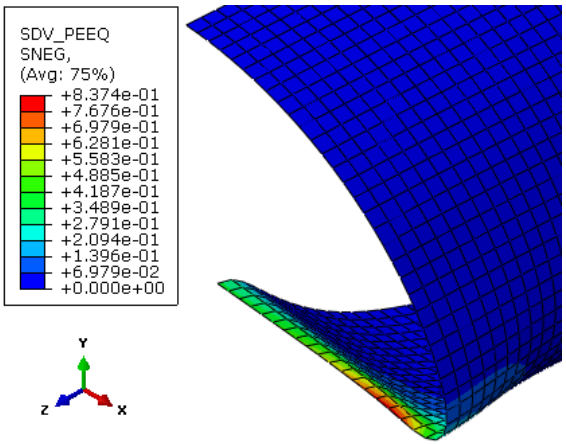

Figure 5.28: Localisation and magnitude of equivalent plastic strains extracted from the integration points closest to the outer pipe surface for simulation 1.

The critical elements are the elements undergoing most equivalent plastic strain while the main principal stress $\sigma_1 > 0$, as the Cockcroft-Latham fracture criterion states that fracture initiates when the equivalent strain reaches the fracture strain [16]. The location of these elements coincide very well with the findings from previous master's theses [5, 7], as seen in Figure 3.21. The location of the maximum equivalent strain was similar for all simulations.

6 Experimental Tests

In this chapter the performed experiments are presented with their respective results. In addition, the following sections contains descriptions of the measurements of the pipes and calibrations of the load cells. Further, an introduction of Digital Image Correlation is given, as it was decided to try and utilize this technology in the experiments.

Initially, it was planned to conduct six experiments in the stretch bending rig. The six experiments planned were:

- Bending without applying horizontal force, with and without constant inner pressure.
- Bending while applying constant horizontal force, with and without constant inner pressure.
- Bending while applying linearly increasing horizontal force, with and without constant inner pressure.

Due to issues with pipe delivery only three pipes were available for testing. Therefore, only experiments without pressure were carried out. Experiments without horizontal force and with constant horizontal force were conducted. Due to calibration issues and a bug in the control program for the horizontal load cell in the experiment involving linearly increasing horizontal force, it was not executed as planned. The pipe specimen was subjected to higher levels of horizontal force than it should have been.

6.1 Measurements of the Pipes

Prior to testing, the pipe thickness and inner diameter of the pipes were measured. Pipe thickness was measured by use of a ultrasonic thickness gage [35], while the inner diameter was measured by use of a caliper. Eight thickness measurements were carried out in the circumferential direction at five different locations along the span. The five locations along the span are illustrated in Figure 6.1. This resulted in a total of 40 thickness measurements for each pipe. The inner diameters were measured at four different directions at each end of the pipes. These measurements were taken before the pipes were cut, meaning at the ends as they are shown in Figure 6.1. A complete list of all measurements can be found in Appendix B.

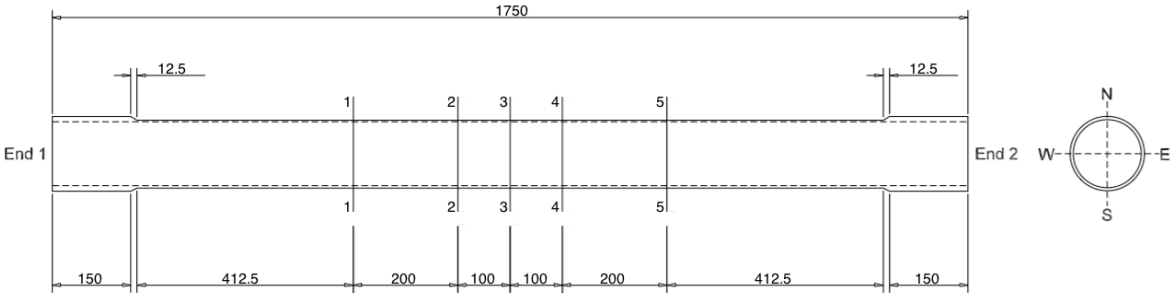

Figure 6.1: Locations for thickness measurements. Displayed measurements are in millimetres.

As explained in Section 5.1.2, the pipes needed to be cut additionally in order to fit in the rig. Figure 6.2 shows the locations of the thickness measurements after the pipes were cut as well as the length of the cut pipeline specimens.

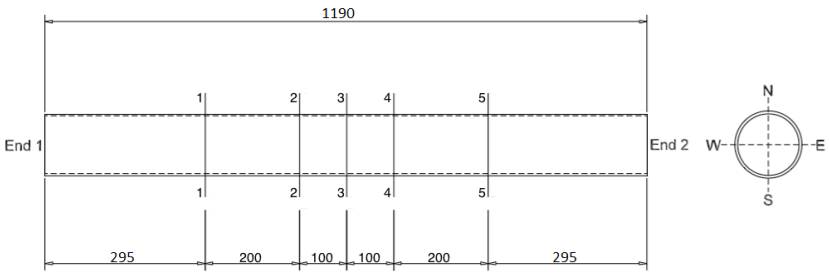

Figure 6.2: Locations for thickness measurements for the cut pipes.

The three tested pipes were labelled Pipe 1, Pipe 2 and Pipe 3. Table 6.1 shows the maximum, minimum and average values of the thicknesses and inner diameters measured for the pipes, including the associated variances and standard deviations. In addition, the measured pipe lengths from mid-weld to mid-weld are given. These lengths were measured

using a measuring tape after the pipes had been mounted in the stretch bending rig for Pipe 2 and Pipe 3. This length was not measured for the first experiment of Pipe 1. The mid-weld to mid-weld lengths was thought fitting for deformable pipe lengths in numerical simulations. The span length from rotation point to rotation point would be same for all pipes. This length was found to be $2146mm$ in Section 5.1.2, by use of the rig drawings. This length was difficult to measure accurately in situ, but it was assumed that there were to be some slack compared to the rig drawings.

Table 6.1: Average values, variance and standard deviation for the pipe measurements.

Pipe	1	2	3
	Thickness		
$t_{avg}[mm]$	4.15	3.92	4.02
$t_{max}[mm]$	4.69	4.31	4.50
$t_{min}[mm]$	3.55	3.60	3.45
$Var(t)[mm^2]$	0.0952	0.0323	0.0699
$St.dev(t)[mm]$	0.3086	0.1798	0.2644
	Diameter		
$D_{avg}[mm]$	122.31	122.74	122.25
$D_{max}[mm]$	122.38	122.85	122.42
$D_{min}[mm]$	122.17	122.47	122.02
$Var(D)[mm^2]$	0.0070	0.0172	0.0198
$St.dev(D)[mm]$	0.0834	0.1310	0.1410
	Pipe length c-c welds		
$L[mm]$	-	1190	1160

The measurements revealed a significant thickness variation throughout the pipes. At the most, the pipe thickness for Pipe 1 varied with over $1mm$ around the cross-section, which is approximately 25% of the average thickness. This significant thickness variation may be a result of the lathing process. On the other hand the inner diameter measurements also varied, which might indicate that for pipes that had not been lathed, thickness also could have varied as much. Most likely the thickness variation was due to a combination of initial variations and the lathing process.

In order to evaluate the accuracy of the thickness and inner diameter measurements, 30 control measurements were taken at the same point using the ultrasonic thickness gage. 30 control measurements were also taken using the caliper by measuring the same distance. The thickness measurements were taken at a arbitrary point on a pipe, while the measurements using caliper were taken between two arbitrary inner diameter points at a pipe

end. Table 6.2 shows the maximum, minimum and average thickness and inner diameter at these arbitrary points, including the associated variances and standard deviations. It may be seen that these control measurements vary less than the measurements taken from different locations on the pipes, and thus the accuracy of the measurements were deemed fairly good compared to how much measurements of the pipes varied.

Table 6.2: Accuracy of measurements.

Thickness		Diameter	
$t_{avg}[mm]$	3.61	$D_{avg}[mm]$	122.51
$t_{max}[mm]$	3.68	$D_{max}[mm]$	122.63
$t_{min}[mm]$	3.58	$D_{min}[mm]$	122.41
$Var(t)[mm^2]$	0.00056	$Var(D)[mm^2]$	0.00240
$St.dev(t)[mm]$	0.02377	$St.dev(D)[mm]$	0.04895

Previous master's theses [5, 6, 7] have all pointed out that the pipe thickness affected the impact response in a large degree. This effect was also seen for simulation regarding bending of pipes in the preliminary study carried out in this thesis. Therefore, it was of interest to evaluate measurements taken with the ultrasonic thickness gage to measurements taken with a micro meter, which is deemed more accurate than the ultrasonic thickness gage. Thickness measurements with both the ultrasonic thickness gage and the micro meter were taken at four different locations at both ends for Pipe 2 and Pipe 3. Four measurements were taken at each point, resulting in a total of 32 measurements for each pipe. Measurements of Pipe 1 were not carried out because the flanges were already welded on, preventing use of the micro meter. The measurements revealed that the ultrasonic thickness gage slightly overestimates the thickness. An average deviation between the ultrasonic thickness gage measurements and the micro meter measurements was found to be $0.16mm$. This is a significant deviation, as it corresponds to 4% of the nominal pipe thickness. As mentioned, a complete list of measurements can be found in Appendix B.

6.2 Load Cell Calibrations

The load cell for the vertical actuator was ordered specifically for the experiments conducted in this thesis. It was calibrated by the vendor for loads up to $300kN$. The horizontal load cell was calibrated on site for loads up to $200kN$ by use of a reference load cell mounted between the horizontal grips. Data from the calibrations of the vertical and the horizontal load cells may be seen in Figure 6.3, which displays the percentage error compared to the respective values from the reference load cells.

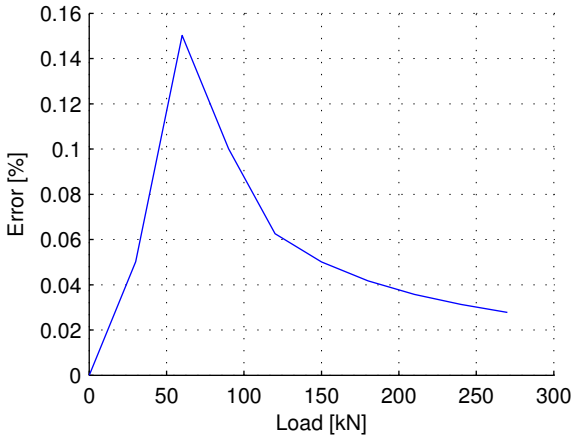

(a) Vertical load cell.

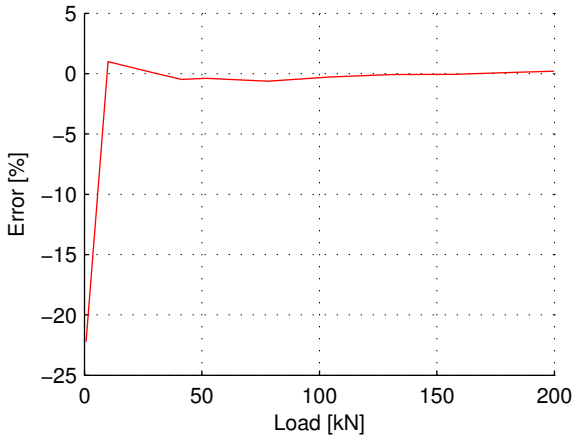

(b) Horizontal load cell.

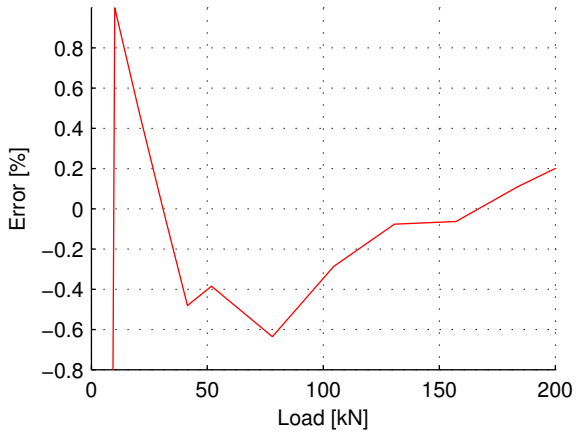

(c) Horizontal load cell, with different range

Figure 6.3: Percentage error for the vertical and horizontal load cells compared to the reference load cells.

For the vertical load cell the error versus the reference load cell peaks at load levels of $60kN$ with an error of 0.15%, as seen in Figure 6.3(a), which again corresponds to an error of $0.090kN$. This will surely not affect the results considerably. The data sheet for the vertical load cell may be found in Appendix E.

Considering the calibration of the horizontal load cell, the error may be relatively large for small loads ($< 10kN$) as seen in Figure 6.3(b). During calibration, measurements for every $10kN$ were used to correct the load cell (i.e. $0kN$, $10kN$, $20kN$ etc.). It is the first measurement, namely the one for $0kN$ which deviates and causes the error to seem so large in the plot. It is difficult to say anything specifically about the error between 0 and $10kN$, but most likely it will be in the same range as for higher loads. For the higher loads the error peaks with 0.6% for loads of $80kN$ as seen in Figure 6.3(c). This results in an error of $0.5kN$. A difference of such small loads will have a negligible effect on the results. The recorded data from the calibration of the horizontal load cell may be found in Appendix E.

6.3 Digital Image Correlation (DIC)

This section presents a brief introduction to DIC. The introduction is based on two articles dealing with DIC, which have been published by Egil Fagerholt and co-workers [36, 37]. The motivations and the main challenges for utilizing DIC in the experiments conducted in this thesis are also presented.

In its basic form the DIC algorithm can be characterized as a "point tracker", i.e. an algorithm that tracks the translation of a specific point on a specimen in a series of images [36]. By comparing an image of the specimen at the current state to an image of the specimen at the reference state, the translation can be found. The basic principle of DIC is based on finding the correlation between these images. Traditionally, this correlation can be found by optimizing a set of degrees of freedom for a pixel subset, by minimizing the sum of the gray-scale difference between the two images within the particular subset [37].

Instead of finding the correlation for each subset individually as done by the traditional DIC algorithm, a global correlation can be obtained for a set of nodes contained in a finite element mesh [36]. Nodal displacements can then be found by minimizing the gray-scale residuals within the mesh region. The nodal displacements are found by iteratively building and solving a linear system of equations, and from this displacement fields can be obtained. From the displacement fields the desired strain fields may be calculated. Figure 6.4 illustrates a image of a specimen showing gray-scale values with its corresponding effective strain map, including failure in the material [36].

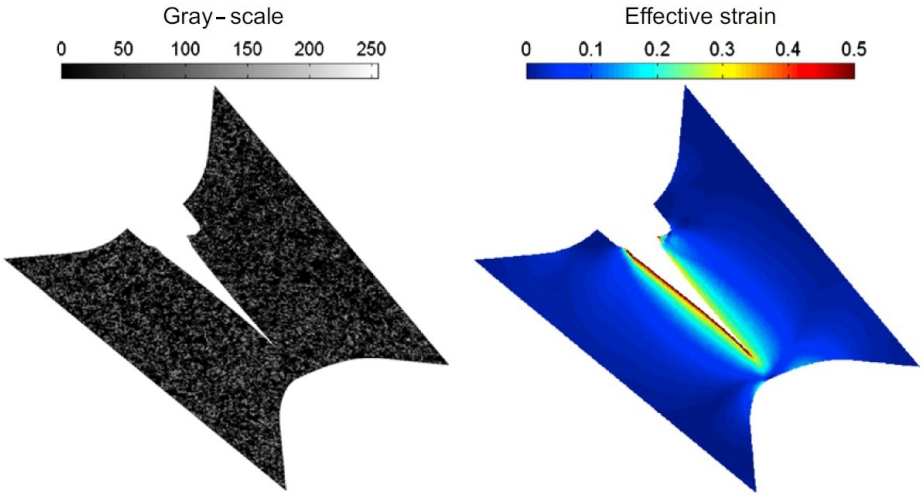

Figure 6.4: Gray-scale image with its corresponding effective strain map [36].

It was decided to try and utilize DIC in the experiments conducted for this thesis. The area of interest in the experiments was the indentation zone. The motivation for this was that displacement and strain fields for this area could be obtained. These fields could serve as comparisons for displacement and strain fields obtained through numerical simulations.

Utilizing DIC in the experiments presented several challenges. One challenge was that the indentation zone underwent rather large rigid body translations in addition to local deformation in the experiments. Therefore, the cameras needed to be placed further away from the pipe than desired in order to be able to photograph the pipe throughout its whole deformation. This was believed to make it more difficult to extract the displacement and strain fields. Another challenge was related to the light sensitivity of the cameras. The lighting in the laboratory where the experiments were conducted was not optimal, as the top side of the pipe was better lit than the bottom side. This presented a challenge during the deformation of the pipe, as the indentation zone was somewhat shadowed. To avoid that direct sunlight made the lighting less optimal, sunscreens were put up. The area subjected to the largest strains was believed to be the area beneath the indenter. It was not possible to obtain DIC data for this area as the indenter blocked the view during bending. However, this was a test to see if it was possible to utilize DIC for these kinds of experiments. DIC was utilized on experiments of Pipe 2 and Pipe 3. However, only data for the experiment on Pipe 2 gave decent results. Figure 6.5 shows the DIC camera set-up for Pipe 2.

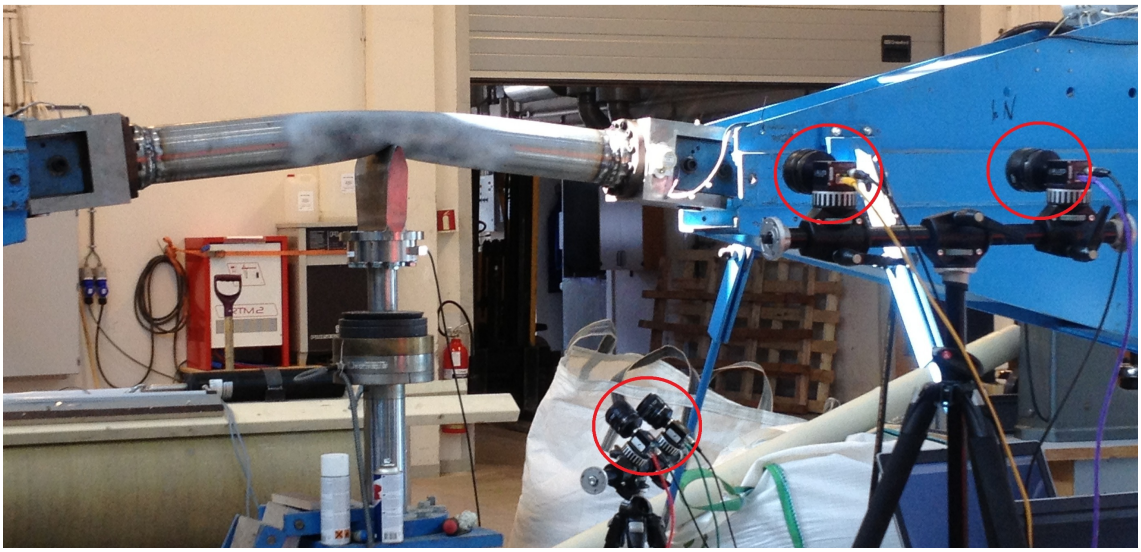

Figure 6.5: DIC camera set-up for Pipe 2. Four cameras are marked with red circles

6.4 Experiments

This section contains a description of how the experiments were conducted for Pipe 1, Pipe 2 and Pipe 3. The experimental set-up is described in Section 5.1. Figure 6.6 shows Pipe 1 mounted in the stretch bending rig prior to testing.

Figure 6.6: Pipe 1 mounted in the stretch bending rig prior to testing.

Pipe 1 was bent with a indenter velocity of $25mm/min$, without being subjected to any horizontal force. It was subjected to the largest vertical deformation as it was desirable to make sure that the rig, welds, bolts and actuators would function properly for large displacements. The pipe was bent to a vertical indenter displacement of $282.6mm$. After bending, the indenter was removed and the pipe was stretched with a linearly increasing horizontal load up to $120.7kN$.

Pipe 2 was subjected to a horizontal stretch force of $55kN$ pre-bending, and this force was kept constant through out the bending step. The pipe were bent with an indenter velocity of $25mm/min$, to a vertical indenter displacement of $208.1mm$. After bending, the horizontal actuators were locked and the indenter was removed. This resulted in reaction forces in the horizontal actuators. After the indenter was removed the reaction forces in the horizontal actuators were decreased to zero. This was followed by stretching of the pipe with a linearly increasing horizontal load up to $139.5kN$.

Initially, Pipe 3 was supposed to be subjected to a horizontal stretching force during bending that would increase linearly from $0kN$ to $55kN$, corresponding to the constant horizontal stretching force for Pipe 2. However, it was evident that the bending step of Pipe 3 did not go as planned, as the force for the vertical actuator during bending was much too high compared to what was expected from the numerical simulations in the preliminary studies in Section 5.4.1. Through investigations it was found that the load cell for the horizontal actuators did not function properly. An offset of $43.9kN$ was discovered. The data file from the experiment showed that the horizontal stretching force had increased linearly from $0kN$ to $58kN$, but because of the offset it was in reality increased linearly

from $43.9kN$ to $101.9kN$. Also, for Pipe 3 the horizontal force during the stretch step was applied very suddenly. It was observed that the horizontal actuator force reached its maximum capacity almost immediately. The application of the horizontal stretch force happened simultaneously with the removal of the indenter. As the pipe was stretched, it pressed down on the indenter. The cause of this is unclear, but it may be that an error occurred during the computer input for the stretch step. However, the pipe was bent with a indenter velocity of $25mm/min$, to a vertical indenter displacement of $198.6mm$ and stretched with a force of $322.0kN$.

An overview of the three experiments that were carried out is presented in Table 6.3 along with the respective average thicknesses measured by the ultrasonic thickness gage.

Table 6.3: Overview of the experiments, with C meaning constant force and LI meaning linearly increasing force.

Pipe	Pipe 1	Pipe 2	Pipe 3
Applied Horizontal Force $[kN]$	Free	C 55	LI 43.9-101.9
Applied Vertical Displacement $[mm]$	282.6	208.1	198.6
Average Thickness $[mm]$	4.15	3.92	4.02

For all three pipe experiments, the angles at both rotation points were measured by clinometers. For Pipe 2 and Pipe 3 two additional clinometers were attached to the forks at each end of the pipes. This was done to find out if there were any difference in rotation between the rotation point of the system and the pipe ends.

For Pipe 2 and Pipe 3 four camera were used for DIC, as seen in Figure 6.5. Two cameras were placed a few meters away from the pipe in order to capture the side of the pipe near the indenter throughout the whole deformation. In addition, two cameras were placed beneath the pipe, capturing the area around the indenter tip. The DIC data for Pipe 3 did not give any reasonable results and was not be used. This was probably a result of poor lighting. However, the results from images taken for Pipe 2 were decent and it was believed that results could be extracted. As can be seen in Figure 6.5, the area around the indentation zone was sprayed with a coating, making it possible to utilize DIC.

6.5 Results

This section presents the results from the experiments carried out with Pipe 1, Pipe 2 and Pipe 3. Figure 6.7 shows the undeformed and the deformed state of Pipe 1.

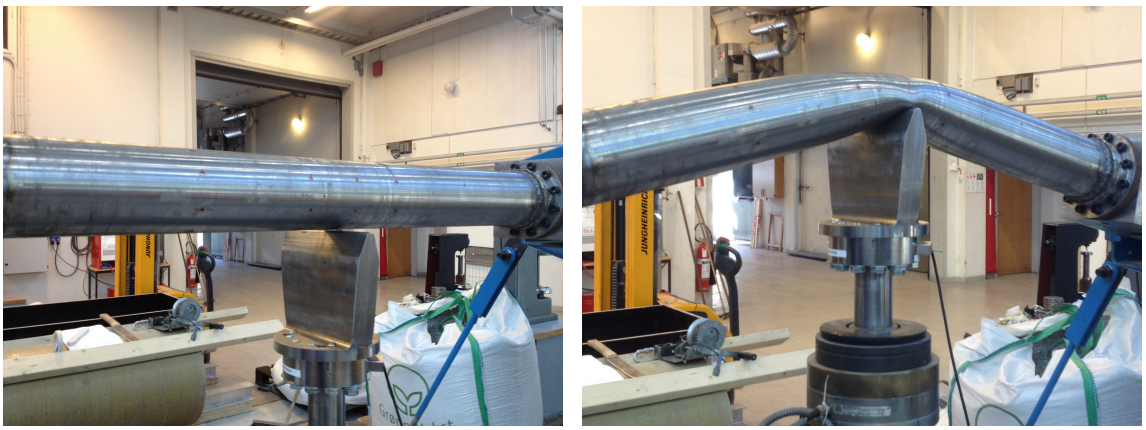

(a) Undeformed Pipe 1.

(b) Deformed Pipe 1.

Figure 6.7: Photo of Pipe 1 in undeformed and deformed state.

Figure 6.8 shows the three pipes after being bent and stretched. Pipe 1 is the pipe at the top, Pipe 2 is in the middle and Pipe 3 is the one at the bottom. Notice that the flanges still are attached for Pipe 3, and that it is more straightened out than Pipe 1 and Pipe 2. Note that the picture is somewhat deceiving for Pipe 2 and Pipe 3, as the indentation zones (red circle) may look as though there is a very sharp indent. However, this is only worn off coating.

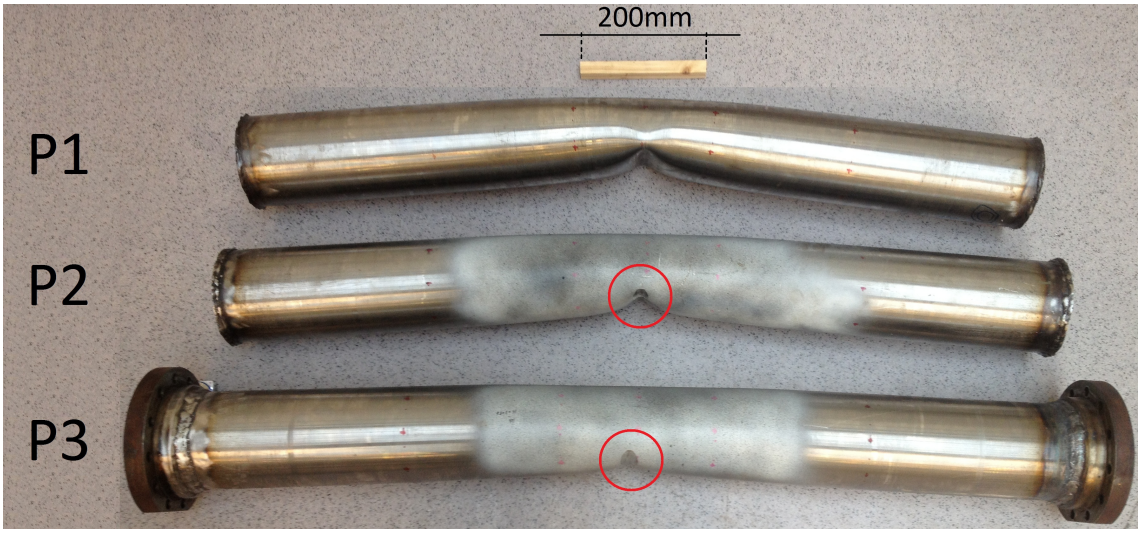

Figure 6.8: Photo of tested pipes. Note that the circled area in the indentation zone for Pipe 2 and Pipe 3 is not local indentations, but worn off coating.

6.5.1 The Bending Step

Force-displacement curves for the bending step from the three experiments done in the stretch bending rig are presented in Figure 6.9. The force-displacement data were measured from the vertical load cell and the vertical actuator. No cracks were visible on the pipes after the bending step.

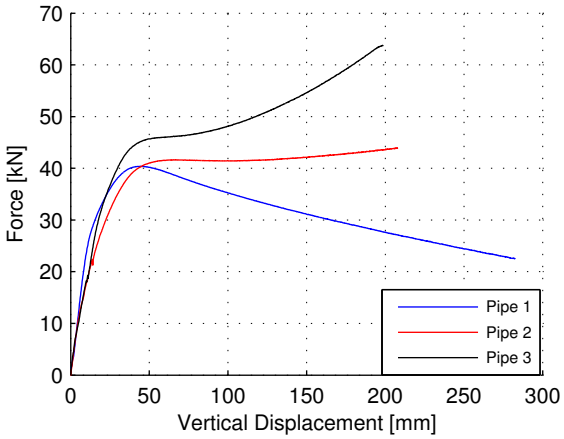

Figure 6.9: Vertical force-displ. path for experimental bending of pipes presented in Table 6.3.

When comparing the stiffness before the initial peak, a difference can be seen in the force-displacement curves. The slope of the curve for Pipe 1 is seen to be significantly steeper than for Pipe 2. As found in Section 5.4.1 and 5.4.4, the initial stiffness is affected by both applied horizontal load and pipe thickness. Pipe 1 had a larger average thickness than Pipe 2, while Pipe 2 was subjected to a constant horizontal force. It is observed that the larger pipe thickness of Pipe 1 may contribute more to the initial stiffness than the constant horizontal force applied to Pipe 2. Regarding Pipe 3, there is a kink in the force-displacement curve where its slope suddenly becomes significantly steeper. The kink appears around a vertical displacement of $20mm$. One possible explanation for this is that the abrupt slope change was caused by a sudden increase in horizontal load due to issues with the load cell.

The force-displacement path for Pipe 1 starts to decline after reaching a peak force. This was expected as the impact tests done in the previous master's theses [5, 6, 7] displayed the same behaviour. For Pipe 2 the force level flattens out and initiates a slight increase. Prior to the experiment, the force level for Pipe 3 was expected to be similar to that of Pipe 2 at maximum vertical displacement. This was clearly not the case, as the difference in force is approximately $20kN$. The difference was thought to be much larger than thickness alone could cause.

Figure 6.10 shows the total horizontal displacement of both the rotation points versus vertical displacement of the indenter for Pipe 1, Pipe 2 and Pipe 3.

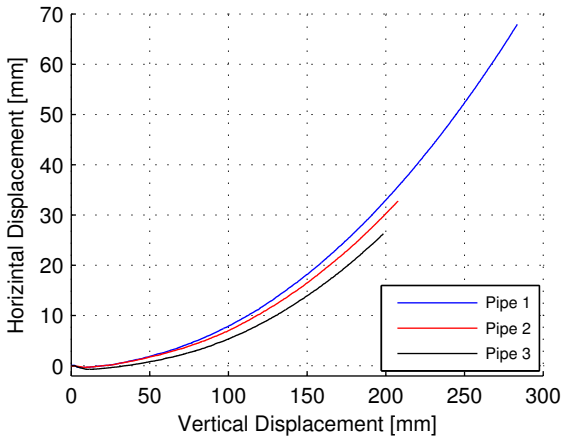

Figure 6.10: Horizontal displ. versus vertical displ.

When looking at Figure 6.10 where the horizontal displacements of the rotation points are compared, it is seen that Pipe 3 undergoes less horizontal displacement. According findings in Section 5.4.4, this suggested that Pipe 3 had been subjected to higher horizontal loads. As previously mentioned, an offset with the magnitude of $43.9kN$ was found for the horizontal load cell. The linearly increasing horizontal load for Pipe 3 during bending was not applied as planned due to problems with the horizontal load cell. Figure 6.11(a) illustrates the recorded application of the horizontal load, while Figure 6.11(b) displays the actual applied loads. The constant horizontal load for Pipe 2 during bending is included in the figures for comparison.

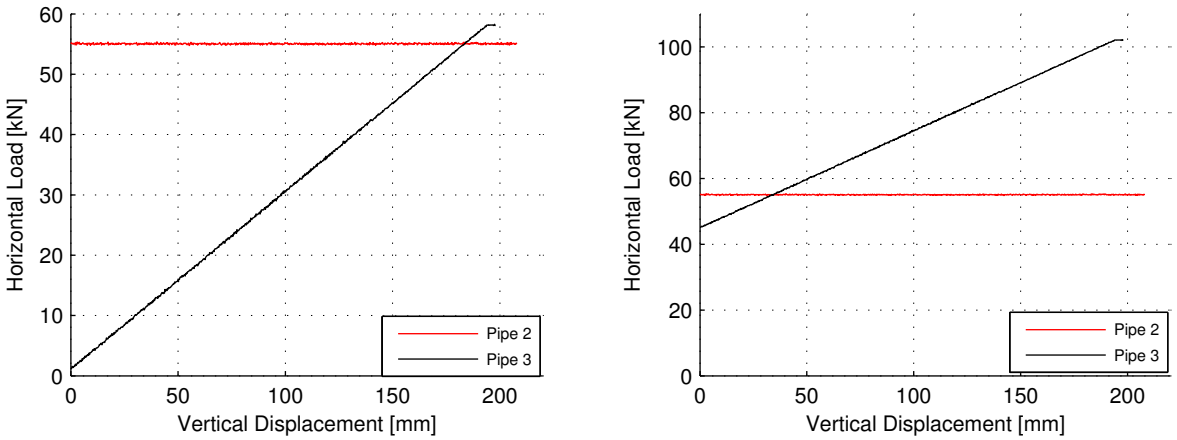

(a) Desired horizontal load.

(b) Actual horizontal load.

Figure 6.11: Desired and actual horizontal load versus vertical displacement for Pipe 3.

As mentioned in Section 6.4, the angle at both rotation points were measured for all pipes. In addition, the angle at both forks were measured for Pipe 2 and Pipe 3. Figure 6.12 displays a sketch of the connection between the pipe and the grips. The location of the clinometer at the rotation point (RP) and the clinometer at the fork is displayed, labelled *1* and *2* respectively.

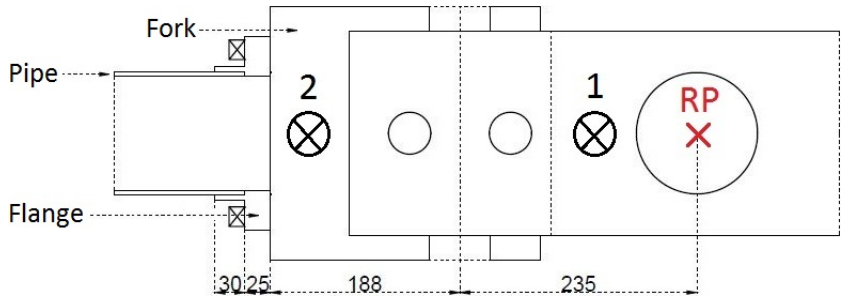

Figure 6.12: Sketch of the connection between the pipe and the rig, with location of two clinometers. (1) represents the clinometer at the rotation point, while (2) represents the clinometer at the fork.

Figure 6.13 displays the average angles at the rotation points for all three pipes and the average angles at the forks for Pipe 2 and Pipe 3 during bending. The continuous curves represents the average angles at the rotation points, while the dashed curves represent the average angles at the forks. The angles are plotted against displacement of the vertical actuator.

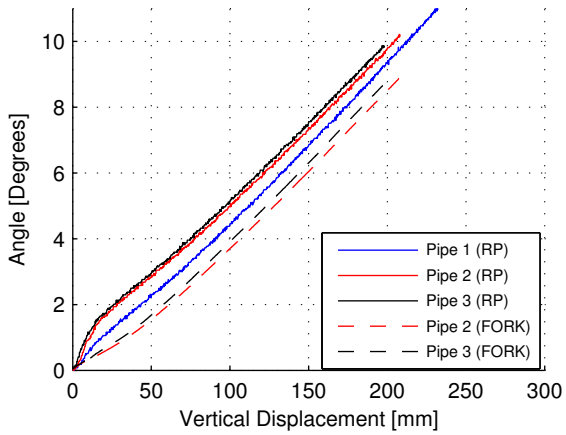

Figure 6.13: Comparison between average angles at rotation points and average angles at forks for the pipes during bending. The angles are plotted against the displacement of the vertical actuator.

Looking at the average angles at the rotation points in Figure 6.13, it can be seen that the angles for Pipe 2 and Pipe 3 deviates from the angles of Pipe 1. In the beginning of the vertical displacement the curves for Pipe 2 and Pipe 3 have a steeper slope than Pipe 1. However, after the initially sharp increase, the slopes of the three curves do not seem to differ significantly. Looking at the curves representing the average angles at the forks for Pipe 2 and Pipe 3, it can be seen that the curves have gentler slopes at the beginning of the vertical displacement. However, the slope of the curves does not seem to differ significantly after the initial deviation. It is clear that for Pipe 2 and Pipe 3 there was a difference between the rotation at the rotation points and at the forks. Throughout the vertical deformation, the average angles at the rotation points and the average angles at the forks seemed to deviate with approximately 1.2° for both Pipe 2 and Pipe 3.

The difference between the measured angles at the rotation points and at the forks for Pipe 2 and Pipe 3 indicates that rotation happened more rapidly in the pipe-rig connection than in the pipe in the initiation phase of the bending step. For Pipe 1, the rapid increase in rotation at the rotation points did not occur, suggesting that this effect may not be as apparent for Pipe 1. Horizontal loading was applied for both Pipe 2 and Pipe 3, and it may be that the pipe was stiffened relatively to the pipe-rig connection, causing the pipe to move more rigidly in the beginning of the bending step. This is illustrated in Figure 6.14. The grips of the stretch bending rig would be the most exposed parts for such bending. It is also possible that the application of horizontal loads made small rotations between the forks and the block bearings or between the block bearings and the grips to occur more easily. The relative rotation would mean that the bending of the pipes would be lagging behind compared to what the recorded vertical displacement suggests. It should be mentioned that local deformation of the pipe may have been initiated even though the global bending was believed to be delayed.

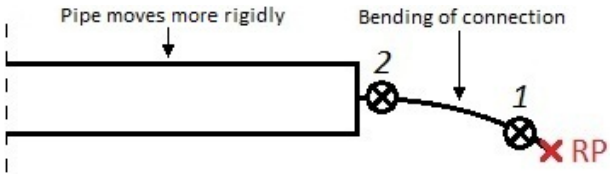

Figure 6.14: Illustration of initial rigid body motion of Pipe 2 and Pipe 3.

The kink before the initial peak force in the force-displacement for Pipe 3 seen in Figure 6.9, could also be a result of the relative rotations. It is seen that the kink occurs at vertical displacement of $10mm$ which is about when the slope of the curves for the angles at the rotation points seem to reach a constant value. Thus, the kink might be a result of that the bending of the pipe fully initiates. However, the force-displacement data for Pipe 2 displayed no such kink.

An estimation on how large vertical displacement the relative rotation corresponds to can be made. Assuming that the length between clinometer *1* at the rotation point and clinometer *2* at the fork is $300mm$ and multiplying by the tangent of the angular difference of $1.2°$ gives a difference in vertical displacement of $6.2mm$.

6.5.2 The Stretch Step

Figure 6.15 displays horizontal load versus total horizontal displacement for the tested pipes. The total horizontal displacement is given as the sum of displacement measured from both horizontal actuators.

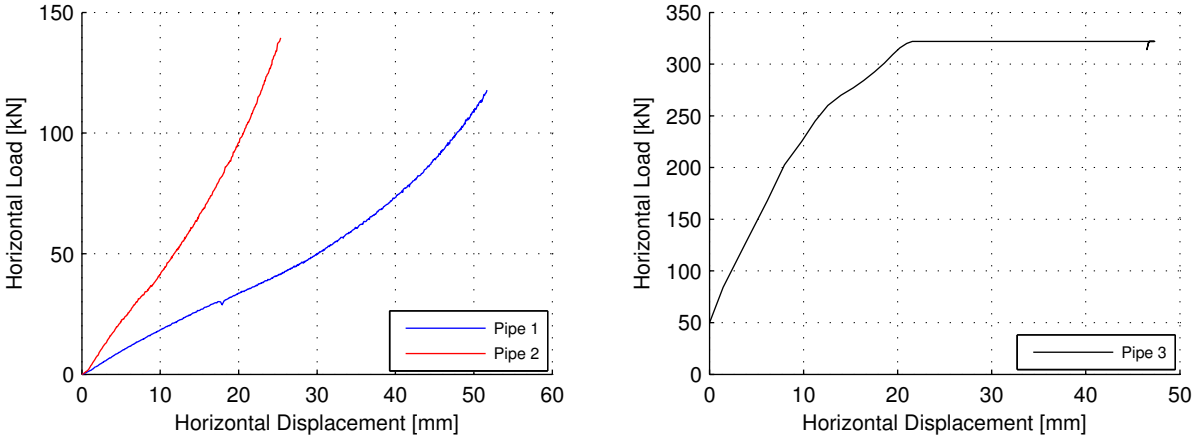

(a) Horizontal load versus total horizontal displacement for Pipe 1 and Pipe 2.

(b) Horizontal load versus total horizontal displacement for Pipe 3.

Figure 6.15: Horizontal force-displacement paths for Pipe 1, Pipe 2 and Pipe 3.

The force-displacement data were measured from the horizontal load cell and the horizontal actuators. Pipe 2 clearly exhibits a significantly stiffer behaviour. This is reasonable as the inner moment arm for Pipe 2 was smaller than for Pipe 1, as Pipe 1 was subjected to almost $100mm$ more vertical displacement. This is the same observation that was made in the three previous mater's theses [5, 6, 7]. A small inner moment arm requires a larger horizontal force in order to straighten out the pipe than if there is a larger inner moment arm. Figure 6.15(b) shows force-displacement for Pipe 3. As seen, both the range of the load and the path itself are completely different from those concerning Pipe 1 and Pipe 2. Clearly an error was done when configuring this stretch step, leading to unfavourable data.

Close up photos of all three pipeline specimens post stretching can be seen in Figure 6.16. Pipe 1, which was subjected to the most transverse displacement and stretched the most, displays distinct surface cracks. Cracks are less evident for Pipe 2 and Pipe 3, but they are still clearly visible. The cracks visible for Pipe 3 are more distinct than for Pipe 2.

Pipe 2 and Pipe 3 were subjected to about the same vertical displacement, but Pipe 3 was stretched to about the double total horizontal displacement. This caused more surface cracks to appear.

Most likely the cracks seen in Figure 6.16 was caused by the fine grooves on the pipe surface originating from the lathing process. These grooves are clearly seen in Figure 6.16(b). When the pipe was stretched it seemed like these grooves had been widened. Fracture appears to have initiated at the bottom of these grooves. Kristoffersen et al. [4] discussed that such an uneven surface may have led to stress and strain concentrations, which initiated cracks at specific locations and that this was of minor importance for the fracture process for original pipes that had not been lathed.

Table 6.4 displays an overview of the data from the experimental tests from both the bending step and the stretch step. Note the difference in horizontal position between the bending step and the stretch step which occurred due to an elastic rebound. Pipe 3 did not elastically rebound as the stretch step was started immediately.

Table 6.4: Overview of the experiments. C - constant horizontal load, LI - linearly increasing horizontal load.

Pipe	Pipe 1	Pipe 2	Pipe 3
		Bending	
Applied Horizontal Load [kN]	Free	C 55	LI 43.9-101.9
Force at Initial Peak [kN]	40.4	41.6	46.0
Max Vertical Load [kN]	40.4	44.0	63.8
Vertical Displacement [mm]	282.6	208.1	198.6
Average Angle at Rotation Points [Degrees]	13.7	10.2	9.9
Average Angle at Forks [Degrees]	-	8.9	8.7
Total Horizontal Displacement [mm]	68.0	32.7	26.3
Horizontal Position Pre-Stretching [mm]	57.4	28.5	26.3
		Stretching	
Max Horizontal Load [kN]	120.7	139.5	322.0
Total Horizontal Displacement [mm]	51.7	25.4	-
Average Angle at Rotation Points [Degrees]	3.9	4.0	1.8
Average Angle at Forks [Degrees]	-	3.8	1.5

(a) Photo of pipe from Pipe 1.

(b) Close-up of Pipe 1.

(c) Photo of pipe from Pipe 2.

(d) Close-up of Pipe 2.

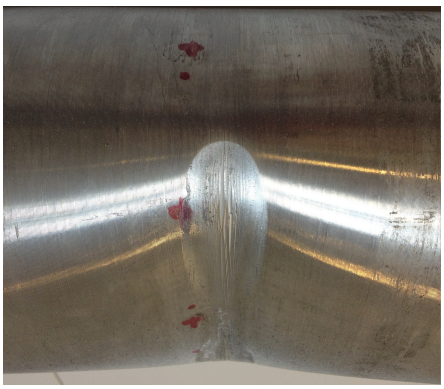

(e) Photo of pipe from Pipe 3.

(f) Close-up of Pipe 3.

Figure 6.16: Photos of the indentation zone from the tested pipes, with close-ups on developed cracks.

6.5.3 Metallurgical Investigations

In the following section a metallurgical investigation, including optical light microscopy, has been carried out for pipeline specimens tested in the stretch bending rig. The main interest was to see if fracture had initiated after bending and subsequent stretching of the pipeline specimens. Optical light microscopy was used. This work was carried out in collaboration with research scientist Dr. Ida Westermann at SINTEF.

Two specimens were cut out from the indentation zone of each pipe as seen in Figure 6.17. Previous master's theses [5, 6, 7] and preliminary simulations carried out in this thesis have all indicated that the largest strains were located in this vicinity, and that it is in this area fracture is most likely to be initiated.

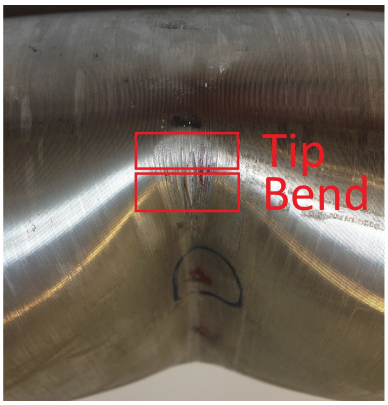

Figure 6.17: Extraction locations of specimens used for metallurgical investigation.

Figures 6.18(a) and 6.18(b) displays an overview of the specimens studied in a optical light microscope. Note that the arrows displayed in Figure 6.18 illustrates from which direction the specimens were inspected. The specimens from Pipe 2 were inspected from the same directions as the specimens from Pipe 1, but no overview photo was taken.

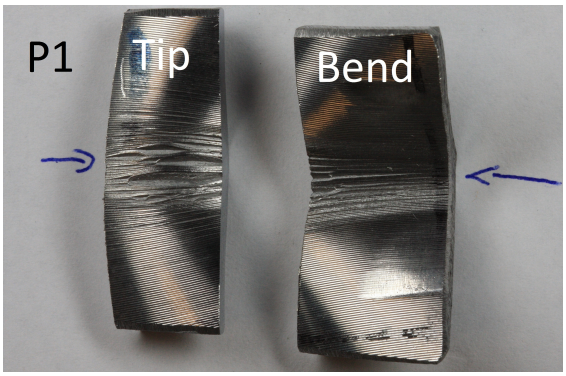

(a) Pipe 1.

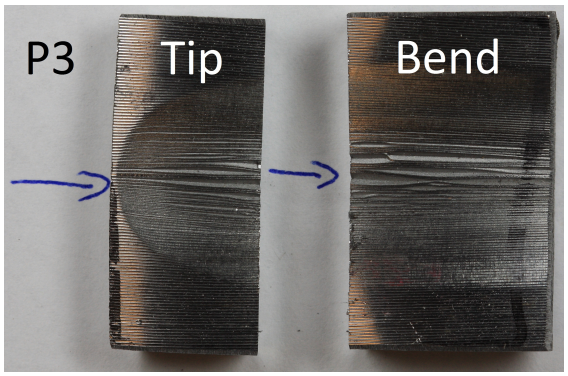

(b) Pipe 3.

Figure 6.18: Overview of specimens from Pipe 1, Pipe 2 and Pipe 3 used for metallurgical investigations. The specimens are extracted from the indentation zone.

Figure 6.19 shows the specimen from the bend of Pipe 1, where surface cracks of about $75\mu m$ were discovered. These surface cracks seemed to be a result of widened lathing grooves. Some of the lathing grooves shown in Figure 6.19(b) have a deformed shape as result of being compressed. It was observed that no other fracture seemed to be present.

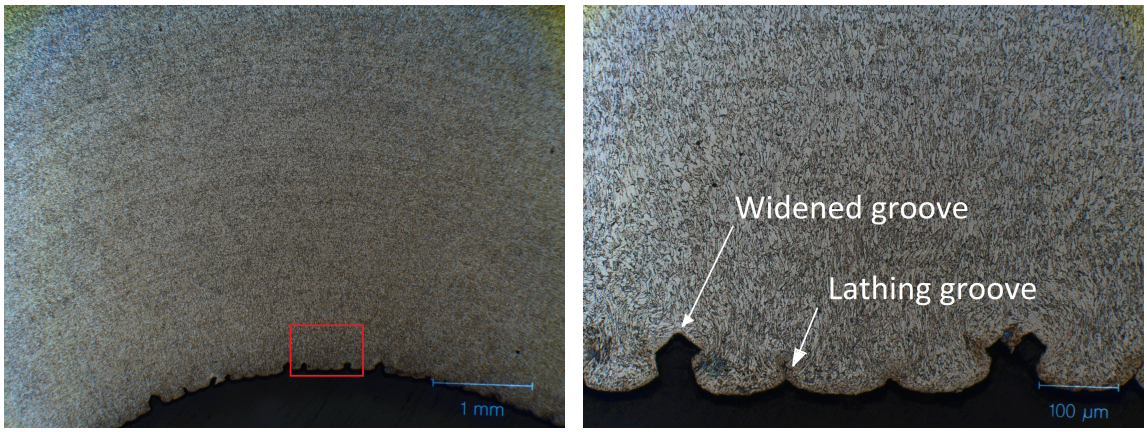

(a) Photo of bend for Pipe 1 (b) Photo of bend for Pipe 1

Figure 6.19: Investigation of specimen from bend for Pipe 1.

Figure 6.21 shows the specimen from the tip of Pipe 1 with distinct lathing grooves. As shown in Figure 6.20(b), small sporadically distributed calcium aluminate and titanium carbonitride particles were present. Some calcium aluminate particles showed signs of being surrounded by voids, which may initiate cracks.

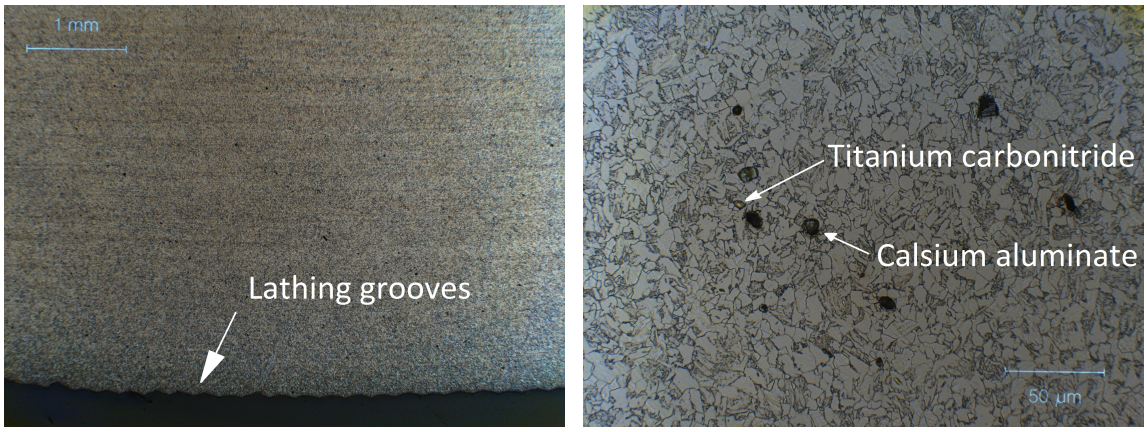

(a) Photo of tip for Pipe 1. (b) Photo of tip for Pipe 1.

Figure 6.20: Investigation of specimen from tip for Pipe 1 near the outer pipe surface.

Figure 6.21(a) shows some calcium aluminate particles located rather close to each other, which may cause ductile fracture through void nucleation, growth and coalescence [15].

Some few internal cracks were observed for the tip from Pipe 1. A internal crack of about $120\mu m$, shown in Figure 6.21(a), was found close to the inner surface which may have been caused by void coalescence.

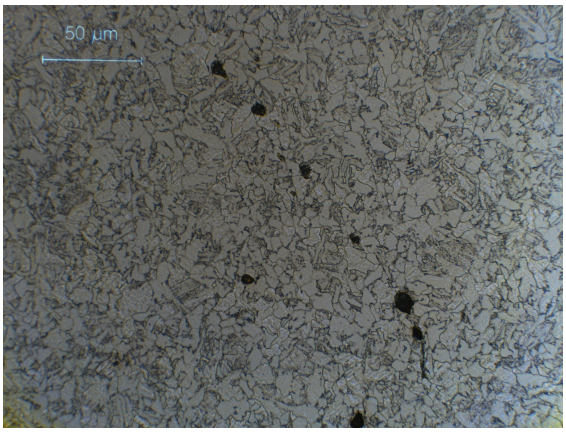

(a) Photo of tip for Pipe 1.

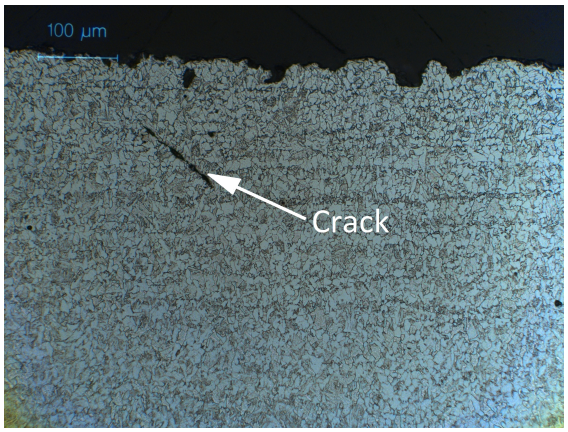

(b) Photo of tip for Pipe 1.

Figure 6.21: Investigation of specimen from tip for Pipe 1 near the inner surface.

Specimens from the bend for Pipe 2 showed similar widening of the lathing grooves as for Pipe 1, which Figure 6.22(a) shows. For Pipe 3, shown in Figure 6.22(b), the grooves were widened significantly more. It was observed that these cracks were approximately $480\mu m$, which is almost 12% of the initial pipe thickness. It should be noted that the specimens extracted from Pipe 1 also had similar cracks. However, the specimens for Pipe 1 were inspected from the direction where the surface cracks were smallest, as seen in Figure 6.18(a).

(a) Photo of bend for Pipe 2.

(b) Photo of bend for Pipe 3.

Figure 6.22: Investigation of specimen from the bend for Pipe 2 and Pipe 3

Figure 6.23 shows the specimen from the bend for Pipe 3, where a localized thickness deformation was observed. Pipe 3 was stretched with significantly higher horizontal force than Pipe 1 and Pipe 2, which most likely caused the deformation localisation.

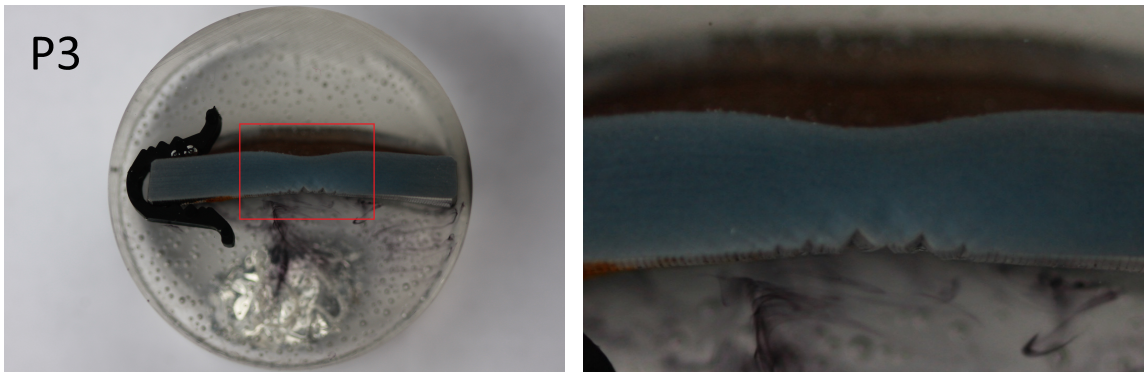

(a) Photo of specimen from bend for Pipe 3. (b) Close-up photo of specimen from bend for Pipe 3.

Figure 6.23: Specimen from bend for Pipe 3, where a localization is seen.

Figure 6.24(a) displays clear material flow patterns for the grains near the indentation surface, whereas Figure 6.24(b) shows much less deformed grains. As pointed out by Kristoffersen et al. [4] in a metallurgical study on impacted pipes, this indicates that the outer side of the pipe wall facing the indenter suffers more deformation than the inner surface.

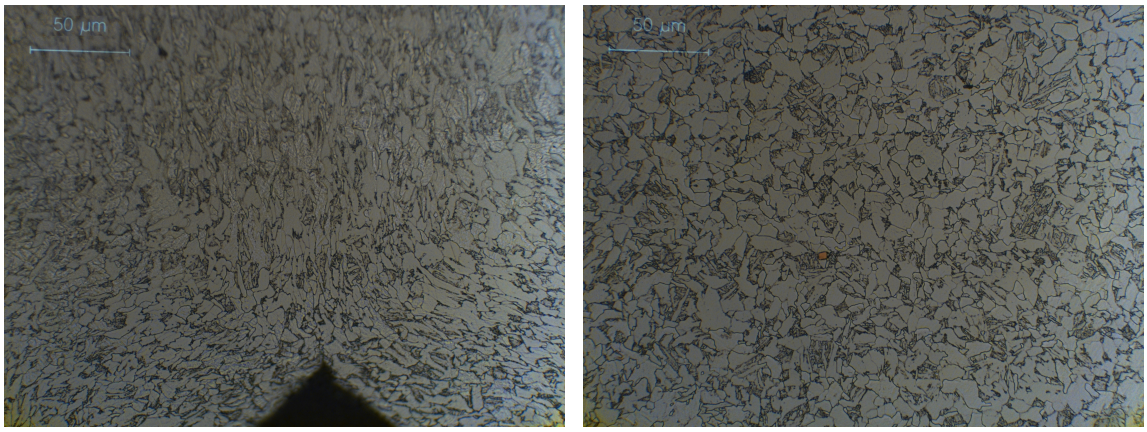

(a) Photo of area at the outer pipe surface. (b) Photo of area at the inner pipe surface.

Figure 6.24: Comparison between highly deformed grains at outer pipe surface and less deformed grains at inner pipe surface from bend for Pipe 2.

6.6 Concluding remarks

From the experiments in the stretch bending rig it was seen that Pipe 1 during bending displayed a stiffer response than Pipe 2 and Pipe 3 before the initial peak. This could be because Pipe 1 had a larger measured pipe thickness. Another possible explanation was found by comparing the average angles at the rotation points and the average angles at the forks for Pipe 2 and Pipe 3 where a relative rotation of about 1.2° was discovered. Rotation at the rotation points happened more rapidly than at the forks in the initiation phase of the bending step, indicating that a rigid body motion of the pipes occurred. Bending of the pipes would be somewhat delayed compared to what the data for vertical displacement would suggest. The relative rotation was thought to be not as large for Pipe 1 meaning this effect would be smaller. Larger relative rotations were thought to occur as a result of horizontal loading.

A kink at the beginning of the vertical force-displacement curve for Pipe 3 in the bending step was seen. This behaviour is believed to have two possible explanations. The horizontal load cell was discovered to be unsynchronized in the experiment of Pipe 3. As it is unknown when the load cell became out of sync, it might be that the horizontal force during bending was applied very suddenly at the vertical displacement where the kink is seen. This could cause a sudden increase of the slope in the force-displacement curve. On the other hand, if the horizontal load cell was unsynchronized before the experiment on Pipe 3 started, the kink might be a result of the discussed difference in the angle measurements. The kink might have occurred as bending of the pipe itself fully initiated. However, no such kink was observed for Pipe 2.

It was seen that applying horizontal forces to the pipes during bending gave larger levels of force for the vertical force-displacement curves after the initial peak. In addition, it was found that applying horizontal forces during bending resulted in less horizontal displacement per vertical displacement.

No surface cracks were visible after the bending step for any of the pipes. However, surface cracks were visible in the indentation zone for all pipes after the stretch step. Pipe 1 and Pipe 3 displayed rather large surface cracks. The largest crack was estimated to about $480\mu m$ for Pipe 3 by use of a optical light microscope, corresponding to approximately 12% of the initial pipe thickness. Pipe 1 also showed similar cracks. Through further metallurgical investigation the surface cracks were seen to be caused by widening of lathing grooves. Fracture seemed to be initiated at the bottom of these grooves. An internal crack with a length of approximately $120\mu m$ was discovered in a sample from the tip of Pipe 1, which was the pipe subjected to the largest vertical displacement and stretched the most. A localization was discovered in a sample from Pipe 3.

7 Finite Element Analyses

In this chapter, finite element analyses of the experiments are presented. Simulations were carried out using Abaqus/Explicit. Shell models were established and used for simulations of both the bending step and the stretch step of the experiments. A comparison on how the isotropic material model and the combined isotropic/kinematic material compared for the experiments done in this thesis was carried out. Models using solid elements were established in order to further analyse how strains develop over the thickness of pipe cross sections. Numerical analyses were carried out to further investigate the effects of axial forces. Simulations of possible future experiments involving inner pressure in the pipeline specimens were also carried out.

7.1 Numerical Models

The shell models used for numerical analyses of the experiments are very similar to the shell models established in Section 5.3.1 in the preliminary studies, regarding geometry and boundary conditions. The primary changes made are implementation of measured pipe length and thickness. The experiments were assumed to behave quasi-statically for the sake of numerical analyses and appropriate energy checks were carried out.

Numerical models using solid elements were established in order to perform further investigations regarding how different loading conditions affects the strains over the pipe thickness. The solid models would also serve as a comparison to the shell models.

In order to simulate the stretch step as performed in the experiments, several modifications had to be done compared to the shell models used in the preliminary studies. These changes are described in the following section.

7.1.1 Shell Models

Shell models were established using symmetry and boundary conditions as described in Section 5.3.1. The same principles were used, where a discrete rigid indenter would deform the pipes, which were free to rotate and translate horizontally about the rotation point.

It was decided to use the nominal mid-surface diameter of $127mm$ for all the shell models. This was decided as the inner diameters of the pipe specimens were not measured after

pipes were cut, and the diameter measurements were likely to vary along with the thickness. The variations of the diameter measurements were also very small compared to thickness measurements. Pipe 3 exhibited the largest deviation from the nominal inner diameter of $123mm$ with an average inner diameter of $122.25mm$, corresponding to a deviation of 0.6%. For comparison, thickness varied with up to $1.14mm$ for Pipe 1, corresponding to deviation of 27% compared to the measured average thickness of $4.15mm$. Pipe thickness was therefore regarded as the most important parameter.

It was thought that using a deformable length that went from mid-weld to mid-weld would be suitable for simulating the experiments. This length was not measured for Pipe 1, and was generally difficult to measure due to variations of the weld. The average mid-weld to mid-weld length of Pipe 2 and 3 were used for all pipes. This length was $1175mm$. From mid-weld and out towards the point of rotation, a rigid part was tied to the deformable pipe, as seen in Figure 7.1. Using rigid rotation in this area would affect the results of the simulations compared to the experiments. As discussed in Section 6.5, when horizontal forces were applied an angular differences occurred between the forks and the points of rotation. Using rigid rotation was believed to make numerical results slightly stiffer than the experiments. The stiffness difference would be likely to occur in the beginning of the bending step. The applied shell thickness would be the only geometric difference between the shell models for the different experiments. As the thickness for shell models is easily interchangeable only one model was made and used to generate input for all simulations.

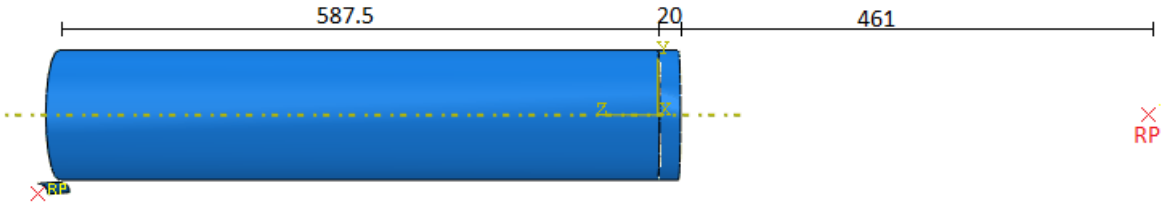

Figure 7.1: Dimensions for the shell model.

The distance from the rotation point to where the rigid part is connected to the deformable pipe was set to $481mm$. This is slightly incorrect. According to the drawings of the rig and Figure 5.7 the distance from the point of rotation to the weld is $478mm$, meaning that only $3mm$ was added to represent the second half of the weld. The total span length for a whole pipe according the rig drawings should be $2146mm$. In the models, the total length applied was $2137mm$, resulting in a difference of $9mm$. This gives an error of 0.4% compared to the total calculated span length. The error is very small and should not affect the numerical results noticeably. The reason this was not changed was that it was discovered after almost all simulations had been carried out. The shell models consisted of a total of 7350 deformable $S4R$ shell elements.

In order to simulate the stretch step, several changes had to be made to the models compared to when only the bending step was of interest as in the preliminary studies. It was important that the velocity of the indenter was zero at the end of the bending step to prevent further

instabilities in following steps. This was achieved by applying a smooth amplitude to a displacement boundary condition for the indenter. The tangent of a smooth amplitude in Abaqus is zero in both the beginning and at the end meaning that the velocity would be zero at the end. This caused an increase in step time, compared to when only the bending step was of interest, as the indenter had to decelerate over some time in order to maintain a stable analysis. The necessary step times were found by trial and error while performing energy checks to ensure that no significant dynamic effects were present.

For removal of the indenter in the analyses, it was found that very small displacement corresponded to large forces. Thus, removing the indenter by simply applying a displacement or velocity boundary condition proved difficult and resulted in severe oscillations. While this surely could be solved by trial and error and finely tuning the boundary conditions, it was decided to take another and more stable approach using load control for unloading the pipes in the simulations. In order to do this, simulations including the stretch step were divided into four steps. At the end of the steps, reaction forces of interest could be obtained. The analysis could then be restarted, and the obtained reaction forces of interest could be applied as linearly decreasing concentrated loads in the following step. Table 7.1 contains a description of the steps used in the analyses including stretch step. The procedure outlined in Table 7.1 follows the experimental procedure of Pipe 2, which was considered the most stable method for the simulations.

Table 7.1: Overview of analyses steps for simulations of bending step and stretch step.

Step	Name	Step Time $[s]$	Description
1	Bending	0.6	Bend the pipe using a smooth displacement boundary condition for the indenter, so that the velocity of the displacement is zero at the end of the step.
2	Remove	0.1	Fix horizontal degree of freedom in the point of rotation. Restart analysis while applying the obtained reaction force for the indenter as linearly declining to zero over the step time.
3	Unload	0.5	Remove the indenter. Free horizontal degree of freedom in the point of rotation and restart analysis, while applying the obtained horizontal reaction force as linearly declining to zero over the step time.
4	Stretch	0.6	Stretch the pipe using a linearly increasing load which goes up to $75kN$ over the step time. No restart necessary between stretch and unload steps.

When using load control for the indenter, the vertical translational degree of freedom was no longer constrained. Thus, in order for the dynamic equilibrium equations to be maintained, the indenter was given a mass of $0.010ton$. The numerical value of the mass itself is somewhat irrelevant as long as the simulations behaved in a quasi static manner.

7.1.2 Solid Models

Numerical models using solid elements were established with a refined mesh in the indentation area for Pipe 1 and Pipe 2. Solid reduced integration $C3D8R$ elements were used. These elements only have displacement degrees of freedom and therefore they are not very good at representing bending deformations. Slåttedalen and Ørmen[5] found that using two such elements over the thickness of the pipes gave satisfactory results for global response for simulations of the impact experiments. This was thought to apply also for simulations of experiments conducted in the stretch bending rig.

Solid models had to be established individually for the tested pipeline specimens as the thickness differed. Measured average thicknesses of $4.15mm$ and $3.92mm$ were applied for Pipe 1 and Pipe 2 respectively. These thicknesses were applied as it was seen that shell models with these thicknesses gave good fits with experimental data. Two cubical $C3D8R$ elements were used over the thickness for the larger part of the deformable pipe. For the $100mm$ closest to the indenter the mesh was refined so that there were six elements over the thickness. The mesh transition may be seen in Figure 7.2. In total, the solid models consisted of about 130 000 elements.

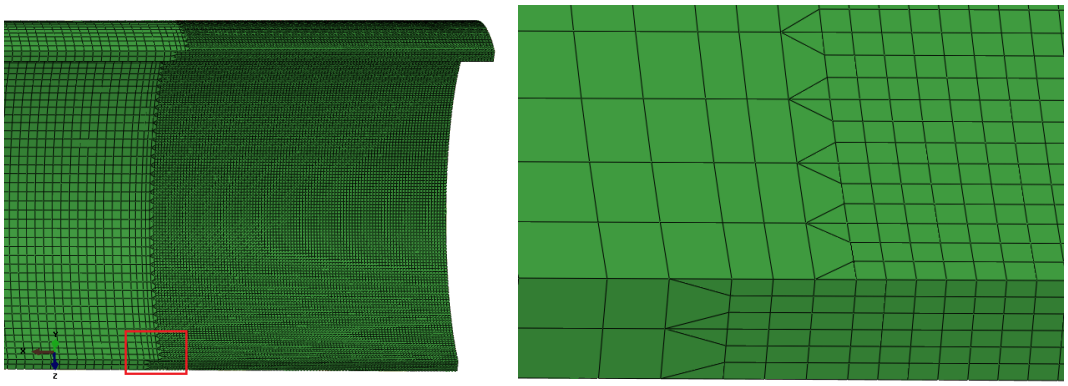

(a) Mesh for solid model

(b) Transition zone.

Figure 7.2: Mesh for solid models with refined mesh in the area of indentation.

It was found difficult to create a good mesh transition using Abaqus/CAE. The meshing of the pipes was therefore done using SALOME, which is an open source software that provides more advanced meshing techniques. The meshed pipes were then converted and imported to Abaqus/CAE, where boundary conditions and loads were applied as for the shell models. In SALOME the pipes were intentionally made a bit too long, so that a rigid element constraint could be applied using Abaqus in order to obtain the correct deformable length. Applying a rigid element constraint would allow for application of rigid rotation about an offset reference point representing the point of rotation in the stretch bending rig. This constraint had to be applied at element boundaries, and the boundary most

fitting with the desired deformable length was chosen. Thus, the measurements differ with up to $1mm$ in the models compared to the measurements shown in Figure 7.3. As the deformations are very small in that area and mostly rigid body motions occur, the effect of this will surely be negligible. As for the shell models, the total span length applied in the models were made slightly too small with a deviation of 0.4% compared to what it should have been. This should not affect the simulations noticeably.

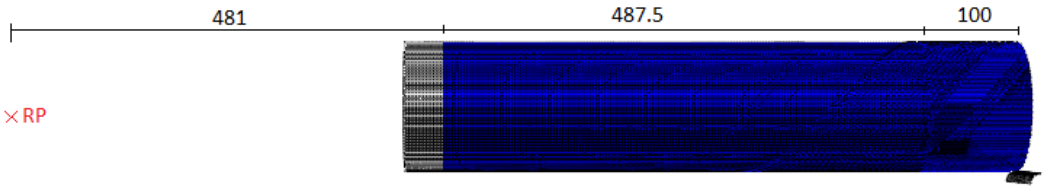

Figure 7.3: Dimensions for solid models.

The same assumptions regarding geometry made for the shell models were also applied for the solid models, meaning that the nominal mid surface diameters of $127mm$ were used.

For applying contact between the indenter and the pipe, the general contact algorithm was used. This algorithm provides the option to apply contact as "all with self". When the pipe was imported to Abaqus/CAE from SALOME all geometry in the model was lost and only elements remained. If contact were to be applied using the contact pairs algorithm, as for the shell models, elements would have to be selected individually. The general contact algorithm also uses the penalty method for applying contact in Abaqus/Explicit [17].

The solid models were made using *meters* instead of *millimeters*. This affected the units for other input parameters. Mass was applied as kg/m^3 and Pa was used instead of MPa. Thus another material card was used as input. The material card used for the solid models was scaled appropriately and can be found in Appendix C.

The solid models were mainly used for simulations of the bending step due to high computational demand. However, one simulation of the stretch step of Pipe 1 was carried out in order to see if there was any difference for shell and solid models. This model followed the procedure in Table 7.1, but restart analysis was not used for practical purposes, as the analysis was performed by NTNU's supercomputer Vilje. Instead, relevant reaction forces obtained from shell models were applied as linearly decreasing in order to obtain a stable analysis.

For the analysis using solid elements where only the bending step was of interest a velocity boundary condition was used for the indenter in order to deform the model. A velocity of $1m/s$ was applied to the indenter using a smooth amplitude to increase the velocity over $0.01s$. Using this amplitude the total step time was $0.146s$ and $0.114s$ for Pipe 1 and Pipe 2 respectively. Numerical noise in the reaction force for the indenter was clearly visible using

these step times and velocity of $1m/s$, but compared with trial models using longer step time and lower velocity, smoothed results were almost identical.

7.2 Material Model Comparison

The different material models established in the previous theses [5, 6, 7] differ in how they capture the global response. A comparison between the isotropic material model calibrated by Slåttedalen and Ørmen in 2010 and the combined isotropic/kinematic material model calibrated by use of inverse modelling by Aune and Hovdelien in 2012 was made using the shell model for Pipe 1 with the measured average thickness of $4.15mm$ applied. The material cards used as input for the material models can be found in Appendix C.

Figure 7.4 presents a comparison between numerical results and experimental data for Pipe 1. Figure 7.4(a) displays vertical force for the indenter versus vertical displacement for the bending step. Figure 7.4(b) shows applied horizontal load versus total horizontal displacement for the stretch step. The force-displacament curves for the bending steps is lightly smoothed for visibility.

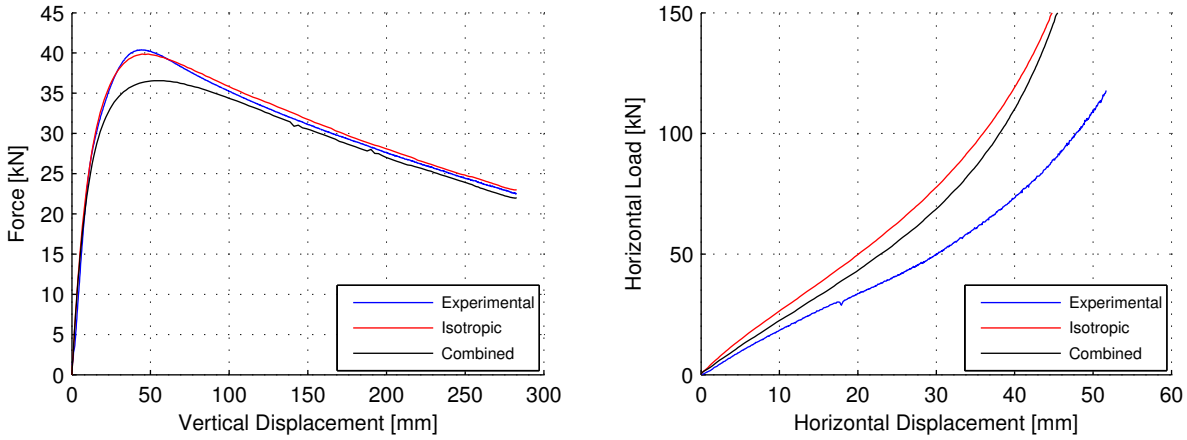

(a) Bending step of Pipe 1.

(b) Stretch step of Pipe 1.

Figure 7.4: Comparison for isotropic and combined isotropic/kinematic material models for shell model of Pipe 1 versus experimental results.

As seen in Figure 7.4(a), for the bending step the isotropic material model gives a global response almost identical to experimental data when considering force-displacement for the indenter. The combined material model differs around the peak force with a deviation of approximately $4kN$ and exhibits a more rounded shape than the isotropic material model. As the force level declines both material models coincide well with the experimental data and the slope seems identical.

For the stretch step, as seen in Figure 7.4(b), both numerical results are too stiff compared to the experimental results when considering horizontal load versus horizontal displacement.

As the isotropic material model proved to give very good results for the bending step it was decided to use this material model in the further simulations.

7.3 Simulations of the Experiments

This section presents numerical simulations of the experiments and comparisons between experimental and numerical results. Shell models were used to analyse both the bending step and the stretch step of Pipe 1 and Pipe 2, while solid models were used to analyse the bending steps of Pipe 1 and 2. One simulation using solid elements for the stretch step of Pipe 1 was carried out. For Pipe 3, a shell model was used to analyse the bending step. Simulations of the stretch step of Pipe 3 was not attempted as the experiment was not executed as planned. Numerical results using DIC for Pipe 2 are also presented and compared with the numerical results obtained from analyses using Abaqus/Explicit. DIC data from the experiment of Pipe 3 did not provide good enough results for comparisons. The isotropic material model was used in all the following simulations. Results concerning the reaction force of the indenter is smoothed for visibility in all plots. Table 7.2 gives an overview of simulations concerning the experimental tests. Input parameters such as applied vertical displacement, measured pipe thickness, horizontal loads are displayed. It is also noted which simulations were run with shell and solid models.

Table 7.2: Overview of numerical models for the experimental pipes. C - Constant horizontal load, LI - Linearly increasing horizontal load, Sh - Shell, So - Solid

Pipe	Pipe 1	Pipe 2	Pipe 3
Vertical Displacement $[mm]$	282.6	208.1	198.6
Measured Average Thickness $[mm]$	4.15	3.92	4.02
Horizontal Load $[kN]$	-	C 55	LI 43.9-101.9
Bending Step	Sh, So	Sh, So	Sh
Stretch Step	Sh, So	Sh	-

7.3.1 The Bending Step

Figure 7.5 shows numerical results for force-displacement of the indenter during the bending step for the solid and shell models of Pipe 1 and 2, compared to the experimental data. The average pipe thicknesses obtained by use of the ultrasonic thickness gage is applied for these simulations. These thicknesses were $4.15mm$ and $3.92mm$ for Pipe 1 and Pipe 2 respectively. For Pipe 1, both models correspond well with the experimental data. The shell and the solid model proves to give very similar results for the global response. As the force declines after the initial peak, the shell model looks to be marginally stiffer than the solid model and the experimental results. Stiffer response from the shell model was expected as the solid model has a more refined mesh.

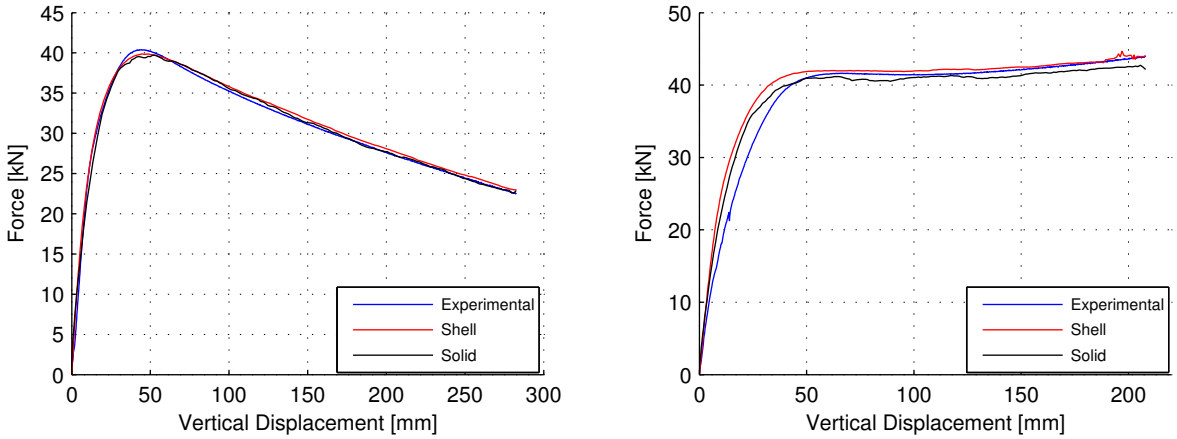

(a) Bending step for Pipe 1.

(b) Bending step for Pipe 2.

Figure 7.5: Force-displacement for the indenter using shell and solid models of Pipe 1 and Pipe 2.

For bending of Pipe 2 the numerical results deviate from the experimental data when stiffness before the initial peak is considered. This was expected as rigid rotation between the point of rotation and the pipe was applied in the model and a relative rotation was discovered in the experimental data. As the force level flattens out the curves coincides better. This indicates that the applied thickness in the models is able to represent the thickness of the physical pipes. The shell model once again exhibits a slightly stiffer behaviour than the experimental data, while the solid model lies a bit lower.

Figure 7.6 displays a comparison between angles at the rotation point obtrained from numerical similations and experimental data for Pipe 1 and Pipe 2. Only the results from the shell models are displayed as the global results from shell and solid models were very similar. Angles were recorded at both sides in the experiments and the average angles are displayed in the figure. As mentioned in Section 6.4, angles were recorded both at the rotation points and at the forks for Pipe 2 and Pipe 3. For Pipe 1, only the angles at the rotation points were recorded. For positions of the clinometers recording the angles, see Figure 6.12.

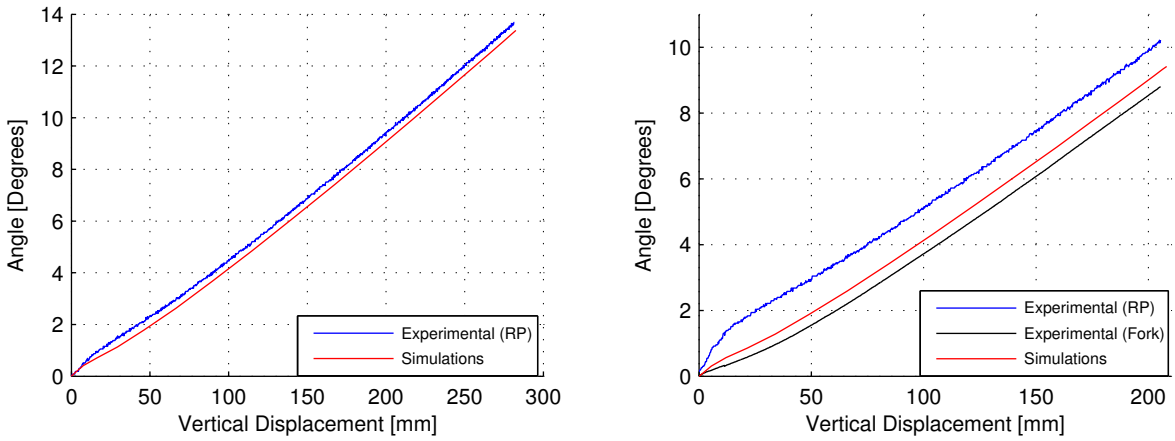

(a) Bending step for Pipe 1.

(b) Bending step for Pipe 2.

Figure 7.6: Comparison between angles recorded during experiments and angles obtained from simulations using shell models for Pipe 1 and Pipe 2.

For Pipe 1, the angles at the rotation points in the experiments correspond quite well with the simulations. This indicates that the connection from forks to rotation points in the experiment of Pipe 1 acted quite rigidly during the course of vertical displacement. If the angles at the forks had been measured for Pipe 1 it is likely that they would have been very similar to the angles at the rotation points.

As seen in Figure 7.6(b), for Pipe 2 the angle obtained from the simulation deviates from both the experimental angles. The rigid rotation from the simulation lies in between the experimental angles at the forks and at the rotation points. As the angle at the fork is overestimated by numerical model, the phase of bending of the pipe in the simulation is ahead of the experimental data.

Figure 7.7 displays numerical results for total horizontal displacement versus vertical displacement for the indenter compared with experimental data for Pipe 1 and Pipe 2.

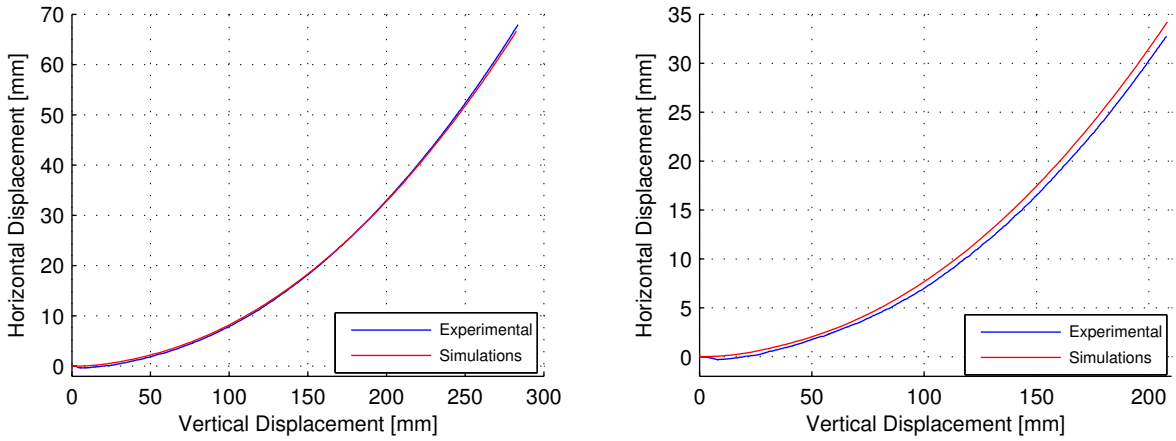

(a) Bending step for Pipe 1.

(b) Bending step for Pipe 2.

Figure 7.7: Total horizontal displacement of rotation points versus vertical displacement for shell models of Pipe 1 and Pipe 2 compared with experimental results.

For Pipe 1, the experimental data and the results from the numerical simulations once again coincide very well. For Pipe 2 there is a slight deviation. It is seen that the difference between the simulation and the experimental results seem to slightly increase over the course of vertical displacement. This complies with the stiffer behaviour of the shell model considering force-displacement for the indenter in Figure 7.5(b). As the horizontal load for Pipe 2 was applied before the vertical displacement of the indenter was initiated both in the model and in the experiment, the slight initial difference is believed to be caused by some sort of slack in the connections in the stretch bending rig.

Figure 7.8 shows a comparison for equivalent plastic strains for simulations of Pipe 1 and Pipe 2 at maximum vertical displacement at the end of the bending step. The equivalent plastic strain allows locating the elements exposed to the most severe strain history. Results for both the shell models and the solid models are displayed. For the shells, the strains displayed are extracted from the integration point closest to the outer surface.

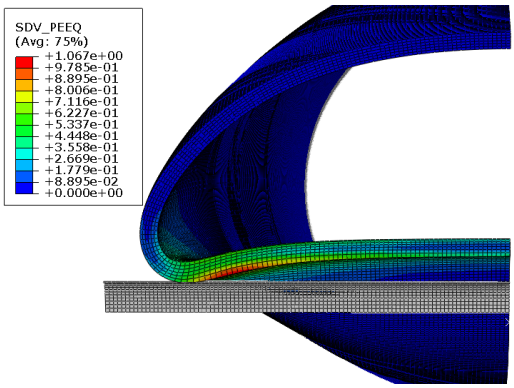

(a) Solid model of Pipe 1.

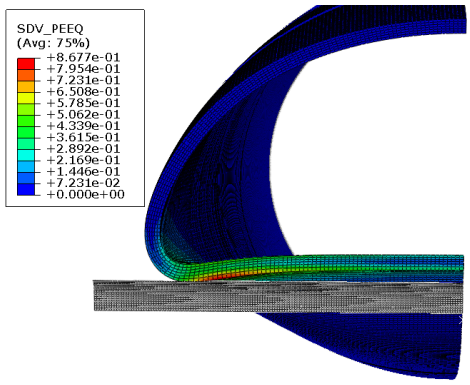

(b) Solid model of Pipe 2.

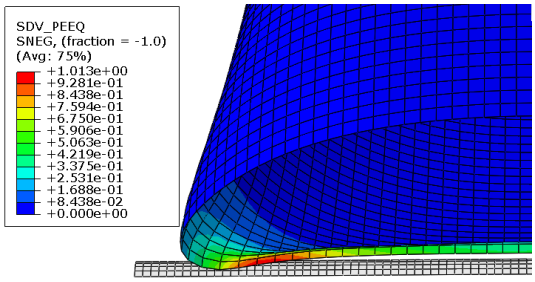

(c) Shell model of Pipe 1 displaying values for outer surface.

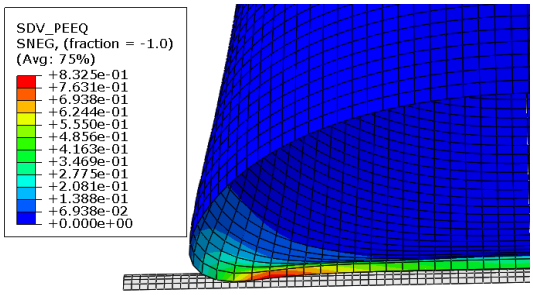

(d) Shell model of Pipe 2 displaying values for outer surface.

Figure 7.8: Equivalent plastic strain for Pipe 1 and Pipe 2 at maximum vertical displacement for solid and shell models.

The values of the equivalent plastic strains are very similar for the solids and shells. However, a difference in the strain history was discovered. This is shown and explained when the strain history for both the bending step and the stretch step is compared in Figure 7.17. Pipe 1 displays larger strains than Pipe 2. This is reasonable as Pipe 1 was subjected to larger vertical displacement. The largest equivalent plastic strains occur in the same area for both pipes. The areas showing the largest equivalent plastic strains are the same areas where surface cracks were observed after stretching the pipes in the experiments. By inspection of the most strained areas in Figure 7.8, it is found that the elements experience tension in the thickness direction and compression in the longitudinal direction of the pipes at the end of the bending step.

Figure 7.9 displays the values and locations of the Cockcroft-Latham damage parameter for Pipe 1 at the end of the bending step. Both the solid and shell model are displayed, with two figures for the shell model displaying values for the inner and outer surface respectively. The value of the damage parameter is larger on the inside of the pipes than on the outside. This is because the outer surface of the area in question is mostly in compression during the bending step, and the Cockcroft-Latham criterion does not increase for negative values

of the largest principle stress. The shell model showing values for the inner surface displays larger values than the solid model. No visible cracks were discovered in the experimental pipes after the bending step.

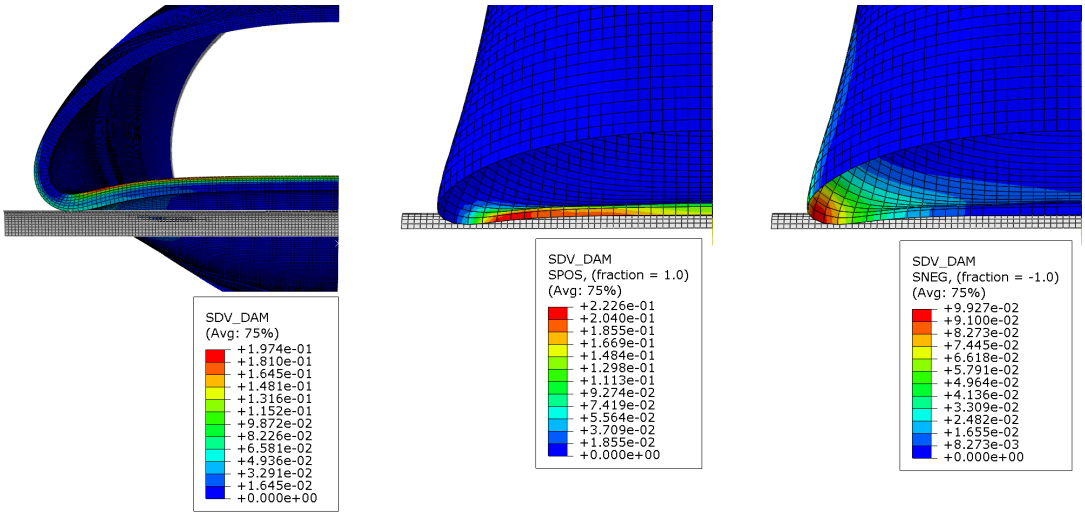

(a) Solid model.

(b) Shell model displaying values for inner surface.

(c) Shell model displaying values for outer surface.

Figure 7.9: Value of damage parameter at maximum vertical displacement for Pipe 1.

Digital Image Correlation was utilized for the experiments concerning Pipe 2 and Pipe 3. However, only the recordings for Pipe 2 gave any reasonable results. Figure 7.10 and Figure 7.11 displays graphical comparisons between the results obtained using DIC and Abaqus. The regarded results are out of plane displacements and in-plane principal strains.

Concerning out of plane displacements, the DIC results had to be corrected as it was difficult to fix the coordinate system properly. This was done by subtracting the displacement for a node, which had negligible out of plane displacement, from the node of interest. The nodes in question are highlighted in Figure 7.10(a). The out of plane displacements obtained using DIC are compared versus results for a corresponding node from the shell model in Figure 7.12(a). As seen the results are comparable, but a deviation is evident. A part of the deviation may be explained by that it was difficult to extract data from the exact same spot using Abaqus. However, compared to the Abaqus results, the out of plane displacement found using DIC initiates later. This might indicate that the bending of the pipe initiated more slowly in the experiments compared to the simulations, as suggested by the angular differences.

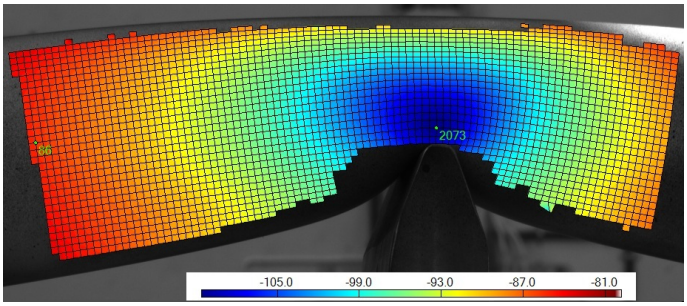

(a) Out of plane displacement using DIC.

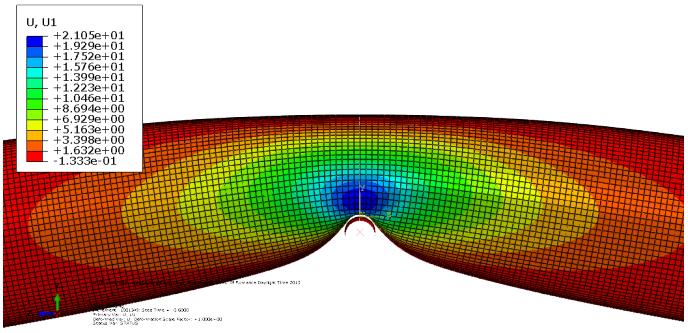

(b) Out of plane displacement for Abaqus shell model.

Figure 7.10: Comparison of out of plane displacement between DIC and Abaqus results for Pipe 2.

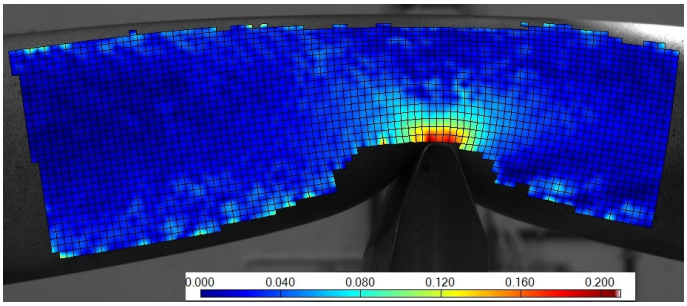

(a) Max in-plane principal strain using DIC.

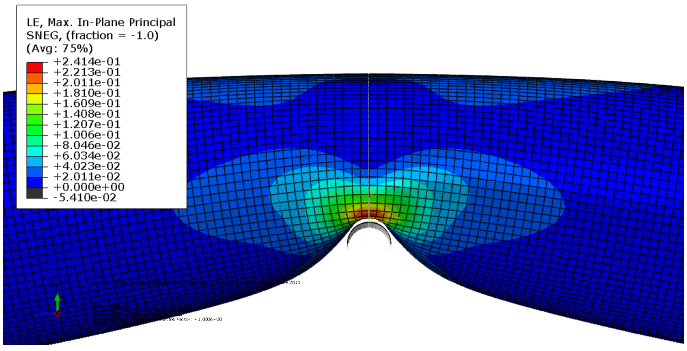

(b) Max in-plane principal strain for Abaqus shell model.

Figure 7.11: Comparison of in-plane principal strain between DIC and Abaqus results for Pipe 2.

When considering the results concerning in-plane principal strains displayed in Figure 7.12(b), there was a lot of numerical noise in the DIC results. Still, when comparing the numerical values versus the results from the shell model they seem to provide decent results. The strains were extracted from the elements which are coloured red in Figure 7.11(a). The DIC results are heavily smoothed because of the numerical noise.

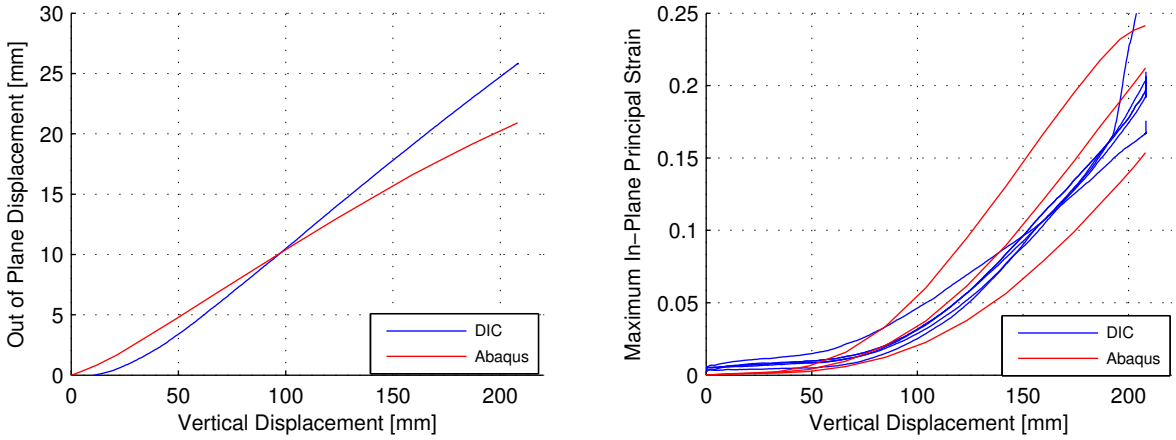

(a) Out of plane displacement.

(b) Maximum in-plane principal strain.

Figure 7.12: DIC versus Abaqus results for out of plane displacement and maximum in-plane principal strains.

For simulations regarding the bending step of Pipe 3, a clear deviation was seen when the measured average thickness of $4.02mm$ was applied. As seen in Figure 7.13(a), the experimental and numerical results deviate both before and after the initial peak. While the deviation in initial stiffness could be partly explained by the angular differences between forks and rotation points in the experiment, the evident deviation after the initial peak most likely occurred because the applied shell thickness was too low to represent the experimental pipe. Figure 7.13(b) displays a results for the shell model with an increased shell thickness of $4.27mm$. This is a severe increase compared to the measured average thickness obtained using the ultrasonic thickness gage. As discussed in Section 6.1, the ultrasonic thickness gage was believed to overestimate the pipe thickness. The global response coincides better with the experimental data with the increased thickness, but the increase in thickness was thought to be very high. A deviation concerning the initial elastic stiffness is still evident, in correspondence with the difference in rotations observed in the experiments. Also, close to maximum vertical displacement, the slope of the curves starts to deviate. This may suggest a deviation in the applied horizontal loads. As a volatile stretch step occurred for Pipe 3, which may have affected the load cell, it can be that the discovered offset of $43.9kN$ is not entirely correct for the bending step, as the load cell was checked after the stretch step.

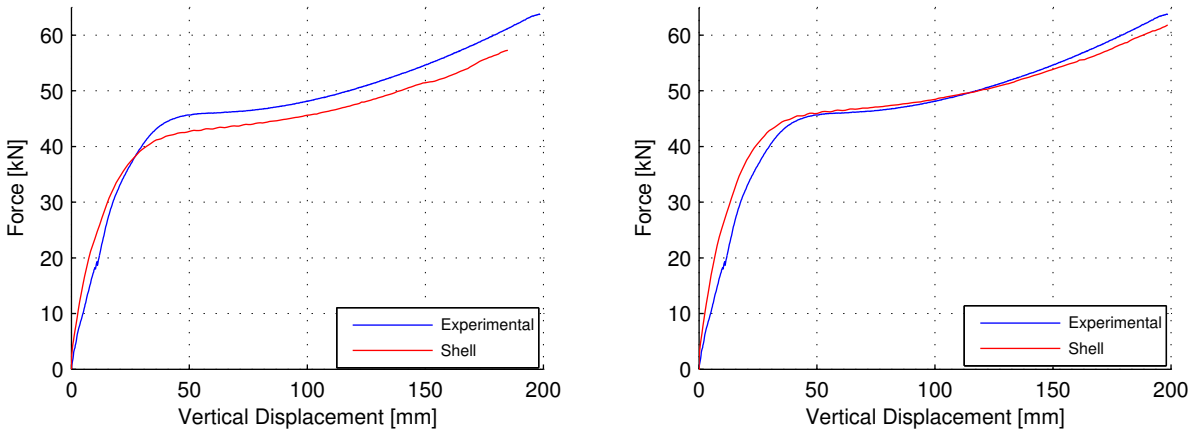

(a) Bending step using average thickness $t = 4.02mm$. (b) Bending step using corrected thickness $t = 4.27mm$.

Figure 7.13: Force-displacement for the indenter from shell models of Pipe 3 compared with experimental results.

Figure 7.14 displays the recorded angles for Pipe 3 versus the the angles obtained from the simulation.

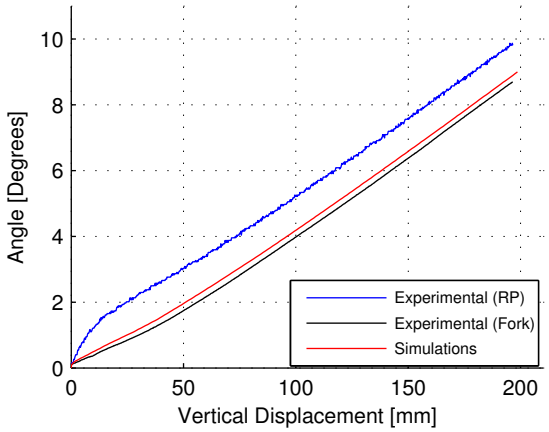

Figure 7.14: Comparison between angles recorded during experiments and angles obtained using shell model of Pipe 3 with corrected thickness $t = 4.27mm$.

This plot displays the same tendencies that was found for Pipe 2 in Figure 7.6(b). The results from the simulation is closest to the angle at the forks. The deviation is likely to have caused a delay in the bending of the pipe in the experiment compared to the simulations, explaining the deviation in initial stiffness.

7.3.2 The Stretch Step

The stretch step for Pipe 1 was simulated using both the shell and solid model, while only the shell model was used to simulate the stretch step for Pipe 2 because of the high computational demand.

Figure 7.15 displays results from simulations using shell models of the stretch step for Pipe 1 and Pipe 2 and for the solid model of Pipe 1. Both for Pipe 1 and Pipe 2 the numerical results deviate from the experimental data as the results from the analyses proves to be much stiffer.

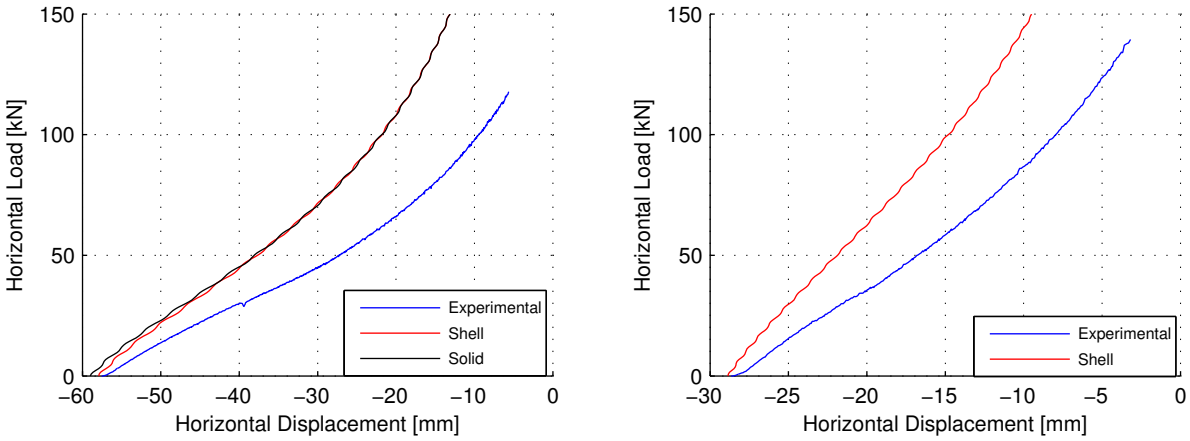

(a) Stretch step for Pipe 1.

(b) Stretch step for Pipe 2.

Figure 7.15: Horizontal load versus total horizontal displacement of the rotation points for shell models of Pipe 1 and Pipe 2 and the solid model for Pipe 1, versus experimental data.

As seen in Figure 7.15, the horizontal position has not been zeroed at the start of the stretch step. The horizontal position from the numerical results at the start of the stretch step is found to be very close to the experimental position. A slight deviation regarding the starting position is observed for both pipes, indicating that also the simulations of the unloading steps, described in Table 7.1, provide a too stiff response. The solid model for Pipe 1 gives a very similar response as the shell model with a slight deviation in the very beginning of the stretch step. This may be caused by oscillations in the simulations. Surface cracks through about 12% of the initial pipe thickness was discovered for Pipe 1. These cracks occurred due to the grooves produced by the lathing process, and thus they were not caught by the simulations. However, Pipe 2 showed less signs of surface fracture and still the simulation deviates just as much as the simulations for Pipe 1.

Figure 7.16 shows equivalent plastic strain for the outer surface of the shell models of Pipe 1 and Pipe 2, and the solid model of Pipe 1 after being stretched with a horizontal load of $150kN$.

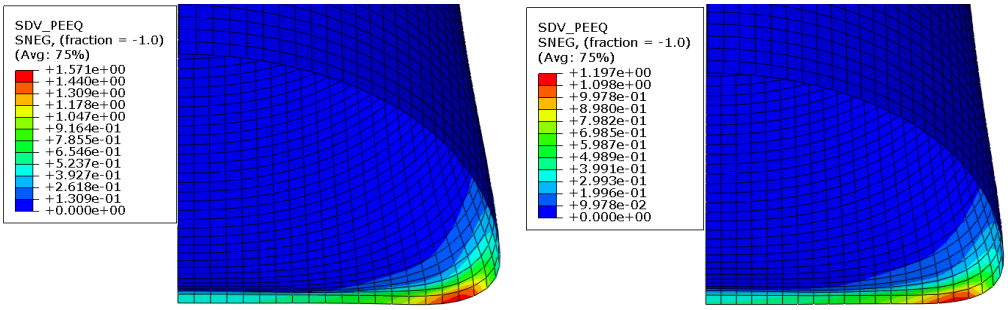

(a) Pipe 1. (b) Pipe 2.

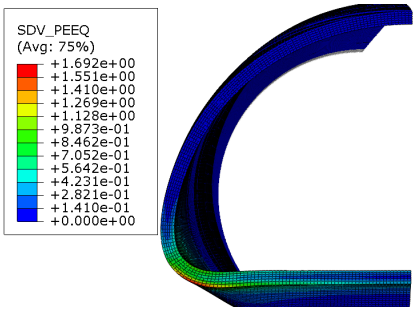

(c) Pipe 1.

Figure 7.16: Equivalent plastic strain for Pipe 1 and Pipe 2 after stretching.

The areas showing the largest equivalent plastic strains have now been stretched in the longitudinal direction and the equivalent strains have increased. As the models behaved too stiff compared to the experiments and thus were not stretched as far as in the experiments due to the load controlled stretch step in the simulations, it is likely that even larger strains occurred in the real specimens. Also, the shell model underestimates the strains compared to the solid model. Figure 7.17 shows how the strains in longitudinal directions vary versus the strains in the thickness direction for the elements displaying largest equivalent strains at the end of the stretch step. results from both the bending step and the stretch step is included. For the solid model of Pipe 2, only results from the bending step is included, as the stretch step was not simulated using this model.

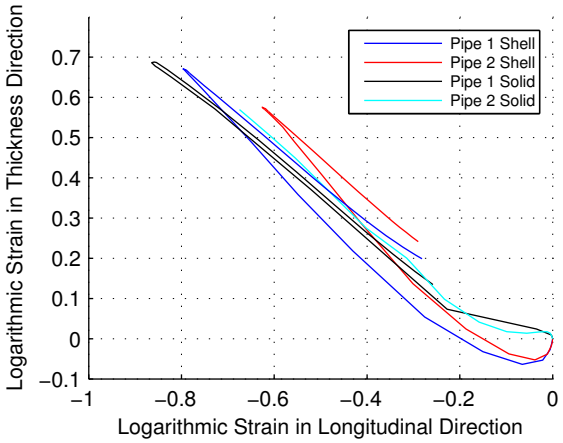

Figure 7.17: Strain history for experimental pipes.

The most strained elements for the shell models goes into compression in the thickness direction in the very beginning of the bending step. This does not happen for the solid models and explains why the difference between the equivalent plastic strains in Figure 7.8, which displays equivalent plastic strains at the end of the bending step for Pipe 1 and Pipe 2, is so small. The shell models clearly underestimates the strains compared to the solid models. The solid model for Pipe 1 displays compressive logarithmic strains in the longitudinal direction approaching 0.9 during the bending step and at the end of the stretch these strains are reduced to about 0.3 in compression. Models for Pipe 2 display less strains, but the deviation in force-displacement is still as large as for Pipe 1.

Figure 7.18 displays the value of the Cockcroft-Latham damage parameter post stretching for the shell model of Pipe 1. For the solid model, damage was unfortunately not included as the SIMLab Metal Model library was not compiled correctly on the computer where the analyses was performed. After stretching the value for the damage parameter is largest at the outer surface, in contrast to after bending, where it was largest at the inner surface. This is because the tension/compression zone is reversed during stretching. However, damage in the models does not occur before the damage parameter reaches the value of 1. At the end of stretching, a value of 0.416 is displayed for Pipe 1 and is still far from fracture. Fracture in the experimental pipes was believed to occur because of the lathing grooves, and such fracture would not appear in the models.

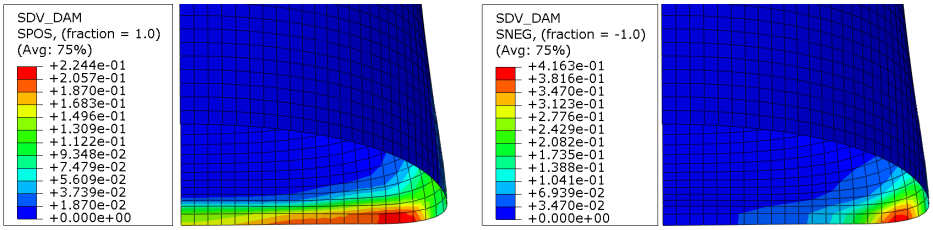

(a) Shell model displaying values for inner surface.

(b) Shell model displaying values for outer surface.

Figure 7.18: Value of damage parameter after stretching for shell model of Pipe 1.

7.4 Effects of Axial Forces

As the pipes in the experiments were subjected to different vertical displacements it was difficult to compare results for pipes subjected to different levels of horizontal loads directly. In order to investigate the effects of axial forces it was decided to use the solid model for Pipe 2 and repeat the simulation with linearly increasing horizontal load, and without applying horizontal load. By using exactly the same geometry, effects of axial forces could be studied separately. The loads were applied horizontally as they would have been using the stretch bending rig. As the solid model for Pipe 2 were used, a total vertical displacement of 208.1mm was applied for the indenter. Only the bending step was considered, as it is only during bending that the horizontal loads will be present.

Figure 7.19 displays a comparison for the equivalent plastic strain for the three simulations at maximum vertical displacement.

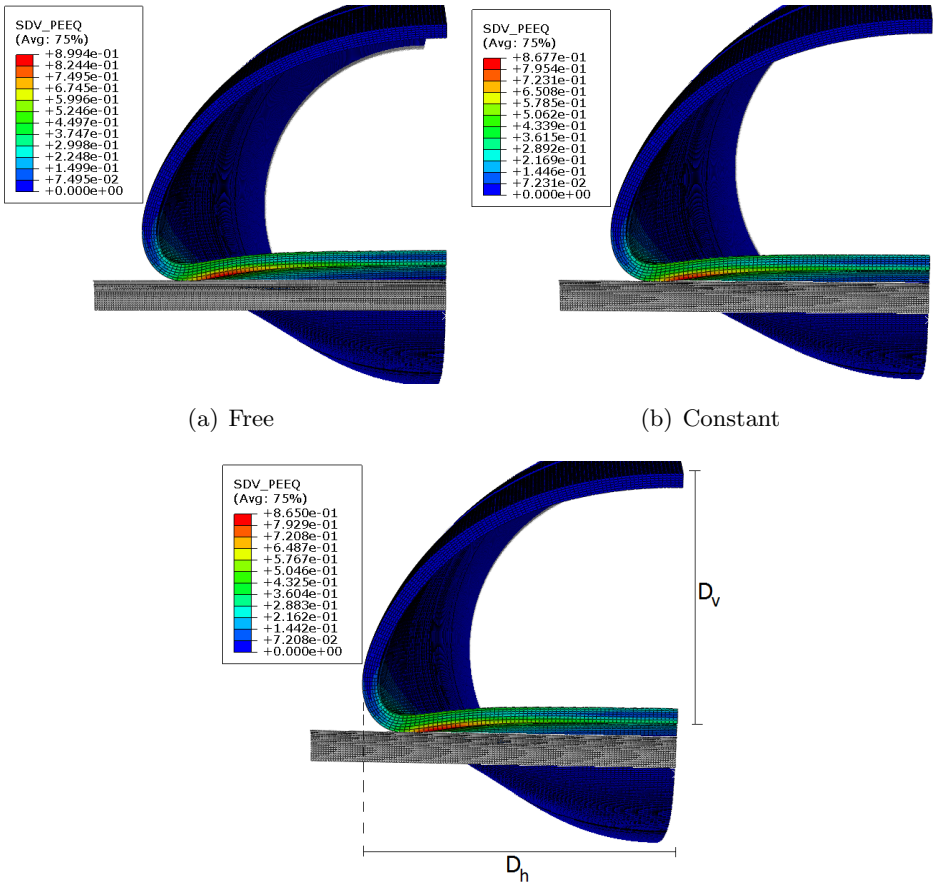

(a) Free (b) Constant

(c) Linearly increasing

Figure 7.19: Comparison of equivalent plastic strain for application of different horizontal loads.

Data for the deformed diameters in the models were extracted at maximum vertical displacement. The diameters of interest are shown in Figure 7.19(c), where D_h is the horizontal deformed diameter and D_v is the vertical deformed diameter. By looking at these measurements, differences in the geometry of the deformed cross sections could be compared. It is seen that the deformed cross sections are very similar for all three simulations, with maximum equivalent plastic strain in the same area. Table 7.3 summarizes results from Figure 7.19 with numerical values for the deformed diameters of the pipes and maximum equivalent plastic strain.

Table 7.3: Comparison for solid model of Pipe 2 subjected to different horizontal loads. D_v - vertical deformed diameter, D_h - horizontal deformed diameter.

	Free	Constant Load	Linearly Increasing Load
D_v $[mm]$	68.7	68.5	68.6
D_h $[mm]$	172.0	171.8	171.8
Max Equivalent Plastic Strain [%]	89.9	86.7	86.5

The values for deformed vertical and horizontal diameters are almost identical for all simulations, indicating that no evident differences occur in the deformed cross sections. Maximum equivalent plastic strain is marginally larger for the free pipe, indicating larger strains in the indentation area when axial forces are not present. This is reasonable as the horizontal loads will decrease the compressive strains in the longitudinal direction. Figure 7.20 displays the strain history in terms of strain in the thickness direction and strain in the longitudinal direction of the pipes, for the elements experiencing the largest equivalent plastic strains. For the horizontally loaded pipes, this was the same element. For the free pipe maximum equivalent plastic straining occurred a shift of two elements outward from the center, compared to the horizontally loaded pipes. For the unloaded pipe, strains for both the element displaying the maximum strains and strains for the same element as for the loaded pipes are displayed in the figure.

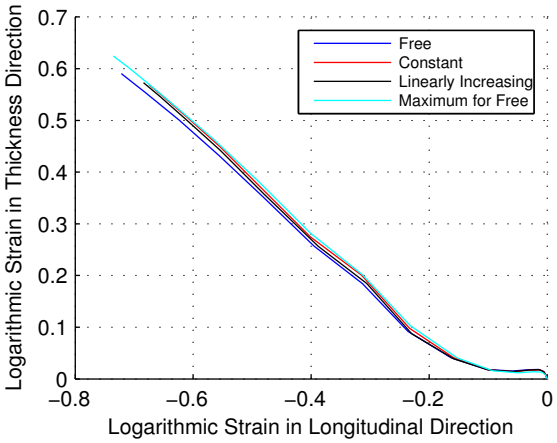

Figure 7.20: Strain history for pipes subjected to different horizontal loads.

The strains for the horizontally loaded pipes are almost identical at maximum vertical displacement. A difference is evident for the unloaded pipe which displays larger strains. This may indicate that pipes subjected to axial loads during bending is of less risk to fracture. However, the difference is very small for the applied horizontal loads of $50kN$.

Figure 7.21 displays force-displacement for the indenter for the three simulations, along with the corresponding horizontal loads applied versus vertical displacement. As found in the preliminary studies, both the horizontally loaded pipes follow different paths when force-displacement is regarded, but they end up at the same point.

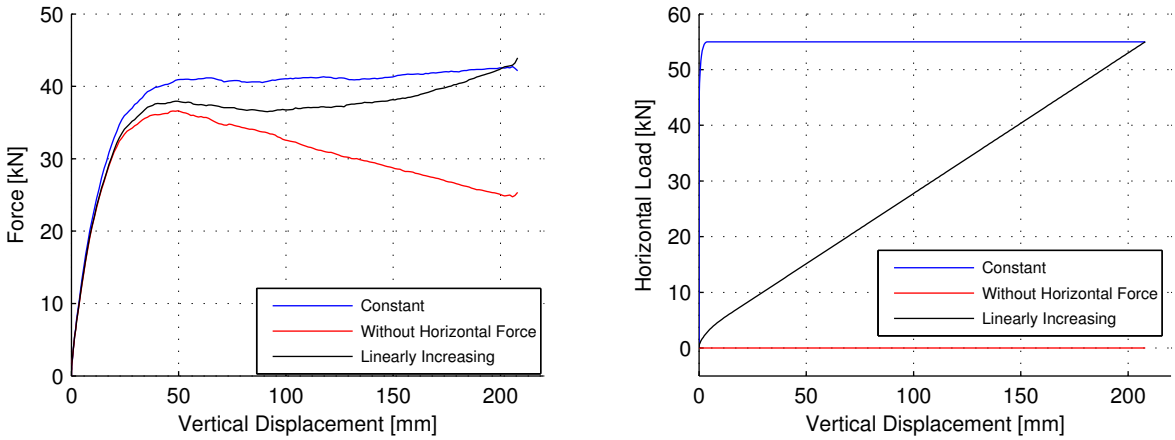

(a) Comparison for force-displacement of the indenter. (b) Horizontal Load versus vertical displacement.

Figure 7.21: Results from applying different horizontal loads to solid model of Pipe 2.

7.5 Effects of Inner Pressure

Experiments with pressurized pipes was not conducted, but numerical models were established. For investigating the effects of applying inner pressure, two additional simulations using the solid model for Pipe 1 was performed. One simulation was performed while applying pressure of 10MPa on the whole inner surface of the pipe, including the end cap, as it would have been performed in the experiments. One simulations was also carried out while applying inner pressure of 10MPa on the end cap, only in order to see how the results would compare against pressurizing the whole pipe. Applying pressure on the end cap only would be the same as applying axial forces of $118.5kN$ to the pipe. As the solid model for Pipe 1 was used, a vertical displacement of $282.6mm$ was applied. In order to model pressure in these simulations, element sets had to be imported from SALOME, which was the software used for meshing of the pipes. Only the bending step was simulated.

Figure 7.22 displays a comparison of equivalent plastic strains for the deformed cross sections in the indentation zone at maximum vertical displacement.

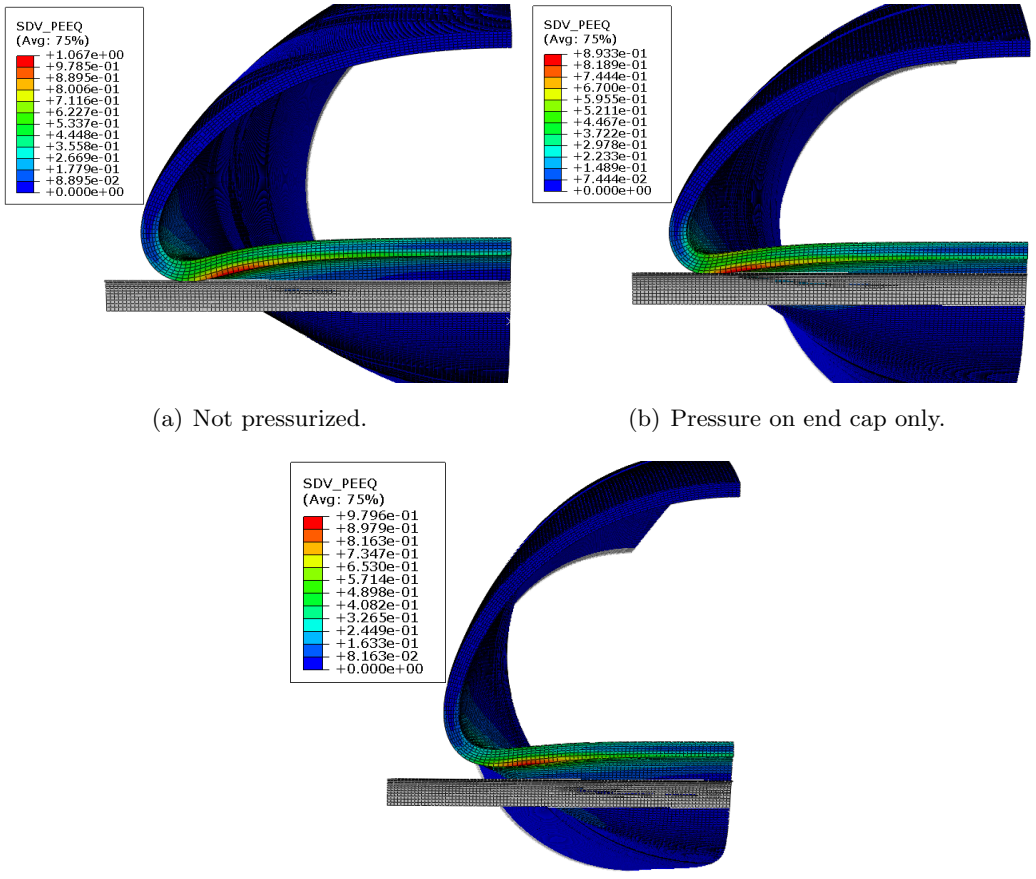

(a) Not pressurized.

(b) Pressure on end cap only.

(c) Pressurized pipe.

Figure 7.22: Comparison equivalent plastic strain for pressurized and non-pressurized pipes.

As seen in the figure, the pressurized pipe displays a very different deformed shape. This is because the pressure stiffens the cross section and thus reduces the amount of local deformation that occur. The results from Figure 7.22(c) are summarized in Table 7.4 with deformed diameters and maximum equivalent plastic strain. Diameter measurements are explained in Figure 7.19(c).

Table 7.4: Comparison for solid model of Pipe 1 subjected to pressure and pressure on end cap only. D_v - vertical deformed diameter, D_h - horizontal deformed diameter.

	Non-pressurized	Pressurized	Pressurized End Cap
D_v $[mm]$	56.2	80.2	56.1
D_h $[mm]$	181.6	167.8	181.2
Max equivalent plastic strain [%]	106.7	98.0	89.3

As seen in Table 7.4, the pressurized pipe displays very different values compared with the non-pressurized pipe and the pipe subjected to axial loading in form of pressure on the end cap only. The shape is very different, but also differences in maximum equivalent plastic strain is evident. The non-pressurized pipe, which represents Pipe 1, displays the largest values of equivalent plastic strain. The pressurized pipe displays values higher than the pipe subjected to axial force, but lower values than the free pipe. In correspondence with findings from the previous section, this indicates that applying axial forces will reduce the maximum strains in the indentation zone during bending of the pipe. Applying pressure to the whole pipe should result in inner equilibrium of the pressure resultants. However, for the pressurized simulation it was discovered that inner equilibrium of the pipe was not fulfilled. Figure 7.23 displays a comparison between the force from the indenter, and the vertical reaction force from the rotation point for the simulations of the non-pressurized pipe and the pressurized pipe. The reaction forces are multiplied by a factor of -1 for comparison. It is seen that the reaction forces are not equal to the indenter force for the pressurized simulation. This indicates that a mistake occurred in the application of inner pressure. However, The difference in the reaction forces is not large and the above comparisons are still believed to provide decent data. The mistake is likely to have occurred as element sets were imported from SALOME.

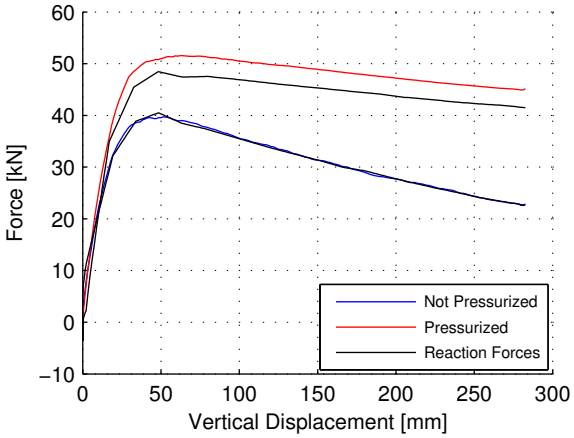

Figure 7.23: Comaprison for indender force-displacement and reaction forces in rotation point for non-pressurized and pressurized pipe.

Looking at the force-displacement paths for the indenter in Figure 7.24, it is clear that the pressurized pipe behaves much stiffer than the non-pressurized pipe. After the initial peak, the force for the pressurized pipe starts to decline, as for the non-pressurized pipe. The pressurized pipe also exhibits a stiffer behaviour than the pipe subjected to axial forces through application of pressure on the end cap before the initial peak.

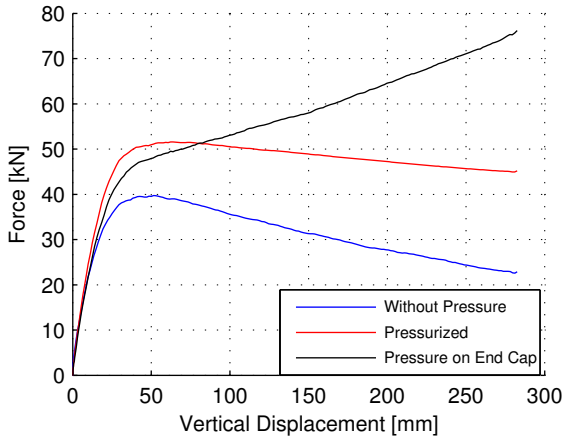

Figure 7.24: Comparison for non-pressurized, pressurized and pressurized end cap for solid model of Pipe 1.

Figure 7.25 displays a comparison of the strain history for the elements displaying the largest equivalent plastic strains in the simulations for the non-pressurized, pressurized and axially loaded pipe. Strains in the thickness direction are plotted versus strains in the longitudinal direction of the pipes.

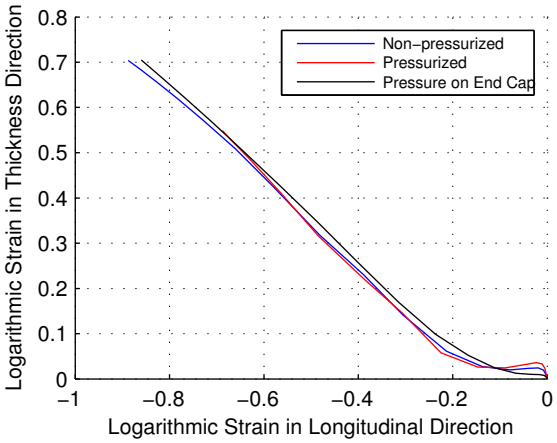

Figure 7.25: Comparison of strains for critical elements for the non-pressurized, pressurized and axially loaded pipe.

The pipe with pressure on the end cap only, which is axially loaded, clearly displays a less severe strain history. Strains occurring in the critical element for the pressurized pipe are very similar to those of the free pipe.

8 Discussion

Experimental work was carried out using the stretch bending rig at the Department of Structural Engineering, NTNU. Three pipeline specimens were tested, where the pipes were first bent at low velocities of $25mm/min$ using a wedge shaped indenter, before being stretched. This was done in an attempt to simulate the scenario were an offshore pipeline is hooked by an object and dragged along the seabed, before rebounding due to large axial forces when released from the object. During bending, the pipes were subjected to different levels of horizontal loads to represent axial loads that builds up when a pipeline is dragged out of position. Pipe 1 was not subjected to any horizontal load, Pipe 2 was subjected to constant horizontal load of $55kN$. Pipe 3 was supposed to be subjected to a linearly increasing horizontal load of 0-$55kN$ during the course of deformation, corresponding to the load level of Pipe 2. Due to an offset for the horizontal load cell the pipe was instead subjected to a horizontal load increasing from $43.9kN$ to $101.9kN$. As a result of a bug in the software controlling the stretch bending rig the stretch step of Pipe 3 was not executed as planned, leading to unfavourable data.

For Pipe 2 and Pipe 3 the angles of rotation were measured at two different places. The angles were measured both close to the points of rotation and at the forks, close to the pipe itself. Figure 8.1 displays force displacement for the indenter for bending of Pipe 1-3, and the recorded angles during bending.

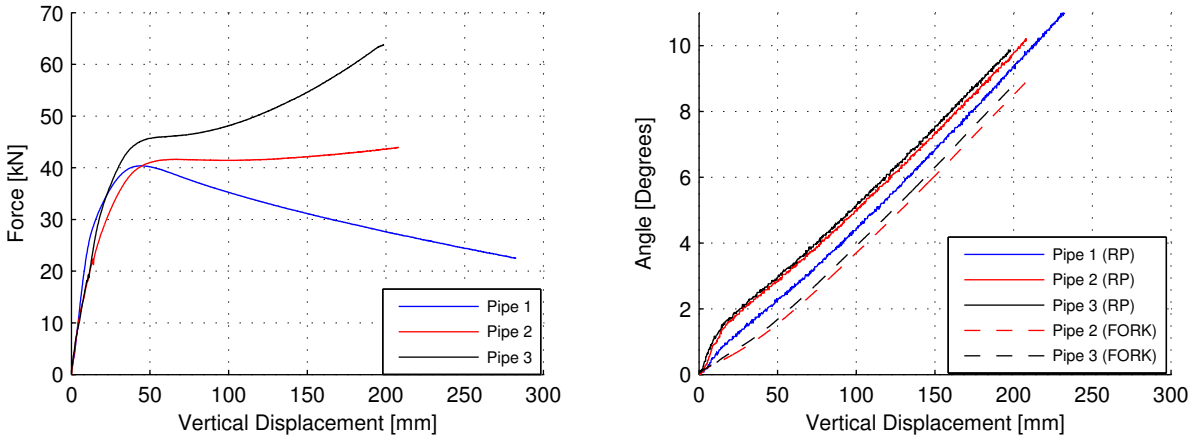

(a) Force-displacement for the indenter.

(b) Angles at the rotation points and at the forks.

Figure 8.1: Force-displacement for the indenter during bending of the pipes and recorded angles versus vertical displacement.

As seen in Figure 8.1(b), the experimental data revealed a difference in the measured angles during bending, and it was evident that rotation at the points of rotation happened more rapidly than at the forks in the initiation phase of the bending steps for Pipe 2 and Pipe 3. This indicated that bending between the forks and the rotation points happened more rapidly than bending of the pipes in the start of the bending step.

Pipe 1 proved to exhibit a stiffer behaviour than Pipe 2 and Pipe 3 at the very start of the bending step, as seen in Figure 8.1(a). As Pipe 1 was not subjected to any horizontal loads this was not expected beforehand. However, two possible reasons were found to be likely. The first reason was that Pipe 1 displayed the largest measured average thickness of the pipes. As this would contribute to increasing the stiffness it could explain some of the deviation. The second reason was the deviation between the measured angles at the forks and at the points of rotation for Pipe 2 and 3. As seen in Figure 8.1(b) a deviation of 1.2° was discovered. The deviation may stem from parts rotating relatively to each other, or it may be that the grips of the stretch bending rig were slightly bent. The angles at the rotation points of Pipe 2 and Pipe 3 also differs from the angles of Pipe 1, suggesting that a lesser deviation between the forks and the points of rotation would have been evident for Pipe 1. This was confirmed by numerical simulations, where simulations using rigid rotation between the rotation point and the pipe proved to give a very good match for Pipe 1, while failing to represent the stiffness before the initial peak for Pipe 2 and Pipe 3. It is believed that the applied horizontal load for Pipe 2 and Pipe 3 may have stiffened the pipes so that initial bending deformation occurred more rapidly in the parts between the forks and the points of rotation than in the pipes at the beginning of the bending step. It may also be that the application of horizontal loads caused the different connecting parts to more easily rotate relatively to each other. In order to improve future experiments it can be suggested to weld together or sandblasted the forks and the block bearings at the interacting surfaces to try and prevent the relative rotation. This would however not prevent bending of the grips. Attempting to map the vertical displacement resulting from relative rotation may also be possible and can be used to correct the force displacement curve.

After the bending step, no cracks were found by visual inspection for any of the pipes. However, surface cracks were visible in the indentation zone for all pipes after the stretch step. Pipe 1 and Pipe 3 displayed rather large surface cracks. The largest surface crack was estimated to about $480\mu m$ for Pipe 3 by use of a optical light microscope, corresponding to approximately 12% of the initial pipe thickness. Pipe 1 also showed similar cracks. Through further metallurgical investigation the surface cracks were seen to be caused by widening of lathing grooves. Fracture seemed to be initiated at the bottom of these grooves. Such an uneven surface could have led to stress and strain concentrations, thereby initiating cracks at specific locations. This is believed to be of minor importance for the fracture process for original pipes, where the outer surface is not lathed. Further metallurgical study revealed some sporadically distributed calcium aluminate particles that could cause ductile fracture through void nucleation, growth and coalescence. However, almost no internal fracture was

discovered for the stretched pipes. Only a crack of approximately $100\mu m$ was discovered near the inner surface for the tip specimen of Pipe 1.

Pipe 1 was subjected to larger vertical displacement during bending than Pipe 2 and Pipe 3. In order to obtain more easily comparable data it is recommended that pipes are subjected to the same vertical displacement in future experiments. The testing procedure slightly differed for Pipe 1 and Pipe 2, which were considered as the successful experiments. For Pipe 1 the indenter was removed while the rotation points were free to move horizontally. For Pipe 2 the horizontal actuators were locked during removal of the indenter to prevent stretching by the applied horizontal load. The testing procedure should be standardized and the pipes should be subjected to the same vertical displacement for better comparisons between experimental data. Applying more or less identical vertical displacement will also improve the comparability of stretch step data as necessary loads to stretch the pipes are mostly dependent on the inner moment arm. Thus, if the vertical displacement is the same, the pipes may be stretched to the same displacement or load level for better comparisons of the deformed cross section concerning shape and fracture. Applying horizontal loads to the specimens during bending will force the elastic rebound to be executed in two steps as it will be impossible to remove the indenter and at the same time unload the horizontal actuators without causing the pipe to be stretched. As it is of interest to apply horizontal loads during bending the testing procedure for Pipe 2 may be recommended, where the horizontal actuators are locked while the indenter is removed. The suggested procedure is as follows:

1. Apply the desirable horizontal load and/or inner pressure.
2. Bend the pipe specimen to the desired vertical displacement using displacement control for the vertical actuator. $25mm/min$ was used in the experiments conducted in this thesis.
3. Lock the horizontal actuators, while removing the indenter using displacement control.
4. Release and unload the horizontal actuators using load control.
5. Stretch the pipeline specimen until the desired load or displacement is reached, using load control for the horizontal actuators.

Digital Image Correlation (DIC) was set up and used for experiments of Pipe 2 and Pipe 3. However, only data recorded for Pipe 2 proved to be good enough for further use. The poor quality of the data obtained from Pipe 3 was most likely due to poor lighting conditions. Obtaining good results also proved difficult due to the large rigid body motions of the pipes. The large rigid body motions made it difficult to set a working coordinate system for analysing the data. However, the DIC data for Pipe 2 compared relatively well to numerical simulations carried out using Abaqus/Explicit. During bending in the experiments the indentation zone, which is the area of most interest, is covered by the indenter, making it impossible to record data for that area. Thus, only data from outside

this area may be obtained. For the stretch step it may be possible to mount cameras in such a way that they look specifically at the indentation zone. If this were to work properly it could provide valuable data concerning the actual strains which develops during stretching of pipeline specimens after bending.

Two different material models for X65 steel were used for the numerical simulations, namely the isotropic material model calibrated by direct calibration by Slåttedalen and Ørmen [5] and the combined isotropic/kinematic material model calibrated by inverse modelling by Aune and Hovdelien [7]. As in previous theses regarding the impact step, it was found that the isotropic material gave an excellent compliance for simulations of the bending step. The combined material model did not capture the initial peak for force-displacement of the indenter from the bending step. Both material models failed to represent the stretch step in a satisfactory manner.

The isotropic model was calibrated on the basis of tensile strains only. As the most strained areas in the pipe specimens experienced large compressive strains before being stretched, this may explain why the isotropic model fail to represent the stretch step satisfactorily. The combined isotropic/kinematic material model was calibrated based on compression tests with reversed loading, where the specimens were compressed up to 40% logarithmic strain. However, simulations of the bending step showed that the most strained areas experienced compressive logarithmic strains approaching 90%. Notched compression tests with reversed loading carried out by Kristoffersen et al. [4], were compressed to logarithmic strain values of 40%, 60%, 80% and 90%. From these tests a tendencies to ductility reduction became more evident and both the 60% and 80% specimen showed signs of cleavage fracture. It may be that calibrating a combined isotropic/kinematic material model based on larger compressive strains from compression test with reversed loading could improve the correspondence between the simulated stretch step and the experiment. However, strain history plots from the simulations of Pipe 1 and 2 showed that the strain history was more severe for Pipe 1 due to the larger vertical displacement. Also, more surface cracks were seen in Pipe 1 than in Pipe 2. These surface cracks were not caught by the simulations. More surface cracking in the experimental pipes was believed to make for a larger deviation between numerical and experimental results for the stretch step. Still, deviations in force-displacement was found to be just as large for Pipe 2 as for Pipe 1. This may indicate that other factors also are important.

As mentioned, metallurgical investigations revealed surface cracks corresponding to 12% of the initial pipe thickness, which arose from lathing grooves during stretching. The numerical models failed to capture this effect, as they were modelled with smooth surfaces. This difference most likely contributed to some of the deviation seen between the simulated stretch step and the experiments. For future experiments it is therefore recommended to grind down the lathing grooves in order to obtain smooth pipe surfaces.

A specimen cut out from the bend of Pipe 3 revealed a localization in form of necking, which were not seen in any numerical models. No attempts were made to simulate the stretch step of Pipe 3, as it was considered a failure, but if localizations were to be present in any of the other tested pipes this could be part of the reason why the stretch step is overestimated in the numerical models. In numerical simulations, localizations are often highly mesh sensitive, and may require a very refined mesh in order to be captured. The solid models established in this thesis had six elements over the thickness in the indentation zone. It may be that a numerical model with a much more refined mesh could capture possible localization. The deviation between numerical results and experimental data for the stretch steps may come down to mesh sensitivity.

Figure 8.2 displays a comparison of numerical results obtained using the shell models and experimental results for force-displacement of the indenter during the bending step.

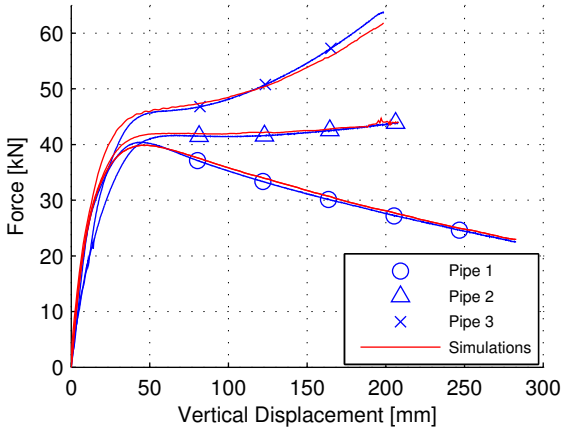

Figure 8.2: Comparison for force displacement of the indenter for numerical simulations versus experimental data for the bending step.

The excellent agreement for Pipe 1 is believed to be a result of less relative rotation between the forks and the rotation points occurring during the initiation phase of the bending step. When the numerical results for the angles at the rotation points were compared to experimentally recorded angles, the results were fairly similar. For Pipe 2 and 3, deviations were evident. In the simulations the rotation between the forks and the rotations point were made rigid, thus indicating that the connection between the pipe and the rig behaved more rigidly during the experiment for Pipe 1 than for Pipe 2 and Pipe 3.

For the numerical simulations of Pipe 1 and Pipe 2 the average thickness measured by use of the ultrasonic thickness gage were applied, and the numerical results compared well to the experimental data from the bending step. The ultrasonic thickness gage was found to overestimate thickness measurements of the pipes compared to a micro meter, which was considered more accurate. Due to the irregular thickness of the pipes it seems quite random as to which thickness applied in the simulations fits best with the experimental data. The

approach of first fitting the numerical simulations using shell models and then creating solid models with the desired thickness seems to work. However, for Pipe 3 it was found necessary to add thickness of $0.27mm$ in order to get decent results using the shell model. This corresponds to an increase of 6.8% compared to nominal pipe thickness, which is quite a lot. As previously mentioned, an offset of $43.9kN$ was discovered for the horizontal load cell after the experiment for Pipe 3. The load cell was checked after the volatile stretch step, and it may be that the rapid increase in load during the stretch step affected the load cell further. This would mean that the offset discovered for the horizontal load cell would not apply for the bending step of Pipe 3.

Numerical simulations indicated that applying axial or horizontal forces while bending pipes will reduce straining in the indentation zone. Thus, it is possible that pipes subjected to axial forces are less susceptible to fracture, as the critical areas in the pipes would suffer less compressive strains during bending. This needs to be verified by a series of experimental tests where pipes are subjected to the same vertical displacement and different horizontal loads.

Numerical models for pressurized pipes were established. The shell model used in the preliminary studies was able to replicate the experimental findings of Jones and Birch [23], where a reduction in local deformation of 30.6% was discovered when inner pressure of 10 MPa was applied to model. Global equilibrium was also checked for the pressurized shell model. It was found that the vertical reaction forces obtained from the indenter and at the rotation point were equal in opposite directions, meaning that applying inner pressure did not affect the global equilibrium. A deviation was found in global equilibrium for the solid model used to investigate effects of inner pressure. The deviation most likely occurred as a result of the process to apply pressure using element sets imported from another software, and pressure was then not applied correctly. The bending stiffness of the pipes were increased by applying inner pressure, due to a stiffening effect for the cross section. The established models for inner pressure should be able to represent experimental tests of pressurized pipes in the stretch bending rig.

It was of great interest to compare results from the low velocity bending experiments conducted in this thesis to the impact experiments conducted in previous theses, in order to see if the same fracture mechanisms occurred. As the impact experiments were carried out without subjecting the pipes to any horizontal loads, Pipe 1 would be best suited for a comparison. Table 8.1 displays transverse displacement and angle at rotation points for Pipe 1 after the bending step in the stretch bending rig and for Pipe A and B after being tested in the pendulum accelerator. The span length in the stretch bending rig was initially $2.15m$ compared to $1.0m$ in the pendulum accelerator for the previously conducted impact tests. This results in a large difference for the plastic limit loads, which is also compared in the table.

Table 8.1: Comparison between low velocity bending and impact experiments.

Pipe	Pipe 1	Pipe A	Pipe B
Transverse Displacement $[mm]$	283	141	294
Angle at Rotation Points $[Degrees]$	14	12	30
Plastic Limit Load $[kN]$	59.1	118.5	117.6

Figure 8.3 shows force-displacement for the indenter for the three pipes displayed in Table 8.1. Pipe A and Pipe B were were subjected to impact with velocities of $3.23m/s$ and $5.13m/s$ respectively. The large difference in force in Figure 8.3 is mostly due to the difference in span length.

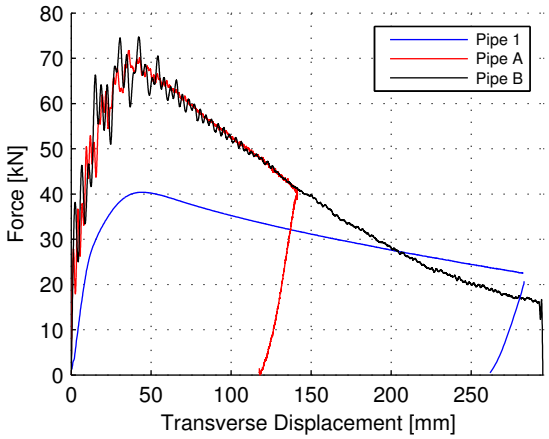

Figure 8.3: Force versus transverse displacement for Pipe 1, Pipe A and Pipe B.

The low bending tests with subsequent stretching showed a negligible amount of internal cracks after being stretched. However, surface cracks of about 12% of the initial pipe thickness was observed in the bend at the indentation zone. Dynamic impact tests with subsequent stretching investigated by Kristoffersen et al. [4] showed both through-thickness cracks and surface cracks. The through-thickness cracks showed zones of classic brittle cleavage fracture with no indication of ductility, which were the first to appear during stretching. In addition, the through-thickness cracks displayed zones indicating ductile fracture, which propagated at a later stage in the stretch step. Cracked particles were discovered.

Pipe K and L were subjected to impact only, and studied metallurgically. While Pipe K was subjected to higher velocity impact similar to Pipe B, Pipe L was subjected to the same impact velocity as Pipe A, implying that the angles at the ends were similar to those of Pipe 1. The similar angles at the ends should give a comparable cross-sectional

deformation, meaning that Pipe L should be comparable to Pipe 1. An estimation of the external work done on the pipes can be made by calculating the area under the force-displacement curves in Figure 8.3. By leaving the elastic rebound out of the calculation and using the trapezoidal rule the external work was found to be $8.65kJ$ and $7.70kJ$ for Pipe 1 and Pipe A respectively. The deviation in external work is not that far apart and suggests that the Pipe 1 should be comparable to Pipe L.

Cracks were found in both pipes subjected to impact only. For pipe K, both surface cracks and internal cracks causing fracture through 75% of the thickness were evident. These cracks probably emerged during the elastic rebound after impact [4]. Investigations of the fracture surface for the surface crack suggested cleavage fracture. For pipe L, cracks were less detectable. However, a internal crack of about $300\mu m$ was discovered. As Pipe 1 showed almost no sign of internal fracture after bending and stretching, and pipe L showed internal cracks when subjected to impact only, it is possible that cracks observed in the dynamic tests are related to stress waves produced by the impact. Brittle cleavage fracture could be triggered by impact and elastic rebound. The fractures discovered in the dynamic tests, may also be dependent of the strain-rate sensitivity of X65 steel. The larger contact force for the impact experiments, applied over a much shorter duration, could produce such effects.

9 Conclusion

Surface cracks were found for all tested pipeline specimens after being subjected to low velocity bending and subsequent stretching. Cracks were not visible after bending only. Metallurgical investigations revealed no significant internal fracturing. It was found that the surface cracks initiated in the grooves produced by lathing process. Such fracture would be almost impossible to replicate in numerical analyses, but is not realistic in the real scenario where an offshore pipeline is subjected to impact, as it will not have been lathed. Comparisons with pipes subjected to impact and similar cross-sectional deformations suggest that low velocity bending of pipes does not produce the same fracture mechanisms as is produced by impact.

Numerical simulations corresponded well with experiments performed in the stretch bending rig when the bending step was considered. However, a deviation in initial stiffness was seen for pipes subjected to axial loads. The deviation was most likely caused by a detected relative rotation in the parts connecting the pipe to the stretch bending rig, making the response of the numerical models stiffer as rigid rotation between the rotation point and the pipe was applied. Numerical simulations failed to replicate the experimental stretch step in a satisfactory manner as numerical results proved to be too stiff. A simulation of the stretch step was not improved for an experimental pipe showing less surface cracks and experiencing a less severe strain history. A localization in form of necking was observed in the metallurgical study for one of the pipeline specimens. Such localizations are highly mesh sensitive in numerical simulations and it may be that a numerical model with a much more refined mesh could be able to represent the stretch step in a better fashion.

Numerical shell models underestimated the strains in the indentation zone compared to solid models with a more refined mesh. It was found in numerical simulations that application of axial loads reduces the strains in the indentation zone of the pipes during bending, possibly making them less susceptible to fracture after low velocity bending and subsequent stretching.

10 Further Work

This chapter presents the suggested further work on the topics investigated in this thesis.

Future testing of pipelines in the stretch bending rig should follow a standardized procedure in order to make experimental data more comparable. It is suggested that all pipes are exposed to same vertical displacement and that the following procedure is used:

1. Apply the desirable horizontal load and/or inner pressure.
2. Bend the pipe specimen to the desired vertical displacement using displacement control for the vertical actuator. $25mm/min$ was used in the experiments conducted in this thesis.
3. Lock the horizontal actuators, while removing the indenter using displacement control.
4. Release and unload the horizontal actuators using load control.
5. Stretch the pipeline specimen until the desired load or displacement is reached, using load control for the horizontal actuators.

For future experiments it is recommended that the pipe-rig connection in the stretch bending rig is stiffened. Sandblasting the interacting surfaces between the forks and the block bearings may give less relative rotation. These parts may also be welded together. It is also recommended that multiple clinometers are used to check for any relative rotation.

Experiments concerning pressurized pipes were not conducted in this thesis and is left for further work. The pressurized experiment should follow the same procedure as experiments subjected to different horizontal loads.

It still remains to calibrate a combined isotropic/kinematic material model based on compression tests with reversed loading for larger strains. Specimens can be compressed to strains comparable to the values in the critical areas for pipes subjected to bending, which were in numerical simulations found to be approximately 90%, before being stretched to failure. This could improve simulations of the stretch step. The stretch step may also be highly mesh sensitive and it is suggested that a model using a lot more elements over the thickness is made and compared with experimental data.

Bibliography

[1] Det Norske Veritas. *Interference between Trawl Gear and Pipelines, DNV-RP-F111.* DNV, 2010.

[2] Petroleumstilsynet v/Rune Solheim. *Presentasjon sikkerhetsforum 29.11.2007 alvorlige hendelser.* Petroleumstilsynet, `http://www.ptil.no/getfile.php/Tilsyn%20p%C3%A5%20nettet/vrige/5_07_siforum_alvorlige_hendelser.pdf`, Cited date: [31.01.2013].

[3] Statoil. *Annual Report 2008 Operations North Sea.* Statoil `http://www.statoil.com/AnnualReport2008/en/CountrySpotlight/Norway/Pages/3-1-7-1_OperationsNorthSea.aspx`, Cited date: [31.01.2013].

[4] M. Kristoffersen, T. Børvik, I. Westermann, M. Langseth, and O.S. Hopperstad. *Impact against an X65 steel pipe - An experimental investigation.* Structural Impact Laboratory, Department of Structural Engineering, Norwegian University of Science and Technology. Submitted for Possible Journal Publication, 2013.

[5] K. Slåttedalen and A. Ørmen. *Impact Against Offshore Pipelines.* Master's Thesis, Structural Impact Laboratory, Department of Structural Engineering, Norwegian University of Science and Technology, 2010.

[6] J. Fornes and S. Gabrielsen. *Impact Against Offshore Pipelines.* Master's Thesis, Structural Impact Laboratory, Department of Structural Engineering, Norwegian University of Science and Technology, 2011.

[7] V. Aune and M.S. Hovdelien. *Impact Against Offshore Pipelines.* Master's Thesis, Structural Impact Laboratory, Department of Structural Engineering, Norwegian University of Science and Technology, 2012.

[8] A.G. Hanssen, T. Auestad, T. Tryland, and M. Langseth. *The Kicking Machine: A Device for Impact Testing of Structural Components.* International Journal of Crash-Worthiness, 8(4), page 385-393, 2003.

[9] S.G. Thomas, S.R. Reid, and W. Johnson. *Large deformations of thin-walled cicular tubes under transcerse loading - I.* International Journal of Mechanical Science, Vol.18, page 325-333, 1976.

[10] A.R. Watso, S.R. Reid, W. Johnson, and S.G. Thomas. *Large deformations of thin-walled cicular tubes under transcerse loading - II.* International Journal of Mechanical Science, Vol.18, page 387-397, 1976.

[11] A.R. Watson, S.R. Reid, and W. Johnson. *Large deformations of thin-walled cicular tubes under transcerse loading - III.* International Journal of Mechanical Science, Vol.18, page 501-509, 1976.

[12] O.S. Hopperstad and T. Børvik. *Compendium in TKT4135 Mechanics of Materials.* Department of Structural Engineering, Norwegian University of Science and Technology, 2012.

[13] T. Børvik. *Lecture notes on The Tension Test in TKT4135 Mechanics of Materials.* Department of Structural Engineering, Norwegian University of Science and Technology, 2012.

[14] A.S. Khan and S. Huang. *Continuum Theory of Plasticity.* John Wiley and Sons, Inc., New York, 1995.

[15] T.L. Anderson. *Fracture Mechanics - Fundamentals and Applications.* Taylor and Francis Group, Third Edition, 2005.

[16] S. Dey. *High-Strength Steel Plates Subjected to Projectile Impact.* PhD Thesis, Structural Impact Laboratory, Department of Structural Engineering, Norwegian University of Science and Technology, 2004.

[17] SIMULIA. *Abaqus Analysis Users Manual.* SMULIA, Abaqus Documentation Collection, 6.11 edition, 2013.

[18] J.L. Chaboche and J. Lemaitre. *Mechanics of Solid Materials.* Cambridge University Press, page 161-252, 1990.

[19] SIMULIA. *Abaqus Theory Manual.* SMULIA, Abaqus Documentation Collection, 6.11 edition, 2013.

[20] G.R. Johnson and W.H. Cook. *Fracture Characteristics of Three Metals Subjected to Various Strains, Strain Rates, Temperatures and Pressures.* Engineering Fracture Mechanics, 21(1), page 31-48, 1985.

[21] M.G. Cockcroft and D.J. Latham. *Ductility and the Workability of Metals.* Journal of the Institute of Metals, 96, page 33-39, 1968.

[22] K.M. Mathisen. *Lecture Notes TKT4197 Nonlinear Finite Element Analysis.* Department of Structural Engineering, Norwegian University of Science and Technology, 2012.

[23] N. Jones and R.S. Birch. *Low-Velocity Impact of Pressurised Pipelines.* International Journal of Impact 37, page 207-219, 2010.

[24] A. Manes, R. Porcaro, H. Ilstad, E. Levold, M. Langseth, and T.Børvik. *The Behaviour of an Offshore Steel Pipeline Subjected to Bending and Stretching.* Structural Impact Laboratory, Department of Structural Engineering, Norwegian University of Science and Technology, 2011.

[25] J. Croxon. *The Properties of Steel Grade X65.* eHow `http://www.ehow.com/list_7492075_properties-steel-grade-x65.html`, Cited date: [29.01.2013].

[26] C.K. Oh, Y.J. Kim, J.H. Beak, and W.s. Kim. *Development of Stress-Modified Frature Strain for Ductile Fracture of API X65 Steel.* International Journal of Fracture 143, page 119-133, 2007.

[27] Tenaris. *Seamless Tubes Manufacturing Process.* `http://www.tenaris.com/en/aboutus/productionprocesses.aspx`, Cited date: [29.04.2013].

[28] A. Ghiotti, S. Fanini, S. Bruschi, and P.F. Bariani. *Modelling of the Mannesmann Effect.* CIRP Annals - Manufacturing Technology 58, page 255-258, 2009.

[29] Det Norske Veritas. *Submarine Pipeline Systems, DNV-OS-F101.* DNV, 2005.

[30] G.E. Dieter. *Bend and Shear Testing. Mechanical Behaviour Under Tensile and Compressive Loads.* ASM Hand book, Mechanical Testing and Evaluation, chap. 8, page 99-108, 2000.

[31] B. Opheim. *Bending of Thin-Walled Aluminum Extrusions.* PhD Thesis, Department of Structural Engineering, Norwegian University of Science and Technology, 1996.

[32] Structural Impact Laboratory. *Simlab Metal Model Theory Manual.* Structural Impact Laboratory, Department of Structural Engineering, Norwegian University of Science and Technology, rev fall 2012 edition, 2012.

[33] A.H. Clausen. *Stretch Bending of Aluminium Extrusions.* Department of Structural Engineeing, Norwegian University of Science and Technology, 1999.

[34] A.H. Clausen, O.S. Hopperstad, and M. Langseth. *Stretch Bending Rig. Experimental Set-Up.* Report R-9-96, Department of Structural Engineeing, Norwegian University of Science and Technology, 1996, revised 1999.

[35] T. Nelligan. *Ultrasonic Thickness Gaging.* `http://www.olympus-ims.com/en/applications-and-solutions/introductory-ultrasonics/introduction-thickness-gaging/`, Cited date: [15.05.2013].

[36] E. Fagerholt, T. Børvik, and O.S. Hopperstad. *Measuring Discontinuous Displacement Fields in Cracked Specimens Using Digital Image Correlation with Mesh Adaptation and Crack-Path Optimization.* Structural Impact Laboratory, Department of Structural Engineering, Norwegian University of Science and Technology, 2012.

[37] E. Fagerholt, E. Østby, T. Børvik, and O.S. Hopperstad. *Investigation of Fracture in Small-Scale SENT Tests of a Welded X80 Pipeline Steel Using Digital Image Corre-*

lation with Node Splitting. Structural Impact Laboratory, Department of Structural Engineering, Norwegian University of Science and Technology, 2012.

Appendices

A Material Certificate

Figure A.1 shows composition of the steel grade X65

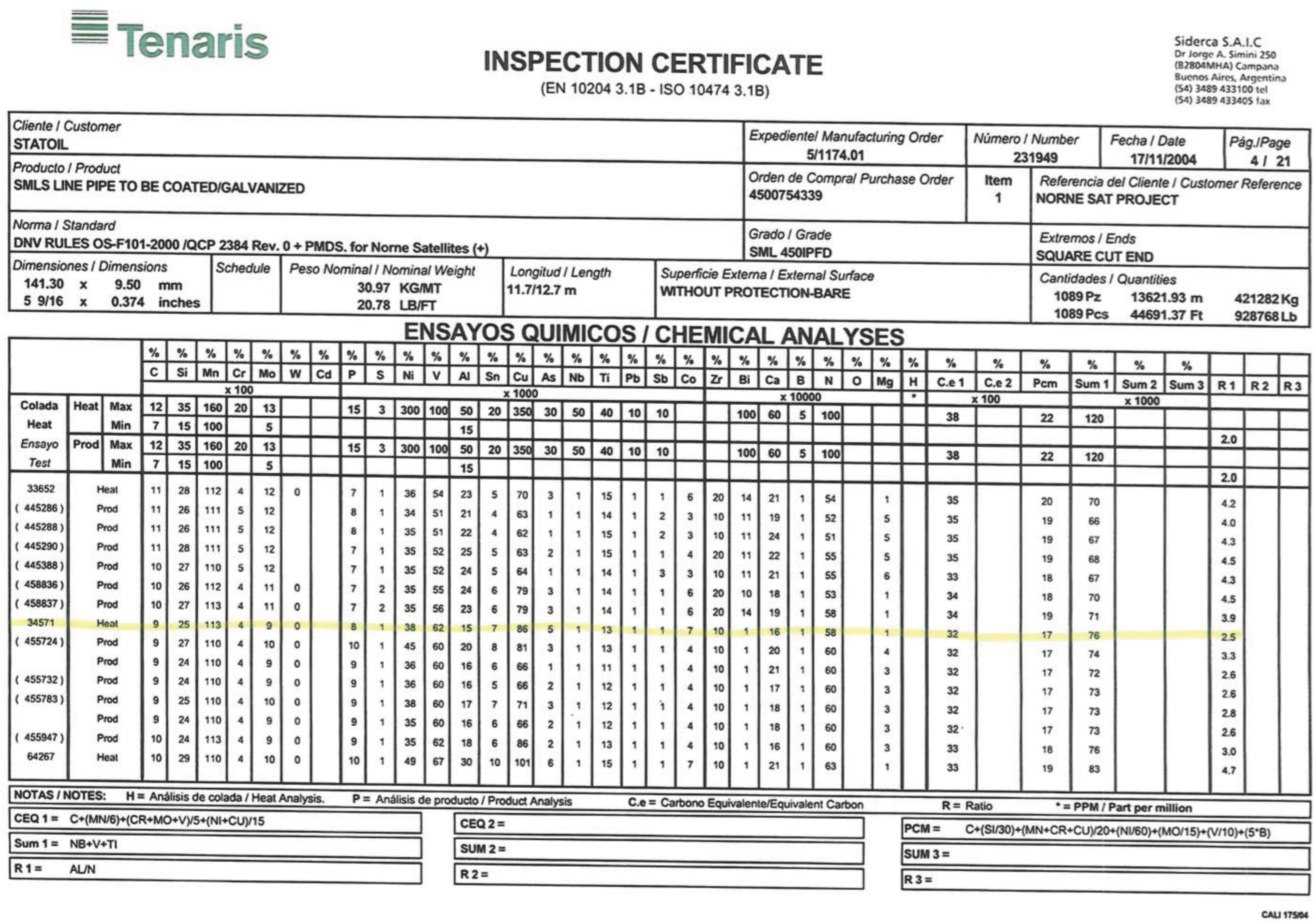

Tenaris

INSPECTION CERTIFICATE

(EN 10204 3.1B - ISO 10474 3.1B)

Siderca S.A.I.C
Dr Jorge A. Simini 250
(B2804MHA) Campana
Buenos Aires, Argentina
(54) 3489 433100 tel
(54) 3489 433405 fax

Cliente / Customer
STATOIL

Expediente/ Manufacturing Order
5/1174.01

Número / Number
231949

Fecha / Date
17/11/2004

Pág./Page
4 / 21

Producto / Product
SMLS LINE PIPE TO BE COATED/GALVANIZED

Orden de Compra/ Purchase Order
4500754339

Item
1

Referencia del Cliente / Customer Reference
NORNE SAT PROJECT

Norma / Standard
DNV RULES OS-F101-2000 /QCP 2384 Rev. 0 + PMDS. for Norne Satellites (+)

Grado / Grade
SML 450IPFD

Extremos / Ends
SQUARE CUT END

Dimensiones / Dimensions
141.30 x 9.50 mm
5 9/16 x 0.374 inches

Schedule

Peso Nominal / Nominal Weight
30.97 KG/MT
20.78 LB/FT

Longitud / Length
11.7/12.7 m

Superficie Externa / External Surface
WITHOUT PROTECTION-BARE

Cantidades / Quantities
1089 Pz 13621.93 m 421282 Kg
1089 Pcs 44691.37 Ft 928768 Lb

ENSAYOS QUIMICOS / CHEMICAL ANALYSES

			%	%	%	%	%	%	%	%	%	%	%	%	%	%	%	%	%	%	%	%
			C	Si	Mn	Cr	Mo	W	Cd	P	S	Ni	V	Al	Sn	Cu	As	Nb	Ti	Pb	Sb	Co
			x 100							x 1000												
Colada Heat	Heat	Max	12	35	160	20	13			15	3	300	100	50	20	350	30	50	40	10	10	
		Min	7	15	100		5							15								
Ensayo Test	Prod	Max	12	35	160	20	13			15	3	300	100	50	20	350	30	50	40	10	10	
		Min	7	15	100		5							15								
33652	Heat		11	28	112	4	12	0		7	1	36	54	23	5	70	3	1	15	1	1	6
(445286)	Prod		11	26	111	5	12			8	1	34	51	21	4	63	1	1	14	1	2	3
(445288)	Prod		11	26	111	5	12			8	1	35	51	22	4	62	1	1	15	1	2	3
(445290)	Prod		11	28	111	5	12			7	1	35	52	25	5	63	2	1	15	1	1	4
(445388)	Prod		10	27	110	5	12			7	1	35	52	24	5	64	1	1	14	1	3	3
(458836)	Prod		10	26	112	4	11	0		7	2	35	55	24	6	79	3	1	14	1	1	6
(458837)	Prod		10	27	113	4	11	0		7	2	35	56	23	6	79	3	1	14	1	1	6
34571	Heat		9	25	113	4	9	0		8	1	38	62	15	7	86	5	1	13	1	1	7
(455724)	Prod		9	27	110	4	10	0		10	1	45	60	20	8	81	3	1	13	1	1	4
	Prod		9	24	110	4	9	0		9	1	36	60	16	6	66	1	1	11	1	1	4
(455732)	Prod		9	24	110	4	9	0		9	1	36	60	16	5	66	2	1	12	1	1	4
(455783)	Prod		9	25	110	4	10	0		9	1	38	60	17	7	71	3	1	12	1	1	4
	Prod		9	24	110	4	9	0		9	1	35	60	16	6	66	2	1	12	1	1	4
(455947)	Prod		10	24	113	4	9	0		9	1	35	62	18	6	86	2	1	13	1	1	4
64267	Heat		10	29	110	4	10	0		10	1	49	67	30	10	101	6	1	15	1	1	7

			%	%	%	%	%	%	%	%	%	%	%	%	%	%			
			Zr	Bi	Ca	B	N	O	Mg	H	C.e 1	C.e 2	Pcm	Sum 1	Sum 2	Sum 3	R 1	R 2	R 3
			x 10000							*	x 100			x 1000					
Colada Heat	Heat	Max		100	60	5	100				38		22	120					
		Min															2.0		
Ensayo Test	Prod	Max		100	60	5	100				38		22	120					
		Min															2.0		
33652	Heat		20	14	21	1	54		1		35		20	70			4.2		
(445286)	Prod		10	11	19	1	52		5		35		19	66			4.0		
(445288)	Prod		10	11	24	1	51		5		35		19	67			4.3		
(445290)	Prod		20	11	22	1	55		5		35		19	68			4.5		
(445388)	Prod		10	11	21	1	55		6		33		18	67			4.3		
(458836)	Prod		20	10	18	1	53		1		34		18	70			4.5		
(458837)	Prod		20	14	19	1	58		1		34		19	71			3.9		
34571	Heat		10	1	16	1	58		1		32		17	76			2.5		
(455724)	Prod		10	1	20	1	60		4		32		17	74			3.3		
	Prod		10	1	21	1	60		3		32		17	72			2.6		
(455732)	Prod		10	1	17	1	60		3		32		17	73			2.6		
(455783)	Prod		10	1	18	1	60		3		32		17	73			2.8		
	Prod		10	1	18	1	60		3		32		17	73			2.6		
(455947)	Prod		10	1	16	1	60		3		33		18	76			3.0		
64267	Heat		10	1	21	1	63		1		33		19	83			4.7		

NOTAS / NOTES: H = Análisis de colada / Heat Analysis. P = Análisis de producto / Product Analysis C.e = Carbono Equivalente/Equivalent Carbon R = Ratio * = PPM / Part per million

CEQ 1 = C+(MN/6)+(CR+MO+V)/5+(NI+CU)/15
CEQ 2 =
PCM = C+(SI/30)+(MN+CR+CU)/20+(NI/60)+(MO/15)+(V/10)+(5*B)
Sum 1 = NB+V+TI
SUM 2 =
SUM 3 =
R 1 = AL/N
R 2 =
R 3 =

CALI 175/04

Figure A.1: Material Certificate for Steel Grade X65

B Measurement of Pipes

The following appendix contains data from the measurements of Pipe 1, Pipe 2 and Pipe 3.

The pipes were measured with respect to thickness and inner diameter. This was done to identify possible variations throughout the pipes. The thickness was measured by a PosiTector Ultrasonic Thickness Gage (UTG), while the inner diameter was measured by a digital calliper. First, the accuracy of the measurement tools was investigated. This was done by taking 30 measurements of the same point. From this the variance and the standard deviation of the measurements was found. The results from this investigation is presented in Table B.1. The accuracy of the UTG was also checked by measuring the thickness at various points, using a micro meter in addition to the UTG. Here, an average error in the UTG measurements was found in addition to the associated variance and standard deviation, see Table B.2.

The thickness was measured at eight circumferential points at five different sections along the span. Figure B.1 shows the location of these sections as well as the reference direction of the pipes, which is named North, East, South and West. The eight thickness measurements at each section was named N, NE, E, SE, S, SW, W and NW. The result was 40 thickness measurements for each pipe, which is presented in Table B.4, Table B.5 and Table B.6. In addition, the average thickness, the variance and the standard deviation for each pipe is presented.

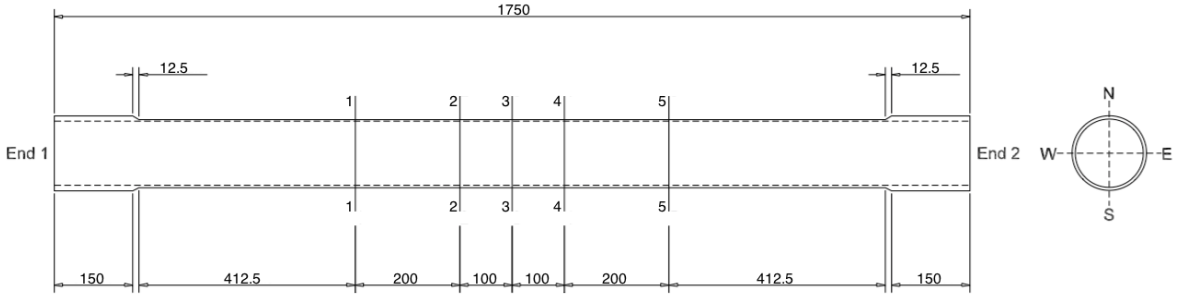

Figure B.1: Locations for thickness measurements.

The inner diameter was measured at four different directions at both ends of the pipes. These were named N-S, E-W, NE-SW and NW-SE, where the directions refers to Figure B.1. Measured inner diameter is presented in Table B.3. In addition, the average inner diameter, the variance and the standard deviation for each pipe is presented.

Table B.1: Accuracy of measurements.

Test number	Thickness [mm]	Test number	Diameter [mm]
1	3,59	1	122,49
2	3,60	2	122,56
3	3,64	3	122,50
4	3,58	4	122,44
5	3,62	5	122,41
6	3,58	6	122,63
7	3,60	7	122,47
8	3,58	8	122,50
9	3,68	9	122,45
10	3,63	10	122,62
11	3,60	11	122,49
12	3,64	12	122,50
13	3,61	13	122,54
14	3,63	14	122,53
15	3,59	15	122,54
16	3,60	16	122,53
17	3,58	17	122,55
18	3,61	18	122,49
19	3,60	19	122,49
20	3,63	20	122,48
21	3,62	21	122,58
22	3,60	22	122,52
23	3,66	23	122,53
24	3,59	24	122,50
25	3,60	25	122,48
26	3,61	26	122,53
27	3,61	27	122,48
28	3,59	28	122,45
29	3,60	29	122,54
30	3,59	30	122,45
t_{avg}	**3,61**	**D_{avg}**	**122,51**
Var(t)	**0,000564889**	**Var(D)**	**0,002395667**
St.dev(t)	**0,023767391**	**St.dev(D)**	**0,048945548**

Table B.2: Comparison between Micro Meter and UTG thickness measurements at pipe ends.

		Mikrometer				Ultrasonic			
		1	2	3	4	1	2	3	4
Pipe 2 End 1	N	9,52	9,50	9,53	9,51	9,69	9,69	9,68	9,68
	W	9,05	9,03	9,02	9,03	9,17	9,15	9,16	9,17
	S	9,27	9,27	9,26	9,26	9,51	9,53	9,54	9,52
	E	9,73	9,74	9,72	9,74	9,89	9,88	9,88	9,89
Pipe 2 End 2	N	9,19	9,20	9,20	9,21	9,27	9,26	9,27	9,28
	W	9,17	9,17	9,16	9,16	9,23	9,23	9,25	9,23
	S	9,40	9,39	9,39	9,40	9,45	9,46	9,47	9,46
	E	9,59	9,60	9,58	9,59	9,66	9,67	9,68	9,67
Pipe 3 End 1	N	9,60	9,61	9,63	9,61	9,78	9,81	9,82	9,78
	W	9,28	9,27	9,25	9,27	9,43	9,43	9,43	9,43
	S	9,68	9,69	9,66	9,68	9,80	9,81	9,82	9,84
	E	9,93	9,96	9,94	9,93	10,09	10,07	10,08	10,09
Pipe 3 End 2	N	9,40	9,37	9,42	9,41	9,66	9,66	9,60	9,61
	W	9,42	9,41	9,41	9,42	9,55	9,56	9,56	9,56
	S	9,89	9,87	9,92	9,89	10,14	10,14	10,15	10,15
	E	9,93	9,96	9,95	9,93	10,24	10,26	10,28	10,29

		Error: Ultrasonic - Mikrometer			
		1	2	3	4
Pipe 2 End 1	N	0,17	0,19	0,15	0,17
	W	0,12	0,12	0,14	0,14
	S	0,24	0,26	0,28	0,26
	E	0,16	0,14	0,16	0,15
Pipe 2 End 2	N	0,08	0,06	0,07	0,07
	W	0,06	0,06	0,09	0,07
	S	0,05	0,07	0,08	0,06
	E	0,07	0,07	0,10	0,08
Pipe 3 End 1	N	0,18	0,20	0,19	0,17
	W	0,15	0,16	0,18	0,16
	S	0,12	0,12	0,16	0,16
	E	0,16	0,11	0,14	0,16
Pipe 3 End 2	N	0,26	0,29	0,18	0,20
	W	0,13	0,15	0,15	0,14
	S	0,25	0,27	0,23	0,26
	E	0,31	0,30	0,33	0,36

Average error	0,16
Var(error)	0,00563906
St.dev(error)	0,07509369

Table B.3: Inner diameter measurements of all pipes.

	Pipe 1		Pipe 2		Pipe 3	
Position/Side	1	2	1	2	1	2
N-S	122,23	122,36	122,85	122,83	122,40	122,42
E-W	122,38	122,38	122,85	122,84	122,14	122,09
NE-SW	122,17	122,36	122,66	122,80	122,33	122,35
NW-SE	122,38	122,21	122,63	122,47	122,02	122,26

	Pipe 1	Pipe 2	Pipe 3
D_{avg}	122,31	122,74	122,25
Var(D)	0,00696094	0,01716094	0,01981094
St.dev(D)	0,08343223	0,13099976	0,14075133

Table B.4: Thickness measurements of pipe 1.

Pipe 1

Position	1	2	3	4	5
N	3,55	3,80	3,96	4,02	3,94
N-E	3,68	3,86	4,10	3,91	3,81
E	4,21	4,37	4,50	4,26	4,18
S-E	4,45	4,57	4,44	4,29	4,35
S	4,62	4,58	4,50	4,48	4,69
S-W	4,30	4,20	4,13	4,30	4,43
W	4,15	3,97	4,06	4,24	4,43
N-W	3,59	3,59	3,69	3,91	3,88

t_{avg}	4,15
Var(t)	0,09523244
St.dev(t)	0,30859753

Table B.5: Thickness measurements of pipe 2.

Pipe 2

Position	1	2	3	4	5
N	3,71	3,91	3,97	3,88	3,74
N-E	3,97	4,07	4,12	3,94	3,83
E	4,10	4,14	4,15	3,95	3,97
S-E	4,31	4,26	4,14	4,06	4,24
S	3,90	3,80	3,77	3,85	4,07
S-W	3,82	3,66	3,79	3,81	4,09
W	3,60	3,62	3,76	3,90	3,94
N-W	3,63	3,75	3,78	3,94	3,81

t_{avg}	3,92
Var(t)	0,03233594
St.dev(t)	0,17982196

Table B.6: Thickness measurements of pipe 3.

Pipe 3

Position	1	2	3	4	5
N	3,96	3,66	3,83	3,95	3,96
N-E	4,09	4,05	4,25	4,29	4,12
E	4,10	4,41	4,49	4,42	4,15
S-E	3,97	4,44	4,50	4,34	4,15
S	3,93	4,18	4,17	4,11	4,08
S-W	4,13	4,06	3,93	3,92	4,20
W	3,82	3,61	3,48	3,45	3,90
N-W	3,92	3,63	3,62	3,72	3,93

t_{avg}	4,02
Var(t)	0,069881
St.dev(t)	0,26435015

C Material Input

Combined Material Model

Input for combined isotropic/kinematic material model using mm, s and $tons/mm^3$.

```
*Material, Name = x65
*Density
 7.85000e-09
*Include, input = depvar_SMM.inc
*User material, Constants = 27
**      EFLAG,         YFLAG,      RMAPFLAG,         HFLAG,         VFLAG
           1,             1,             0,            12,             0
**      TFLAG,         DFLAG,         SFLAG,        STFLAG,             E
           0,             1,             0,             0,  2.08000e+05
**         PR,        SIGMA0,       THETAR1,          QR1,       THETAR2
 3.00000e-01,  2.99000e+02,  4.00000e+03,  1.60000e+02,  1.00000e+02
**        QR2,       THETAR3,          QR3,       THETAX1,          QX1
 4.00000e+02,  0.00000e+00,  0.00000e+00,  5.04010e+04,  1.29000e+02
**    THETAX2,          QX2,         BETA,          DCR             s0
 1.27900e+03,  1.00000e+02,  0.00000e+00,            1,  1.59500e+03
**        Phi,        Gamma
 1.00000e+00,  1.00000e+00
```

Isotropic Material Model 1

Input for isotropic material model using mm, s and $tons/mm^3$.

```
*Material, Name = x65
*Density
 7.85000e-9
*Include, input = depvar_SMM.inc
*User material, Constants = 23
**     EFLAG,        YFLAG,     RMAPFLAG,        HFLAG,        VFLAG
           1,            1,            0,            1,            0
**     TFLAG,        DFLAG,        SFLAG,       STFLAG,            E
           0,            1,            0,            0,  2.08000e+05
**        PR,       SIGMA0,      THETAR1,          QR1,      THETAR2
 3.00000e-01,  4.65500e+02,  3.79500e+02,  6.27100e+02,  2.20700e+03
**       QR2,      THETAR3,          QR3,         BETA,          DCR
 1.27100e+02,            0,            0,            0,            1
**        s0,          Phi,        Gamma
 1.59500e+03,  1.00000e+00,  1.00000e+00
```

Isotropic Material Model 2

Input for isotropic material model using m, s and kg/m^3.

```
*Material, Name = x65
*Density
 7.85000e+3
*Include, input = depvar_SMM.inc
*User material, Constants = 23
**      EFLAG,         YFLAG,      RMAPFLAG,         HFLAG,         VFLAG
           1,             1,             0,             1,             0
**      TFLAG,         DFLAG,         SFLAG,        STFLAG,             E
           0,             1,             0,             0,  2.08000e+11
**         PR,        SIGMA0,       THETAR1,           QR1,       THETAR2
 3.00000e-01,  4.65500e+08,  3.79500e+08,  6.27100e+08,  2.20700e+09
**        QR2,       THETAR3,           QR3,         BETA,           DCR
 1.27100e+08,             0,             0,             0,             1
**         s0,           Phi,         Gamma
 1.59500e+09,  1.00000e+00,  1.00000e+00
```

D Principal Rig Drawings

The following appendix contains the principal rig drawings, which includes:

- Drawing with original pipe dimensions
- Drawing of pipe-rig connection
- Drawing of the water accumulator system

Note that the pipes were not used as sketched, as they needed to be shortened in order to fit the rig.

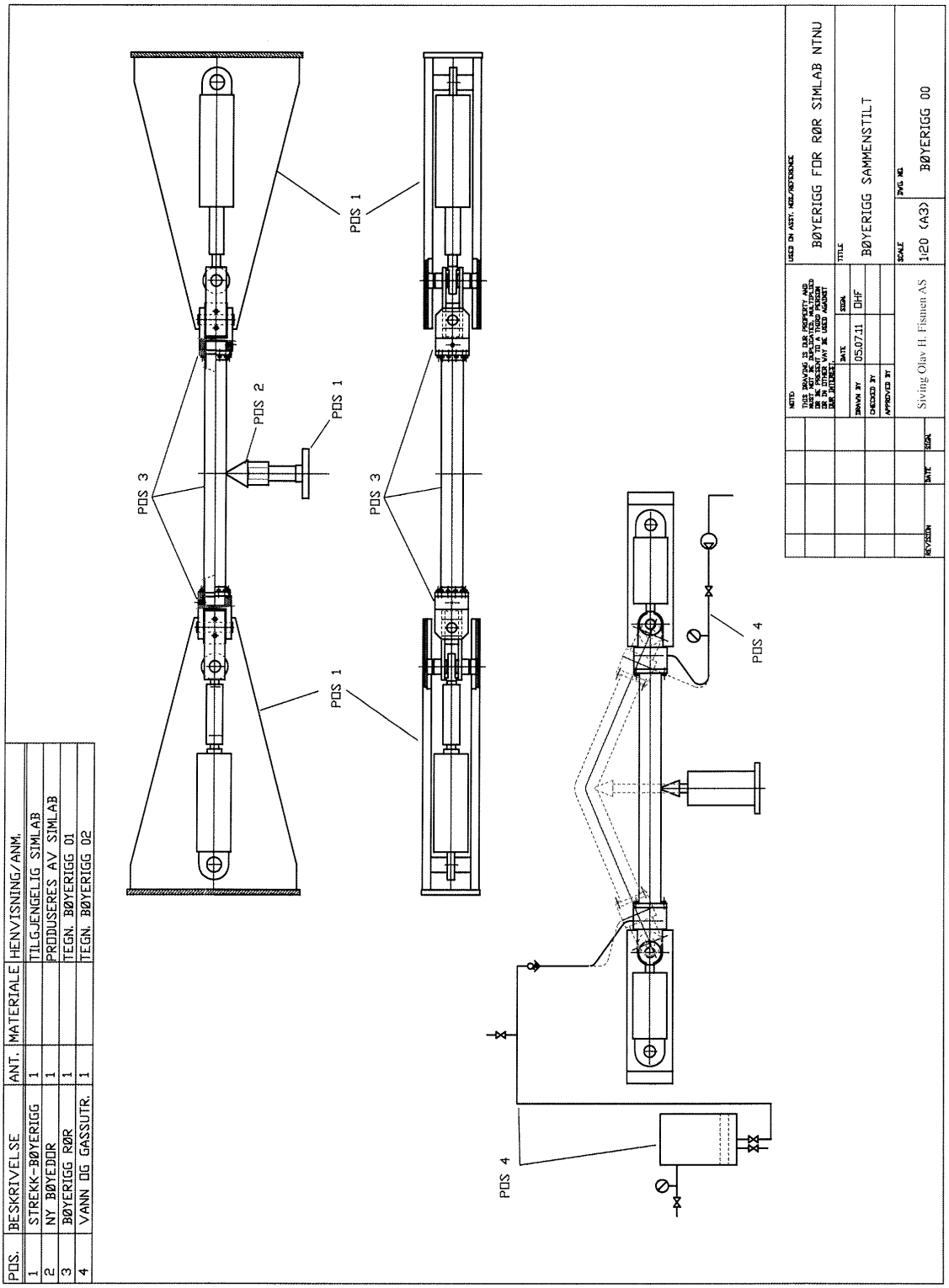
POS. | BESKRIVELSE | ANT. | MATERIALE | HENVISNING/ANM.
1 | STREKK-BØYERIGG | 1 | | TILGJENGELIG SIMLAB
2 | NY BØYEDØR | 1 | | PRODUSERES AV SIMLAB
3 | BØYERIGG RØR | 1 | | TEGN. BØYERIGG 01
4 | VANN OG GASSUTR. | 1 | | TEGN. BØYERIGG 02
POS 1
POS 2
POS 3
POS 4
BØYERIGG FOR RØR SIMLAB NTNU
BØYERIGG SAMMENSTILT
Siving Olav H. Fismen AS
1:20 (A3)
BØYERIGG 00

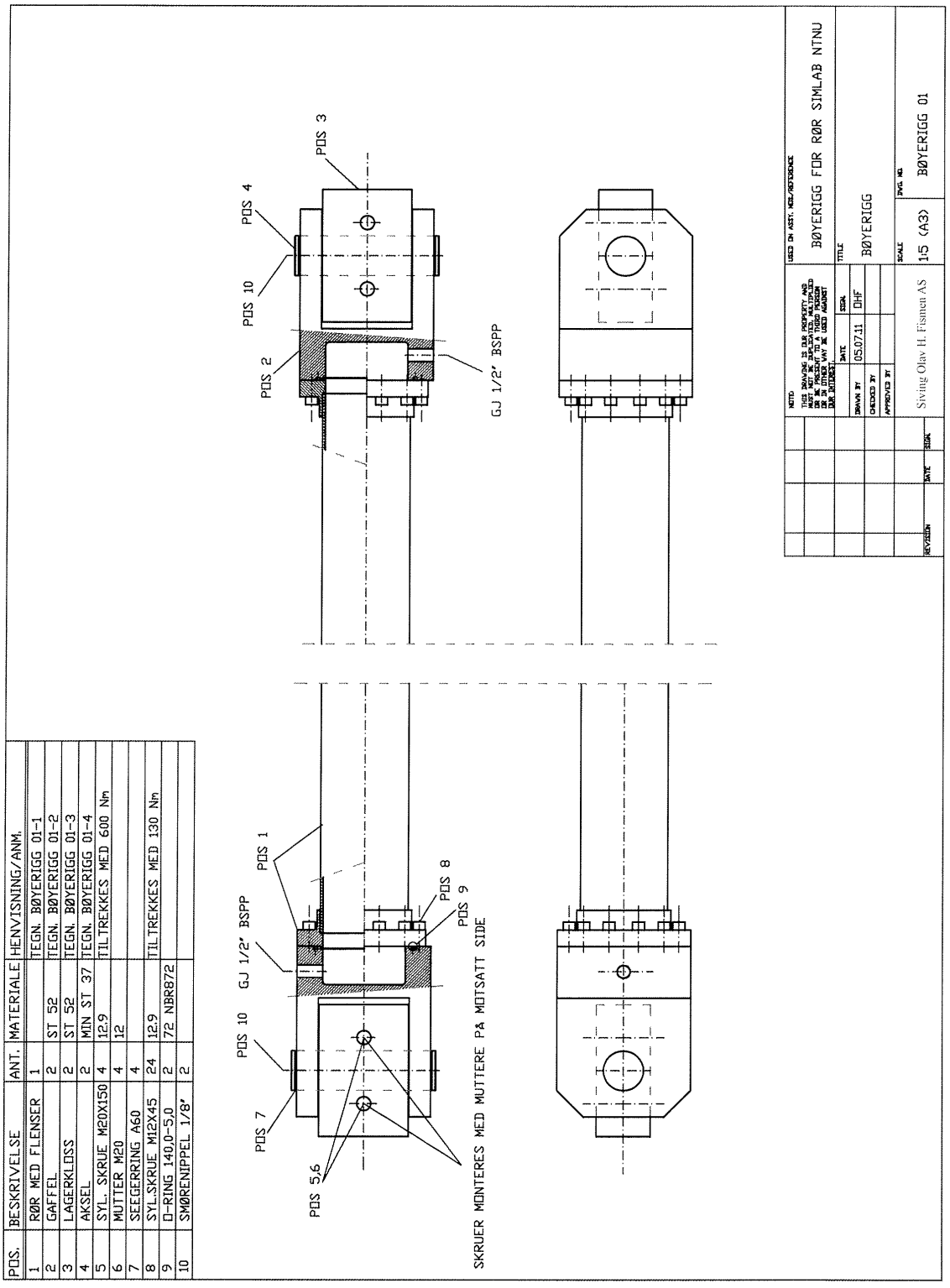
POS. | BESKRIVELSE | ANT. | MATERIALE | HENVISNING/ANM.
1 | RØR MED FLENSER | 1 | | TEGN. BØYERIGG 01-1
2 | GAFFEL | 2 | ST 52 | TEGN. BØYERIGG 01-2
3 | LAGERKLOSS | 2 | ST 52 | TEGN. BØYERIGG 01-3
4 | AKSEL | 2 | MIN ST 37 | TEGN. BØYERIGG 01-4
5 | SYL. SKRUE M20X150 | 4 | 12.9 | TILTREKKES MED 600 Nm
6 | MUTTER M20 | 4 | 12 |
7 | SEEGERRING A60 | 4 | | |
8 | SYL.SKRUE M12X45 | 24 | 12.9 | TILTREKKES MED 130 Nm
9 | O-RING 140,0-5,0 | 2 | 72 NBR872 |
10 | SMØRENIPPEL 1/8" | 2 | |
POS 1
POS 2
POS 3
POS 4
POS 5,6
POS 7
POS 8
POS 9
POS 10
GJ 1/2" BSPP
GJ 1/2" BSPP
SKRUER MONTERES MED MUTTERE PÅ MOTSATT SIDE
NOTE
DRAWN BY
DATE
05.07.11
SIGN
DHF
CHECKED BY
APPROVED BY
REVISION
Sving Olav H. Fismen AS
BØYERIGG FOR RØR SIMLAB NTNU
BØYERIGG
SCALE
1:5 (A3)
BØYERIGG 01

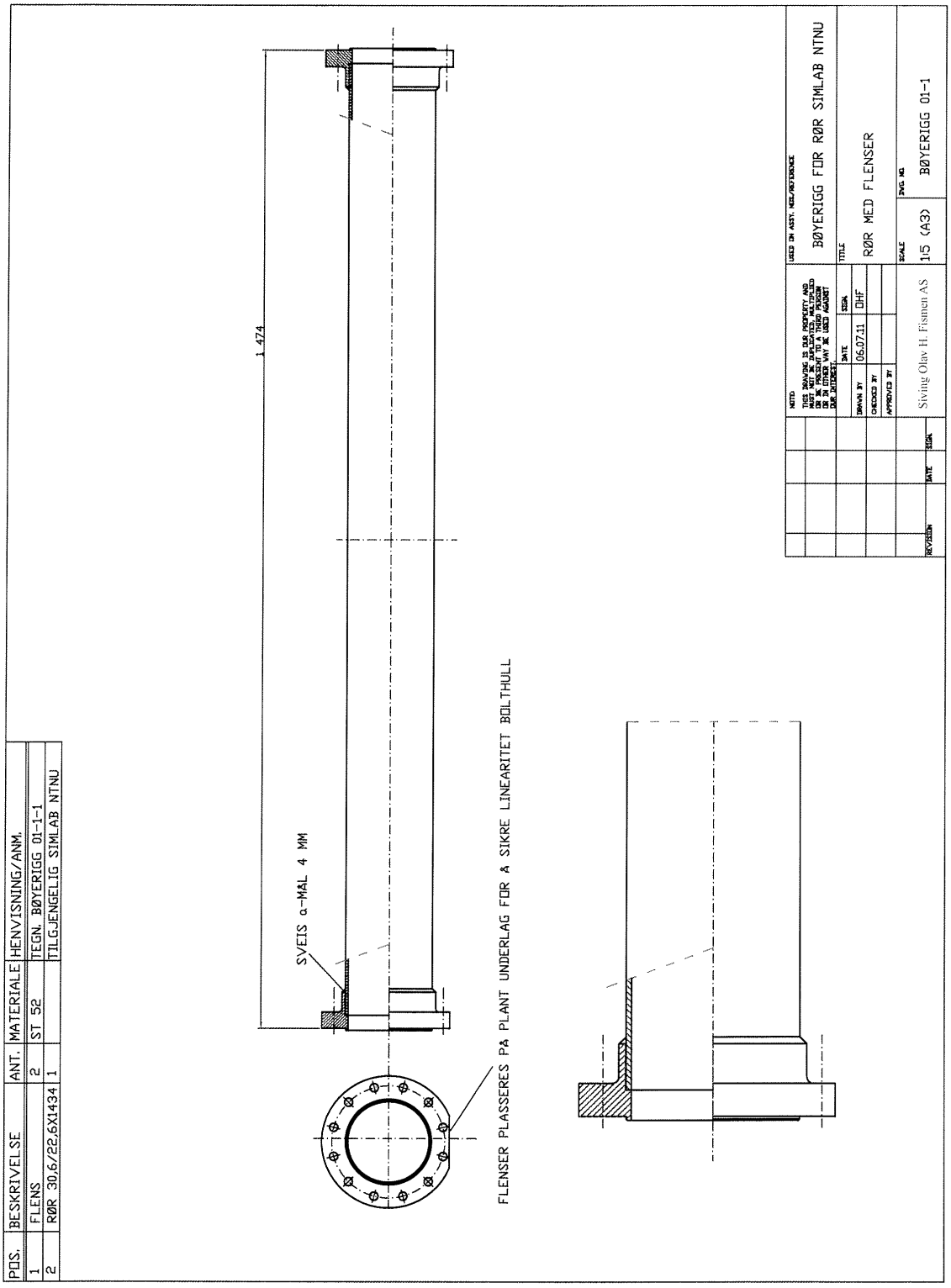
POS. BESKRIVELSE ANT. MATERIALE HENVISNING/ANM.
1 FLENS 2 ST 52 TEGN. BØYERIGG 01-1-1
2 RØR 30,6/22,6X1434 1 TILGJENGELIG SIMLAB NTNU
1 474
SVEIS a-MÅL 4 MM
FLENSER PLASSERES PÅ PLANT UNDERLAG FOR Å SIKRE LINEARITET BOLTHULL
BØYERIGG FOR RØR SIMLAB NTNU
RØR MED FLENSER
Siving Olav H. Fismen AS
1:5 (A3)
BØYERIGG 01-1

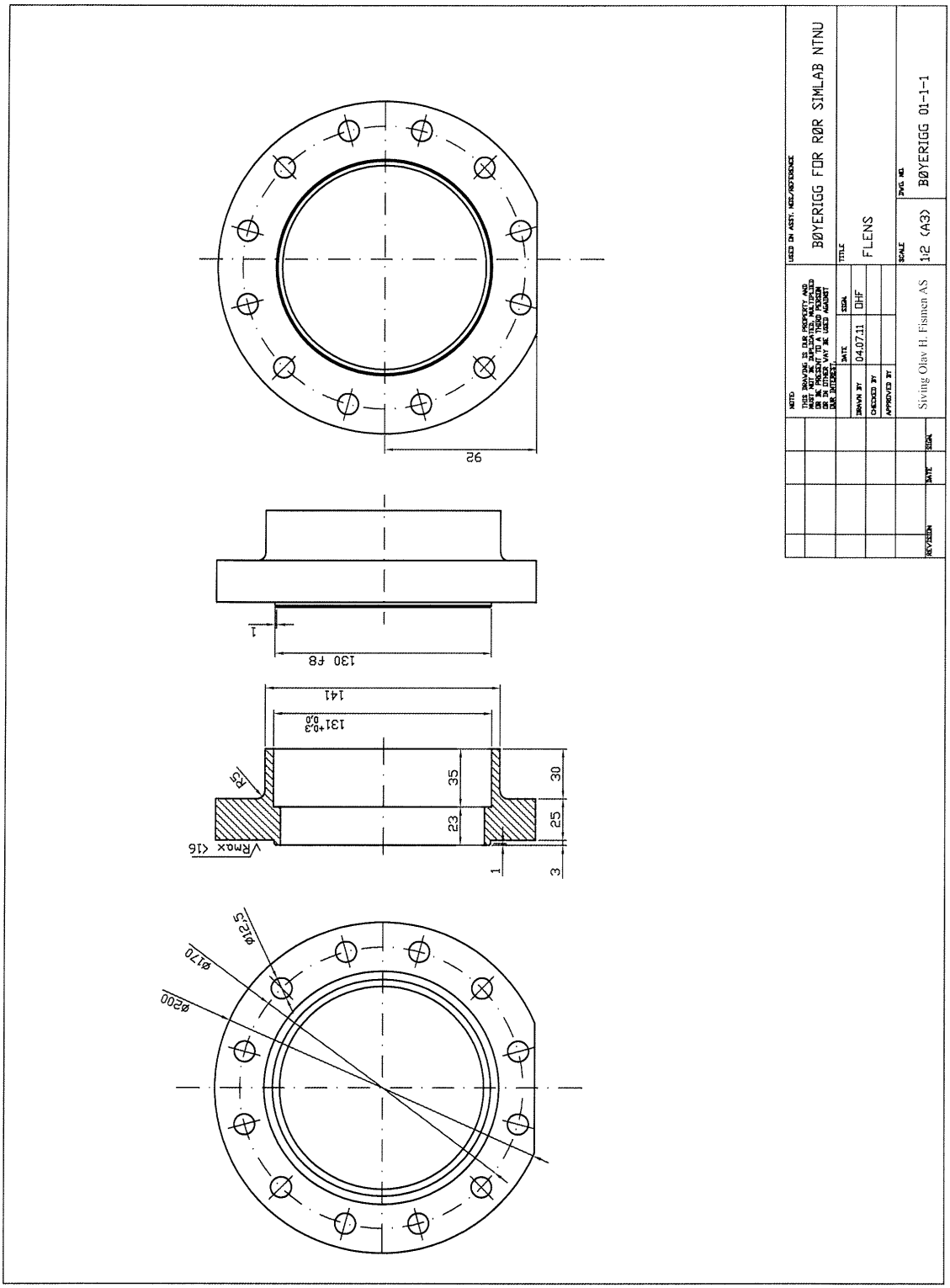
BØYERIGG FOR RØR SIMLAB NTNU
FLENS
BØYERIGG 01-1-1
1:2 (A3)
Siving Olav H. Fismen AS
04.07.11
DHF
92
130 f8
1
141
131+0.3
0
35
23
30
25
3
1
R5
√Rmax (16
Ø125
Ø170
Ø200

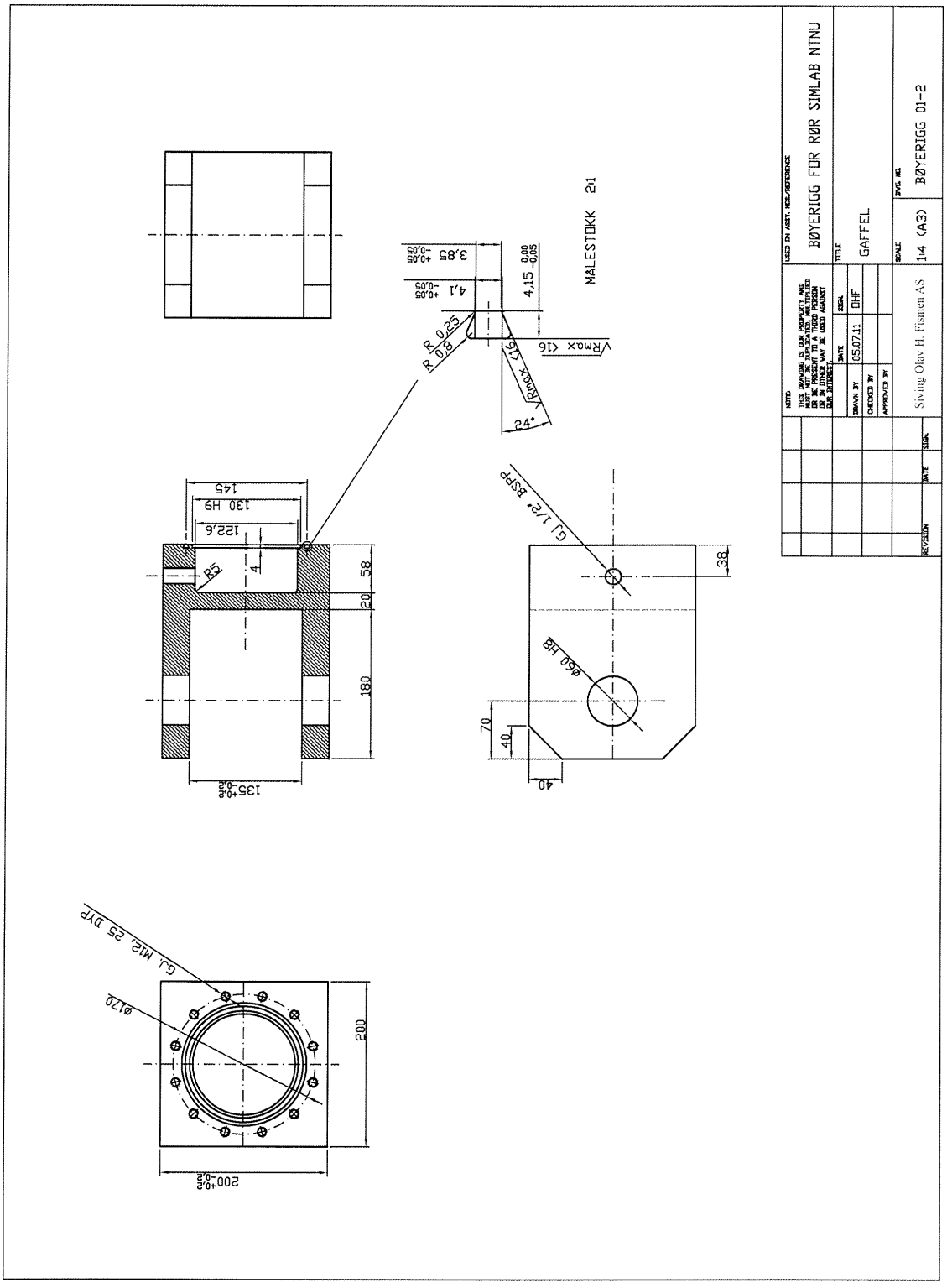
MÅLESTOKK 2:1
BØYERIGG FOR RØR SIMLAB NTNU
GAFFEL
BØYERIGG 01-2
14 (A3)
Siving Olav H. Fismen AS
05.07.11
DHF
Gj. M12 25 DYP
Ø170
200
180
58
20
4
38
40
70
24°

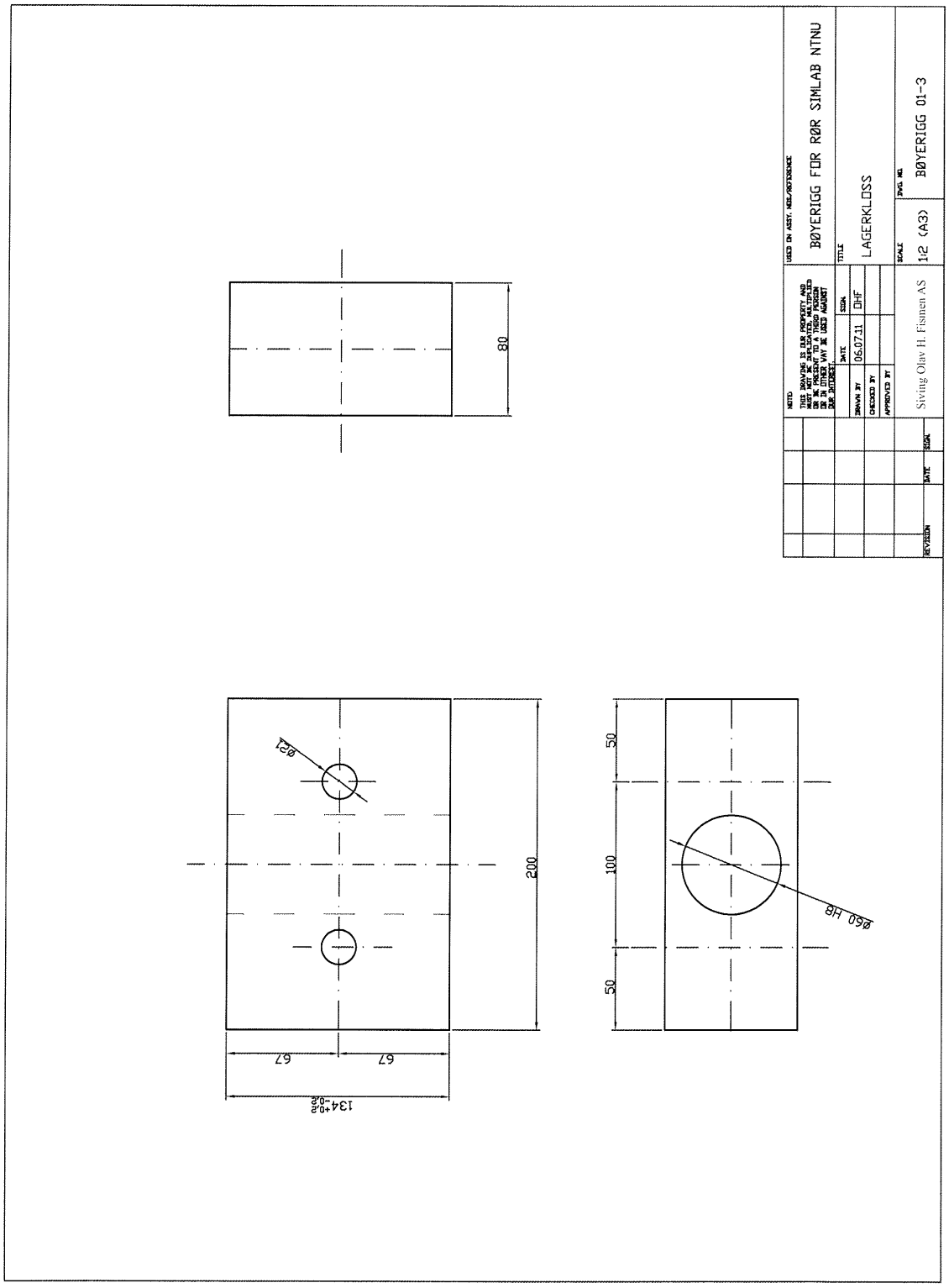
80
200
67
67
$134^{+0.8}_{-0.8}$
Ø20
50
100
50
Ø60 H8
BØYERIGG FOR RØR SIMLAB NTNU
LAGERKLOSS
06.07.11
DHF
1:2 (A3)
BØYERIGG 01-3
Siving Olav H. Fismen AS

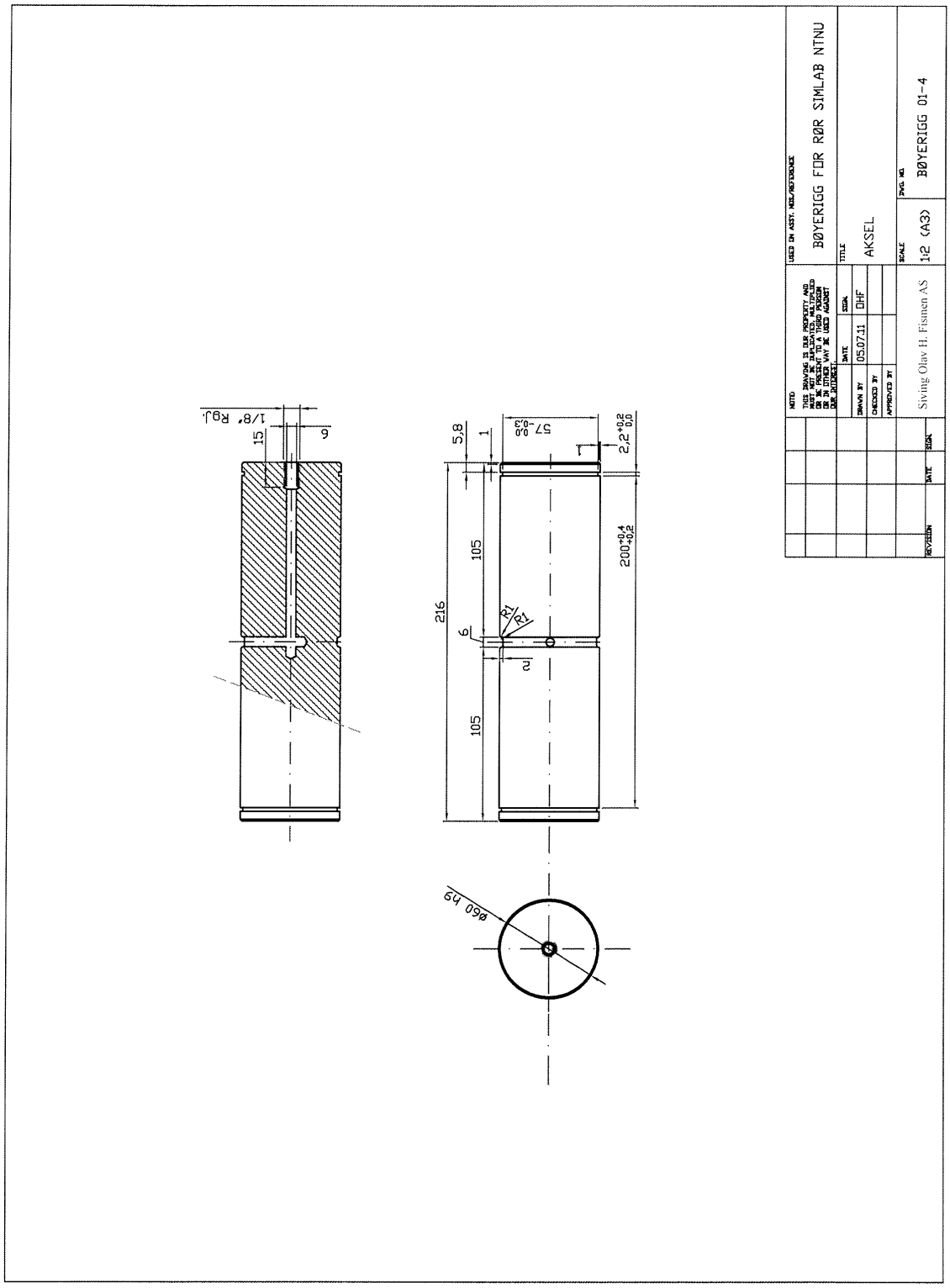
1/8" Rgj.
15
6
5,8
1
57 0,5
2,2+0,2 0,0
105
200+0,4 +0,2
216
6
R1
R1
12
105
Ø64 Ø60
BØYERIGG FOR RØR SIMLAB NTNU
AKSEL
DHF
05.07.11
12 (A3)
BØYERIGG 01-4
Sving Olav H. Fismen AS

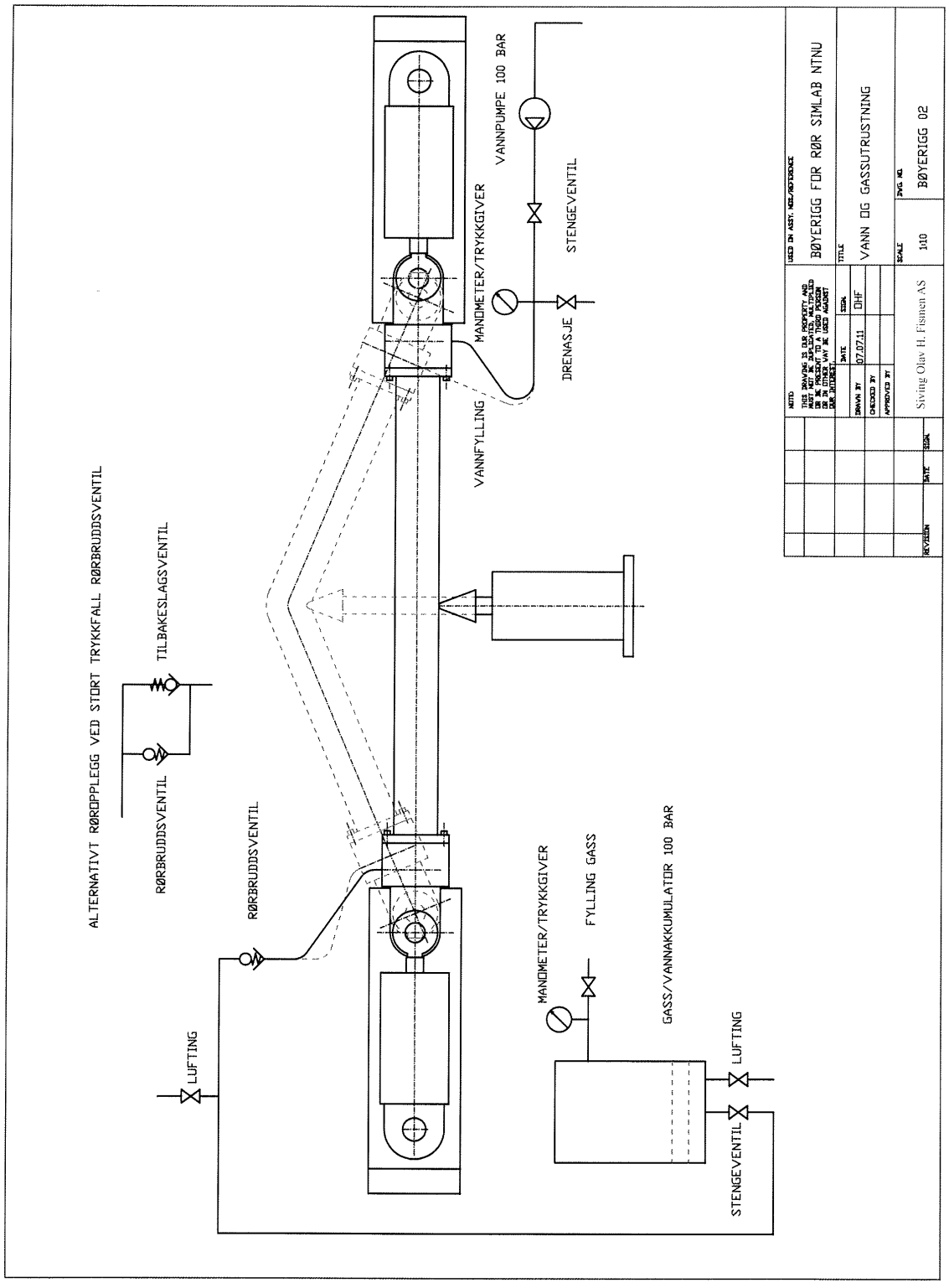
ALTERNATIVT RØROPPLEGG VED STORT TRYKKFALL RØRBRUDDSVENTIL
TILBAKESLAGSVENTIL
RØRBRUDDSVENTIL
RØRBRUDDSVENTIL
LUFTING
VANNFYLLING
MANOMETER/TRYKKGIVER
VANNPUMPE 100 BAR
STENGEVENTIL
DRENASJE
MANOMETER/TRYKKGIVER
FYLLING GASS
GASS/VANNAKKUMULATOR 100 BAR
LUFTING
STENGEVENTIL
BØYERIGG FOR RØR SIMLAB NTNU
VANN OG GASSUTRUSTNING
Sivng Olav H. Fismen AS
110
BØYERIGG 02

E Calibrations for Stretch Bending Rig

This appendix contains the current calibration data for the measuring equipment for the stretch bending rig. The calibration data for the vertical load cell is provided by the vendor and is given in Italian.

The other calibrations were done in the in the period 19.11.2012 - 18.03.2013 and are given in Norwegian.

The calibration data is presented in the following order:

1. Vertical Load Cell
2. Horizontal Position 1
3. Horizontal Position 2
4. Vertical Position
5. Angle at Rotation Point 1
6. Angle at Rotation Point 2
7. Horizontal Load Cell. Calibration for the horizontal load cell has since been corrected for the offset during the experiment for Pipe 3.
8. Vertical Amplifier

Calibrations done for the clinometers measuring the angles at the forks are not included here.

AEP transducers®

41010 Cognento (MODENA) Italy Via Bottego 33/A Tel. 059 346441 Fax. 059 346437
E-mail : aep@aep.it Internet: http://www.aep.it

Progettazione, produzione e vendita di:
- CELLE DI CARICO, DINAMOMETRI
- TRASDUTTORI DI PRESSIONE, MANOMETRI DIGITALI
- STRUMENTAZIONE ELETTRONICA

Design,manufacture and sale of:
- *LOAD CELLS, DYNAMOMETERS*
- *PRESSURE TRANSDUCERS, DIGITAL PRESSURE GAUGES*
- *ELECTRONIC INSTRUMENTS*

RAPPORTO DI TARATURA N° : 02716 13 C

Data : 17/01/2013

Collaudo eseguito secondo l'istruzione: IS-09-06-01-R2

SISTEMA CAMPIONE

Oggetto :	Macchina Campione di Forza	Dinamometro Campione :	Dinamometro
Costruttore	Galdabini	Costruttore	galdabini
Tipo :	MTC/1000	Tipo :	100t
N° di Serie :	33674	N° di Serie :	33847
Portata massima :	1000kN	Carico nominale:	1000kN

Campione munito di certificato valido di taratura N° 09-0487-02 (INRIM)

Incertezza della macchina campione (2σ) 500ppm

SISTEMA IN TARATURA

Oggetto :	Cella di carico	Sensibilità nominale :	2 mV/V
Costruttore	AEP transducers	Resistenza di Ingresso :	816 Ohm
Tipo :	TC430T	Resistenza di Uscita :	700 Ohm
N° di Serie :	912226	Alimentazione di riferimento :	10 V
Carico nominale:	30000 kg	Collegamento	4 Fili
Tipo di Taratura :	COMPRESSIONE	Lotto di Produzione n°:	10206

MISURE

MISURE kg	Carico ↓ mV/V	Scarico ↑ mV/V
0	0.0000	-0.0000
3000	0.1993	0.1992
6000	0.3993	0.3987
9000	0.5993	0.5987
12000	0.7992	0.7987
15000	0.9992	0.9987
18000	1.1992	1.1987
21000	1.3992	1.3987
24000	1.5992	1.5986
27000	1.7992	1.7987
30000	1.9999	

Errore di Linearità : 0.036 %
Errore di Zero : -0.001 %
Errore di Isteresi : -0.030 %

Operatore Tecnico : Incerti Mirco

Il Centro di taratura ACCREDIA LAT N°093 collabora con i settori di produzione della AEP transducers per assicurare la riferibilità delle misure al Sistema Internazionale delle Unità (SI)

Kalibrering horisontalposisjon X1

Dato: 19.11.2012

Målt mm	Forskøvet mm	Målt V
579	-138	-9.00
549	-108	-7.01
519	-78	-5.00
488	-47	-3.00
457	-16	-1.00
441	0	0.00
426	15	1.00
395	46	3.00
363	78	5.01
332	109	7.01
302	139	9.01

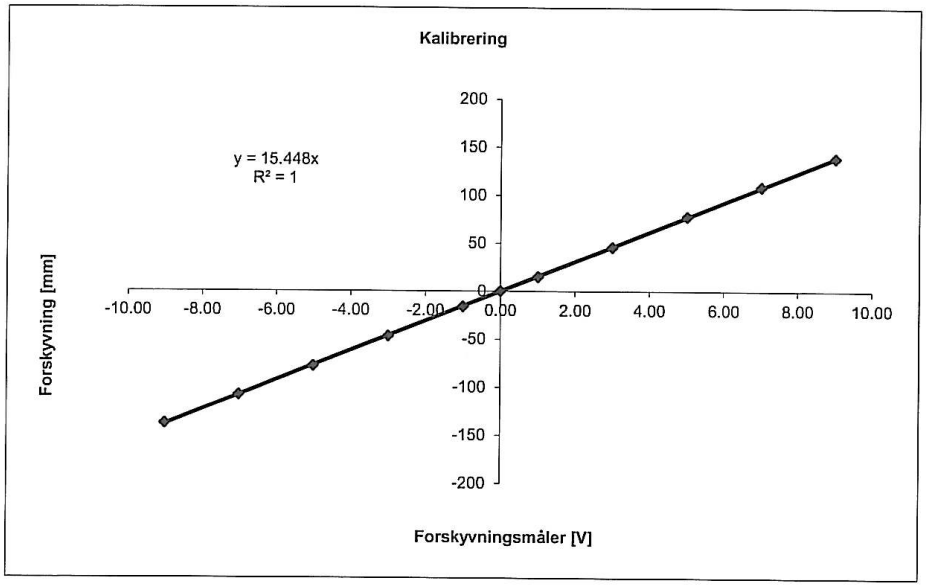

Faktor: 10V = 154.48mm

Kalibrering horisontalposisjon X2

Dato: 19.11.2012

Målt mm	Forskøvet mm	Målt V
543	-140	-9.01
512	-109	-7.01
481	-78	-5.00
450	-47	-3.00
419	-16	-1.00
403	0	0.00
388	15	1.01
357	46	3.01
325	78	5.02
295	108	7.01
264	139	9.02

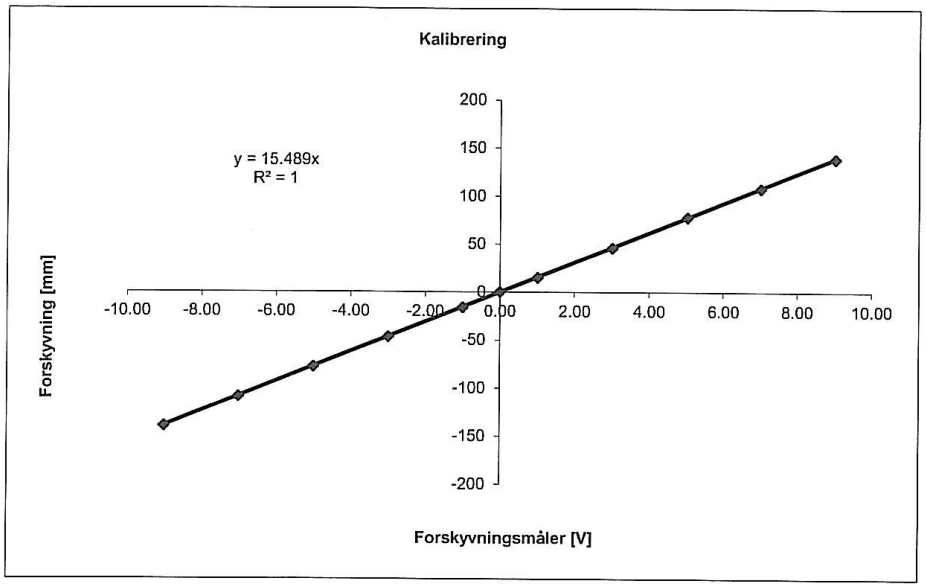

Faktor: 10V = 154.89mm

Kalibrering vertikalposisjon

Dato: 19.11.2012

Målt mm	Forskøvet mm	Målt V
418	-229	-9.00
469	-178	-7.00
519	-128	-5.00
570	-77	-3.00
621	-26	-1.00
647	0	0.00
673	26	1.00
724	77	3.00
775	128	5.00
825	178	7.00
877	230	9.00

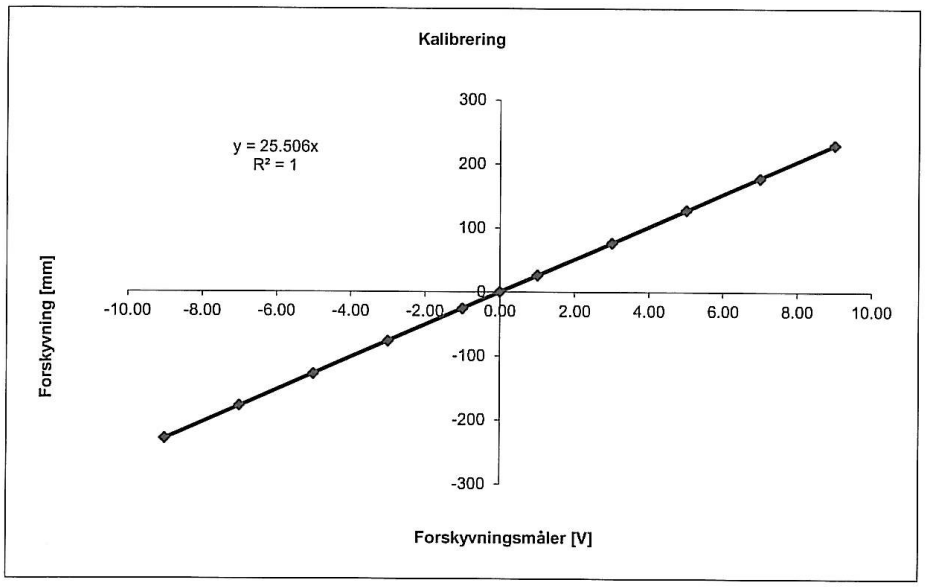

Faktor: 10V = 255.06mm

Kalibrering Vinkel X1

Dato: 19.11.2012

Målt Deg	Målt V
-15.8	-1.02
-1.9	-0.19
4.6	0.21
11.1	0.61
17.5	0.99
23.6	1.36
28.6	1.67
32.9	1.92

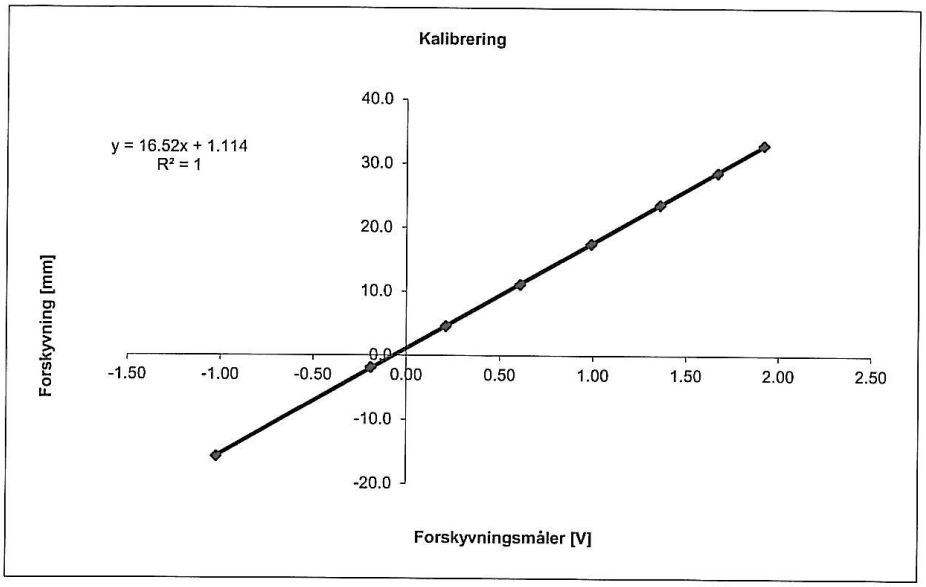

Faktor: 1V = 16.52Deg

Kalibrering Vinkel X2

Dato: 19.11.2012

Målt Deg	Målt V
-12.2	-0.75
-1.9	-0.13
3.2	0.18
8.4	0.49
13.6	0.81
18.7	1.11
23.0	1.37
30.3	1.80

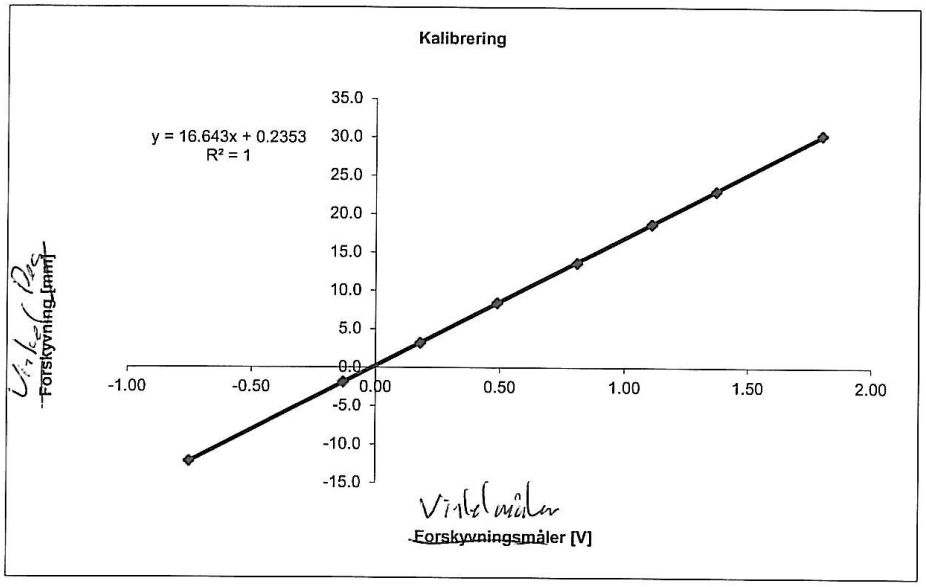

Faktor: 1V = 16.64Deg

Kalibrering horisontal lastcelle

Dato: 11.03.2013
Ref Celle: NKT584 (300kN)

Ønsket	Referanse Lastcelle	Målt	Korrigert 0.9856
	0.7	0.9	0.9
10	10.1	10.1	10.0
30	20.5	20.7	20.4
30	30.9	31.4	30.9
40	41.4	42.2	41.6
50	51.8	52.8	52.0
75	78.1	79.7	78.6
100	104.5	106.3	104.8
125	130.7	132.7	130.8
150	157.2	159.6	157.3
175	183.8	186.3	183.6
190	199.9	202.4	199.5

0.98561009

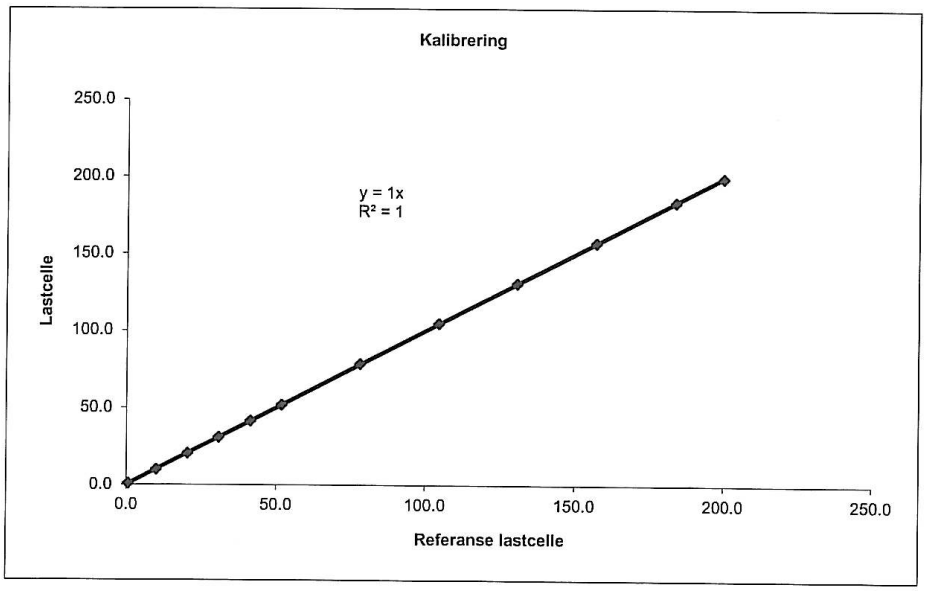

Faktor: 10V = 325.2kN

Kalibrering vertikal forsterker

Dato: 18.03.2013

Referanse mV/V	Målt V	Korrigert
-2.00	-10.394	-10.457
-0.50	-2.542	-2.605
-0.20	-0.977	-1.040
-0.10	-0.456	-0.519
-0.05	-0.195	-0.258
0.00	0.063	0.000
0.05	0.325	0.262
0.10	0.586	0.523
0.20	1.107	1.044
0.50	2.672	2.609
2.00	10.508	10.445

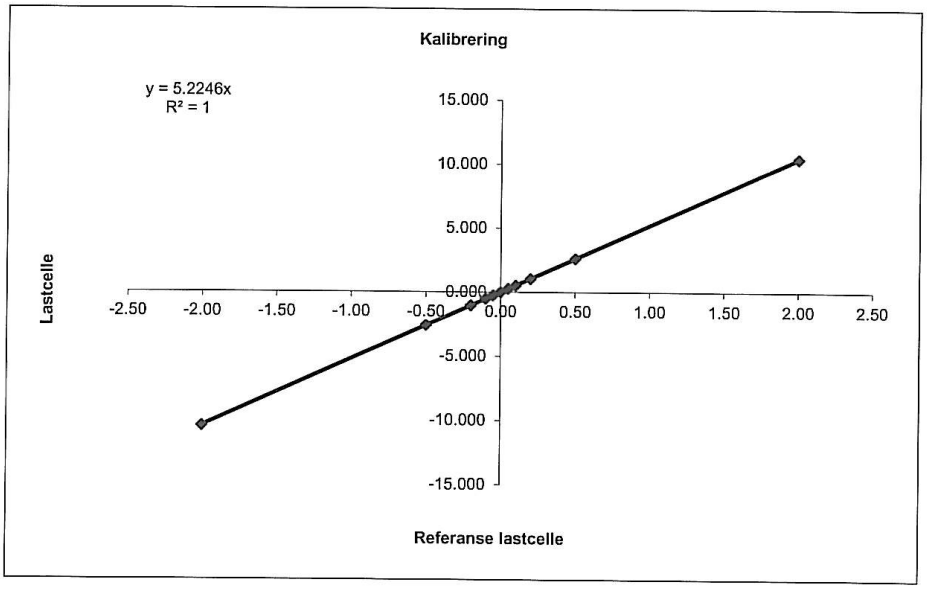

Faktor: 2mv/V celle ganges med 0.957 for maks utslag

50 kN: 10V= 47.85kN

300kN: 10V= 287.1kN